



**NIFS-PROC-91**

JSPS-NRF-NSFC A3 Foresight Program Seminar Proceedings of  
Japan-China Joint Seminar on Atomic and Molecular Processes  
in Plasma

July 30 – August 4, 2012, Lanzhou, China

Edited by Fumihiro Koike, Chenzhong Dong, and Xiaobin Ding

Feb. 01, 2013

**JSPS-NRF-NSFC A3 Foresight Program Seminar**  
**Proceedings of Japan-China Joint Seminar on Atomic and**  
**Molecular Processes in Plasma**

July 30 – August 4, 2012, Lanzhou, China

Edited by

Fumihiro Koike, Chenzhong Dong, and Xiaobin Ding

**Abstract**

As one of the activities of JSPS-NRF-NSFC A3 Foresight Program in the field of Plasma Physics (NSFC: No.11261140328), Japan-China Joint Seminar on Atomic and Molecular Processes in Plasma was held on July 30 – August 4, 2012, in Lanzhou, China. The total number of the officially registered participants was 37, in which 14 from Japan, 21 from China, 1 from Germany, and 1 from Ireland. This seminar is the extension of the last three seminars that were held on March 6 – 11, 2004 in Lanzhou, China, on October 6 -12, 2007 in Dunhuang, China, and on October 26 – 31, 2009 in Xi'an, China.

In the nuclear fusion plasma, there are quite a variety of atomic processes such as ionization, excitation, di-electronic recombination, collisional electron transfer, cascade radiation, and cascade Auger decay over the wide range of plasma temperature. The knowledge of those processes is indispensable for the evaluation and improvement of the plasma properties. Especially, in these years, the property of tungsten ions has become a subject of urgent investigations since tungsten has been considered as one of the plasma facing wall materials. Because of the diversity of the subject, it is desirable to investigate them by international collaboration groups. The present seminar may contribute to realize the above stated aim; especially it has given an opportunity for the collaborative workers to illustrate their achievements. The present seminar summarizes the collaborative researches for the last decade and proposes the issues for the future prospect.

Key words:

atomic processes, plasma spectroscopy, excitation, ionization, recombination, charge transfer, X-ray, polarization spectroscopy, atomic database, tokamak, divertor, LHD, molecular processes, atomic structures, radiative recombination, di-electronic recombination

## Preface

As one of the activities of JSPS-NRF-NSFC A3 Foresight Program in the field of Plasma Physics (NSFC: No.11261140328), Japan-China Joint Seminar on Atomic and Molecular Processes in Plasma was held on July 30 – August 4, 2012, in Lanzhou, China. This seminar is the extension of the last three seminars that were held on March 6 – 11, 2004 in Lanzhou, China, on October 6 -12, 2007 in Dunhuang, China, and on October 26 – 31, 2009 in Xi'an, China.

Since the first seminar in 2004, the researchers from both Japan and China carried out a number of significant studies in atomic and molecular processes in relation to the fusion plasma. The proposal of the present joint seminar has placed its intention not only on the presentations of the collaborative studies, but also on offering an opportunity for the wide range of researchers from both countries to be acquainted with each other, who would have made an extensive exchange of information about the recent progress of the research activities, and also would have made an extensive discussion about the plan of the future collaborations.

In the present seminar, the total number of 31 oral talks was presented by experts from Japan, China, Germany and Ireland. The total number of the officially registered participants was 37, in which 14 from Japan, 21 from China, 1 from Germany, and 1 from Ireland. In the opening remarks, firstly, Professor Chenzhong Dong of Northwest Normal University, Lanzhou presented a warm address. Professor Shigeru Morita of National Institute for Fusion Science, Japan gave a cordial greeting to the seminar.

The seminar was in always a friendly and active atmosphere. As of the intermission of the seminar, participants visited Labrang Monastery and Institute of Modern Physics of Chinese Academy of Science. During the seminar, the participants exchanged their new research results, discussed about the outlook for new research fields. They tried to promote further developments in mutual collaborations between the countries and the experts. It has given an atmosphere that a subsequent meeting should be desirable to be planned in the near future.

The present issue of the proceedings has collected 19 papers from the delegates of the seminar. It covers the spectroscopic properties of atoms and ions in the plasma, the collisions of electrons or ions with atoms or ions in the plasma, the analysis and diagnostics of the confinement fusion plasma especially for the properties of tungsten atoms and ions, and, further, topics from wide area of atomic physics related to plasma. The present issue also includes the scientific program of the seminar, the group photo as well as the list of

participants.

On behalf of the organizing committee, we would like to express our sincerest thanks to all the participants who made active contributions not only in the formal presentations but also in the fruitful discussions. We would like to acknowledge everybody who devoted very hard work for preparing the seminar. Finally, we would like to acknowledge the administrative as well as the financial supports from Northwest Normal University, and the National Institute for Fusion Science.

Chenzhong Dong

Local Chairperson,

Northwest Normal University, Lanzhou, China

Fumihiro Koike

Organizing Committee,

Kitasato University, Sagamihara, Japan

Xiaobin Ding

Organizing Committee

Northwest Normal University, Lanzhou, China

# Contents

Preface

Contents

Photo of Participants

## Papers

Light emission from sputtered or backscattered atoms on tungsten surfaces under ion irradiation .....	1
SAKAI Yasuhiro, KATO Daiji, KENMOTSU Takahiko, SAKAUE A. Hiroyuki, NOGAMI Keisuke, FURUYA Kenji, and MOTOHASHI Kenji	
Laboratory Experiments for Revealing Soft X-ray Emissions from Solar Wind Charge Exchange.....	7
TANUMA Hajime	
Spectroscopy of highly charged tungsten ions with Electron Beam Ion Traps.....	11
SAKAUE A. Hiroyuki, KATO Daiji, MORITA Shigeru, MURAKAMI Izumi, YAMAMOTO Norimasa, OHASHI Hayato, YATSURUGI Junji, and NAKAMURA Nobuyuki	
LIBS detection of heavy metal elements in liquid solutions by using wood pellet as sample matrix .....	17
WENG Guan hong, SUN Duixiong, SU Maogen, and DONG Chenzhong	
A comparative study of the laser induced breakdown spectroscopy in single- and double-pulse laser geometry.....	26
SUN Duixiong, SU Maogen, DONG Chenzhong, WEN Guan hong, CAO Xiangnian	
Dielectronic Recombination of Highly Charged Heavy Ions Studied with the Tokyo Electron Beam Ion Trap .....	37
Zhimin Hu, Xiaoying Han, Yueming Li, Daiji Kato, Xiaomin Tong, and Nobuyuki Nakamura	
Doubly Excited States and Their Dissociation Processes of Simple Molecules.....	42
Karin Takahashi, Yosuke Sakata, Yuta Hino, and Yasuhiro Sakai	

Dielectronic recombination of Br-like tungsten ions .....	50
Li Maijuan, Fu Yanbiao, Su Maogen, Dong Chenzhong and Koike Fumihiro	
Preliminary result on quantitative analysis using Zn-like tungstenEUV spectrum in Large Helical Device.....	61
Shigeru MORITA, Chunfeng DONG, Erhui WANG, Daiji KATO, Motoshi GOTO, Masahiro KOBAYASHI, Izumi MURAKAMI, Tetsutarou OISHI, Hiroyuki SAKAUE, Zhengying CUI, Hangyu ZHOU,Liqun HU, Bo LU, Zhenwei WU, and Ling ZHANG	
Study of EUV spectra from low- and medium-Z impurity ions basedon a grazing-incidence flat-field EUV spectrometer in HL-2Atokamak.....	78
Hangyu Zhou, Zhengying Cui, Shigeru Morita, Ping Sun, MotoshiGoto, BingzhongFu, BeibinFeng, Ping Lu, Qingwei Yang, and XuruDuan	
X-ray and Auger electron study of highly charged ions usingresonant coherent excitation.....	87
Y. Nakano, A. Hatakeyama, Y. Nakai, K. Komaki,E. Takada , T. Murakami, and T. Azuma,	
Theoretical aspects of electron correlations and termdependences in the electronic states of highly charged ions .....	93
F. Koike, H. Funaba, M. Goto1, D. Kato, T. Kato, S. Morita,I. Murakami, H. A.Sakaue, S. Sudo, C. Suzuki, N. Tanuma, A. Sasaki , and X. B. Ding	
Absolute $K\alpha$ line spectroscopy for cone-guidedfast-ignition targets.....	101
NISHIMURA Hiroaki, ZHANG Zhe, NAMIMOTO Takuya, FUJIOKA Shinsuke,KOGA Mayuko, SHIRAGA Hiroyuki, OZAKI Tohru, NISHIKINO Masaharu,KAWACHI Tetsuya, PIROZHKOV Alex. S., KONDO Kiminori, OKANOYasuaki, FG-02 Experimental Campaign Team, and AZECHI Hiroshi	
Potential of cold $K\alpha$ radiation generated by an intense ion beamfor cold dense plasma diagnostics.....	107
KAWAMURA Tohru, HORIOKA Kazuhiko, and KOIKE Fumihiro	
Atomic process modeling based on plasma microfield.....	113
NISHIKAWA Takeshi	
Multiple Ionization Dynamics of Ar <sub>2</sub> by Slow Highly ChargedIons .....	119
ICHIMURAAatsushi1 and OHYAMA-YAMAGUCHI Tomoko	

Theoretical Investigation of Total and State-Dependent Charge Exchange in O <sup>6+</sup> Collisions with Atomic Hydrogen .....	125
Y. Wu, P. C. Stancil, D. R. Schultz, Y. Hui, H. P. Liebermann, and R. J. Buenker	
Observations of EUV spectra from tungsten and lanthanide ions in LHD .....	133
SUZUKI Chihiro, KOIKE Fumihiko, MURAKAMI Izumi, KATO Takako, GOTO Motoshi, NAKANO Tomohide, TAMURA Naoki, SUDO Shigeru, HARTE Colm S, and O'SULLIVAN Gerard	
Lasing Potential of Extreme Ultraviolet Light Using Recombining Nitrogen Plasma .....	139
YAMAMURA Shuhei, OZAWA Takuya, HORIOKA Kazuhiko, and KAWAMURA Tohru	
Agenda .....	145
Seminar Program .....	147
Participants List .....	150

# The 4th China-Japan Joint Seminar on Atomic and Molecular Processes in Plasma

Jul. 30-Aug. 4, 2012, Lanzhou, China



# Light emission from sputtered or backscattered atoms on tungsten surfaces under ion irradiation

SAKAI Yasuhiro, KATO Daiji<sup>†</sup>, KENMOTSU Takahiko<sup>§</sup>, SAKAUE A. Hiroyuki<sup>†</sup>,  
NOGAMI Keisuke, FURUYA Kenji<sup>#</sup>, and MOTOHASHI Kenji<sup>\*</sup>

*Department of Physics, Toho University, Funabashi, Chiba 274-8510, Japan*

*<sup>†</sup>National Institute for Fusion Science, Toki, Gifu 509-5292, Japan*

*<sup>§</sup>Department of Biomedical Engineering, Doshisha University, Kyotanabe, Kyoto 610-0394, Japan*

*<sup>#</sup>Department of Molecular and Material Science, Kyushu University Kasuga, Fukuoka 816-8580, Japan*

*<sup>\*</sup>Department of Biomedical Engineering, Toyo University, Kawagoe, Saitama 350-8585, Japan*

## Abstract

We measured the intensity of light emission from sputtered atoms on tungsten surfaces under the irradiations of Kr<sup>+</sup> ion and Ar<sup>+</sup> ion, as a function of the perpendicular distance from the surface. Using the analysis of decay curve, we estimated the mean vertical velocity component in direction normal to the surface. We found that the estimated mean velocity had much differences according to the excited state. For example, although the estimated mean vertical velocity component normal to the surface from the 400.9 nm line((5d<sup>5</sup>(6S)6p <sup>7</sup>P<sub>4</sub>→(5d<sup>5</sup>(6S)6s <sup>7</sup>S<sub>3</sub> transition) was 5.6±1.7 km/sec, that from the 386.8 nm line((5d<sup>4</sup>(6S)6p <sup>7</sup>D<sub>4</sub>→(5d<sup>5</sup>(6S)6s <sup>7</sup>S<sub>4</sub> transition) was 2.8±1.0 km/sec. However, for different projectiles and energies, we found no remarkable changes in the velocity.

Key words: tungsten surface, sputtering, ion-beam induced light emission, mean velocity, excited atoms

## 1. Introduction

Among much material currently examined, tungsten(W) is considered to be the most suitable candidate as plasma-facing materials for plasma reactor because it has many favorable properties [1,2] such as high melting point, high thermal conductivity, low sputtering yield, low tritium retention, and no chemical erosion. However, high emission probability of radiation from the excited atoms emitted from the wall surface due to interaction with various energetic particles is one of the weak points. Cooling processes of the plasma due to radiation from excited neutral atoms sputtered from the wall surface are an important atomic process in fusion plasma, because neutral atoms penetrate into the plasma across the magnetic fields [3]. In particular, it is very important to know the kinematics of the excited atoms produced in the sputtering processes, because the penetration depth into the plasma depends on the velocity of the eroded atoms. We measured the mean velocity of excited W atoms in direction normal to surface by observing ion-beam induced light emission(IBLE). In this study, although we chose Kr<sup>+</sup> and Ar<sup>+</sup> ions as the projectile, the sputtering data of light ions, such as hydrogen, is demanded in nuclear fusion research. Therefore, positioning of this study will be the first step of investigation of sputtering processes on tungsten surfaces as a nuclear fusion research.

Optical emission spectroscopy is one of the most powerful techniques for studying high-temperature plasmas because it does not disturb the plasma. Since the velocity measurement of excited atoms by observing IBLE is influenced by the survival probability [4,5] of the excited state, we have often measured the photo emission intensity as a function of the perpendicular distance  $z$  away from the surface. Excluding the vicinity of the surface,

the intensity decreases in exponential. In fact, the probability changes with the surface condition depending especially on oxygen adsorption in case of some metals and semiconductors [4]. The decay of the photo emission intensity  $I$  as a function of  $z$  provides an information on the mean velocity with normal direction of the excited atoms. In general, this intensity decay follows the well-known relation,

$$I = \sum_k I_{0k} \exp\left(-\frac{z}{\langle v_{\perp} \rangle \tau_k}\right). \quad (1)$$

Where  $I_{0k}$  is the intensity from a particular transition  $k$  at the surface ( $z=0$ );  $\langle v_{\perp} \rangle$  is the vertical velocity component normal to the surface,  $\tau_k$  is the lifetime of the excited state.

In this paper, we discuss about why the mean velocities with normal direction of excited W atoms have difference with excited states.

## 2. Experimental setup

The experiments were carried out at a beam line of medium current ion implanter (ULVAC IM-200MH-FB) in National Institute for Fusion Science (NIFS). A schematic of the experimental apparatus is shown in Fig.1, which had been described previously [6]. Briefly, this apparatus consists of an ion beam source, a collision chamber, and a visible spectrometer. When ion beam entered onto the surface at normal incidence angle, a number of visible emission spectra were observed through a visible spectrometer, which was set in direction parallel to the surface. The available impact energy was from 30 to 60 keV, and we can use the ion beam current of 50 micro ampere. A target was a tungsten plate set on a movable stage. The size of plate was  $100 \times 100 \times 0.1$  (thickness) cubic mm. The spectrometer has 1200 grooves/mm diffraction gratings, its focal length is 50 cm. We used a charge coupled device (CCD) as the detector for light signals. We measured the light intensity as a function of the distance  $z$  from the surface by moving the stage linearly, where  $z = 0$  was defined as the position where the intensity is maximum [7]. The pressure of the chamber was maintained below  $7 \times 10^{-5}$  Pa by a turbo molecular pump during the measurements. It reached less than  $1 \times 10^{-5}$  Pa when the ion beam did not irradiate the tungsten surface.

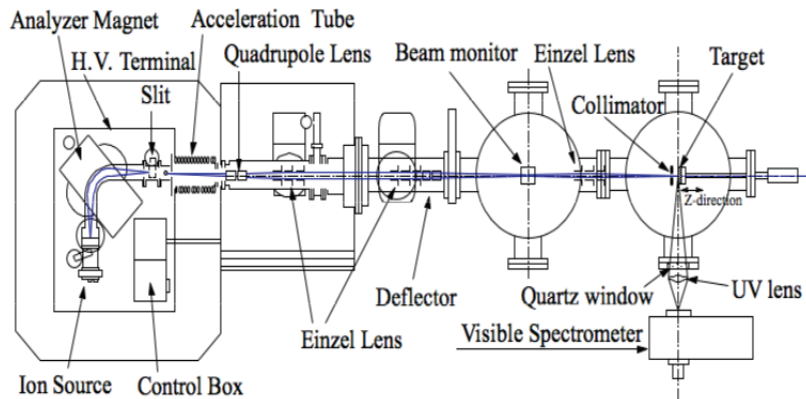


Fig.1 A schematic illustration of the experimental apparatus

## 3. Results and discussions

### 3.1 Optical emission spectra of excited tungsten atoms under $\text{Kr}^+$ irradiation

Tungsten (W) has an electric configuration of  $5d^4 6s^2$  ( $^5D_4$ ) in ground state. In general, the light emission observed in a visible light range is originated from the transition between excited states. Figure 2 shows a typical high resolution two-dimensional (2D) raw image

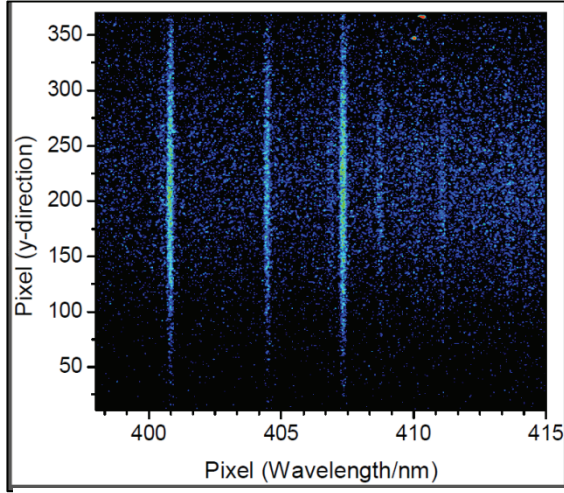


Fig.2 A typical high resolution 2D raw image taken by the CCD detector.

taken by the CCD detector under Kr<sup>+</sup> (35 keV) irradiation of a polycrystalline tungsten surface in the wavelength of 398-415 nm. The horizontal axis corresponds to the wavelength, and vertical axis is the position in y-direction. This image was observed at z=0.5 mm from the surface. We were able to obtain this image in only 2 minutes. The strong 400.9 nm line was assigned to WI  $5d^5(6S)6p\ ^7P_4 \rightarrow 5d^5(6S)6s\ ^7S_3$  transition, which has been used to the standard for quantification of W sputtering in the actual fusion reactor. In the experiment, we confirmed that the intensity of this line was proportional to the ion current. This means that no secondary processes, such as multiple collisions between ions and excited W atoms ( $5d^5(6S)6p\ ^7P_4$ ), and self-absorption of

photons by W atoms, affect photon emission.

A typical survey light emission spectrum converted from the 2D raw imaging is shown in Fig.3. Several strong lines from sputtered W atoms were observed in the wavelength of 380-440 nm. Every line appears on the successive state considered to be surface luminescence. Even if projectile energies were different, the intensity ratio of each peak in a spectrum did not change in essence. The wavelengths and transitions of strong lines labeled from “A” to “K” are summarized in Table 1. Although all WI lines belong to 6p→6s/5d transitions, they are classified into four types of transitions that consist of a combination of two upper and two lower states:  $5d^56p \rightarrow 5d^56s$  (A, D, H, and I),  $5d^56p \rightarrow 5d^46s^2$  (K),  $5d^46s6p \rightarrow 5d^56s$  (B, E, and F), and  $5d^46s6p \rightarrow 5d^46s^2$  (C, G, and J).

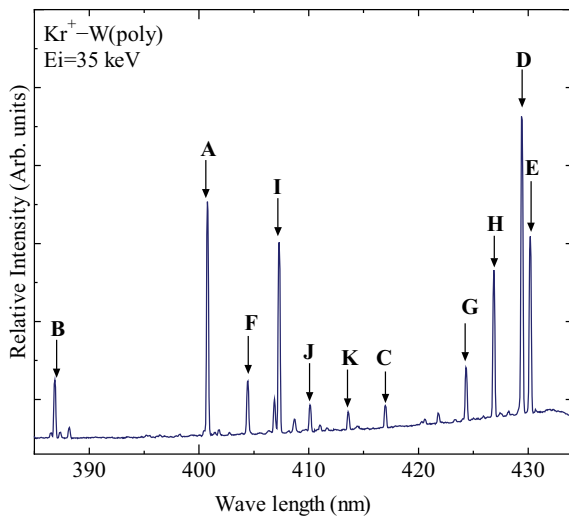


Fig.3 A typical survey optical emission spectrum obtained at z=0.5 mm

Table 1 Strong lines of the visible emission spectrum observed for W surfaces under irradiation by Kr<sup>+</sup> (35 keV) ions.

Labels	wavelength(nm)	Transitions
A	400.88	$5d^5(6S)6p, ^7P_4 \rightarrow 5d^5(6S)6s, ^7S_3$
B	386.80	$5d^46s(6D)6p, ^7D_4 \rightarrow 5d^5(6S)6s, ^7S_3$
C	417.12	$5d^46s(6D)6p, ^7D_4 \rightarrow 5d^46s^2, ^5D_3$
D	429.46	$5d^5(6S)6p, ^7P_2 \rightarrow 5d^5(6S)6s, ^7S_3$
E	430.21	$5d^46s(6D)6p, ^7D_3 \rightarrow 5d^5(6S)6s, ^7S_3$
F	404.56	$5d^46s(6D)6p, ^5F_2 \rightarrow 5d^5(6S)6s, ^7S_3$
G	424.44	$5d^46s(6D)6p, ^7D_5 \rightarrow 5d^46s^2, ^5D_4$
H	426.94	$5d^5(6S)6p, ^7P_4 \rightarrow 5d^5(6S)6s, ^7S_3$
I	407.44	$5d^5(6S)6p, ^7P_3 \rightarrow 5d^5(6S)6s, ^7S_3$
J	410.27	$5d^46s(6D)6p, ^5P_3 \rightarrow 5d^46s^2, ^5D_4$
K	413.75	$5d^5(6S)6p, ^7P_3 \rightarrow 5d^46s^2, ^5D_2$

### 3.2 Mean vertical velocity of excited tungsten atoms under $\text{Kr}^+$ irradiation

We measured mean normal velocity  $\langle v_{\perp} \rangle$  of the excited tungsten atoms sputtering from polycrystalline tungsten surfaces with small oxygen coverage ( $< 0.04$ ) by irradiation of high flux density ion beam in the present study. We have already reported that the mean normal velocity of excited  $\text{W}(5d^5(^6\text{S})6p^7\text{P}_4)$  atoms was  $5.6 \pm 1.7$  km/s on average, when  $\text{Kr}^+$  ions (33-60keV) were used as the projectile[6]. This value was obtained by analyzing the photon-emission intensity of the “A” line as a function of the distance from the surface. The curve was well fitted with the eq.(1). We carried out experiments of some impact energies 35, 45, 55, 60 keV, and found that the mean velocity was not dependent on impact energies as expected simply from Thompson-Sigmund velocity distributions [8]. Since each mean velocity included large error of about 20%, however, the value of  $5.6 \pm 1.7$  km/s was an average value of those experiments.

In this study, we analyzed not only the excited state of  $\text{W}(5d^5(^6\text{S})6p^7\text{P}_4)$  but another excited state. Both the line “B” and “C” have the same initial excited state including quantum number J, which is the  $(5d^46s(^6\text{D})6p, ^7\text{D}_4)$  state. We show the intensity curves of the WI 386.8 and 417.1 nm lines, “B” and “C” lines, as a function of the distance from the surface  $z$  in 35keV  $\text{Kr}^+$  energy, in Fig.4. As a natural consequence, the experimental points fell on a same curve. The curve consisted of two decay line components like an “A” case. Considering the excited state of which lifetime is 185 ns [9], we can estimate the mean vertical velocity from the line of the steeper slope. We obtained the value of  $3.5 \pm 1.3$  km/s under  $\text{Kr}^+$  (35 keV) irradiation. Figure 5 shows the mean vertical velocity of W atoms of which excited state is  $(5d^46s(^6\text{D})6p, ^7\text{D}_4)$ , as a function of the projectile energy. No remarkable energy dependence at the mean velocity was confirmed as a result of the experiment with various projectile energies of  $\text{Kr}^+$ , even if each value included large error bar. This uncertainty is due to the surface condition depending especially on oxygen adsorption and the uncertainty of the fitting parameter. The obtained average

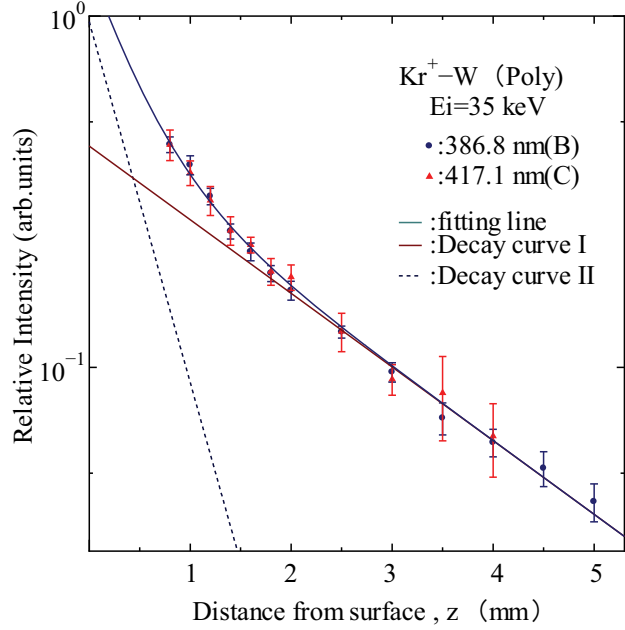


Fig. 4 Semi-log plot of photon intensity for “B” and “C” lines as a function of the distance from the surface.

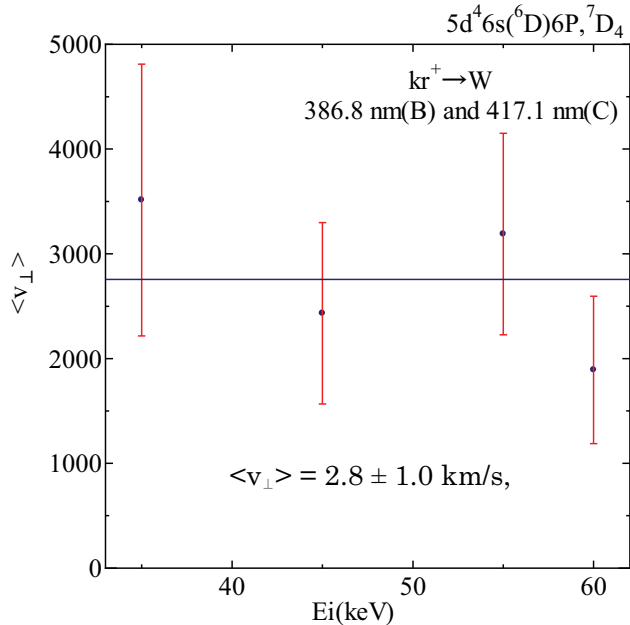


Fig. 5 The mean vertical velocity of excited W atoms  $(5d^46s(^6\text{D})6p, ^7\text{D}_4)$  as a function of the projectile energy.

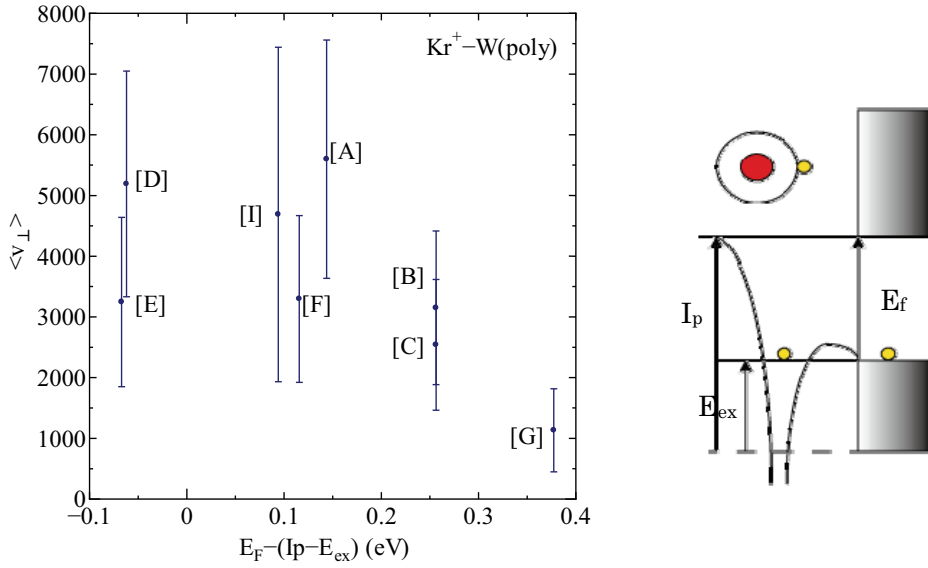


Fig. 6 The mean vertical velocity of various excited states of W as a function of the energy gap between the work-function  $E_f$  and  $I_p$  minus excitation energy  $E_{ex}$ .

value of the mean vertical velocity was  $2.8 \pm 1.0$  km/s, which differs from the “A” case very much.

In other case, for example the analysis of line “D”, “E”, “F”, and “G”, we confirmed that the obtained mean vertical velocities had no projectile energy dependence. However each average value was different as expected. Therefore, we tried to draw the mean vertical velocity graphs as a function of the energy gap between the work-function  $E_f$  and  $I_p$  minus excitation energy, as shown in Fig.6. In spite of a small excitation energy difference, it seems that the mean vertical velocity depends on the energy gap between the work-function  $E_f$  and  $I_p$  minus excitation energy  $E_{ex}$ . For example, compared with others, the case of “G” has lower velocity, and its energy gap is large. Therefore, we can build hypothesis. Only the atom which escaped the non-radiative transition near the surface is observed. So, observed excited W atoms are the survivors. When the energy gap is small, the interaction occurs with the surface, and slow excited atoms may be eliminated.

### 3.3 Mean vertical velocity of excited tungsten atoms under $Ar^+$ irradiation

We also measured mean normal velocity  $\langle v_{\perp} \rangle$  of the excited W under  $Ar^+$  irradiation. In this case, except that several peaks by the recoil  $Ar^+$  ion appeared in the optical emission spectra, there are no remarkable changes in the peak intensity ratios in comparison with any  $Kr^+$  cases. Since the peak originated by  $Ar^+$  ion had slightly wide peak width due to the Doppler broadening, we could distinguish  $Ar^+$  peak from the excited W peaks.

Figure 7 shows the intensity curves of the W 400.9 nm lines, “A”, as a function of the distance from the surface  $z$  in 45keV  $Ar^+$  energy, together with the  $Kr^+$  case. Both lines were well fitted with a double exponential function. Although the mean vertical velocity estimated by the fitting procedure was almost same as  $Kr^+$  case in error bar when we assume the lifetime of the excited  $5d^5(6S)6p^7P_4$  state of W,  $\tau = 59.4$ ns [10], for the steeper decay curve, each slope of the gentle curve was different. The slope in  $Ar^+$  case was slightly looser than that in  $Kr^+$ . We do not have suitable explanation about this phenomenon now.

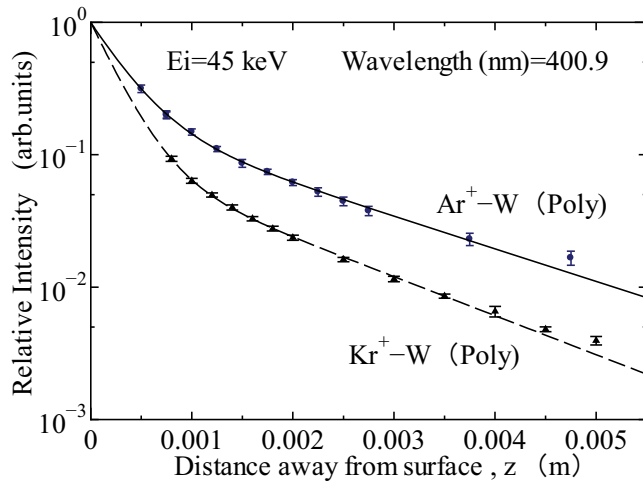


Fig. 7 Semi-log plots of photon intensity obtained by two experiments of Ar<sup>+</sup> and Kr<sup>+</sup> ion irradiations for “A” lines as a function of the distance from the surface.

in 45keV Ar<sup>q+</sup> ( $q=1-9$ ) irradiation on Al and Al<sub>2</sub>O<sub>3</sub> surfaces. However among different excited states, the mean normal velocity was different each other. Since observed excited W atoms are the survivors, when the energy gap is small, the interaction occurs with the surface, and slow excited atoms may be eliminated. In addition, although we found the difference of the slopes between Ar<sup>+</sup> and Kr<sup>+</sup> cases, we cannot explain this factor now.

#### Acknowledgement

This work was conducted with the support and under the auspices of the NIFS Collaboration Research Program (NIFS09KBAF002, NIFS12-KBA008). Besides, this work was partly supported by the Grant-in-Aid for Scientific Research (A) (23246165) and by the JSPS-NRF-NSFC A3 Foresight Program in the field of Plasma Physics (NSFC: No. 11261140328).

#### References

- [1] J. Roth, E. Tsitrone, A. Loarte, et al., *J. Nucl. Mater.* **390–391** (2009) 1–9.
- [2] R. Neu, ASDEX Upgrade Team EU PWI Taskforce and JET EFDA Contributors, *Plasma Phys. Control. Fusion* **53** (2011) 124040-1–124040-24.
- [3] V. Philipps, *J. Nucl. Mater.* **415** (2011) 52–59.
- [4] S. Tsurubuchi, T. Nimura, *Surf. Sci.* **513** (2002) 539–548.
- [5] T. Nimura, S. Tsurubuchi, *Jpn. J. Appl. Phys.* **41** (2002) 826–831.
- [6] K. Motohashi et al. 2012. *Nucl. Instrum. Meth. B*, **283**, 59
- [7] M. Suchanska, *Prog. Surf. Sci.* **54** (1997) 165–209.
- [8] M.W. Thompson, *Phys. Rep.* **69** (1981) 335.
- [9] M. D. Campbell-Miller et al., *J. Opt. Soc. Am. B* **13**, 2115 (1996).
- [10] E.A. Den Hartog et al., *J. Opt. Soc. Am.* **B4** (1987) 48.

#### 4. Conclusion

An IBLE study of tungsten surfaces under irradiation of 30-60 keV Kr<sup>+</sup> and Ar<sup>+</sup> ion was conducted. Mean normal velocities of excited W atoms sputtered from the surface was measured by analyzing the photon intensity as a function of distance from the surface. No remarkable change of the mean normal velocity was found among different projectiles and projectile energies. The estimated mean vertical velocity is about 5.6 km/s for excited W\*(6p <sup>7</sup>P<sub>4</sub>). This velocity corresponds to the kinetic energy of ~30eV, and the value is close to one of Al line (396.2nm)

# Laboratory Experiments for Revealing Soft X-ray Emissions from Solar Wind Charge Exchange

TANUMA Hajime

*Department of Physics, Tokyo Metropolitan University, 1-1 Minami-Ohasawa, Hachioji,  
Tokyo 192-0397, Japan  
e-mail: tanuma-hajime@tmu.ac.jp*

## Abstract

We have observed the emission spectra in collisions of  $O^{8+}$  ions with He and  $H_2$  targets in the soft X-ray region with a window-less silicon drift detector at collision energy of 3.56 keV/u. The dominant emission corresponds to the 1s–2p transition of the  $O^{7+}$  ion produced by a single-electron capture reaction. Other emission lines are the 1s–3p, 1s–4p, and 1s–5p transitions of  $O^{7+}$ , and also the 1s<sup>2</sup>–1s2p transition of  $O^{6+}$  produced by a double-electron capture. The experimental spectra have been reproduced by the state-selected capture cross sections calculated by the two-center atomic orbital close-coupling method with the consideration of the cascade processes.

**Keywords:** solar wind charge exchange, multiply charged ions, charge exchange reaction, soft X-ray emission, atomic orbital close coupling calculation

## 1. Introduction

The solar wind charge exchange (SWCX) means the electron capture of multiply charged ions contained within the solar wind in collisions with neutral matters within the heliosphere, and has been regarded as a dominant mechanism of the soft X-ray emission in the solar system [1, 2]. In order to analyze the X-ray spectra observed with the observatory satellites quantitatively in detail, the X-ray emission cross sections of the SWCX processes are needed for astrophysicists.

As preliminary experiments, we have measured the soft X-ray emission spectra in collisions of  $O^{7+}$  and  $N^{6+}$  with He at 20 keV/charge by using a window-less Si(Li) detector [3]. Recently we have introduced a new window-less detector and constructed a new experimental setup to reduce the ion beam velocity to that of the solar wind, i.e. 200–900 km/s, which corresponds to 0.2–4.2 keV/u.

In this manuscript, we have reported experiments on the collisions of  $O^{8+}$  ions with He and  $H_2$  target gases at collision energy of 3.56 keV/u. The measured spectra have been compared with the theoretical calculation for understanding of the emission mechanism.

## 2. Experiment

The bare oxygen ions were produced with a 14.25 GHz electron cyclotron resonance (ECR) ion source with introduction of  $^{18}\text{O}^{16}\text{O}$  gas into a plasma chamber. The ions were extracted from the plasma by an electric potential of 5–10 kV, and the  $^{18}\text{O}^{8+}$  ion beam were directed into a collision cell after the charge-state separation by a  $110^\circ$  double-focusing dipole magnet. We applied the high voltage to the collision cell in order to achieve the solar wind velocity of ions. The collision cell was filled with target gas of either He and  $\text{H}_2$ . The target gas pressure in the cell was kept lower than  $1.3 \times 10^{-3}$  Pa to maintain the single-collision conditions. Soft X-ray emissions following the charge exchange collisions of ions with He and  $\text{H}_2$  were observed at the magic angle,  $54.7^\circ$  from the ion beam axis with a window-less silicon drift detector (SDD100145WL, Princeton Gamma-Tech) to obtain the absolute emission cross sections. The SDD detector was calibrated using the Mn  $K\alpha$  emission of 5.9 keV from  $^{55}\text{Fe}$ , and its energy resolution was 145 eV for this photon energy.

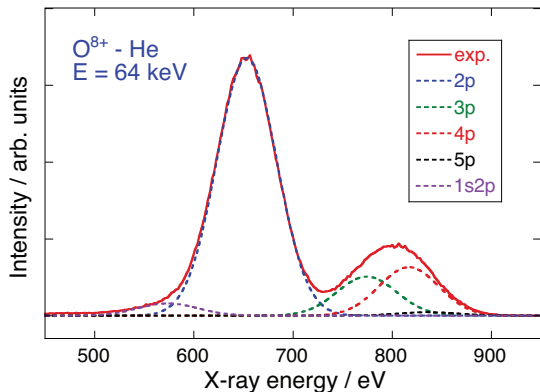


Figure 1: The soft X-ray emission spectrum measured with the SDD detector in collisions of  $\text{O}^{8+}$  ions with He gas at a collision energy of 64 keV.

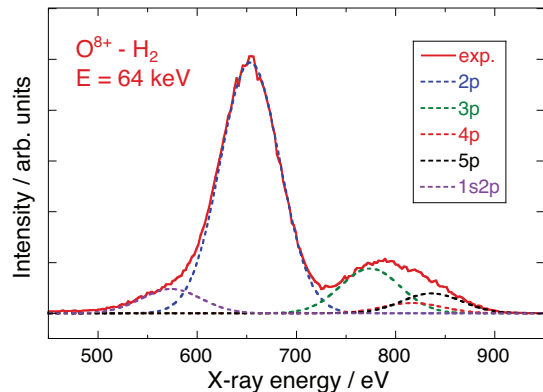


Figure 2: The soft X-ray emission spectrum measured with the SDD detector in collisions of  $\text{O}^{8+}$  ions with  $\text{H}_2$  gas at a collision energy of 64 keV.

### 3. Results

The spectra observed in collisions of  $^{18}\text{O}^{8+}$  with He and  $\text{H}_2$  at collision energy of 64 keV (3.56 keV/u) are shown in Figures 1 and 2, respectively. The dominant peak at 654 eV corresponds to the 1s–2p transition of  $\text{O}^{7+}$  ions, and the small peaks of the 1s–3p transition at 775 eV and the 1s–4p transition at 817 eV could be distinguished after the deconvolution using gaussian functions with the full width half maximum of 71 eV for each transition. The same tendency has been observed in all collision systems and at all collision energies. And also the 1s<sup>2</sup>–1s2p transition of  $\text{O}^{6+}$  ions at 569 eV, which are produced in the double electron capture collision, has been found in these spectra.

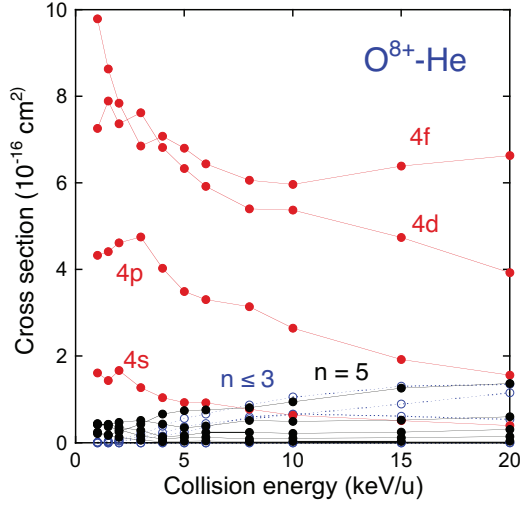


Figure 3: The state-selective one-electron capture cross sections in collisions of  $O^{8+}$  with He calculated by the TC-AOCC method.

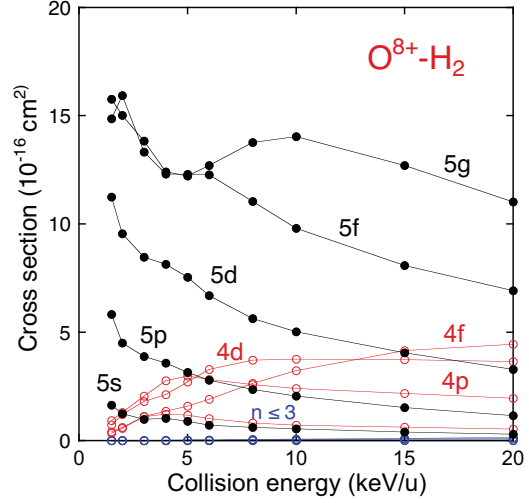


Figure 4: The state-selective one-electron capture cross sections in collisions of  $O^{8+}$  with  $H_2$  calculated by the TC-AOCC method.

We have performed the theoretical calculation for the state-selective one-electron capture cross sections with two-center atomic orbital close-coupling (TC-AOCC) method [4]. Figure 3 and 4 are the results of the TC-AOCC calculations in collisions of  $O^{8+}$  with He and  $H_2$ , respectively. As can be seen in these figures, the dominant capture levels in these collisions are predicted as the principal quantum number  $n = 4$  for He target and 5 for  $H_2$ . But, the 1s–2p transitions have the prominent intensities in both collision systems. The emission spectra obtained using the theoretical capture cross sections at collision energy of 4 keV/u with considering the cascade transitions from higher states are shown in Figures 5 and 6. In the  $O^{8+}$ -He collision, the theoretical spectrum shows very good agreement with the experimental result, except the contribution of the double capture. On the other hand, the theoretical spectrum has significant discrepancy with the experimental one in the case of  $H_2$  target. The TC-AOCC calculation does not consider the molecular structure of the target. Therefore we think it is the reason why the discrepancy between the experimental and theoretical spectra.

#### 4. Conclusion

The soft X-ray emission spectra in collisions of  $O^{8+}$  with He and  $H_2$  have been observed and compared with the theoretical calculation. The emission mechanism has been understood as the single-electron capture and the cascade processes. In this work,

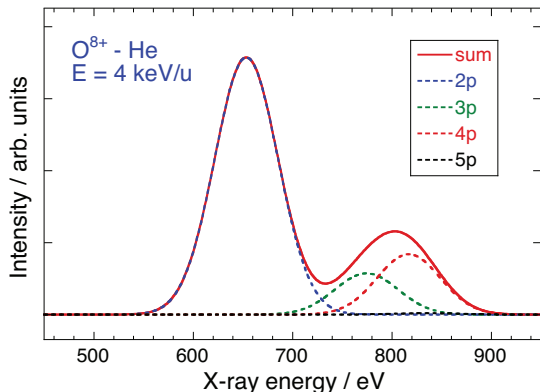


Figure 5: The soft X-ray emission spectrum calculated with the cross sections by the TC-AOCC method in collisions of  $O^{8+}$  ions with He gas at a collision energy of 4 keV/u.

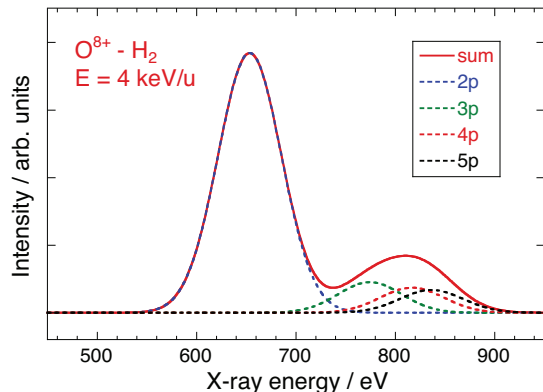


Figure 6: The soft X-ray emission spectrum calculated with the cross sections by the TC-AOCC method in collisions of  $O^{8+}$  ions with  $H_2$  gas at a collision energy of 4 keV/u.

the resonance line of  $1s^2S-np^2P$  have been observed. However, the forbidden line  $1s^2S-2s^2S$  must be considered to simulate the emission spectra which are observed by the satellite perfectly.

### Acknowledgement

This work was performed as research collaboration between the atomic physics group and the experimental astrophysics group in Tokyo Metropolitan University. The TC-AOCC calculations have been carried out by Ling Liu and Jianguo Wang in Institute of Applied Physics and Computational Mathematics, Beijing. This work was supported in part by Grants-in-Aid for Scientific Research from the Japanese Society for Promotion of Science (No. 21246017, and 23244083) and the JSPS-CAS Core-University Program in the field of “Plasma and Nuclear Fusion”. Also this work was partly supported by the JSPS-NRF-NSFC A3 Foresight Program in the field of Plasma Physics (NSFC: No. 11261140328).

### References

- [1] T. E. Cravens, 2002 *Science* **296**, 1042.
- [2] R. Fujimoto *et al.*, 2007 *Publ. Astron. Soc. Japan* **59**, S133.
- [3] T. Kanda *et al.*, 2011 *Phys. Scr.* **T144** 014025.
- [4] L. Liu *et al.*, 2010 *J. Phys. B: At. Mol. Opt. Phys* **43** 144005.

# Spectroscopy of highly charged tungsten ions with Electron Beam Ion Traps

SAKAUE A. Hiroyuki<sup>1</sup>, KATO Daiji<sup>1</sup>, MORITA Shigeru<sup>a</sup>, MURAKAMI Izumi<sup>1</sup>,  
Yamamoto Norimasa<sup>2</sup>, OHASHI Hayato<sup>3</sup>, YATSURUGI Junji<sup>3</sup>,  
and NAKAMURA Nobuyuki<sup>3</sup>

<sup>1</sup>*National Institute for Fusion Science, Toki, Gifu 509-5292, JAPAN*

<sup>2</sup>*Chubu University, Kasugai, Aichi, 487-8501, JAPAN*

<sup>3</sup>*Institute for Laser Science, The University of Electro-Communications,  
Chofu, Tokyo 182-8585, JAPAN*

## Abstract

We present spectra of highly charged tungsten ions in the extreme ultra-violet (EUV) by using electron beam ion traps. The electron energy dependence of spectra is investigated of electron energies from 490 to 1440 eV. Previously unreported lines are presented in the EUV range, and some of them are identified by comparing the wavelengths with theoretical calculations.

**Keywords:** Highly charged ions, Tungsten, EBIT.

## 1. Introduction

Tungsten will be used for the material of divertor plates in ITER because of higher threshold energies for sputtering by light ion bombardment, the highest melting point in the chemical elements, and less tritium retention than that in carbon based materials. However, since extremely high particle- and heat-fluxes of intermittent edge plasma transports (*e.g.* edge-localized-mode) in ITER would cause serious damages to such components, tungsten is considered to be one of the most abundant impurities in the ITER plasma. Emission lines of highly charged tungsten ions thus play an important role in the spectroscopic diagnostics of the ITER plasma, and consequently the spectroscopic data of tungsten ions have been studied at several facilities<sup>1-3</sup>.

An electron beam ion trap is a useful device for the systematic spectroscopic studies of tungsten ions<sup>4-7</sup>. We have been using two kinds of EBIT; one of them is the high-energy EBIT (Tokyo-EBIT)<sup>8</sup> constructed at the University of Electro-Communications (UEC), and another is the low-energy compact EBIT (called “CoBIT”)<sup>9-11</sup> developed for spectroscopic studies of moderate charge state ions. We

have constructed two CoBIT, and installed them at the UEC and National Institute for Fusion Science. The electron energy range of CoBIT and the Tokyo-EBIT is 0.1 - 2 keV and 2 - 200 keV, respectively, and the accessible charge states of tungsten are about 10 – 40 and 40 – 74, respectively. The complementary use of them thus enables us to acquire the atomic data of tungsten ions for almost the whole range of charge states. In this paper, we reported the data of CoBIT.

## 2. Experimental apparatus

In the present EBIT experiments, we used the low-energy compact EBIT. In the EBIT, an electron beam emitted from an electron gun is compressed with a pair of superconducting magnets. Since ions ionized by the electron beam are trapped by the electrostatic potential well in the axial direction and also by the electronic space charge potential in the radial direction, they can be successively ionized toward higher charge states. The parameters of CoBIT are listed in TABLE 1.

FIGURE 1 show the present experimental setup for CoBIT. CoBIT has six ports currently used for an EUV spectrometer, gas injector, pinhole camera, visible spectrometer and K-Cell injector. The EUV spectrometer is of a slit-less type especially designed for CoBIT. Since the trapped ions are excited by a thin electron beam, the EBIT represents a line source so that an entrance slit can be omitted. A laminar-type diffraction grating (1200 gr/mm or 2400 gr/mm depending on wavelength) is used to focus the radiation on the surface of a back illuminated CCD (PIXIS-XO:400B).

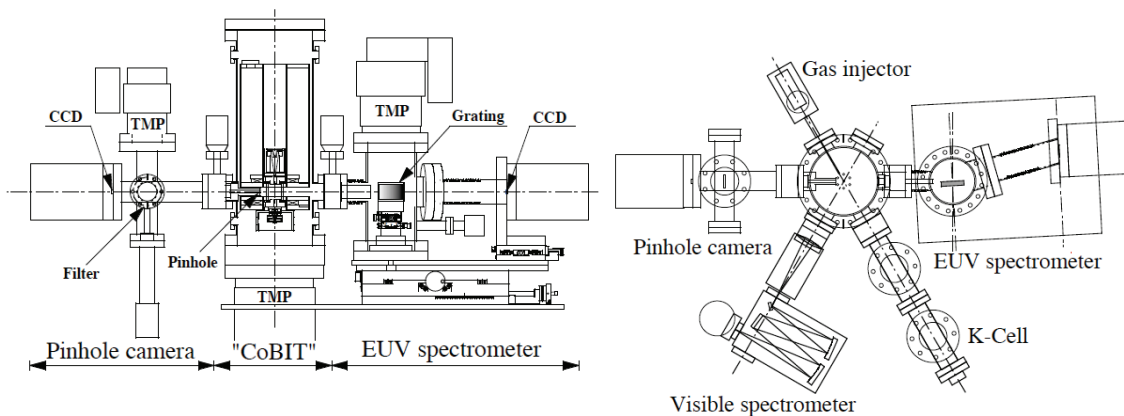


FIGURE 1. The experimental apparatuses of CoBIT.

The visible spectrometer is also installed. The pinhole camera is used to monitor the electron beam shape, which is important for evaluating the EBIT performance and also for determining the absolute electron density. The characteristics of the spectrometers are also listed in TABLE 1.

**TABLE 1.** Specification of CoBIT apparatuses.

<b>Compact EBIT (CoBIT)</b>		
Electron energy (keV)	0.1~2	
Electron current (mA)	10	
Maximum magnetic field (T)	0.2	
Coolant	LN <sub>2</sub>	
EUV spectrometer (grating)	30-002 (Shimadzu)	30-001 (Shimadzu)
Groove number (l/mm)	1200	2400
Incident angle (degree)	87	88.65
Incident distance (mm)	237	237
Useful wavelength range (nm)	5-20	1-6
CCD detector	PIXIS-XO:400B, Princeton Instruments	

### 3. Results and discussion

FIGURE 2 shows EUV spectra obtained by using CoBIT with electron energies between 490 and 1440 eV. The corrections for the spectrometer response and the detector efficiencies were applied to the spectra shown in this figure. It is clear from the figure that the overall EUV spectra show significant dependence on the electron energy. The two peaks denoted by A and B are considered to be the emissions from the maximum charge state ion at each electron energy because they were not seen in the spectra with lower electron energies. For example, when the electron energy  $E_e$  increases from 620 to 670 eV, the maximum tungsten ion charge  $q$  produced in CoBIT is increased from 22+ to 23+. The emission lines of W XXII, which could not be seen at  $E_e = 620$  eV, were observed at 27Å (Peak A) and 34Å (Peak B) at  $E_e = 670$  eV. As electron energy increases from 490 to 1440 eV, the charge states of the ions emitting these lines vary from W XIX to W XXXIII ( $W^{20+} \sim W^{34+}$ ). In each spectrum, the emission lines from three or four charge states of highly charged tungsten ions are observed simultaneously. As the charge state increases, wavelengths of these emission lines (Peaks A and B) shift to the shorter wavelength-region.

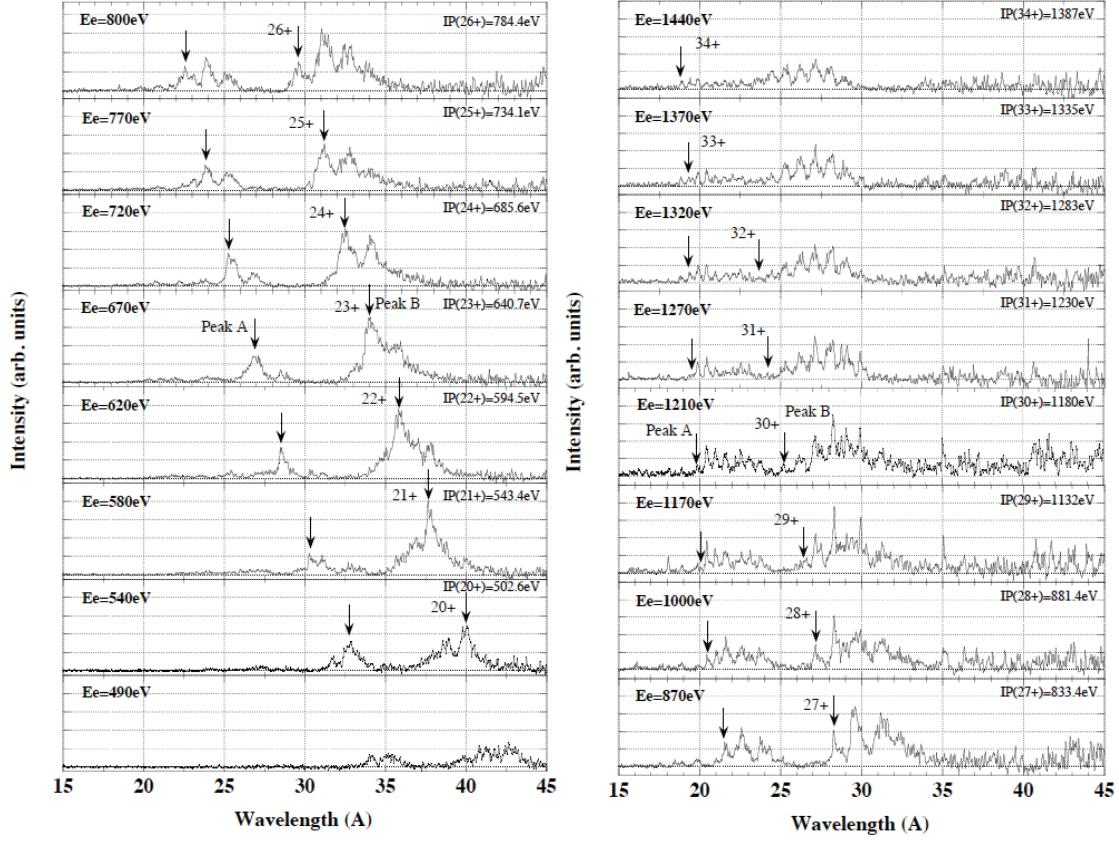


**FIGURE 2.** Typical EUV spectra of highly charged tungsten ions obtained at electron energy  $E_e$  from 490eV to 1440eV in CoBIT.  $IP(q^+)$  is the  $q$ th ionization energy of tungsten ion.

FIGURE 3 shows the charge state dependence of the wavelengths for the peaks A and B. Circles and triangles are the experimental values for the peaks A and B, respectively. The solid line, dotted line and dash-dot line are the calculated wavelength corresponding to the 5f-4d, 5g-4f and 6g-4f transition manifolds, respectively. The calculated wavelength was obtained by averaging the wavelengths of all the transitions in each manifold weighted by the line strengths, which were calculated in an originally developed collisional-radiative model using atom data which were calculated by using the HULLAC code<sup>12</sup> in so-called configuration mode. In the configuration mode, each energy level is not calculated, and only a configuration averaged energy of a given configuration and a total angular momentum  $J$  is concerned. Therefore, the configuration interaction is not considered in this calculation. The charge dependence of peak B agrees with that of the 5g-4f transition.

The experimental value of peak A agrees with that of the 6g-4f transition for the charge state of the tungsten ions lower than 28+. When the charge state becomes higher than 28+, the wavelength of peak A appears corresponding to that of the 5f-4d transition. When the charge state of the tungsten ions is lower than 28+, since the 4d-shell is closed in the ground state and the 4f-shell becomes the valence-shell, the 5f-4d excitation is an inner-shell excitation process. Probably, the 5f-4d radiative transition has a smaller branching ratio to the Auger processes; the emission line thus disappears for the lower charge states. Since it happens that the wavelength of the 6g-4f transition gets close to that of the 5f-4d transition at the charge states of 27- 28+, the measured wavelength curve of Peak A appears to transfer to that of 6g-4f transition at these charges states.

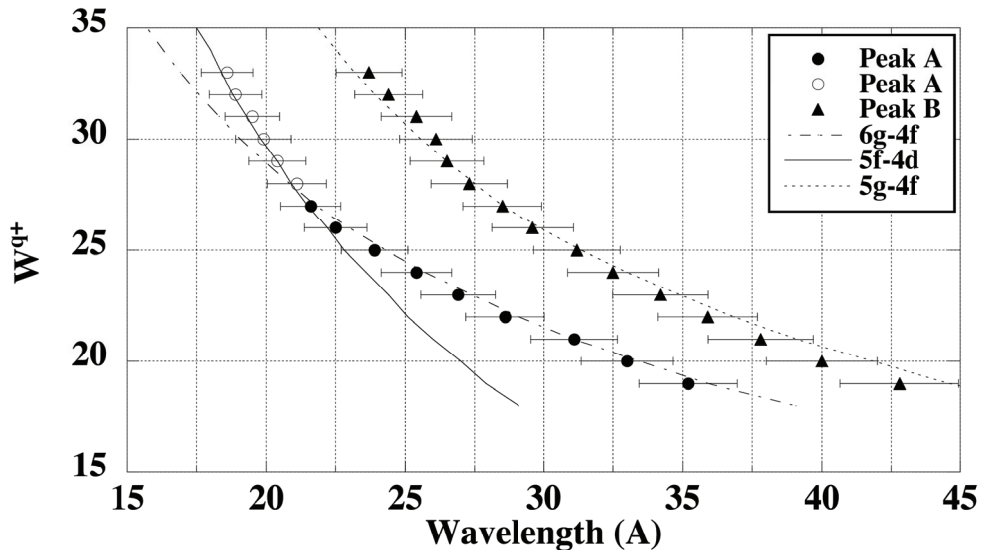


FIGURE 3. The wavelength shift of EUV emission lines

### Acknowledgements

This work was partly supported by the JSPS-NRF-NSFC A3 Foresight Program in the field of Plasma Physics (NSFC: No.11261140328), the NIFS Collaboration Research program (NIFS10KOAJ003) and Grant-in-Aid for Scientific Research (A) (23246165) and (B) (22340175).

## References

1. T. Pütterich *et al.*, J. Phys. B **38**, 3071 (2005).
2. M. B. Chowdhuri *et al.*, Plasma and Fusion Research **2**, S1060 (2007).
3. J. Clementson and P. Beiersdorfer, J. Phys. B **43**, 144009 (2010).
4. J. Clementson and P. Beiersdorfer, Phys. Rev. A **81**, 052509 (2010).
5. Y. Ralchenko *et al.*, J. Phys. B **40**, 3861 (2007).
6. S. Wu and R. Hutton, Can. J. Phys. **86**, 125 (2008)
7. Y. Podpaly *et al.*, Phys. Rev. A **80**, 052504 (2009)
8. N. Nakamura *et al.*, Phys. Scr. **T73**, 362 (1997).
9. N. Nakamura *et al.*, Rev. Sci. Instrum. **79**, 063104 (2008).
10. H. A. Sakaue *et al.*, J. Phys.:Conf. Ser. **163**, 012020 (2009).
11. H. Ohashi *et al.*, Rev. Sci. Instrum. (2011) in press.
12. A. Bar-Shalom, M. Klapisch, and J. Oreg, J. Quant. Spectr. Rad. Transf. **71**, 179 (2001)

# LIBS detection of heavy metal elements in liquid solutions by using wood pellet as sample matrix

Wen Guanhong, Sun Duixiong, Su Maogen<sup>1</sup> and Dong Chenzhong

*Key Laboratory of Atomic and Molecular Physics & Functional Materials of Gansu Province, College of Physics and Electronic Engineering, Northwest Normal University, Lanzhou, 730070, China*

*Joint Laboratory of Atomic and Molecular Physics, Northwest Normal University and Institute of Modern Physics of Chinese Academy of Sciences, Lanzhou 730070, China*  
*e-mail: sumg@nwnu.edu.cn*

## Abstract

Laser-induced breakdown spectroscopy (LIBS) has been applied to the analysis of heavy metals in liquid samples. A new approach was presented to improve the detection limit and minimize the sample matrix effects, in which dried wood pellets absorbed the given amounts of Cr standard solutions and then were baked because they have stronger and rapid absorption properties for liquid samples as well as simple elemental compositions. In this work, we have taken a typical heavy metal Cr element as an example, and investigated the spectral feasibility of Cr solutions and dried wood pellets before and after absorbing Cr solutions at the same experimental conditions, respectively. The results were demonstrated to successfully produce a superior analytical response for heavy metal elements by using wood pellet as sample matrix according to obtained LOD of 0.07 ppm for Cr element in solutions.

**Keywords:** LIBS, Limit of detection, Cr element

## 1. Introduction

Laser-induced breakdown spectroscopy (LIBS), as a rapid, inexpensive, and useful analytical tool for the analysis of elemental composition of materials in solid, liquid and gaseous state, has been extensively studied in recent decades [1-3]. This technique is based on the analysis of the emission spectral lines of the elements present in the sample by focusing high laser power on the sample [4], and have some advantages of no sample preparation, multielemental, and its capability of remote and in situ analysis of material in any phase over other analytical techniques [5-10]. In past years, most of LIBS studies mainly focused on the solid samples since that uniform surface, greater sensitivity and repeatability can be provided. However, the investigations in liquid samples were less than those in solid samples due to the following several problems of affecting the analytical

performance of LIBS, such as splashing, surface ripples, extinction of emitted intensity and a shorter plasma life-time [11-14].

To minimize the problems mentioned above, in recent years some LIBS experiments of liquid-to-solid matrix conversion have been employed in the determination of detection limits by constructing the calibration curves of the line peak intensity versus the corresponding concentration for the elements under study. Typical examples are as follows. Cáceres et al. [15] reported on a quick-freeze method for the quantitative analysis of trace metal ions in liquids applying this technique, the results show that the detection limits of Na and Al elements can be up to a few ppm in Na and Al water solutions over the 0.01-1% concentration range. Pace et al. [16] made the investigations on converting liquid solutions into dried solid pellets of calcium hydroxide by mixing with CaO because of its simple chemical composition with relatively few lines. Detection limits of Cr, Pb, Cd and Zn elements were in the range of 1-120 ppm. Wu et al. [17] reported the studies on the determination of metal elements in solutions with filter paper and analyzed the effects of soaking time to detection limits of As and Na elements.

In this work, we choose a kind of wood as an analysis matrix based on the idea of liquid-to-solid matrix conversion since that wood can be easily crushed into powder and pressed into pellets after baking, and those pellets have stronger and rapid absorption properties for liquid samples. We investigated the spectral feasibility of Cr solutions and dried wood pellets before and after absorbing liquid solutions at the same experimental conditions in order to identify their elemental compositions and the variation of intensity and signal-to-background ratio (S/B) of emission lines. Calibration curves were drawn employing wood pellets soaking with Cr solutions of known concentration in order to evaluate the sensitivity of the method and determine the detection limits. The aim of this investigation is to find a simple detection method suitable for quantitative measurements of heavy metal elements in liquid samples. In addition, the investigations of optimum experimental conditions for such matrix were also included in this study.

## 2. Experimental

Schematic diagrams of the LIBS systems used for a static liquid and a solid target were shown in Fig. 1 (a) and (b), respectively. A Nd:YAG laser with a fundamental wavelength of 1064 nm, pulse width of 8 ns, repetition frequency of 10 Hz, was focused on the sample surface by means of a 40 cm focal length lens and employed to generate the plasma, the pulse energy could be adjusted successively. Plasma emission was collected through a quartz lens with focal length of 10 cm which used to form a 1:1 image of the plasma onto

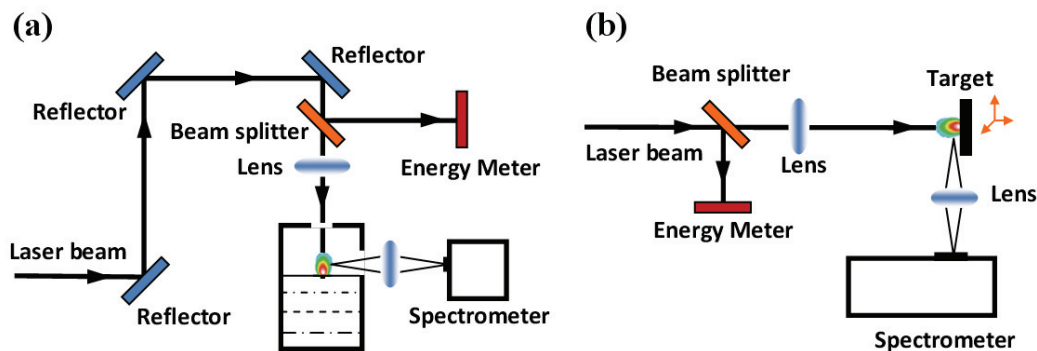


Figure 1: Experimental setups used for LIBS measurements using two different configurations. (a) the arrangement used for static liquid sample. (b) the arrangement used for solid sample.

the entrance slit of a Czerny-Turner type of spectrometer (Shamrock SR-500i, diffraction grating of 1200 groves/mm). The spectrometer was equipped with charge-coupled device detector (iStar-DH734-18F-03, Andor technology) preceded by an image intensifier. A digital delay generator (DG535, Stanford Research system) was used to synchronize the laser and detector and control the delay time between plasma ignition and detector. The plasma spectra were acquired by averaging 50 spectra. In order to obtain the intensities of lines in the same relative scale, the spectra response of intensity is calibrated by detarium and tungsten halogen lamps (Aracight-D-CAL 1205001).

In this study, Cr was chosen as an analytical element because it is one of typical heavy mental, and there are many previous works that can be provided better comparison with other matrix. Here, five standard solutions with Cr concentrations of 100, 500, 1000, 2000, 3000 ppm were prepared by dissolving the given amounts of potassium bichromate ( $K_2Cr_2O_7$ , 99.9% purity) in the deionized water. For direct analysis, liquid solutions were placed into a cup of 2 cm diameter and 6 cm height with a laser entrance hole of 15 mm diameter on the top and a collection hole of 10 mm diameter on the side in order to avoid the sputtering of liquids. A kind of wood, poplar planted in the Northwest Territories in China, was chosen as a matrix of transforming liquid samples into solid samples, which were crushed into powder and pressed to pellets of 20 mm diameter and 4 mm thick by a hydraulic machine oil press under a pressure of 20 MPa during 3 min, and then adsorbing 5 ml standard solutions. After baking two hours in an over at 60 °C solid pellets were obtained.

### 3. Results and discussion

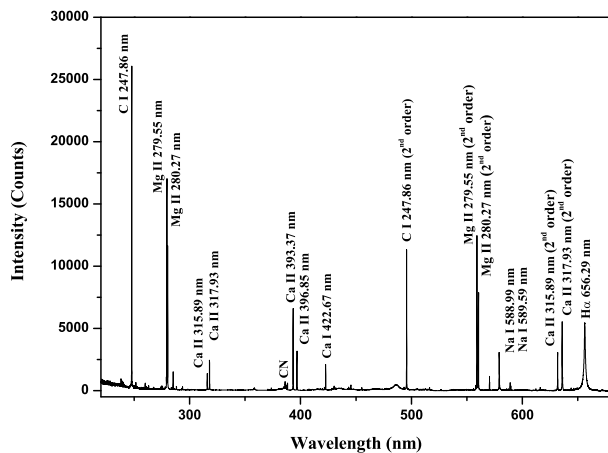


Figure 2: Typical LIBS spectrum of wood pellet with wavelength 210-690 nm recorded at delay time of 1000 ns, gate time of 2000 ns and laser pulse energy of 80 mJ.

The strong resonance Cr I line at 425.43 nm and Cr II line at 283.56 nm were selected as a suitable analytical line for direct elemental analysis in samples. Since the number density of the species of Cr in plasma is low due to their low concentration in the samples, self absorption effect may be neglected within the experimental uncertainty. Therefore, these lines are good candidates for detection limits due to its strength compared with other emission lines.

In order to examine whether dried wood pellets are suitable for sample matrix or not, we must investigate their elemental composition. LIBS spectra for all of them had been measured at laser energy of 80 mJ/pulse and identified in the spectral range of 210-690 nm. As an example, a typical LIBS spectrum was shown in Fig. 2. The spectral lines were identified by using the NIST atomic spectral database [18]. It is identified that the emission lines are atomic or single ionized lines of C, Mg, Na and Ca elements, some strong lines for each element were also labeled. It is evident that there are no emission lines of Cr element for all of pellets.

Furthermore, a comparison of LIBS spectra of 3000 ppm Cr solution and dried wood pellet after absorbing it in the range 424-437 nm were shown in Fig. 3, respectively. The corresponding strong emission lines are also identified and labeled. It can be seen from two figures that the line intensities in the LIBS spectra of dried wood pellet after absorbing solution is found to be much higher than that of Cr solution of same concentrations using

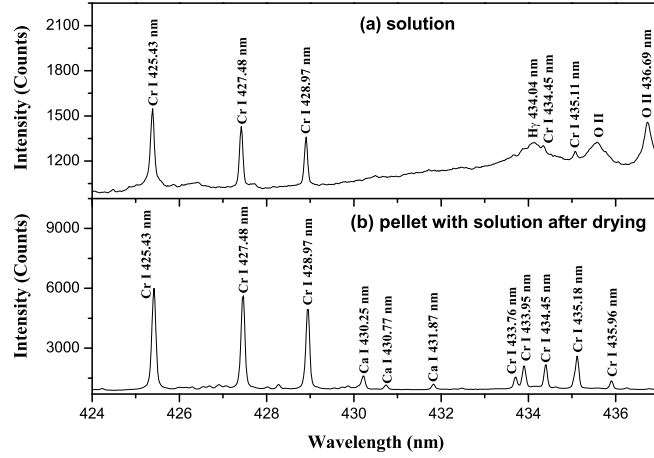


Figure 3: A comparison of LIBS spectra in the range 424 - 437 nm from 3000 ppm Cr solution and dried wood pellets absorbed 3000 ppm Cr solution, respectively.

the same parameters of laser beam. It is obviously seen that the  $H_{\gamma}$  and O II lines originated from  $H_2O$  in Cr solution have been disappeared in the dried wood pellet after absorbing. The signal-to-background ratio (S/B) of Cr have been greatly enhanced.

To determine the optimum experimental conditions a series of temporal- and spatial-resolved experiments were performed. Fig. 4 shows the variation of intensity and signal-to-background ratio (S/B) of emission line Cr I 425.43 nm with the delay time at the different spatial distances. Here, the gate width was fixed to 500 ns. It can be seen from this figure that the optimum signal-to-background ratio of Cr element in wood pellets was from 1000 to 3000 ns at the spatial distance of 2.2 mm. That is, the signal acquired with a distance of 2.2 mm and a delay time of 1000 ns were sufficient to suppress background signals from continuum plasma radiation, and a gate width of 2000 ns was chosen to guarantee well visible emission.

To investigate the detection capacity at the matrix of wood pellets, the calibration curves of Cr element were obtained by drawing the line peak intensity against their relative concentrations. Based on the calibration curves, the analytical performance of LIBS technique was evaluated for the detection of Cr in samples. Detection limits were calculated in the low concentration region. It is determined by means of the expression  $LOD=3\frac{\sigma}{S}$ . where  $\sigma$  is the relative standard deviation of the background, and S is the sensitivity given by the slope of the corresponding calibration curve [6,8,19].

Fig. 5 shows the calibration curves of the strong resonance Cr I line at 425.43 nm and Cr

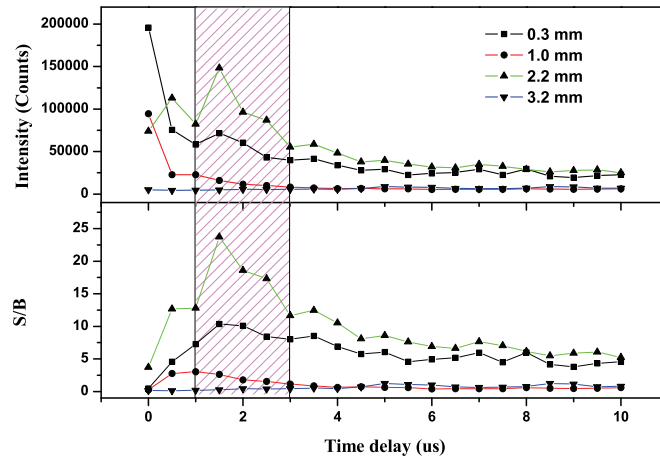


Figure 4: Variation of intensity and S/B of emission line Cr I 425.43 nm with the delay time at the different spatial distance.

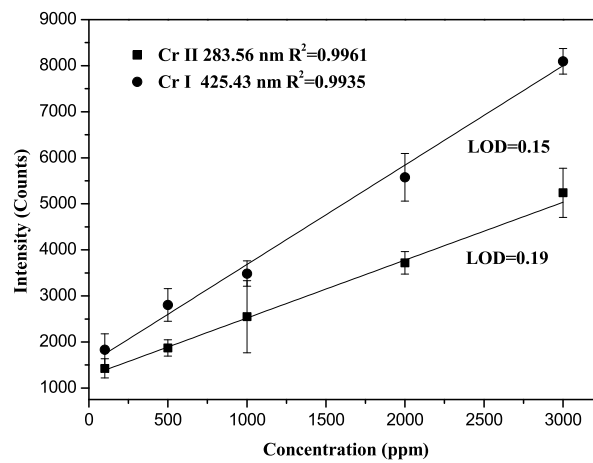


Figure 5: Calibration curves for Cr I 425.43 nm and Cr II 283.56 nm in dried wood pellets absorbed standard solutions.

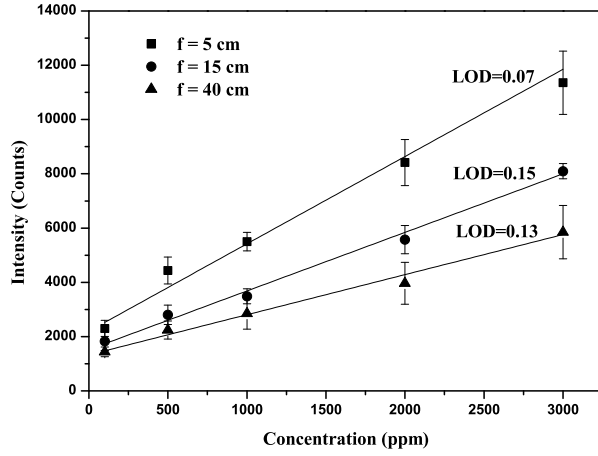


Figure 6: Calibration curves for Cr I 425.43 nm in wood pellets with three different focal lengths.

Table 1. Comparison of detection limits (ppm) in the different focal length lens and those reported in the literature.

Focal length (cm)	$R^2$	RSD%	LODs(ppm)	
			present work	other works
5	0.9723	6.41%	0.07	0.4 <sup>[8]</sup> , 0.16 <sup>[9]</sup> , 0.1 <sup>[13]</sup>
10	0.9935	6.79%	0.15	1.2 <sup>[16]</sup> , 39 <sup>[20]</sup>
15	0.9795	10.16%	0.13	30 <sup>[21]</sup> , 1.1 <sup>[22]</sup>

II line at 283.56 nm, respectively. In this figure each data point represents the mean value of 50 individual measurements, and the error bars show the calculated standard deviation, which represent the variation in our measurements. Calibration curves of the elements in the wood pellets matrix have well linear fitting within the experimental uncertainty. The LODs for Cr were found to be 0.15 and 0.17 ppm for atomic line 425.43 and ionized line 283.56 nm, respectively.

In order to investigate the effects of focal length to LODs, similar optimum procedures for changing the lens of 5 and 15 cm focal length have also been performed. Fig. 6 shows the calibration curves of Cr I line at 425.43 nm with three different focal lengths. The obtained LOD values, the mean relative standard deviation RSD% and the correlation coefficients  $R^2$  were listed in Table 1. The correlation coefficients  $R^2$  indicate good linearity. And we can find that these detection limits are better than those reported in the

other literature [8,9,13,16,20-22].

#### 4. Conclusion

In conclusion, LIBS technique has been applied for the analysis of heavy metal element in liquid samples by taking Cr standard solutions as examples, which based on the idea of transforming the elements dissolved in liquids into the elements distributed inside dried wood pellets. It is advantageous that dried wood pellets obviously improved the detection limit of heavy element in liquid by minimizing the water matrix. The LOD value of 0.07 ppm for Cr in solutions has been obtained. The results were demonstrated to successfully produce a superior analytical response for heavy metal elements by using wood pellet as sample matrix.

#### Acknowledgement

This work is supported by the National Nature Science Foundation of China (Grant No. 11064012, 91126007) and the JSPS-NRF-NSFC A3 Foresight Program in the field of Plasma Physics (NSFC: No.11261140328).

#### References

- [1] D A Rusak, B C Castle, B W Smith et al. *Critical Reviews in Analytical Chemistry*, **27**, 257 (1997).
- [2] P Yaroshchuk, R J S Morrison, D Body et al. *Applied Spectroscopy*, **58**, 1353 (2004).
- [3] N Aras, S Ü Yeşiller, D A Ateş et al. *Spectrochimica Acta Part B*, **74-75**, 87 (2012).
- [4] C Pasquini, J Cortez, L M C Silva et al. *J. Braz. Chem. Soc.*, **18**, 463 (2007).
- [5] A K Rai, F Y Yueh and J P Singh. *Applied Optics*, **42**, 2078 (2003).
- [6] M Sabsabi and P Cielo. *Applied Spectroscopy*, **49**, 499 (1995).
- [7] V K Singh, V Rai and A K Rai. *Lasers Med Sci*, **24**, 27 (2009).
- [8] F Y Yueh, R C Sharma, J P Singh et al. *J. Air & Waste Manage. Assoc.*, **52**, 1307 (2002).
- [9] A Kumar, F Y Yueh, T Miller et al. *Applied Optics*, **42**, 6040 (2003).
- [10] P Yaroshchuk, R J S Morrison, D Body et al. *Spectrochimica Acta Part B*, **60**, 986 (2005).
- [11] D A Cremers, L J Radziemski and T R Loree. *Applied Spectroscopy*, **38**, 721 (1984).
- [12] Z J Chen, H K Li, M Liu et al. *Spectrochimica Acta Part B*, **63**, 64 (2008).
- [13] G Arca, A Ciucci, V Palleschi et al. *Applied Spectroscopy*, **51**, 1102 (1997).
- [14] L St-Onge, E Kwong, M Sabsabi et al. *Journal of Pharmaceutical and Biomedical*

Analysis, **36**, 277 (2004).

[15] J O Cáceres, J T López, H H Telle et al. Spectrochimica Acta Part B, **56**, 831 (2001).

[16] D M D Pace, C A D'Angelo, D Bertuccelli et al. Spectrochimica Acta Part B, **61**, 929 (2006).

[17] J Q Wu, L Chang, L M Liu et al. Applied Laser, **30**, 340 (2010).

[18] NIST electronic database, <http://physics.nist.gov/PhysRefData>.

[19] V Thomsen, D Schatzlein and D Mercurio. Spectroscopy, **18**, 112 (2003).

[20] M Y Yao, J L Lin, M H Liu et al. Applied Optics, **51**, 1552 (2012).

[21] N K Rai and A K Rai. Journal of Hazardous Materials, **150**, 835 (2008).

[22] N K Rai, A K Rai, A Kumar et al. Applied Optics, **47**, G105 (2008).

# A comparative study of the laser induce breakdown spectroscopy in single- and double-pulse laser geometry

SUN Duixiong, SU Maogen, DONG Chenzhong\*, WEN Guanhong, CAO Xiangnian  
*Key Laboratory of Atomic and Molecular Physics & Functional Material Gansu Province, College of Physics and Electronic Engineering, Northwest Normal University, Lanzhou, 730070, China.*  
\*e-mail: dongcz@nwnu.edu.cn

## Abstract

A time resolved laser induced breakdown spectroscopy technique (LIBS) was used for the investigation of emission signal enhancement on double-pulse LIBS. Two Q-switched Nd:YAG lasers at 1064 nm wavelength have been employed to generate laser-induced plasma on aluminum-based alloys. The plasma emission signals were recorded by spectrometer with ICCD detector. Spectral response calibration was performed by using deuterium and tungsten halogen lamps. Time evolution of the plasma temperature and electron density was investigated in SP and DP experiments. Based on the investigation of plasma parameters, the enhancements of emission line intensities were investigated, and the mechanisms of it were discussed.

**Keywords:** Plasma diagnostics, Intensity calibration, Emission signal enhancement.

## 1.Introduction

Laser induced breakdown spectroscopy (LIBS) has attracted much attention for several decades, as it concerns many advantages in physical and chemical analysis, such as multi-elemental analysis without any type of sample preparation, real time analysis, stand-off analysis, *in situ* analysis, apparatus or experimental simplicity, inexpensiveness, robustness, and quickness [1, 2, 3, 4, 5, 6, 7]. However, compared with other conventional spectrometric methods such as ICP-OES or ICP-MS [8], a single-pulse (SP) LIBS is less sensitive. To improve its sensitivity, double-pulse (DP) LIBS is applied and creatively modified in analytical researches.

Since the DP LIBS approach was first suggested by Piepmeier and Malmstadt[9] in 1969, and Scott and Strasheim[10] in 1970, the analytical benefits of using double-pulse LIBS attract many research groups [11, 12, 13]. Although it is clear that DP LIBS yields enhanced signal but the exact reason behind it is not yet well understood[14, 15, 17]. According to different researches, the reasons of the signal enhancement may refer to the formation of a reduced pressure atmosphere[18, 19, 20, 21]. Mukherjee *et al* [22] proposed that, the longer length of plasma plume and higher plasma temperature caused

enhancement of emission signal. Angel *et al* [15] reported nearly 40 times enhanced signal and from the scanning electron microscopy images of the plasma generated by SP and DP LIBS they inferred that, the enhancement of emission signal intensity is a result of larger plasma and enhanced material removal. In the collinear geometry, Cristoforetti *et al*[20] reported that the second plasma is created and evolves in a rarified gas atmosphere enclosed by the shock wave produced by the first pulse. Although the increases were related to the excitation energy levels of the emission lines[16], the reason why it exist a large variety of enhancements in the literature is not well understood. In consequence, the studies from different researches did not draw the same conclusion concerning the mechanisms of the emission signal enhancement.

In this work, a set-up which can perform single- and double-pulse LIBS with collinear beams geometry configuration is introduced for the analysis of aluminum-based alloy sample at atmospheric pressure in air. Time resolved technique are used to investigate the plasma characteristics in SP and DP experiments, The optimum delay time and inter-pulse delay time for maximum the emission signal are obtained, based on these optimized experimental parameters, the emission signal enhancement mechanisms are discussed by investigating the time behaviorial of the plasma temperature and electron density.

## 2. Experimental set-up

The experimental set-up has been reported in previous works[23, 24] and is only described briefly here. A schematic diagram of the experimental set-up is shown in Fig. 1. Two Nd: YAG laser (Spectra-Physics, PRO-350) with a fundamental wavelength of 1064 nm, pulse width of 8 ns, repetition frequency of 10 Hz, is employed to generate the plasma. For single-pulse experiments, the second Laser beam is focused on the target surface with the laser energy 60 mJ while the first laser is closed. For the double-pulse experiments, first laser is opened and the laser beam is reflected on the same direction as second laser beam by beam splitter, and the laser energy is set to 30 +30 (mJ). The focusing lens to sample distance is set to 2 mm less than the lens focal length, in order to avoid the air breakdown in front of the target. The target is positioned on the 3-D translation stage in order to make each fresh spot ablated to avoid forming the deep-crater on the target surface. The space integrated emission of laser-induced plasma is collected through a quartz lens with focal length of 100 mm which is used to form a 1:1 image of the plasma onto the entrance slit of an Cerny-Turner type of spectrometer (Shamrock SR-500i, focal length of 0.5 m, diffraction grating of 2400 groves/mm). The spectrometer is equipped with intensified charge-coupled device detector (iStar-DH734-18F-03, Andor technology). The wavelength range of spectrum is covered from 200 to 900 nm with spectral resolution

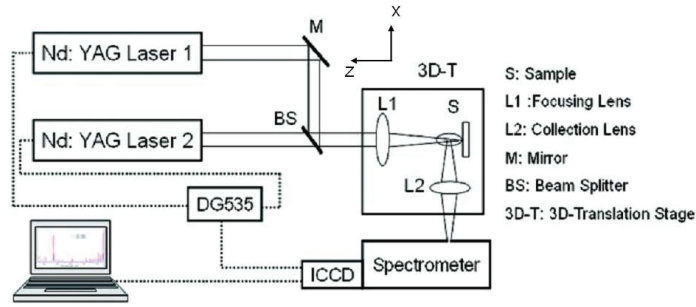


Figure 1: Schematic representation of the experimental set-up.

of 0.03 nm at 546 nm.

A digital delay generator (DG535, Stanford Research system) is used to synchronize the laser and detector. The focused and the imaging lens are all positioned on the translation stage to keep stability of the plasma and its image when adjusted the position of the image of the plasma onto the spectrometer slit.

All the experimental operations including sample movement and spectral acquisition parameters set (number of spectra averaged, acquisition delay, gate width and MCP's gain), were controlled by the PC and performed in air at atmospheric pressure.

Aluminum-based alloy with 13 elements is chosen to be the sample because excellent work on its LIBS analysis.

### 3. Results and discussion

#### 3.1 Spectral response calibration

In LIBS analysis, the spectrometer sensitivity (spectral response) is essential for the determination of plasma temperature and especially for the calculation of the elemental concentration by CF-LIBS[25]. Each component of a LIBS detection system has a certain spectral response, the response depends on wavelength, that means not all wavelengths are transmitted through or reflected off optical components with the same transfer efficiency. In addition, the detector used to record the light has a response function. Therefore, only if the absolute characterization of the spectral response has been made, it is possible to report data that reflects the behaviour of the LIBS plasma itself, rather than a combination of the LIBS plasma and experimental equipment.

In this work, the spectral response is calibrated by deuterium lamp which covered with the wavelength region 200-400 nm, tungsten halogen lamp is used to calibrate the spectral response with the wavelength region 400-900 nm. These two lamps, traceable to NIST[26], are supplied with a calibration curve. Fig.2. shows the measured curve

of spectral response and the calibration curve given by NIST in the wavelength region 200-400 nm, with the help of these two curves, the calibration function can be obtained under a certain experimental condition. Fig.3. shows the spectra from mercury lamp, it is clear that after the intensity calibration, the intensity of 253.65 nm mercury line is highest compared to all other lines in the spectrum. The same procedure is carried out for intensity calibration in the wavelength region 400-900 nm using tungsten halogen lamp.

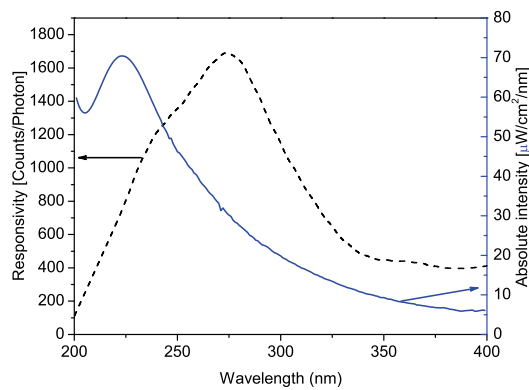


Figure 2: Spectral response and calibration curve of Czerny-Turner spectrometer measured with calibrated deuterium lamp in the range from 200-400 nm

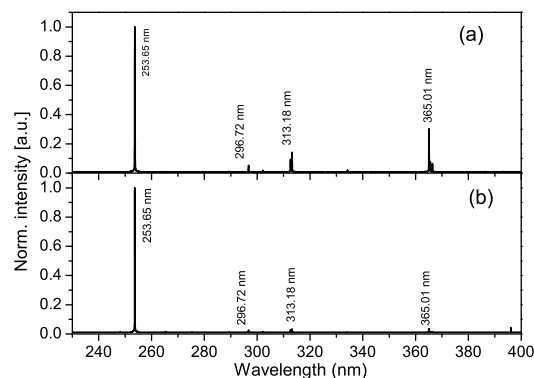


Figure 3: Spectral intensity of mercury lamp, (a) experimental data without intensity calibration (b) calibrated data using deuterium lamp

### 3.2 Optimization of the experimental parameters and characteristics of emission signal

The laser-induced plasma have a relative short lifetime, the radiation of the laser-induced plasma include strong bremsstrahlung, ionic, atomic, and molecular emissions

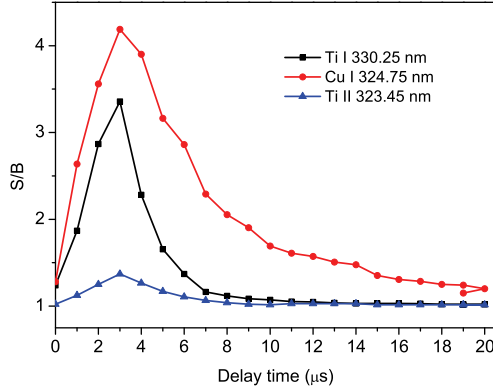


Figure 4: Signal-to-background ratio as a function of delay time for single-pulse laser ablation with a gate width of 1  $\mu$ s..

sequentially on a time frame. In order to suppress the background signals from continuum plasma radiation, a short gate width time is chosen to avoid strong changes in plasma temperature and electron number density during the measurement and to guarantee well-visible emission signals for all elements. According to the previous study[23], the gate width with 1  $\mu$ s is good for recording the emission signal from minor and trace elements in a certain delay time. Fig. 4 shows the signal-to-background (S/B) ratio as a function of delay time for single-pulse experiments, it can be seen that the optimum delay time to obtain the maximum S/B is about 3  $\mu$ s. Generally, at this delay time stage, strong continuum emission become weak, and the intensity of the emission line reached its maximum. Therefore, the delay time is kept at 3  $\mu$ s in order to most emission lines from different elements can be detected simultaneously with relative larger S/B ratio. For DP LIBS, the time delay between two laser pulse is fixed at 2  $\mu$ s, according to our previously study, this inter-pulse delay time is good for maximum emission signal enhancement.

Fig.5 shows the characteristics of the partial spectra detected in SP and DP experiments. It's clear that not only the emission signal is enhanced in DP experiments, but for emission lines of Ni, Pb, Zn, which were not detected in SP experiments because of the lower contents, are detected in DP experiments.

### 3.3 Plasma parameters and mechanisms of emission signal enhancement

The plasma parameters such as electron temperature and electron density provide important information regarding the characterization of the laser induced plasma. Assuming the Local Thermodynamical Equilibrium (LTE), the Saha-Boltzmann plot method [27, 28] is applied to determine plasma temperatures. Eqs.(1) and (2) are considered respectively

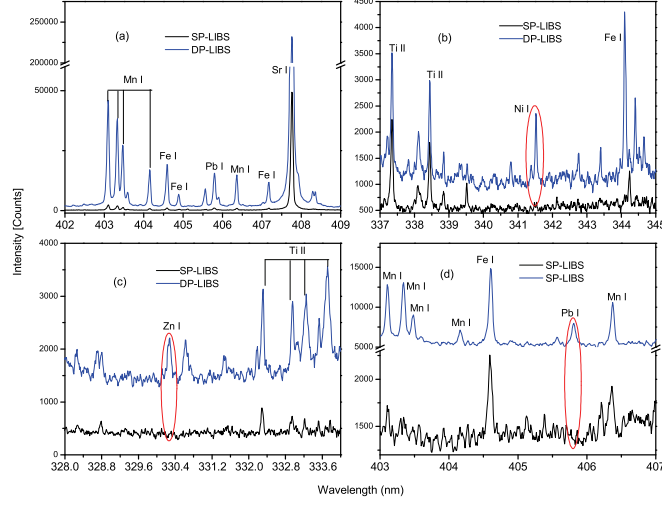


Figure 5: Emission signal characteristics in SP and DP experiments .

for neutral lines and for ionic lines:

$$\ln \frac{I_I \lambda_I}{g_I A_I} = -\frac{1}{kT} E_k^I + \ln \left( hc \frac{N_0}{Z_0(T)} \right) \quad (1)$$

$$\ln \frac{I_{II} \lambda_{II}}{g_{II} A_{II}} - \ln \left( \frac{2(2\pi m k)^{3/2} T^{3/2}}{h^3 N_e} \right) = -\frac{1}{kT} \times (E_k^{II} + E_{IP}) + \ln \left( hc \frac{N_0}{Z_0(T)} \right) \quad (2)$$

where the indexes  $I$  and  $II$  correspond to neutral and ionic lines, respectively.  $I$  is the intensity of the emission line,  $\lambda$  is the wavelength of the emission line(m),  $g$  is the statistical weight (dimensionless),  $A$  is the transition probability ( $s^{-1}$ ),  $E_k$  is the excitation energy level (eV),  $k$  is Boltzmann's constant ( $eV K^{-1}$ ),  $T$  is the plasma temperature (K),  $h$  is Plank's constant( $eV s$ ),  $c$  is the speed of light ( $m s^{-1}$ ),  $N_0$  is the particles density of the considered element in the plasma ( $m^{-3}$ ),  $Z_0(T)$  is the partition function (dimensionless),  $m$  is the electron mass (Kg),  $N_e$  is the electron density ( $m^{-3}$ ) and  $E_{IP}$  is the ionization energy (eV) of the considered element. An equation similar to the Boltzmann-plot equation is obtained:

$$\ln \left( \frac{I_I \lambda_I}{g_I A_I} \right)^* = -\frac{1}{kT} E_k^* + \ln \left( hc \frac{N_0}{Z_0(T)} \right) \quad (3)$$

where  $E_k^I$  for neutral lines and  $E_k^* = E_k^{II} + E_{IP}$  for ionic lines.

The electron density is determined from the Stark broadening of emission line. The full width at half maximum (FWHM) of a line can be used to determine the electron number

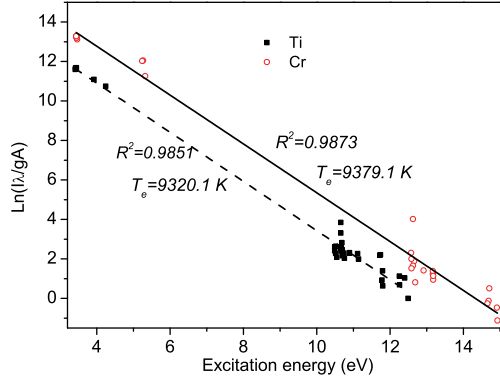


Figure 6: Saha-Boltzmann plot obtained from the emissivities of Ti and Cr spectral lines in SP-LIBS. The delay time is 8  $\mu$ s.

density, using the following relation[29, 30]:

$$\Delta\lambda = 2\omega\left(\frac{N_e}{10^{16}}\right) + 3.5A\left(\frac{N_e}{10^{16}}\right)^{(1/4)}(1 - BN_D^{-1/3})\omega\left(\frac{N_e}{10^{16}}\right) \quad (4)$$

where  $\omega$  is the electron width parameter, which is a weak function of temperature,  $A$  is the ion broadening the parameter,  $N_e$  is the electron density,  $B$  is a coefficient equal to 1.2 or 0.75 for ionic or neutral lines, and  $N_D$  is the number of particles in the Debye sphere. The contribution due to the ion broadening is very small and can be neglected, therefore, the electron density can be extract by:

$$\Delta\lambda = 2\omega\left(\frac{N_e}{10^{16}}\right). \quad (5)$$

Based on Eqs.(3) and (5), an iterative procedure can be used to obtain the plasma temperature  $T$  and the electron density  $N_e$ . In the present work, 41 Ti lines and 25 Cr lines are used to establish Saha-Boltzmann plot, Ca I 393.3 nm line is used to estimate the electron density, the instrument broadening for emission line of 393.3 nm is subtracted, and the electron width parameters  $\omega$  is obtained form reference[31].

As an example, Fig.6 shows the Saha-Boltzmann plot obtained from the emissivities of Ti and Cr spectral lines in SP-LIBS. Continuous lines represent the result of a linear best fit. Note that the best fit lines corresponding to different species are practically parallel, *i.e.* the temperature of all the species in the sample is the same, according to the predictions of LTE assumption.

For LTE to hold in a plasma, the collision with electrons have to dominate over the radiative processes, this condition requiring a sufficiently large electron density. A crite-

riterion proposed by McWhirter[32] was based on the existence of a critical electron density for which collisional rates are at least ten times the radiative rates. For an energy gap difference  $\Delta E$  between the transition levels, the criterion for LTE is :

$$N_e \geq 1.6 \times 10^{12} T^{1/2} (\Delta E)^3 \text{ cm}^{-3} \quad (6)$$

where  $T$  is the plasma temperature. However, the McWhirter criterion is a necessary but not sufficient condition for LTE to hold. Therefore, one more criterion is necessary to check the existence of LTE. In addition to Eqs. (6) for calculating the electron density, Saha equation[33] can also be used to determine the electron density. From comparing the electron density obtained from Eqs. (6) (independence on LTE) and Saha equation (dependence on LTE), one can assess the existence of LTE. In this work, we found that the electron density obtained using Eqs.(6) and Saha equation have a good agreement before  $5 \mu\text{s}$  and  $3 \mu\text{s}$  in SP and DP LIBS, respectively, *i.e.* the plasma more close to the LTE in that time stage.

Fig. 7 shows the evolution of the plasma temperature in SP and DP experiments as a function of the delay time. It decrease fast at the beginning of  $10 \mu\text{s}$  in SP experiments as well as DP experiments, after  $10 \mu\text{s}$  later, the plasma temperature decrease slowly. Moreover, the plasma temperature in DP experiments is less than that in SP experiments, although the total energy of the laser pulses is same. Fig. 8 shows the evolution of the electron density in SP and DP experiments, the time evolution behaviour of the electron density in SP and DP LIBS is the same as the plasma temperature. In DP LIBS, the sequential laser pulses can ablate more material from the target surface, this may cause the emission signals enhancement, but with the first plasma decaying, the interaction between the second plasma and first plasma become weak, *i.e.* the collision between electron and atoms and ions become weak, therefore, the plasma temperature and electron density is less than that measured in SP LIBS.

From the temporal behavior of the plasma temperature and electron density, the emission signal enhancement mechanisms in DP experiments can be explained as following: For DP LIBS in collinear geometry, there are two plausible processes occurring in the plasma plume: (1) absorption of the second laser pulse in the plume of the plasma initiated by the first laser pulse and (2) new plasma formation by the remaining second laser pulse. In the collinear case both pulses have the same axis of propagation and are directed orthogonal to the sample surface. The first laser pulse is used to ablate pre-ablative first plasma, and then with the plasma expanding and after a certain time delay, the second laser pulse may penetrate to the plasma plume to generate the second plasma, meanwhile, partial energy of the laser pulse may be absorbed by the first plasma plume. Actually, it

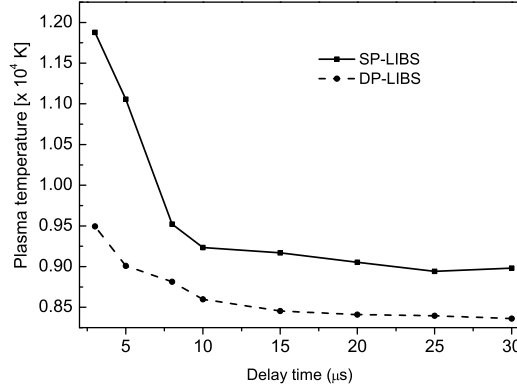


Figure 7: Time evolution of the plasma temperature in SP and DP experiments, the laser energies are set to 60 mJ (SP) and 30+30 (mJ)(DP), respectively.

is difficult to isolate these two processes in collinear geometry scheme. According to the comparative investigation of plasma parameters in SP and DP LIBS, we consider that new plasma production by second laser pulse dominate this process, absorption of the second laser pulse by the first plasma is weak. Our conclusion is agreement with Céline *et al.*[16] study, they found that the interaction of the plasma and laser depend on the delay between the two laser pulses in collinear geometry, for inter-pulse delay  $\Delta t > 1\mu\text{s}$ , the plasma produced by the first pulse is essentially transparent to the second pulse, the second pulse is not able to interact with the residual plasma.

#### 4. Conclusions

In the framework of LIBS analysis on aluminum samples, time resolved SP and the DP LIBS experiments is carried out. In collinear geometry, the emission signal enhancement is observed. From comparative investigation of the plasma parameters in SP and DP experiments, emission signal enhancement mechanisms is discussed qualitatively. Actually, the emission signal enhancement is very complexity, it dependents on many factors, such as laser energies, inter-pulses delay time, background gases and so on. In DP LIBS, the dynamic behaviour of the plasma is also different with SP LIBS condition, therefore, the further studies for deeper physical mechanisms of emission signal enhancement must consider the different factors and to develop physical models.

#### Acknowledgement

This work is supported by the National Natural Science Foundation of China (Grants

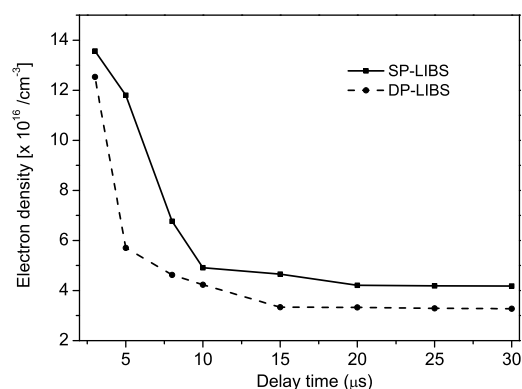


Figure 8: Time evolution of the electron density in SP and DP experiments.

Nos. 10847007, 10876028, 11064012, 10964010, 91126007)

## References

- [1] Cremers D. A, Appl. Spectrosc., **41**, 572 (1987)
- [2] Sabsabi M, Cielo P, Appl. Spectrosc., **49**, 499 (1995)
- [3] Rusak D A, Castle B C, Smith B W et al, Anal. Chem., **17**, 453 (1998)
- [4] St-Onge, Sabsabi M, Spectrochim. Acta Part B, **55**, 299 (2000)
- [5] Arca G, Ciucci A, Palleschi V, Appl. Phys. B, **63**, 185 1996
- [6] Lee D H, Han S C, Kim T H et al, Anal. Chem., **83**, 9456 (2011)
- [7] Tsai S J J, Chen S Y, Chung Y S, Anal. Chem., **78**, 7432 (1996)
- [8] Winefordner J D, Gornushkin I B, Correll T et al, J. Anal. At. Spectrom., **19**, 10612004,
- [9] Piepmeier E H, Malmstadt H V, Anal. Chem., **41**, 700 1969
- [10] Scott R H, Strasheim A, Spectrochim. Acta Part B, **25**, 311 (1970)
- [11] Cremers D A, Radziemski L J, Loree T R, Appl. Spectrosc., **38**, 721 (1984)

- [12] Uebbing J, Brust J, Sdorra W et al, *Appl. Spectrosc.*, **45**, 1419 (1991)
- [13] St-Onge L, Detalle V, Sasabi M, *Spectrochim. Acta Part B*, **57**, 121 (2002)
- [14] Straitis D N, Eland K L, Angle S M et al, *Appl. Spectrosc.*, **55**, 1297 (2001)
- [15] Angel S M, Straitis D N, Eland K L et al, *J. Anal. Chem.*, **369**, 320 (2001)
- [16] Gautier C, Fichet P, Menut D et al, *Spectrochim. Acta Part B*, **60**, 0265 (2005)
- [17] Scaffidi J, Angel S M, Cremers D A, *Anal. Chem.*, **78**, 24 (2006)
- [18] Sattmann R, Sturm V, Noll R, *Appl. Phys.*, **28**, 2181 (1995)
- [19] Corsi M, Cristoforetti G, Giuffrida M, *Spectrochim. Acta. Part B*, **59**, 723 (2004)
- [20] Cristoforetti G, Legnaioli S, Palleschi V, *Spectrochim. Acta. Part B*, **59**, 1907 (2004)
- [21] Noll R, Sattmann R, Sturm V, *J. Anal. At. Spectrom.*, **19**, 419 (2004)
- [22] Mukherjee P, Chen S, Witanachchi S, *Appl. Phys. Lett.*, **74**, 1546 (1999)
- [23] Peng L L, Sun D X, Su M G et al, *Optics & Laser Technology*, **44**, 2469 (2012)
- [24] Han J T, Sun D X, Su M G et al, *Analytical letters*, **45**, 1936 (2012)
- [25] Taschuk M T, Godwal Y, Tsui Y Y et al, *Spectrochimica Acta Part B*, **63**, 525 (2008)
- [26] National Institute of Standards and Technology, [http://physics.nist.gov/PhysRefData/ASD/lines\\_form.html](http://physics.nist.gov/PhysRefData/ASD/lines_form.html)
- [27] Yalcin S, Crosley D R, Smith G P et al, *Appl. Phys. B*, **68**, 121 (1999)
- [28] Aguilera J A, Aragón C, *Spectrochim. Acta Part B*, **59**, 1861 (2004)
- [29] Colon C, Hatem G, Verdugo E et al, *Appl. Phys.*, **73**, 4752 (1993)
- [30] Ahmed R, Baig M A, *J. Appl. phys.*, **106**, 03307 (2009)
- [31] Griem H R, *Spectral line broadening by plasma*, Academic Press. New York, 1974
- [32] McWhirter R W P, *Spectral intensities*, in: R.H. Huddleston, S.L. Leonard (Eds.), *Plasma Diagnostic Techniques*. Academic Press, 1965, Chapter 5.
- [33] Aragón, Aguilera J A, *Spectrochimica Acta Part B*, **63**, 893 (2008)

# Dielectronic Recombination of Highly Charged Heavy Ions Studied with the Tokyo Electron Beam Ion Trap

Zhimin Hu<sup>1</sup>, Xiaoying Han<sup>2</sup>, Yueming Li<sup>2</sup>, Daiji Kato<sup>3</sup>, Xiaomin Tong<sup>4</sup>,  
and Nobuyuki Nakamura<sup>1,3</sup>

1) *Inst. for Laser Science, The Univ. of Electro-Communications,  
Tokyo 182-8585, Japan*

2) *Inst. of Applied Physics and Computational Mathematics, Beijing 100088, China*

3) *National Institute for Fusion Science, Toki, Gifu 509-5292, Japan*

4) *University of Tsukuba, Tsukuba, Ibaraki 305-8577, Japan*

*e-mail: n\_nakamu@ils.uec.ac.jp*

## Abstract

We present recent results at the Tokyo electron beam ion trap (Tokyo-EBIT) for the angular distribution of x-rays emitted in dielectronic recombination processes. Since the observation angle of the Tokyo-EBIT is restricted to 90° with respect to the electron beam, it is impossible to obtain the angular distribution directly. We have thus combined the differential x-ray measurements at 90° and the integral measurements through ion-abundance to obtain the asymmetric parameter. By comparing with the theoretical result by Fritzsche *et al.* [Phys. Rev. Lett. 103, 113001 (2009)], anomalously strong effects of the Breit interaction on the angular distribution has been clearly demonstrated.

**Keywords:** dielectronic recombination, highly charged ion, electron beam ion trap, relativistic effect, Breit interaction,

## 1. Introduction

X-rays emitted from the excited states formed by collisions with an unidirectional electron beam can have an anisotropic angular distribution and polarization, due to the uneven population of the magnetic sublevels. The degree of anisotropy depends on the extent of the deviation from the even populations of the excited magnetic sublevels. Anisotropy (or polarization) of x-ray lines is thus important because it can be used as a diagnostic tool for laser-produced plasma, such as anisotropic velocity distribution of electron.

The anisotropy is also important in the atomic physics point of view. Recently, Fritzsche *et al.* [1] have theoretically studied the Breit interaction effects on the angular distribution of the X-rays emitted in dielectronic recombination (DR), which is the combination of the dielectronic capture (DC) and the successive radiative stabilization (RS),

$$e^- + A^{q+} \xrightarrow{DC} A^{(q-1)+**} \xrightarrow{RS} A^{(q-1)+} + h\nu. \quad (1)$$

The angular distribution of the electric dipole emission can be expressed by the angular distribution coefficient  $W(\theta)$  [2] as

$$W(\theta) = 1 + \beta P_2(\cos \theta) \quad (2)$$

where  $\theta$  denotes the angle of emission,  $P_2$  the Legendre polynomial, and  $\beta$  the anisotropy parameter, which is related to the alignment parameter  $\mathcal{A}_2$  [1, 3] as  $\beta = \mathcal{A}_2/\sqrt{2}$  for the  $J = 1 \rightarrow 0$  transition.  $\mathcal{A}_2$  is determined by the magnetic sublevel distribution of the intermediate state  $A^{(q-1)+**}$  produced by DC, and for  $J = 1$  intermediate states, it is expressed as

$$\mathcal{A}_2 = \sqrt{2} \cdot \frac{\sigma_{\pm 1} - \sigma_0}{2\sigma_{\pm 1} + \sigma_0}, \quad (3)$$

where  $\sigma_{M_J}$  denotes the population of the magnetic sublevel with the magnetic quantum number  $M_J$ . Fritzsche *et al.* found that the Breit interaction dominates the alignment parameter and thus brings about a qualitative change in the angular distribution. According to their result, the angular distribution of the  $[1s2s^22p_{1/2}]_1 \rightarrow [1s^22s^2]_0$  transition following the dielectronic capture into initially Li-like heavy ions has a maximum at  $90^\circ$  with respect to the electron beam when the Breit interaction is considered whereas it has a minimum at  $90^\circ$  when only the Coulomb interaction is considered. They thus proposed to measure the angular distribution (or the polarization) of this DR X-ray or the alignment parameter of the intermediate state for the sensitive test of the Breit interaction effect on DR processes of HCIs.

In this paper, we present the experimental determination of the angular distribution for the transition proposed by Fritzsche *et al.* using an electron beam ion trap (EBIT) in Tokyo. As an alternative to the direct angular distribution measurement, the alignment parameter is obtained from the combination of the differential X-ray measurement at  $90^\circ$  and the integral resonant strength measurement through the ion-abundance inside the EBIT.

## 2. Experiment

In the present study, the angular distribution of the x-rays emitted from DR into Li-like Au was obtained by the combination of two experiments, x-ray measurement at  $90^\circ$  [4, 5] and ion abundance measurement [6, 7]. In the X-ray measurement, the electron beam energy was scanned from 44.8 to 46.3 keV with a scanning rate of 20 ms/scan. A high-purity Germanium detector placed at  $90^\circ$  with respect to the electron beam was used to detect the x-rays. On the other hand, in the ion-abundance measurement, the electron

Table 1: Experimental results. The error ( $1\sigma$ ) listed in the table corresponds to the error of the least square fitting weighted by the statistical uncertainties.

$R_{A/B}^{X\text{-ray}}$	$R_{A/B}^{\text{ion}}$	$W_A(90^\circ)$	$\mathcal{A}_2$
$13.0 \pm 0.9$	$12.3 \pm 0.9$	$1.06 \pm 0.11$	$-0.17 \pm 0.31$

energy scan was done quasi-statically in order to obtain the relative DR cross section  $[\sigma_{\text{Li}}^{\text{DR}}]$  of Li-like Au from the ion-abundance ratio between Be-like and Li-like Au ( $n_{\text{Be}}/n_{\text{Li}}$ ) using the following formula, which is established only at the equilibrium condition (see Ref. [6] for the derivation):

$$[\sigma_{\text{Li}}^{\text{DR}}] = \frac{n_{\text{Be}}}{n_{\text{Li}}} - B(E_e), \quad (4)$$

where  $B(E_e)$  denotes the slowly varying function when the ion ratio  $n_{\text{Be}}/n_{\text{Li}}$  is plotted as a function of electron energy. The abundance ratio was obtained by measuring the intensity of ions extracted from the EBIT.

### 3. Results and discussion

The angular distribution function  $W(\theta)$  at  $\theta = 90^\circ$  for the DR x-ray from the intermediate state  $[1s2s^22p_{1/2}]_1$  (A) can be obtained from the following formula [8].

$$W_A(90^\circ) = R_{A/B}^{X\text{-ray}} / R_{A/B}^{\text{ion}}, \quad (5)$$

where  $R_{A/B}^{X\text{-ray}}$  and  $R_{A/B}^{\text{ion}}$  represent the intensity ratio between the intermediate states  $[1s2s^22p_{1/2}]_1$  (A) and  $[1s2s2p_{1/2}^2]_1$  (B) obtained by the x-ray measurement and the ion abundance measurement, respectively. The alignment parameter  $\mathcal{A}_2$  is then obtained by

$$\mathcal{A}_2 = 2\sqrt{2}(1 - W_A(90^\circ)). \quad (6)$$

The experimental results for the intensity ratio are listed in Table 1 together with  $W_A(90^\circ)$  and  $\mathcal{A}_2$  obtained from the results. The experimentally obtained  $\mathcal{A}_2$  is also plotted in Fig. 1 together with the theoretical values [1].

The present experimental result for Li-like Au indicates that the angular distribution of the emitted X-ray has a maximum at  $90^\circ$  (negative  $\mathcal{A}_2$  value), while the prediction with only the Coulomb interaction gives a minimum (positive  $\mathcal{A}_2$  value). As seen in Fig. 1, the theoretical result with the Breit interaction reproduce the experimental result also in quantitatively, whereas that with only the Coulomb interaction, which suggests strong alignment to the  $M_J = \pm 1$  levels, obviously fails to reproduce the experiment. This is a

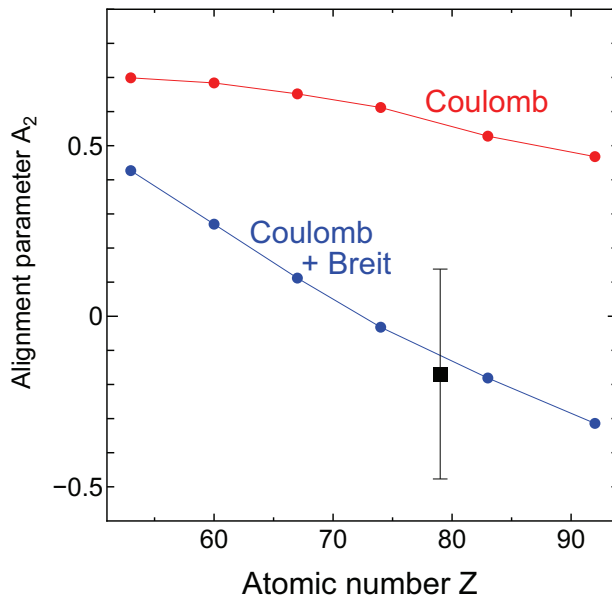


Figure 1: (Color online) Alignment parameter  $\mathcal{A}_2$  for the intermediate state  $[1s2s^22p_{1/2}]_1$  in dielectronic recombination of Li-like ions. The present result for Au ( $Z = 79$ ) is shown by the black square. Theoretical values taken from Ref. [1] are plotted as red dots (Coulomb only) and blue dots (the Breit interaction included).

clear demonstration showing that the Breit interaction dominates the angular distribution of X-rays emitted in DR processes of highly charged heavy ions.

#### 4. Summary and outlook

In summary, the alignment parameter of the intermediate state in the dielectronic recombination for Li-like Au was measured with the Tokyo electron beam ion trap. By the combination of the X-ray measurement at  $90^\circ$  with respect to the electron beam and the relative resonant strength measurement through the ion abundance inside the trap, the angular distribution of the  $[1s2s^22p_{1/2}]_1 \rightarrow [1s^22s^2]_0$  transition was obtained. Comparison with theory has clearly demonstrated the dominance of the Breit interaction.

In order to investigate the  $Z$ -dependence, measurements on Pr ( $Z = 59$ ) and Ho ( $Z = 67$ ) are in progress. For further study, we are planning to build a polarimeter for hard X-rays utilizing the Compton scattering in plastic scintillators [9]. In addition, direct angular distribution measurement is also expected to be performed with the Belfast EBIT [10], the only EBIT that can measure the angular distribution.

## Acknowledgement

This work was supported by KAKENHI 21340111 and partly supported by the JSPS-NRF-NSFC A3 Foresight Program in the field of Plasma Physics (NSFC: No.11261140328).

## References

- [1] S. Fritzsche, A. Surzhykov, and T. Stöhlker, *Phys. Rev. Lett.* **103**, 113001 (2009).
- [2] M. H. Chen and J. H. Scofield, *Phys. Rev. A* **52**, 2057 (1995).
- [3] V. V. Balashov, A. N. Grum-Grzhimailo, and N. M. Kabachnik, *Polarization and Correlation Phenomena in Atomic Collisions* (Kluwer Academic / Plenum Publishers, New York, N.Y., 2000).
- [4] H. Watanabe *et al.*, *J. Phys. B* **34**, 5095 (2001).
- [5] H. Tobiyaama *et al.*, *J. Phys.: Conf. Ser.* **58**, 239 (2007).
- [6] N. Nakamura *et al.*, *Phys. Rev. Lett.* **100**, 073203 (2008).
- [7] H. Watanabe *et al.*, *Phys. Rev. A* **75**, 012702 (2007).
- [8] Z. Hu *et al.*, *Phys. Rev. Lett.* **108**, 073002 (2012).
- [9] S. Gunji *et al.*, *Advances in Space Research* **33**, 1771 (2004).
- [10] H. Watanabe *et al.*, *Nucl. Instrum. Methods B* **205**, 239 (2003).

# Doubly Excited States and Their Dissociation Processes of Simple Molecules

Karin Takahashi\*, Yosuke Sakata†, Yuta Hino†, and Yasuhiro Sakai†

\* *Dept. of Physics, Rikkyo Univ. Nishi-Ikebukuro, Toshima-ku, Tokyo 1718501 Japan*

† *Dept. of Physics, Toho Univ. Miyama Funabashi, Chiba 2748510 Japan*

*e-mail: karin@rikkyo.ac.jp*

## Abstract

To study doubly excited states of simple molecules, total and total ionic generalized oscillator strength distributions (GOSDs) and ionization efficiencies of molecular hydrogen ( $H_2$ ), ammonia ( $NH_3$ ), and methane ( $CH_4$ ) were investigated using scattered electron-ion coincidence technique under magnitude of momentum transfer is not zero conditions. Absolute GOSDs obtained by application of a mixed gas method were very similar to previous OOSDs in shape. From ionization efficiencies obtained, it was clear that optically forbidden doubly excited states exist near 28 and 35 eV for  $H_2$ , near 30 eV for  $NH_3$ , and near 35 eV for  $CH_4$ .

**Keywords:** electron-ion coincidence measurements, molecular hydrogen, ionization efficiency, generalized oscillator strength

## 1. Introduction

Doubly excited states of molecules are super-excited states that lie above the first ionization energy. They can be regarded as Rydberg states that converge to excited states of the molecular ion. Doubly excited states are formed to gain energy from energetic particles such as electrons, and then dissociate auto-ionization or neutral dissociation. Here, when the doubly excited state dissociates via the neutral dissociation, the ion is not formed despite the region above the first ionization energy. Although the probability of doubly excitation is smaller than of direct-ionization, doubly excited states of molecules appear as intermediate state in plasma. Therefore, the process of the production and collapse plays an important role of the atomic processes in plasma.

The photo-ionization experiment is a useful tool to study doubly excited states. Samson *et al.* studied doubly excited states based on analysis of the optically oscillator strength distribution (OOSD) and the ionization quantum yield for simple molecules [1-3]. The ionization quantum yield is defined as the ratio of the photo-ionization cross section  $\sigma_i$  to the photo-absorption cross section  $\sigma_a$ , which is equal to the ratio of the OOSD for ionization to for absorption. From measurements of the ionization quantum yield, Samson *et al.* discovered the existence of doubly excited states for molecular hydrogen [1]. However, studies in electron impact experiments are poor, because scattered electron-ion coincidence measurements are required to obtain the similar information as photo-ionization experiments. In scattered electron-ion coincidence measurements, we can obtain the

ionization efficiency as a function of excitation energy that is electron energy-loss. The ionization efficiency is defined as the ratio of ionic generalized oscillator strength distribution (GOSD) to the total GOSD. GOSDs are important physical quantities obtained in electron impact experiments. The GOSD  $dF/dE$  is defined as the function of the magnitude of momentum transfer  $K^2$  (the difference between the incident electron momentum  $k_i$  and the scattered electron momentum  $k_s$ ) in continuum region,

$$\frac{dF(K^2)}{dE} = \frac{W}{2} \frac{k_i}{k_s} K^2 \frac{d^2\sigma}{dEd\Omega}. \quad (1)$$

Where,  $W$  is electron energy-loss value that is excitation energy of the molecule, and  $d^2\sigma/(dEd\Omega)$  is the double differential cross section. GOSDs are equal to OOSDs at  $K^2 \rightarrow 0$  condition. In contrast, we can obtain the information on optically forbidden transitions at  $K^2 \neq 0$  condition.

In this paper, to obtain the information on optically forbidden doubly excited states of simple molecules, GOSDs and ionization efficiencies of molecular hydrogen ( $H_2$ ), ammonia ( $NH_3$ ), and methane ( $CH_4$ ) have been investigated under  $K^2 \neq 0$  conditions using the scattered electron- ion coincidence technique.

## 2. Experimental setup

The experimental apparatus used was an (e, e+ ion) spectrometer, which had been described previously [4]. This apparatus consisted of a pulsed electron-gun, two time-of-flight (TOF) mass analyzers with which length differs, and an electron energy analyzer. The incident electrons were pulsed by deflection system before the electrons entered to a collision region. In the collision region, the incident electrons collided with target molecules emerged from a gas nozzle at the cross beam geometry. To increase detection efficiency for fragment ions, the short TOF mass analyzer was installed in a direction against the long TOF mass analyzer which was shown in the previous publication [4] (Fig. 1). The short and long TOF mass analyzers had the same interaction region of 20 mm in length, second accelerate regions of 10 mm in length, and drift regions of 225 and 480 mm in length, respectively. They were Wiley-McLaren type analyzer [5]. The formed ions were extracted from the interaction region by applying the pulsed electric field of 200 V/cm. The short TOF mass analyzer had an ability to detect all fragment ions with the initial energy up to 7 eV. Therefore, this analyzer was used for measurement of  $H_2$ . The long TOF mass analyzer which had mass resolution about 100 u was used for measurements of  $NH_3$  and  $CH_4$ . For scattered electrons, the electron energy analyzer used was a simulated hemisphere type called Jost type analyzer [6]. The typical energy resolution was about 0.5 eV full width at half maximum (FWHM). The scattering angle was determined by the ratio of the  $3^1P$  peak intensity to the  $2^1P$  peak intensity in electron energy-loss spectra of helium (He) [7]. In coincidence measurements, ion spectra triggered energy selected scattered electrons were measured as a function of electron energy-loss.

To obtain the absolute GOSDs, we used a mixed gas method. The procedure was shown in a previous report [4]. Briefly, we measured electron energy-loss spectra of mixed gas which consists of He and target molecule. Then the absolute double differential cross section of the target was estimated on the basis of the peak intensity of the  $2^1P$  state of He, using the mixing ratio. Finally, the absolute GOSD was determined from Eq. (1).

### 3. Results and discussion

#### 3.1 molecular hydrogen

The total GOSD and the total ionic GOSD which is the sum of GOSD for  $H_2^+$  and  $H^+$  of  $H_2$  obtained are shown in Fig. 1. The present experimental condition is 200 eV incident electron energy and 6 degree scattering angle. The magnitude of momentum transfer  $K^2$  in present condition is shown in u-axis in Fig. 1. For comparison, the OOSDs from dipole (e, e) and dipole (e, e+ ion) experiments [8] and photon impact experiments [1] are shown in Fig. 1. The peak below the first ionization threshold at 15.4 eV is excitations of the ( $1s\sigma_g$ ) electron. The total ionic GOSD rises from the first ionization threshold, and has the maximum value around at 18 eV electron energy-loss. In Fig. 1, the shapes of the present results are very similar to the shapes of the OOSDs [1,8].

Figure 2 shows the ionization efficiency  $\eta_i$  of  $H_2$  under 200 eV incident electron energy and a scattering angle of 6 degrees. For comparison, the ionization quantum yield from photon impact experiment [1] is shown in Fig. 2 again. The present  $\eta_i$  decreases notably near 28 and 35 eV. This means that doubly excited states exist in these ranges, which decay by neutral dissociation. In addition, the decreasing of present  $\eta_i$  is greater than the photon impact result [1]. Therefore, it is thought that there are contributions from optically forbidden doubly excited states. These results show the presence of optically forbidden doubly excited states near 28 and 35 eV for  $H_2$ .

#### 3.2 ammonia

Figure 3 (a) and (b) show the total GOSD and the total ionic GOSD of  $NH_3$  under 200 eV incident electron energy and a scattering angle of 8 degrees, respectively, together with previous OOSD results, for shape comparison. They were obtained by the dipole (e, e) experiment [9], the dipole (e, e+ ion) experiment [10], and the photon impact experiment [2]. The absolute value was shown on the vertical right axis in Fig. 3 (a) and (b). Although the magnitude of present GOSDs are different from OOSDs [2,9,10], the shapes agree well. In the total GOSD of  $NH_3$ , the peak around 7 eV and the shoulder around 10 eV are for excitations from ( $3a_1$ ) to Rydberg states. In the region from ( $3a_1$ )<sup>-1</sup> to ( $1e$ )<sup>-1</sup> ionization threshold, there is contribution from both excitations of ( $1e$ ) electrons and ionizations of ( $3a_1$ ) electrons in the total GOSD of  $NH_3$ . The total GOSD of  $NH_3$  decreases over the ( $1e$ )<sup>-1</sup> ionization threshold. The total ionic GOSD of  $NH_3$  rises from the first ionization threshold ( $3a_1$ )<sup>-1</sup>. In the region from ( $3a_1$ )<sup>-1</sup> to ( $1e$ )<sup>-1</sup> ionization threshold, the total ionic GOSD has a shoulder because of the contributions from both

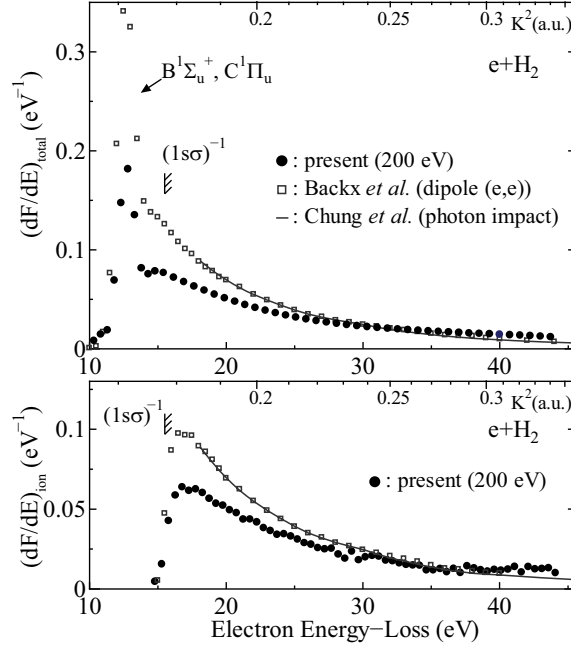


Figure 1: The total GOSD and the total ionic GOSD of  $\text{H}_2$ . The circles represent experimental results under 200 eV incident electron energy and a scattering angle of 6 degrees. The open squares are OOSDs which are results of Backx *et al.* from a dipole (e, e) and dipole (e, e+ ion) experiments [8]. The solid lines are OOSDs which are results of Chung *et al.* from photon impact experiment [1]. The magnitude of momentum transfer  $K^2$  under present condition is shown in u-axis.

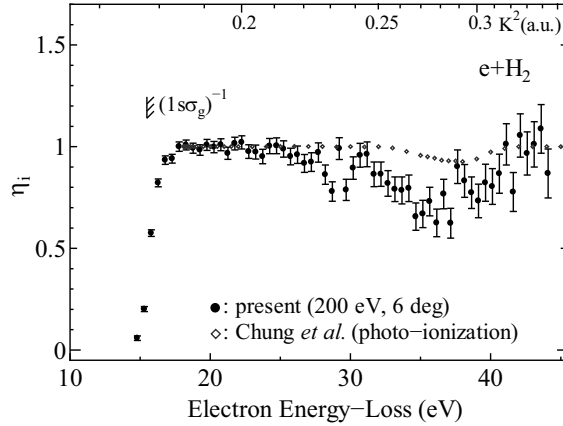


Figure 2: The ionization efficiency of  $\text{H}_2$ . The circles represent experimental results under 200 eV incident electron energy and a scattering angle of 6 degrees. The open diamonds are the results of Chung *et al.* from a photo-ionization experiment [1]. The magnitude of momentum transfer  $K^2$  under present condition is shown in u-axis.

direct-ionization of  $(3a_1)$  electrons and auto-ionization from  $(1e)$  electron excitation. The total ionic GOSD decreases over the  $(1e)^{-1}$  ionization threshold.

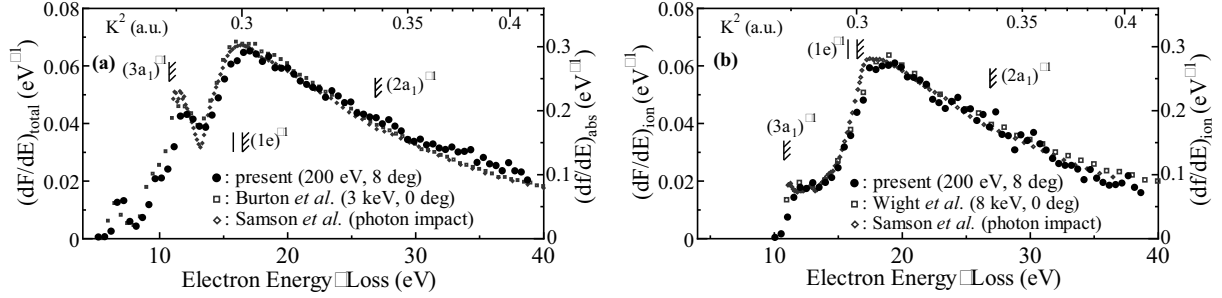


Figure 3: (a) The total GOSD and (b) the total ionic GOSD of  $\text{NH}_3$ . The circles represent experimental results under 200 eV incident electron energy and a scattering angle of 8 degrees. The open squares are OOSDs which are results of dipole  $(e, e)$  [9] and dipole  $(e, e+ \text{ion})$  [10] experiments. The diamonds are OOSDs which are results of Samson *et al.* from photon impact experiment [2]. The magnitude of these OOSDs are shown in right axes, and the magnitude of momentum transfer  $K^2$  under present condition is shown in u-axis.

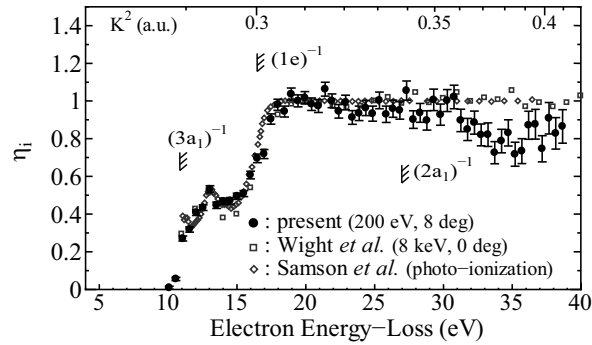


Figure 4: The ionization efficiencies of  $\text{NH}_3$ . The circles represent experimental results under 200 eV incident electron energy and a scattering angle of 8 degrees. The open squares are the OOSD which are results of dipole  $(e, e+ \text{ion})$  experiments [10]. The diamonds are OOSDs which are results of Samson *et al.* from photo-ionization experiments [2]. The  $K^2$  under present condition is shown in u-axis.

The ionization efficiency  $\eta_i$  of  $\text{NH}_3$  obtained under 200 eV incident electron energy and a scattering angle of 8 degrees is shown in Fig. 4. The  $\eta_i$  is not constant in the region over the first ionization threshold at 10.85 eV. This is due to the excitation of  $(1e)$  electrons. Above  $(1e)$  ionization threshold at 15.6 eV,  $\eta_i$  becomes constant. However, the present

$\eta_i$  decrease notably near 35 eV. Because these energies are greater than  $(2a_1)$  ionization threshold, this means that optically forbidden doubly excited states exist in this range, which is decayed by neutral dissociation.

### 3.3 methane

$\text{CH}_4$  has an electric configuration of  $(1a_1)^2(2a_1)^2(1t_2)^6$  in the ground state in  $T_d$  symmetry. The ionization thresholds for the  $(1t_2)$  and  $(2a_1)$  states are 13.6 and 24 eV, respectively.

Figure 5 (a) and (b) show the total GOSD and the total ionic GOSD of  $\text{CH}_4$  obtained under 200 eV incident electron energy and a scattering angle of 8 degrees, together with previous OOSDs, respectively. The OOSDs obtained by the dipole (e, e), the dipole (e, e+ ion) experiments [11], and photon impact experiment [3]. The both of the total GOSD and the total ionic GOSD of  $\text{CH}_4$  are normalized at 20 eV electron energy-loss. The total GOSD of  $\text{CH}_4$  rises from around 9 eV and then increases with shoulders up to  $(1t_2)^{-1}$  ionization threshold. In the region below the first ionization threshold  $(1t_2)^{-1}$ , there is no isolated peak in the total GOSD of  $\text{CH}_4$  because of predissociation. The total GOSD of  $\text{CH}_4$  has maximum around 14 eV and decreases as the electron energy-loss increases. The shape of the total GOSD of  $\text{CH}_4$  is very similar to the shapes of the total OOSDs. The total ionic GOSD of  $\text{CH}_4$  rises from the first ionization threshold  $(1t_2)^{-1}$ , has the maximum around 16 eV, and then decreases as the electron energy-loss increases. The shape of the total ionic GOSD of  $\text{CH}_4$  is also very similar to the shapes of the total ionic OOSDs.

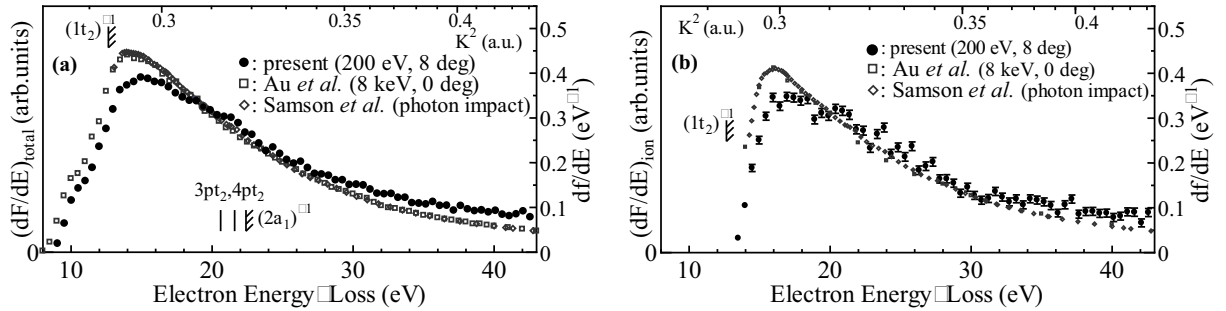


Figure 5: (a) The total GOSD and (b) the total ionic GOSD of  $\text{CH}_4$ . The circles represent experimental results under 200 eV incident electron energy and a scattering angle of 8 degrees. The open squares are OOSDs which are results of dipole (e, e) and dipole (e, e+ ion) [11] experiments. The diamonds are OOSDs which are results of Samson *et al.* from photon impact experiment [3]. The magnitude of these OOSDs are shown in right axes, and the magnitude of momentum transfer  $K^2$  under present condition is shown in u-axis.

The ionization efficiency  $\eta_i$  of  $\text{CH}_4$  obtained under 200 eV incident electron energy and scattering angle of 8 degrees is shown in Fig. 6 with the photo-ionization result by Samson *et al.* [3]. The  $\eta_i$  of  $\text{CH}_4$  rises from the first ionization threshold ( $1t_2$ )<sup>1</sup>. The  $\eta_i$  became constant in the region over around 16 eV which was the energy that the total ionic GOSD has maximum. Although the uncertainty in the  $\eta_i$  is large (about 10-30 %), the  $\eta_i$  decreased at near 30 eV, slightly. This means that optically forbidden doubly excited states of  $\text{CH}_4$  which cause neutral dissociations exist in this range.

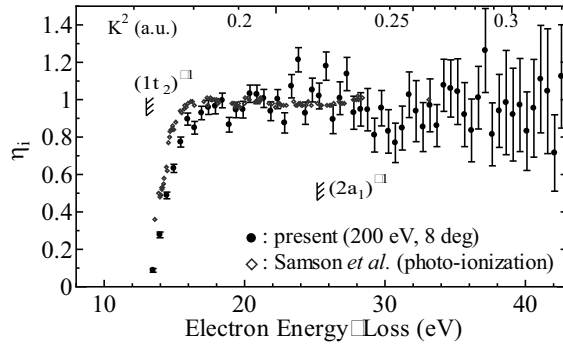


Figure 6: The ionization efficiencies of  $\text{CH}_4$ . The circles represent experimental results under 200 eV incident electron energy and a scattering angle of 8 degrees. The diamonds are OOSDs which are results of Samson *et al.* from photo-ionization experiments [3]. The  $K^2$  under present condition is shown in u-axis.

#### 4. Conclusion

The total GOSDs, total ionic GOSDs, and the ionization efficiencies of  $\text{H}_2$ ,  $\text{NH}_3$ , and  $\text{CH}_4$  under 200 eV incident electron energy and scattering angles of 6 and 8 degrees were investigated. In each total GOSDs and total ionic GOSDs, although the values were different from OOSDs for  $K^2 \neq 0$  condition in present work, the shapes were very similar to OOSDs from dipole (e, e), dipole (e, e+ ion) experiments and photon impact experiments. We have found that the ionization efficiencies decrease notably at near 28 and 35 eV for  $\text{H}_2$ , at near 35 eV for  $\text{NH}_3$ , and at near 30 eV for  $\text{CH}_4$ . Therefore, we have established that optically forbidden doubly excited states exist in these ranges, which are decayed by neutral dissociation.

#### Acknowledgement

This work was supported by Grant-in-Aid for Japan Society for the Promotion of Science (JSPS) Fellows (22-5682) and partly supported by the JSPS-NRF-NSFC A3 Foresight Program in the field of Plasma Physics (NSFC: No. 11261140328).

## References

- [1] Y. M. Chung, E. M. Lee, T. Masuoka and J. A. R. Samson, *J. Chem. Phys.* **99**, 885 (1993).
- [2] J. A. R. Samson, G. N. Haddad, and L. D. Klcoyne, *J. Chem. Phys.* **87**, 6416 (1987).
- [3] J. A. R. Samson, G. N. Haddad, T. Masuoka, P. N. Pareek, and D. A. L. Klcoyne, *J. Chem. Phys.* **90**, 6925 (1989).
- [4] K. Yamamoto, and Y. Sakai, *J. Phys. B: At. Mol. Opt. Phys.* **45**, 055201 (2012).
- [5] W. C. Wiley, and I. H. McLaren, *Rev. of Sci. Instrum.*, **26**, 1150 (1955).
- [6] K. Jost, *J. Phys. E: Sci. Instrum.*, **12**, 1006 (1979).
- [7] T. Y. Suzuki, H. Suzuki, F. J. Currell, S. Ohtani, Y. Sakai, T. Takayanigi, and K. Wakiya, *Phys. Rev. A.*, **57**, 1832 (1998).
- [8] C. Backx, G. R. Wight and M. J. Van der Wiel, *J. Phys. B: Atom. Molec. Phys.* **9**, 315 (1976).
- [9] C. E. Brion, A. Hamnett, G. R. Wight and M. J. Van der Wiel, *J. Electron Spectrosc. Relat. Phenom.* **12**, 323 (1977).
- [10] G. R. Wight, M. J. Van der Wiel and C. E. Brion, *J. Phys. B: Atom. Molec. Phys.* **10**, 1863 (1977).
- [11] C. Backx and M. J. Van der Wiel, *J. Phys. B: Atom. Molec. Phys.* **8**, 3020 (1975).

# Dielectronic recombination of Br-like tungsten ions

Li Maijuan, Fu Yanbiao<sup>1</sup>, Su Maogen, Dong Chenzhong and Koike Fumihiro  
*Key Laboratory of Atomic and Molecular Physics & Functional Materials of Gansu Province, College of Physics and Electronic Engineering, Northwest Normal University, Lanzhou, 730070, China*  
*Joint Laboratory of Atomic and Molecular Physics, Northwest Normal University and Institute of Modern Physics of Chinese Academy of Sciences, Lanzhou 730070, China*  
*Atomic and Molecular Data Research Center, National Institute for Fusion Science, Kitasato 509-5292, Japan*  
*e-mail: fuyb@nwnu.edu.cn*

## Abstract

Accurate data for dielectronic recombination of tungsten ions are essential in modeling of tungsten impurity transport and radiative power loss in International Thermonuclear Experimental Reactor (ITER). Theoretical calculations have been made for dielectronic recombination (DR) rate coefficients of Br-like tungsten ions using a flexible relativistic atomic code (FAC) from 1 eV to 50 keV. Level-by-level calculations are carried out for evaluating the contributions to DR through all the relevant Kr-like tungsten ions autoionizing inner-shell excited configuration complexes:  $(3s^23p^63d^{10})^{-1}4s^24p^5nl'n'l'$  ( $n = 4 - 5$ ,  $n' = 4 - 100$ ,  $l' = 0 - 8$ ),  $(4s^24p^5)^{-1}nl'n'l'$  ( $n = 4 - 6$ ,  $n' = 4 - 100$ ,  $l' = 0 - 12$ ). Comparison of the rate coefficients for  $3s$ ,  $3p$ ,  $3d$ ,  $4s$  and  $4p$  subshell excitations shows that the  $4p$  subshell excitation dominates over the whole temperature region,  $4s$  subshell excitation at low temperature and  $3d$ ,  $3p$  subshell excitations at high temperature can not be neglected. In order to facilitate simple applications, the total DR rate coefficient,  $\Delta n = 0, 1$  and  $2$  core excitations DR rate coefficients are fitted to a empirical formula.

**Keywords:** Br-like tungsten, dielectronic recombination, rate coefficients

## 1. Introduction

Dielectronic recombination (DR) is a basic atomic process in electron-ion collisions. The DR rate coefficients are greater than the radiation recombination (RR) rate coefficients and three-body recombination (TBR) rate coefficients in some highly ionized plasmas [1, 2]. Accurate DR rate coefficients are essential for studying the ionization balance of highly ionized ions in hot plasmas [3, 4]. Tungsten will be used as a plasma-facing material within the divertor region of the International Thermonuclear Experimental Reactor (ITER) due to its high melting point and thermal conductivity, its low tritium retention and erosion rate under plasma loading [5]. For divertor plasma modeling and radiative cooling studies,

Table 1: Investigation of the DR process for tungsten ions.

Charged Tungsten Ions	Methods	Ground configuration	Core-excitions	Fitted
$\overline{W}^{72+[6,7]}$	a, b, c	$1s^2$	$\Delta n = 1 (2s)$	-
$W^{71+[8]}$	d	$1s^2 2s$	$\Delta n = 0, 1 (2s)$	-
$W^{67+} - W^{60+[9,10]}$	b, e	$2s^2 2p^3 - 3s^2 3p^2$	$\Delta n = 1 (2p)$	-
$W^{64+[6,11-14]}$	a, b, c	$2s^2 2p^6$	$\Delta n = 1, 2 (2l)$	the total DR rate coefficients
	b	$2s^2 2p^6$	$\Delta n = 1, 2 (2l)$	
$W^{63+[6,15]}$	a, b, c	$2s^2 2p^6 3s$	$\Delta n = 0, 1 (2p, 3s)$	-
$W^{56+[16,17]}$	b	$2p^6 3s^2 3p^6$	$\Delta n = 0 (3s, 3p)$ $\Delta n = 1 (2l, 3s, 3p)$ $\Delta n = 2 (3p)$	-
$W^{47+[18,19]}$	f	$3p^6 3d_{3/2}^4 3d_{5/2}^5$	$3d_{3/2} \rightarrow 3d_{5/2}$ $\Delta n = 0 (3s, 3p)$ $\Delta n = 1 (3l)$	-
$W^{46+[17,20,21]}$	b	$3s^2 3p^6 3d^{10}$	$\Delta n = 1 (3l)$	the total DR rate coefficients
$W^{45+[17]}$	b	$3p^6 3d^{10} 4s$	$\Delta n = 1 (3p, 3d)$	-
$W^{37+[22]}$	f	$3d^{10} 4s^2 4p^6 4d$	$\Delta n = 0 (4l)$ $\Delta n = 1 (3l, 4l)$ $\Delta n = 2 (4l)$	-
$W^{35+[23]}$	g	$4s^2 4p^6 4d^3$	$\Delta n = 0 (4l)$ $\Delta n = 1 (4p, 4d)$	$\Delta n = 0, 1$ rate coefficients
$W^{29+[2]}$	f	$4p^6 4d^9$	$\Delta n = 0, 1, 2 (4p, 4d)$	the total DR rate coefficients
$W^{28+[24]}$	a, b, c	$4d^{10}$	$\Delta n = 0, 1, 2 (4d)$	-
$W^{20+[25,26]}$	h	$4d^{10} 4f^8$	$\Delta n = 0 (4p, 4d, 4f)$ $\Delta n = 1, 2 (4p, 4d)$	-
	i	$4d^{10} 4f^8$	$\Delta n = 0 (4p, 4d, 4f)$ $\Delta n = 1, 2 (4d, 4f)$	the total DR rate coefficients
$W^{6+[27]}$	a, c	$4f^{14} 5p^6$	$\Delta n = 0 (5p)$ $\Delta n = 1 (4f, 5p)$ $\Delta n = 2 (4f)$	-
$W^{5+[28]}$	a, b, c	$4f^{14} 5p^6 5d$	$\Delta n = 0 (5p)$ $\Delta n = 1 (4f)$ $\Delta n = 2 (4f)$	-

<sup>a</sup> RMBT code

<sup>b</sup> HULLAC code

<sup>c</sup> COWAN code

<sup>d</sup> HCR code

<sup>e</sup> Berlin EBIT experiment

<sup>f</sup> FAC code

<sup>g</sup> DRACULA code

<sup>h</sup> Heidelberg accelerator and storage-ring experiment

<sup>i</sup> AUTOSTRUCTURE and DRACULA code

accurate atomic data for highly ionized tungsten ions are significant, especially data on recombination processes that are vital in the determination of radiation losses. The DR process was surveyed recently in a number of publications for tungsten ions [2, 6 - 28]. For the sake of clarity, a statistics of DR research of tungsten ions were briefly listed in table 1. It is clearly seen that only 21 ions of tungsten have been researched theoretically or experimentally, respectively. Although a large amount of studies have been performed for the DR process of many ionized states of tungsten ions, these data are insufficient at all for ITER. Therefore, in order to extend these works, we calculate and analyse detailedly DR process of Br-like tungsten ions. The relativistic flexible atomic code (FAC) [29] was used to calculate the atomic structure, radiative transition probabilities, and autoionization probabilities.

In this paper we focus on the calculation of DR data and get evolution of DR to temperature. Here, we will give a brief discussion of tungsten ions calculation and analysis in section 3.2, and then present the contribution of inner-shell electron excitation and the total DR rate coefficients in 3.3 and 3.4, finally, to use conveniently the data, present the fitting of  $\Delta n = 0, 1$  and 2 core excitations and the total DR rate coefficients.

## 2. Theory

DR resonance is treated as two-step process in the isolated resonance approximation. In the first step, when a free electron with a specific kinetic energy collides with an ion  $A^{q+}$ , one of the bound electron in the ion  $A^{q+}$  is excited and the free electron is captured, forming a resonance doubly excited state is unstable, in the second step, the resonance doubly excited state decay into a non-autoionization state through emission a photon.

In the isolated resonance approximation, the DR rate coefficient from an initial state  $i$  into a final state  $k$  through an intermediate doubly excited state  $j$ , for electron in the Maxwellian distribution, can be expressed as

$$\alpha_{DR}(i, j, k, T_e) = \left(\frac{h^2}{2\pi m_e k T_e}\right)^{3/2} \frac{g_j}{2g_i} \frac{A_{ji}^\alpha A_{jk}^\gamma}{\sum_{k'} A_{jk'}^\gamma + \sum_{i'} A_{ji'}^\alpha} \exp\left(-\frac{E_{ji}}{k T_e}\right), \quad (1)$$

where  $m_e$  is the electron mass,  $h$  is Plank's constant,  $k$  is Boltzmann's constant,  $g_i$  and  $g_j$  are the statistical weight of the states  $i$  and  $j$ , respectively,  $E_{ji}$  is the resonance energy,  $A_{jk}^\gamma$  is the radiative decay rate, and  $A_{ji}^\alpha$  is the auger decay rate.

In the present calculations, we include detailed the DR contributions through Kr-like autoionizing doubly excited congratulation complexes:  $(3s^2 3p^6 3d^{10})^{-1} 4s^2 4p^5 n l n' l'$  ( $n = 4 - 5$ ,  $n' = 4 - 100$ ),  $3s^2 3p^6 3d^{10} (4s^2 4p^5)^{-1} n l n' l'$  ( $n = 4 - 6$ ,  $n' = 5 - 100$ ), employing FAC code, where DR rate coefficients are calculated directly for  $n' \leq 15$  and results a

Table 2: Energy [eV] levels of the Kr-like tungsten ions calculated. Comparison of FAC results with Ref [31] and recommended NIST data [32].

Index	Level name	J	Calculated Energy(eV)		
			$E^{(FAC)}$	$E^{(Ref)[32]}$	$E^{(NIST)}$
1	$3p^6 3d^{10} 4s^2 4p^6$	0	0.0	0.0	0.0
2	$3p^6 3d^{10} 4s^2 4p^2 4p_{+}^3 4d_{-}^1$	0	148.400	148.622	149.77
3	$3p^6 3d^{10} 4s^2 4p^2 4p_{+}^3 4d_{-}^1$	1	152.992	153.285	153.44
4	$3p^6 3d^{10} 4s^2 4p^2 4p_{+}^3 4d_{-}^1$	3	156.238	156.384	156.72
5	$3p^6 3d^{10} 4s^2 4p^2 4p_{+}^3 4d_{-}^1$	2	157.511	157.791	157.81
6	$3p^6 3d^{10} 4s^2 4p^2 4p_{+}^3 4d_{+}^1$	4	171.987	171.922	172.229
7	$3p^6 3d^{10} 4s^2 4p^2 4p_{+}^3 4d_{+}^1$	2	174.203	174.458	174.700
8	$3p^6 3d^{10} 4s^2 4p^2 4p_{+}^3 4d_{+}^1$	3	179.769	180.072	179.983
9	$3p^6 3d^{10} 4s^2 4p^2 4p_{+}^3 4d_{+}^1$	1	195.716	195.788	194.079
10	$3p^6 3d^{10} 4s^2 4p^1 4p_{+}^4 4d_{-}^1$	2	246.403	246.216	
12	$3p^6 3d^{10} 4s^2 4p^1 4p_{+}^4 4d_{-}^1$	1	268.941	268.706	265.660
13	$3p^6 3d^{10} 4s^2 4p^2 4p_{+}^3 4d_{+}^1$	3	268.893	268.801	
35	$3p^6 3d^{10} 4s^2 4p^2 4p_{+}^3 5s_{+}^1$	1	673.695	673.855	676.100

extrapolated up to  $n' = 100$  by the relevant scaling law  $A^a \propto n^{-3}$  [30], orbital angular momentum  $l'$  includes all possible.

### 3. Results and discussion

#### 3.1 Energy levels of the like-Kr tungsten ions

In order to check the accuracy of the FAC results, we summarized the energy levels of the Kr-like tungsten ions in table 2, which presents the results  $E^{FAC}$ ,  $E^{Ref}$  from [31] and  $E^{NIST}$  from the NIST Atomic Spectra Database calculated by Kramida and Shirai using the Cowan code [32]. As can be seen from table 2, the largest difference is the FAC energy and the recommended NIST value about 0.02-1.24%, only 0.02-0.18% difference for the most of states listed in table 2.

#### 3.2 The $l'$ dependence of the partial DR rate coefficients

The dependence of the DR rate coefficients on the orbital angular momentum  $l'$  of each complex series has been investigated. Figure 1 (a) shows the results of the DR rate coefficients for the intermediate doubly excited states  $(3s^2 3p^6 3d^{10})^{-1} 4l13l'$  and  $(3s^2 3p^6 3d^{10})^{-1} 5l13l'$ . Figure 1 (b) shows the results of the DR rate coefficients for the intermediate doubly excited states  $(4s^2 4p^5)^{-1} 4l13l'$  and  $(4s^2 4p^5)^{-1} 5l13l'$ . As can be seen from the curve, the  $3l$  shell excitations contributions through the resonant configurations with  $l' > 8$  can be neglected. Because the trend is steep decrease as  $l'$  increase, so the complete neglecting of  $3l$  shell excitations contributions with  $l' > 8$  is reasonable. For the  $4l$  shell excitations, it can be seen that the  $(4s^2 4p^5)^{-1} nl13l'$  ( $n = 5 - 6$ ) complex series decrease steeply, so

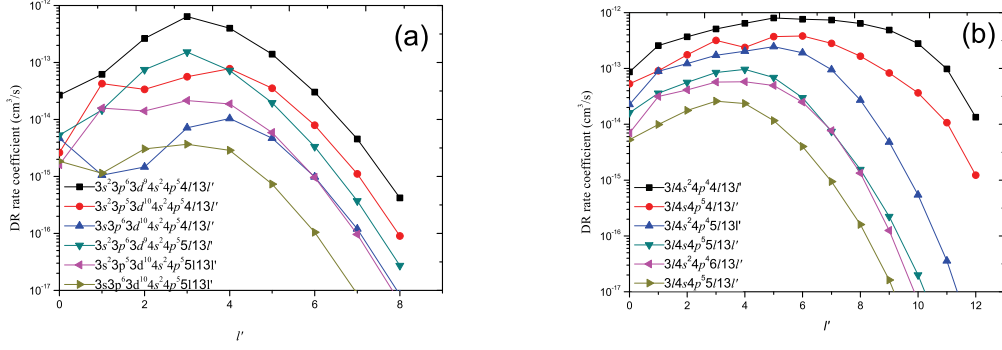


Figure 1: Partial DR rate coefficients for  $W^{39+}$  tungsten ions through the intermediate doubly excited states: (a)  $(3s^2 3p^6 3d^{10})^{-1} 4l 5l 13l'$  and (b)  $3l^{18} (4s^2 4p^5)^{-1} 4l 5l 6l 13l'$  as a function of  $l'$ , at an electron temperature 1250 eV. Each curve gives the sums of coefficients for all the permitted  $l$  and  $l'$  orbitals.

the contributions from  $l' > 12$  can be neglected, the  $(4s^2 4p^5)^{-1} nl 13l'$  complex series vary slowly, but the  $4s^2 4p^4 4l 13q$  and  $4s 4p^5 4l 13q$  complex series contribute at most 0.24% and 0.04% of the total DR rate coefficients of the complex series  $4s^2 4p^4 4l 13l'$  and  $4s 4p^5 4l 13l'$ , so the neglect of the contribution from  $l' > 12$  is justified.

### 3.3 Contribution of inner-shell electron excitation

Figure 2 shows the DR rate coefficients for intermediate doubly states  $(3s^2 3p^6 3d^{10})^{-1} 4s^2 4p^5 nl n' l'$  ( $n = 4 - 5$ ,  $n' = 4 - 100$ ,  $l' = 0 - 8$ ) and  $3l^{18} (4s^2 4p^5)^{-1} nl n' l'$  ( $n = 4 - 6$ ,  $n' = 4 - 100$ ,  $l' = 0 - 12$ ). It can be seen that DR rate coefficients are principal from  $4l$  shell excitations for  $kT_e < 800$  eV, where the DR rate coefficients for  $4p$  subshell electron excitation are the largest, and the  $4s$  subshell excitation cannot be ignored. For  $3l$  shell excitations, DR rate coefficients for  $3d$  subshell excitation are the largest and the DR rate coefficients decrease with decreasing  $l$  quantum number. This result is similar to those for Co-like Pd ions obtained by Zhang *et al* [33]. The peaks of  $4p$  and  $4s$  subshell electron excitations lie to low temperature, because the DR rate coefficients for  $4l$  shell electron excitations near to the ionization limit, the resonances are very strong. For  $3l$  shell electron excitations, the peaks lie to intermediate and high temperature region. As the temperature increases, the DR rate coefficients for  $3d$  shell excitation increase and gradually overlap with the DR rate coefficients for  $4l$  shell excitations. However, the largest contribution for  $3s$  subshell is only 3% of the total DR rate coefficients, so  $3s$  excitation can be neglected. The DR rate coefficients for  $3d$  excitation exceed the  $4s$  subshell excitation at  $kT_e = 1250$  eV. This overtaking is because the DR rate coefficient depend mainly on  $\exp(-E_{ji}/kT_e)$  in equation (1). With increasing of  $-E_{ji}$ , the factor  $\exp(-E_{ji}/kT_e)$  causes the curve to decline

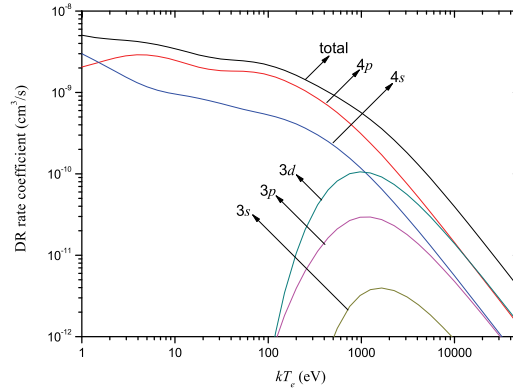


Figure 2: DR rate coefficients for intermediate doubly excited states  $(3s^2 3p^6 3d^{10})^{-1} 4s^2 4p^5 nln'l'$  ( $n = 4 - 5$ ,  $n' = 4 - 100$ ,  $l' = 0 - 8$ ) and  $3l^{18}(4s^2 4p^5)^{-1} nln'l'$  ( $n = 4 - 6$ ,  $n' = 4 - 100$ ,  $l' = 0 - 12$ ). The notations  $3s$ ,  $3p$  and  $3d$  on the curves stand for the respective excited M-shell orbitals. The notations  $4s$  and  $4p$  on the curves stand for the respective excited M-shell orbitals. Total DR rate coefficient is the sum from  $3s$ ,  $3p$ ,  $3d$ ,  $4s$  and  $4p$  subshells excited DR rate coefficients. Each curve gives the sum of coefficients for all the permitted  $l$  orbitals.

gradually. The peak positions of  $3l$  are higher in energy than those of  $4l$ , since the energies for  $3l$  shell excitations are higher than those of  $4l$ . Therefore, DR rate coefficients for  $4s$ ,  $4p$ ,  $3d$  and  $3p$  excitations are very important in the center electron temperature among  $1\text{eV} \sim 20\text{keV}$  for ITER.

Figure 3 shows the contributions of DR rate coefficients of  $\Delta n = 0$ , 1 and 2 core excitations, it can be seen that the total contributions from  $\Delta n = 0$  and 1 core excitations dominate the whole temperature region. Contributions from  $\Delta n = 0$  core excitation are the largest at low-temperature region. As electron temperature more than 750 eV, the  $\Delta n = 1$  core excitation is greater than  $\Delta n = 0$  core excitation. The DR rate coefficients through  $\Delta n = 2$  core excitation increase with increasing electron temperature, about 13% for the total DR rate coefficient at 1000 eV, the largest contribution can reach 23%. So the DR rate coefficients through  $\Delta n = 2$  core excitation can not be neglected.

### 3.4 The total DR rate coefficients

Figure 4 shows the contributions of DR rate coefficients where a free electron is captured to different primary quantum number  $n$  shell. Here DR rate coefficients are calculated by FAC for  $n' \leq 15$ , whereas DR rate coefficients are obtained by extrapolation method

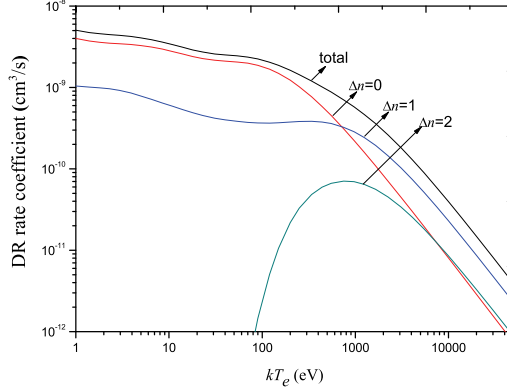


Figure 3: Total DR rate coefficients and the partial contributions from the  $\Delta n = 0, 1$  and  $2$  core excitations as a function of electron temperature, where  $\Delta n = 0, 1$  and  $2$  core excitations DR rate coefficients for intermediate doubly excited states  $(3s^23p^63d^{10})^{-1}4s^24p^5nl'n'l'(n = 4 - 5, n' = 4 - 100, l' = 0 - 8)$  and  $3l^{18}(4s^24p^5)^{-1}nl'n'l'(n = 4 - 6, n' = 4 - 100, l' = 0 - 12)$ .

based on the  $n'^{-3}$  scaling law using equation (2) for  $n' > 15$ .

$$\alpha_{DR}(n') = \alpha_{DR}(n_s) \frac{\left(\frac{n'}{n_s}\right)^{-3} (\sum A^\alpha(n_s) + A^\gamma(n_s))}{\left(\frac{n'}{n_s}\right)^{-3} \sum A^\alpha(n_s) + A^\gamma(n_s)} \exp\left(\frac{-13.6057\left(\frac{1}{n_s^2} - \frac{1}{n'^2}\right)}{kT_e}\right), \quad (2)$$

DR rate coefficients form a free electron captured to primary quantum number  $n' = 4$  subshell only involving the doubly excited states  $(3s^23p^6)^{-1}3d^{10}4s^24p^5$  are clearly least at the whole temperature region. It can be seen that the DR rate coefficients for  $n' = 6$  are larger than  $n' = 5$ , the reason is that the partial  $(4s^24p^5)^{-1}5l5l'$  complex can not autoionize. In general terms, DR rate coefficients will be smaller the greater the value of  $n'$  for  $n' > 5$  at intermediate-high temperature region, this result is similar to those for Co-like gold ions obtained by Meng *et al* [34] and Sn<sup>12+</sup> ions calculated by Fu *et al* [1]. But at the low temperature, the partial DR rate coefficients do not follow, this is mainly because many of the levels belonging to the  $(4s^24p^5)^{-1}4ln'l'$  complex from  $n' = 4 - 10$  lie below the ionization limit.

In order to reproduce conveniently the present results, the total DR rate coefficients,  $\Delta n = 0, 1$  and  $2$  core excitations DR rate coefficients are fitted to the following empirical formula ( $\text{cm}^3/\text{s}$ ):

$$\alpha_{DR}(kT_e) = (kT_e)^{-3/2} \sum_{i=1}^6 A_i e^{-B_i/kT_e} \quad (3)$$

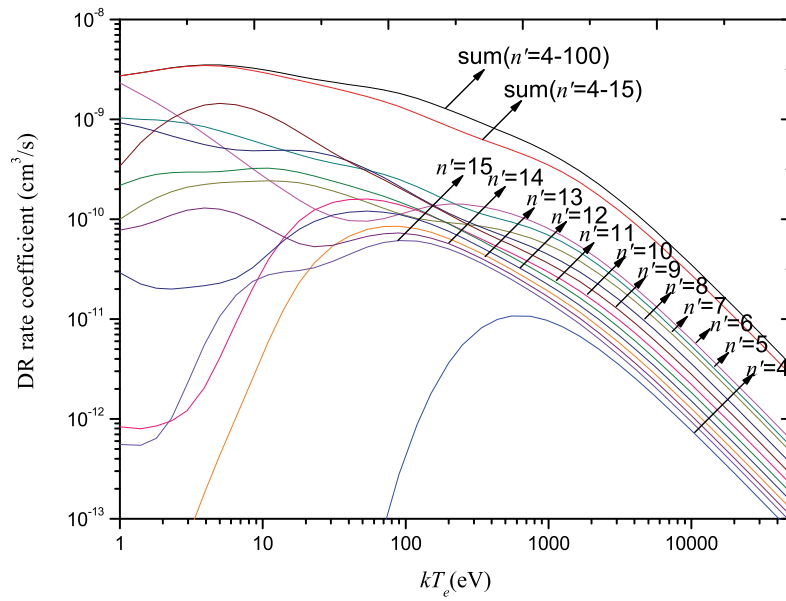


Figure 4: The DR rate coefficients where a free electron is captured to the orbits with primary quantum number ranging from  $n' = 4 - 15$ , which are marked on the individual curve. The tags SUM ( $n' = 4 - 100$ ) and SUM ( $n' = 4 - 15$ ) stands for their sums over  $n' = 4 - 100$ , and over  $n' = 4 - 15$ , respectively.

Table 3: Fitting DR rate coefficients for  $W^{39+}$  ions using equation (3). Numbers in brackets denote powers of 10.

i	total		$\Delta = 0$		$\Delta = 1$		$\Delta = 2$	
	$A_i$	$B_i$	$A_i$	$B_i$	$A_i$	$B_i$	$A_i$	$B_i$
1	1.764(-7)	6.974(+0)	1.058(-7)	5.637(+0)	2.391(-8)	5.162(+0)	9.286(-7)	6.014(+2)
2	5.825(-7)	3.327(+1)	3.530(-7)	2.499(+1)	8.908(-8)	2.903(+1)	3.188(-6)	1.062(+3)
3	2.803(-6)	1.026(+2)	1.045(-6)	7.870(+1)	4.318(-7)	1.001(+2)	6.012(-6)	2.353(+3)
4	5.792(-6)	2.316(+2)	2.488(-6)	3.367(+2)	1.702(-6)	2.748(+2)		
5	1.180(-5)	6.626(+2)	3.836(-6)	1.692(+1)	8.604(-6)	6.951(+2)		
6	2.250(-5)	1.755(+3)			1.492(-5)	1.678(+3)		

where both  $A_i$  and  $B_i$  are adjustable parameters, using the parameters listed in table 3, we can reproduce present calculated  $\Delta n = 0$  and 1 core excitations DR rate coefficients to within 1% and the total DR rate coefficients to within 1.6% for  $kT_e > 5$  eV. It should be pointed out that the DR rate coefficients at low temperatures (especially nearby zero) are extremely sensitive to the exact position (in energy) of the resonances. As contribution for  $\Delta n = 2$  core excitation is very small (under 0.2%) for  $kT_e < 100$  eV, we only reproduce present calculated  $\Delta n = 2$  core excitation DR rate coefficients to with 1%  $kT_e > 100$  eV.

### 3. Conclusion

Based on the flexible atomic code (FAC), theoretical calculations have been presented for the dielectron recombination rate coefficients of  $W^{39+}$  ions. Comparison of the rate coefficients from  $3l$  and  $4l$  shell excitations shows the  $4p$  subshell excitation gives the most important in the whole temperature region, but the contributions of  $4s$  subshell excitation in low temperature region and the contributions of  $3d$  and  $3p$  excitations in the intermediate and high temperature region can be not ignored. In order to facilitate simple applications, the calculated DR rate coefficients are fitted to a empirical formula. Using the parameters we gave, the present calculated total DR rate coefficients can be reproduced within 1.6% for  $kTe > 5$  eV. These results would be beneficial for the study of impurity transport processes and radiative power loss in ITER.

### Acknowledgement

This work was supported by the International Atomic Energy Agency (Grant No. 16266), the National Nature Science Foundation of China (Grant No.10847007, 10964010, 11064012, 11147018), the Major Research Plan of the National Natural Science Foundation of China (Grant No. 91126007), the specialized Research Fund for the Doctoral Program of Higher Education of China (Grant No.20070736001) and the Foundation of Northwest Normal University (NWNNU-KJCXGC-03-21), the JSPS-NRF-NSFC A3 Fore-

sight Program in the field of Plasma Physics (NSFC: No.11261140328).

## References

- [1]Y B Fu, C Z Dong and M G Su. Phys. Rev. A, **83** 062708 (2011).
- [2]B W Li , G O’Sullivan, Y B Fu, et al. Phys. Rev. A, **85** 052706 (2012).
- [3]P Mazzotta, G Mazzitelli, S Colafrancesco and N Vittorio Astron. Astrophys. Suppl. Ser., **133** 403 (1998).
- [4]S M V Aldrovandi and D Pequignot Astron. Astrophys, **25** 137(1973).
- [5]P Quinet, V Vinogradoff, P Palmeri, et al. J. Phys. B: At. Mol. Opt. Phys., **43** 144003 (2010).
- [6]U I Safronova, A S Safronova, and P Beiersdorfer. Can. J. Phys., **89** 581 ( 2009).
- [7]U I Safronova, A S Safronova, and W R Johnson. At. Date Nucl. Date Tables, **43** 144001 (2010).
- [8]A P Ye, Z H Zhu, M L Tan. Chinese Journal of atomic and molecular physics, **12** 3 (in chinese) (1995).
- [9]C Biedermann, R Radtke, R Seidel, et al. J. Phys: Conf. Ser., **163** 012034 (2009).
- [10]C Biedermann and R Radtke. AIP Proc., **1161** 95 (2009).
- [11]U I Safronova, A S Safronova, and P Beiersdorfer. At. Date Nucl. Date Tables, **95** 751 (2009).
- [12]E Behar, P Mandelbaum and J L Schwob. Phys. Rev. A., **59** 2787 (1999).
- [13]E Behar, R Doron, P Mandelbaum and J L Schwob. Phys. Rev. A, **61** 062708 (1999).
- [14]S Balhed, J Nilsen, and P Hagelstein. Phys. Rev. A, **33** 264 (1996).
- [15]U I Safronova, A S Safronova, and Beiersdorfer P. J. Phys. B: At. Mol. Opt. Phys., 42165010 (2009).
- [16]A Peleg, E Behar, P Mandelbaum and J L Schwob. Rev. A, **57** 3493 (1998).
- [17]E Behar, A Peleg, R Doron, P Mandelbaum and J L Schwob. J. Quant. Spectrose. Radiat. Transfer, **58** 449 (1997).
- [18]F C Meng, L Zhou, M Huang, C Y Chen, Y S Wang and Y M Zou. J. Phys. B: At. Mol. Opt. Phys., **42** 105203 (2009).
- [19]F C Meng, C Y Chen, Y S Wang and Y M Zou. J. Quant. Spectrose. Radiat. transfer, **109** 2000 (2008).
- [20]E Behar, P Mandelbaum and J L Schwob. Eur. Phys. J. D., **7** 157 (2010).
- [21]E Behar, R Doron, P Mandelbaum and J L Schwob. Phys. Rev. A, **58** 211 (1998).
- [22]Y Z Zhang, Y B Fu, C Z Dong and M G Su. [J] High Power Laser and Particle Beams, **23** 1087 (in Chinese) (2011).
- [23]C P Ballance, S D Loch, M S Pindzola and D C Griffin. J. Phys. B: At. Mol. Opt.

Phys., **43** 205201 (2010).

[24]U I Safronova, A S Safronova, P Beiersdorfer and W R Johnson. J. Phys. B: At. Mol. Opt. Phys., **44** 035005 (2011).

[25]<http://arxiv.org/abs/1204.2187v1>.

[26]S Schippers, D Bernhardt and A Mller, et al. phys. Rev. A, **83** 012711 (2011).

[27]U I Safronova and A S Safronova. Phys. Rev. A, **85** 032507 (2012).

[28]U I Safronova and A S Safronova. J. Phys. B: At. Mol. Opt. Phys., **45** 085001 (2012).

[29]M F Gu. Astrophys. J., **590** 1131 (2003).

[30]U I Safronova, T Kato and M Ohira. Quant J. Spectrosc. Radiat. Transf, **58**: 193 (1997).

[31]K B Fourinier. Atomic Date and Nuclear Date Tables, **68** 1 (1998).

[32]A E Kramida and T Shirai. Atomic Date and Nuclear Date Tables, **95** 305 (2009).

[33]H Zhang, Y M Li, J Yan and J G Wang. Phys. Rev. A, **71** 042705 (2005).

[34]F C Meng, C Y Chen, X H Shi, Y S Wang, Y M Zou and M F Gu. J. Phys. B: At. Mol. Opt. Phys. **40** 4269 (2007).

## **Preliminary result on quantitative analysis using Zn-like tungsten EUV spectrum in Large Helical Device**

**Shigeru MORITA<sup>1,2</sup>, Chunfeng DONG<sup>1</sup>, Erhui WANG<sup>2</sup>, Daiji KATO<sup>1</sup>,  
Motoshi GOTO<sup>1,2</sup>, Masahiro KOBAYASHI<sup>1,2</sup>, Izumi MURAKAMI<sup>1,2</sup>,  
Tetsutarou OISHI<sup>1</sup>, Hiroyuki SAKAUE<sup>1</sup>, Zhengying CUI<sup>3</sup>, Hangyu ZHOU<sup>3</sup>,  
Liqun HU<sup>4</sup>, Bo LU<sup>4</sup>, Zhenwei WU<sup>4</sup> and Ling ZHANG<sup>4</sup>**

<sup>1</sup> National Institute for Fusion Science, Toki 509-5292, Gifu, Japan

<sup>2</sup> The Graduate University for Advanced Studies, Toki 509-5292, Gifu, Japan

<sup>3</sup> Southwestern Institute of Physics, P.O.Box 432, Chengdu, Sichuan 610041, P.R.China

<sup>4</sup> Institute of Plasma Physics, P.O.Box 1126, Hefei, Anhui 230031, P.R.China

Tungsten study through visible, vacuum ultraviolet (VUV) and extreme ultraviolet (EUV) spectroscopy has been recently started in Large Helical Device (LHD) for developing the diagnostic method in International Thermonuclear Experimental Reactor (ITER) and understanding the tungsten transport in helical system. In order to study the tungsten spectra from core plasmas of LHD, several tungsten spectra are observed in EUV range by injecting a carbon pellet with tungsten. Zn-like tungsten spectrum with 4p-4s transition is clearly identified at 60.9Å in high-temperature phase ( $T_e \geq 2.3\text{keV}$ ) of NBI discharges in addition to several unresolved transition arrays with 6g-4f, 5g-4f, 5f-4d, 5g-4f, 4f-4d and 4d-4p transitions in range of 10-70Å. Radial profile of the Zn-like tungsten is also successfully observed with enough intensity in order of  $10^{16}$  photons. $\text{cm}^{-2}.\text{s}^{-1}$ . The radial emissivity profile reconstructed from the chord-integrated intensity profile is analyzed with combination of HULLAC code for emission coefficient calculation of the Zn-like transition and impurity transport code included ADPAK code for calculation of ionization and recombination rate coefficients. Thus, a total tungsten ion density of  $3.5 \times 10^{10} \text{cm}^{-3}$  at the plasma center is reasonably obtained in discharge with central electron density of  $4 \times 10^{13} \text{cm}^{-3}$  as the first experimental trial. The present result demonstrates that the Zn-like 4p-4s transition is applicable to the tungsten diagnostics in high-temperature plasmas.

## I. Introduction

Recently, atomic structure of tungsten has been widely studied in fusion research because the tungsten was adopted as divertor material of ITER tokamak instead of carbon which has been used for most of fusion devices [1-3]. At present, however, atomic data on the tungsten necessary for the impurity transport study in fusion plasmas are entirely insufficient [4-6], whereas those on intrinsic metallic impurities such as iron are well arranged due to a lot of works done in the fields of plasma spectroscopy and atomic physics [7]. Then, the study on tungsten spectroscopy has been also started in Large Helical Device (LHD) by injecting carbon pellet included a small amount of tungsten. The first purpose for the tungsten spectroscopy in LHD is to find some tungsten lines in higher ionization stages useful for the plasma diagnostics.

Until now, many tungsten line emissions have been measured from high-temperature plasmas in different wavelength ranges of EUV to visible light. At least, however, the spectral line which has been used for the plasma diagnostics is basically only one neutral tungsten line emitted at 4009Å. A typical spectrum of the neutral tungsten observed from LHD is shown in Fig.1. A small tungsten plate is inserted in the divertor region of LHD and the tungsten line is directly observed by focusing the observation chord of an optical fiber with lens. The neutral tungsten line is clearly identified by extending the exposure time of CCD to 1s. Since the tungsten line at 4009Å is well isolated from other lines and the line intensity is not so much weak, it has been frequently used for studying the plasma wall interaction [8]. Unfortunately, the tungsten line emission from the plasma core was entirely insufficient in the EUV range because the tungsten plate inserted in the LHD divertor region was not mostly eroded.

Figure 2 shows the ionization energy of tungsten ion against the charge state [9]. Taking into account LHD temperature range in NBI discharges, as indicated with gray hatched region, the highest charge state of tungsten ions which can be observed from LHD plasmas is probably Ni-like  $W^{46+}$ . Since the central temperature of ITER is very high as indicated with gray striped region, the atomic configuration of L-shell partially ionized tungsten in the plasma core is simple and the impurity diagnostics using such ions is relatively easier. However, the N-shell and O-shell partially ionized tungsten produced in edge plasmas of ITER have many electrons in the bound orbit forming complicated atomic structure. The spectroscopic study of tungsten ions in LHD can give the information on such ions for the edge plasma diagnostics of ITER.

## II. EUV spectra of tungsten from LHD

Typical tungsten EUV spectra measured from LHD using EUV spectrometers [10,11] are plotted as a function of central electron temperature in Figs.3 and 4 at two different wavelength ranges of 10-45Å and 45-70Å, respectively. The EUV spectrum is recorded with sampling time of 5ms and a few frames are summed up for the plots. Several tungsten lines in wavelength range of 25-70Å are already identified as an earlier work [12]. A cylindrical impurity pellet of carbon ( $1.2\text{mm}^\phi \times 1.2\text{mm}^L$ ) with a small amount of tungsten enclosed in the narrow hole [13] is injected in neutral-beam-heated (NBI) plasmas to observe the tungsten spectra. Figures 3(a) and 4(a) show spectra before the impurity pellet injection. Spectral lines from He- and H-like carbon and oxygen only appear in such wavelength ranges except for AlXI at 48.3Å left over from previous discharges with Al pellet injection. All these lines can be a good standard for accurate determination of measured wavelength.

A transition array seen in Figs.3(b)-(g) consists of the following transitions at various ionization stages of tungsten;

- (1) 6g-4f (20-40Å) and 5g-4f (20-45Å) transitions for  $4s^2 4p^6 4d^{10} 4f^9$  configurations
- (2) 5f-4d (18-30Å) and 5g-4f (20-45Å) transitions for  $4s^2 4p^6 4d^9$  configurations.

The shape of the transition array changes according to the electron temperature of LHD plasmas because the radial structure of tungsten ions also changes as a function of electron temperature. The transition array moves to longer wavelength range with electron temperature indicating that the tungsten emission from lower ionization stages exists at longer wavelength range. It should be noticed here that identification of each spectral line is entirely difficult in such tungsten spectra.

A similar transition array is also seen in Figs.4(b)-(g) consisting of the following transitions in various ionization stages of tungsten;

- (1) 4f-4d (45-65Å) transitions for  $4s^2 4p^6 4d^{10} 4f^9$  configurations in  $W^{19+}$ - $W^{27+}$  ions.
- (2) 4d-4p (60-70Å) transitions for  $4s^2 4p^6 4d^9$  configurations in  $W^{27+}$ - $W^{43+}$  ions.

The shape of this transition array does not change so much as a function of electron temperature, which is contrastive to the Fig.3. However, any spectral line can not be identified when the electron temperature is lower, forming a pseudo-continuum spectrum. The spectral lines are visible when the 4d electrons are partially ionized. As a result, it is difficult for these lines seen in Figs. 3 and 4 to apply the impurity transport study of tungsten ions in fusion plasmas.

Zn-like ( $W^{44+}$ ) tungsten spectrum can be observed at 60.9Å if the electron temperature is higher than 2.3 keV, as shown in Fig.5. It should be mentioned here that the wavelength of Zn-like tungsten is not accurately determined. At present, we use the wavelength in the reference [9]. The Zn-like tungsten appears with strong intensity in the range of  $2.3 \leq T_e \leq 3.2$  keV, but it begins to disappear when the electron temperature increases above 3.2 keV, since the  $W^{44+}$  ion does not exist at the plasma center no longer. The Zn-like tungsten at 60.9Å is a little blended with other lines at the shorter and longer wavelength sides. Ga-like tungsten ( $W^{43+}$ ) exists at 60.5Å in shorter wavelength side of Zn-like tungsten at 60.9Å. At the longer wavelength side Ge-like ( $W^{42+}$ ) and Ga-like ( $W^{43+}$ ) tungsten also exist at 61.3Å. The detailed spectral structure near Zn-like tungsten is shown in Fig.5(h) as an extension of Fig.5(d). In the following analysis we select only the part of the Zn-like tungsten.

In addition, another Zn-like tungsten exists near 62Å as the forbidden line. In the same wavelength, however, Cu-like ( $W^{45+}$ ) tungsten is also emitted as the dipole transition. Then, we calculate the intensities of them using HULLAC (Hebrew University Lawrence Livermore Atomic Code) code. The results are shown in Figs.6 (a) and (b) for Zn-like forbidden transition and Cu-like dipole transition, respectively. Here, it should be noticed that the wavelength of the Zn-like tungsten calculated with HULLAC code (60.6Å in Fig.6(a)) is different from the experimental observation (60.9Å) and the wavelength of Cu-like tungsten (62.1Å in Fig.6(b)) is also different from Fig.5(h). In the Fig.6(a) configuration interaction is taken into account between  $4s^2 \ ^1S_0$  and  $4p^2 \ ^1S_0$  levels. If we do not consider the configuration interaction, the Zn-like forbidden transition is of course very weak because the transition is not allowed, as shown in Fig.7. Looking at the temperature dependence of tungsten lines in Fig.5 the tungsten line at 62.1Å can not be observed at  $T_e=2.35$  keV in Fig.5(b), whereas the Zn-like tungsten is clearly observed at 60.9Å. When the electron temperature increases to 2.7 keV, the tungsten line at 62.1Å begins to appear, as seen in Fig.6(c). Therefore, the line at 62.1Å must be Cu-like tungsten. This Cu-like tungsten transition is also applicable to the impurity transport because the configuration is very simple as well as Zn-like transition.

### III. Quantitative analysis of Zn-like transition

Local impurity ion density,  $n_q$ , in charge state of  $q^+$  is determined by continuity equation in cylindrical geometry;

$$\frac{\partial n_q}{\partial t} = -\frac{1}{r} \frac{\partial}{\partial r} (r \Gamma_q) - (\alpha_q + \beta_q) n_e n_q + \beta_{q+1} n_e n_{q+1} + \alpha_{q-1} n_e n_{q-1} \quad , \quad (1)$$

where  $\alpha$  and  $\beta$  are ionization and recombination rate coefficients, respectively. ADPAK (Atomic Data Package) atomic physics code is used for the rate coefficients in the present impurity transport code. Radial impurity flux of,  $\Gamma_q$ , is expressed by diffusive/convective model;

$$\Gamma_q = -D \frac{\partial n_q}{\partial r} + n_q V \quad , \quad (2)$$

where D and V are diffusion coefficient and convective velocity, respectively. Based on these equations, radial profiles of tungsten ions in LHD calculated as a parameter of D and V are shown in Figs.8 (a) and (b), respectively. In LHD D=0.2m<sup>2</sup>/s and V=-1m/s are obtained as the typical value in the previous work [15,16], although the convective velocity depends on the electron density and the ion charge, in particular for heavier impurity. In general, the radial structure of heavy impurity ions is not a large function of D and V because such impurity ions are partially ionized even in the plasma center having many electrons in the bound orbit and the difference of ionization energy is relatively small between adjacent charge states of such heavy impurity ions. Therefore, the charge state of tungsten in the plasma center takes a large function of the electron temperature, as shown in Fig.8(c). The radial density profile of Zn-like W<sup>44+</sup> ions,  $n_w^{44+}$ , largely changes even if the central electron temperature only changes a little. As a result, the charge state of the tungsten ion is strongly affected by the accuracy of the ionization and recombination rate coefficients.

In order to examine the accuracy of the rate coefficients the intensity of Zn-like tungsten is analyzed against the electron temperature using the temperature recovery phase after injection of the carbon pellet with tungsten. A discharge wave form after the impurity pellet is shown in Fig.9. The measured density rise,  $\Delta n_e$ , after the cylindrical carbon pellet injection with size of 12.mm<sup>φ</sup>×1.2mm<sup>L</sup> is  $\Delta n_e=2 \times 10^{13} \text{cm}^{-3}$ , whereas the expected density rise is  $\Delta n_e=3 \times 10^{13} \text{cm}^{-3}$  if all the particles of the impurity pellet are fully confined in the plasma. The gradual increase in the density after the pellet injection from 3.87s to 4.07s is due to the change of edge particle confinement. When the edge temperature decreases in LHD, the edge particle confinement increases because the particle screening by the edge stochastic magnetic field layer is weak [17]. After 0.45s from the pellet injection the electron temperature begins to recover since the electron density decreases. At present, it is unclear whether the density of tungsten ions injected by the impurity pellet also decreases with the electron density or not. However, the tungsten ion density, at least, gradually decreases as a function of time,

even if it decays with recovery of the electron temperature.

The intensity of Zn-like tungsten is analyzed for the electron temperature recovery phase indicated with hatched area in Fig.9. The result is plotted with solid circles in Fig.10 as a function of central electron temperature. The Zn-like tungsten intensity evaluated from Fig.9 takes the maximum value at  $T_e=2.8\text{keV}$  as a sharp function of electron temperature. In the meantime the charge state distribution of tungsten ions in the plasma center of LHD is calculated based on eqs. (1) and (2). The density of Zn-like tungsten at the plasma center calculated with the impurity transport code is also plotted in Fig.10. The electron temperature at which the  $n_W^{44+}$  takes the maximum is 4.5keV in the present impurity transport code. A large difference is clearly seen between the observation and the calculation in Fig.10. The reason is definitely caused by a discrepancy in the ionization and recombination rate coefficients. The difference of the rate coefficients from ADPAK code is determined in several ionization stages of tungsten [5]. The present result shows a similar tendency to the previous result, that is, the recombination rate of ADPAK is small compared to the experiment. In order to compare between the present and previous results quantitatively, however, several data from other ionization stages of tungsten ions are necessary when the impurity transport code is modified. It will be done as the future work.

Radial intensity profile of Zn-like tungsten with 4p-4s transition at  $60.6\text{\AA}$  has been measured using a space-resolved EUV spectrometer in LHD [18]. The absolute sensitivity of the spectrometer is accurately calibrated using bremsstrahlung continuum from LHD [19]. A typical result is shown in Fig.11(a). The centrally peaked profile indicates the Zn-like tungsten ion exists in the plasma center. In order to compare with the impurity transport calculation, the chord-integrated vertical profile of Zn-like tungsten shown in Fig.11(a) is reconstructed into the local emissivity profile using Abel inversion technique. The resultant profile indicated in Fig.11(b) seems to have two components in the Zn-like tungsten at  $60.6\text{\AA}$ . It is probably an effect of the line blending with tungsten emission in lower ionization stage. However, we need further examination on the Zn-like tungsten to conclude the true reason.

We calculate the emission coefficient of 4p-4s transition for the Zn-like tungsten based on HULLAC code. If we do not take into account the configuration interaction for the transition, the emission coefficient is considerably small, as shown in Fig.12(a). In addition, the rate coefficient decreases with electron temperature at  $T_e \geq 0.6\text{keV}$ . The configuration interaction is then necessary for such an allowed transition. The radial profile of Zn-like tungsten is also calculated for both cases with and without configuration interaction, as shown in Fig.12(b). If we do not include the

configuration interaction, the emissivity of Zn-like tungsten is reduced to 60% compared to the emissivity with configuration interaction.

The radial emissivity profile of Zn-like tungsten is also calculated with different electron temperatures, as seen in Fig.13(a). It is clear that the emission moves from the central part to the outside of plasma, when the electron temperature is more than 5keV. In this calculation the tungsten ion density integrated along the whole plasma volume is assumed to be  $10^{-4}$  to the electron density. In order to determine the tungsten density in LHD the local emissivity profile in Fig.11(b) is compared with the transport calculation. The best fitting to the measured profile is obtained at  $T_e=4.6\text{keV}$ . The result is shown in Fig.13(b). From this analysis the  $n_w^{44+}$  is estimated to be  $1.4 \times 10^{-4}$  to the electron density ( $4 \times 10^{13} \text{cm}^{-3}$ ) at the plasma center, if the configuration interaction is included. The total tungsten density in the plasma center can be also estimated to be  $3.5 \times 10^{10} \text{cm}^{-3}$  ( $n_w/n_e=8.8 \times 10^{-4}$ ). When the total radiation loss,  $P_{\text{rad}}$ , from the present tungsten density is calculated with average ion model [20,21], we roughly obtain the value of  $P_{\text{rad}}=4\text{MW}$ . Since the  $P_{\text{rad}}$  in the present discharge ranges in 3-4MW after the tungsten pellet injection (see Fig.9), the  $P_{\text{rad}}$  from the calculation seems to be reasonable. As a result, we can summarize the tungsten density obtained in the present analysis will be also reasonable.

#### IV. Summary

Tungsten spectroscopy has been started in LHD for development of the diagnostic method and study of the impurity transport through deeper understanding of the tungsten spectra. Several tungsten spectra are observed in EUV range by injecting carbon pellet with tungsten. Zn-like tungsten spectrum with 4p-4s transition is identified at  $60.9\text{\AA}$  in high-temperature phase of NBI discharges and the radial profile is successfully observed with enough intensity. The radial emissivity profile reconstructed from the chord-integrated intensity profile is analyzed with combination of HULLAC code for emission coefficient calculation of the Zn-like transition and impurity transport code included ADPAK code for calculation of ionization and recombination rate coefficients. Total tungsten density of  $3.5 \times 10^{10} \text{cm}^{-3}$  is reasonably obtained in the plasma center ( $n_e(0)=4 \times 10^{13} \text{cm}^{-3}$ ) as the first trial of quantitative analysis for tungsten. The present result demonstrates that the Zn-like 4p-4s transition is applicable to the tungsten diagnostics in high-temperature plasmas.

Several subjects on the tungsten diagnostics are also made clear through the present study. In particular, further studies on ionization and recombination rate coefficients of tungsten ions for the impurity transport code are important in addition to emission rate

coefficient of Zn- and Cu-like tungsten ions. Dielectronic recombination plays an important role for modeling the level population and the emission intensity of tungsten ions. Detailed study of the tungsten spectra is necessary for accurate analysis including Zn-like tungsten transition.

### **Acknowledgements**

The authors acknowledge all members of LHD experiment group for their technical supports and fruitful discussions. This work was partially carried out under the LHD project financial support (NIFS12ULPP010). This work was partly supported by the JSPS-NRF-NSFC A3 Foresight Program in the field of Plasma Physics (NSFC: No.11261140328).

## References

- [1] D.W.Ignat et al., Nucl. Fusion **39** (1999) 2137.
- [2] R.Neu, R.Dux, A.Kallenbach, et al., Nucl. Fusion **45** (2005) 209.
- [3] J.Roth, E.Tsitrone, T.Loarer et al., Plasma Phys. Control. Fusion **50** (2008) 103001.
- [4] K.Asmussen, K.B.Fournier, J.M.Laming et al., Nucl. Fusion **38** (1998) 967.
- [5] T.Putterich, R.Neu, R.Dux et al., Plasma Phys. Control. Fusion **50** (2008) 085016.
- [6] J.Yanagibayashi, T.Nakano, A.Iwamae et al., J.Phys.B **43** (2010) 144013.
- [7] K.Mori, M.Otsuka and T.Kato Atomic Data Nucl. Data Tables **23** (1979) 195.
- [8] A.Thoma, K.Asmussen, R.Dux, et al., Phys. Control. Fusion **39** (1977) 1487.
- [9] A.E.Kramida and T.Shirai Atomic Data Nucl. Data Tables **95** (2009) 305.
- [10] M.B.Chowdhuri, S.Morita, M.Goto, et al., Rev.Sci.Instrum. **78** (2007) 023501.
- [11] M.B.Chowdhuri, S.Morita and M.Goto Appl.Optics **47** (2008) 135.
- [12] M.B.Chowdhuri, S.Morita and M.Goto Plasma Fusion Res. **2** (2007) S1060.
- [13] R.Katai, S.Morita, M.Goto et al., Jpn. Soc. Appl. Phys. **46** (2007) 3667.
- [14] T.Putterich, R.Neu, C.biedermann et al., J.Phys.B **38** (2005) 3071.
- [15] H.Nozato, S.Morita, M.Goto et al., Phys.Plasmas **11** (2004) 1920.
- [16] H.Nozato, S.Morita, M.Goto et al., Phys.Plasmas **13** (2006) 092502.
- [17] M.B.Chowdhuri, S.Morita, M.Kobayashi et al., Phys.Plasmas **16** (2009) 062502.
- [18] C.F.Dong, S.Morita, M.Goto et al., Rev. Sci. Instrum. **81** (2010) 033107.
- [18] C.F.Dong, S.Morita, M.Goto et al., Rev. Sci. Instrum. **82** (2011) 113102.
- [20] D.E.Post and R.V.Jensen Atomic Data Nucl. Data Tables **20** (1977) 397.
- [21] T.Putterich, R.Neu, R.Dux et al., Nucl. Fusion **50** (2010) 025012.

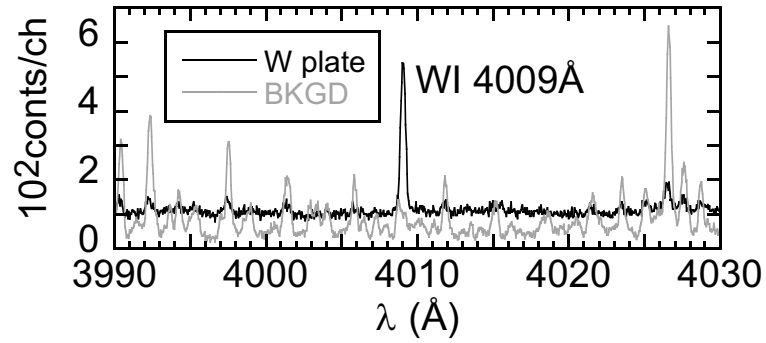


Fig.1 Visible spectra of tungsten at 4.5-U port looking at tungsten plate inserted in divertor region (black line) and at 10-O port as background emission (gray line).

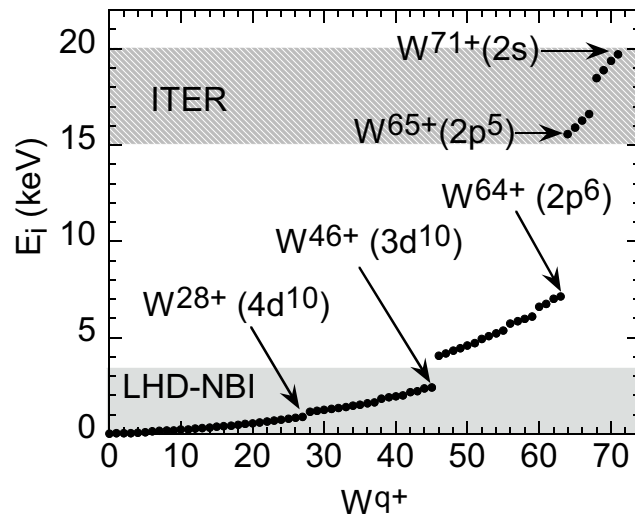


Fig.2 Ionization energy of W ions with charge state of  $q^+$ . Hatched and striped areas indicate electron temperature ranges at  $T_e=E_i$  for NBI discharges in LHD and typical discharges in ITER, respectively.

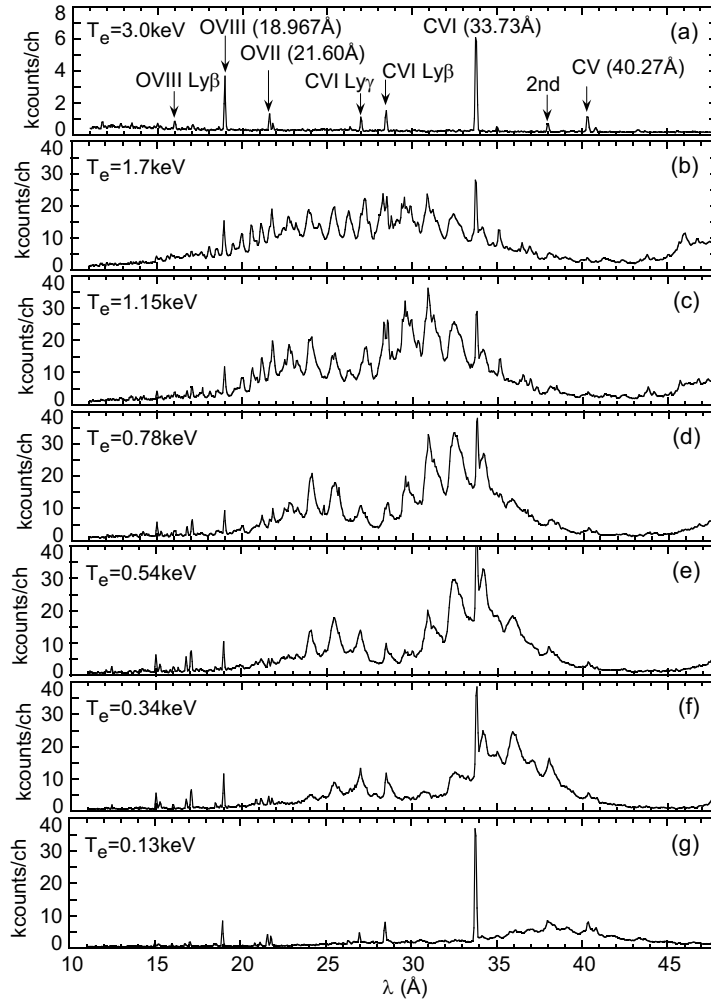


Fig.3 Tungsten EUV spectra at 10-45Å with 6g-4f, 5g-4f, 5f-4d and 5g-4f transitions in different electron temperature ranges of (b) 1.7keV, (c) 1.15keV, (d) 0.78keV, (e) 0.54keV, (f) 0.34keV and (g) 0.13keV observed after carbon pellet injection with tungsten. Reference spectrum at  $T_e=3.0\text{keV}$  before pellet injection is plotted in (a).

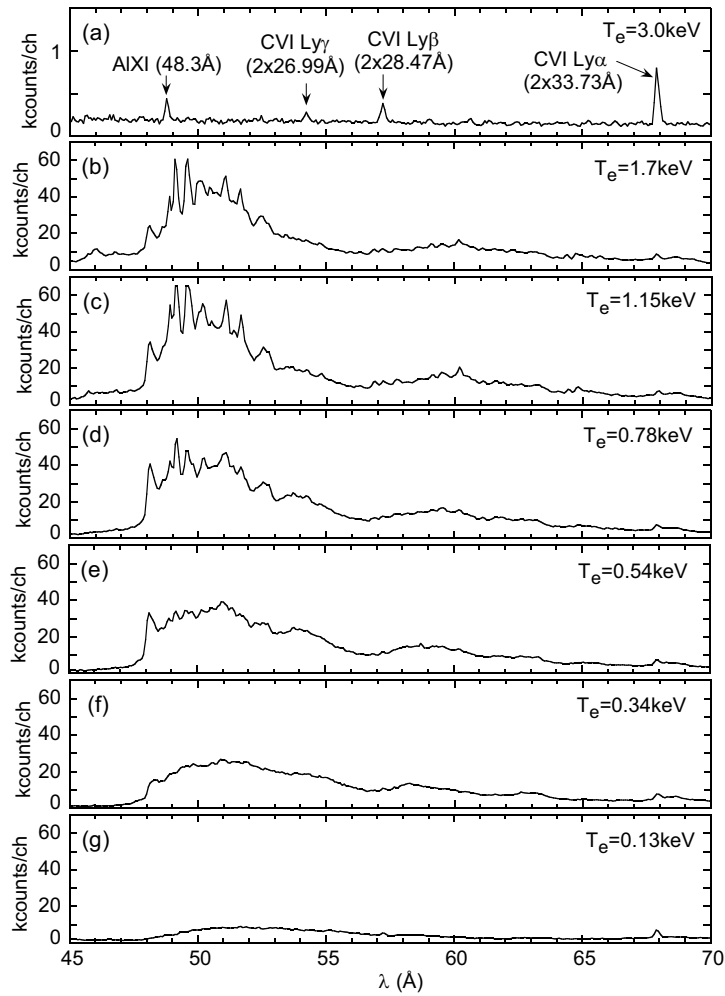


Fig.4 Tungsten EUV spectra at 45-70Å with 4f-4d and 4d-4p transitions in different electron temperature ranges of (b) 1.7keV, (c) 1.15keV, (d) 0.78keV, (e) 0.54keV, (f) 0.34keV and (g) 0.13keV observed after carbon pellet injection with tungsten. Reference spectrum at  $T_e=3.0\text{keV}$  before pellet injection is plotted in (a).

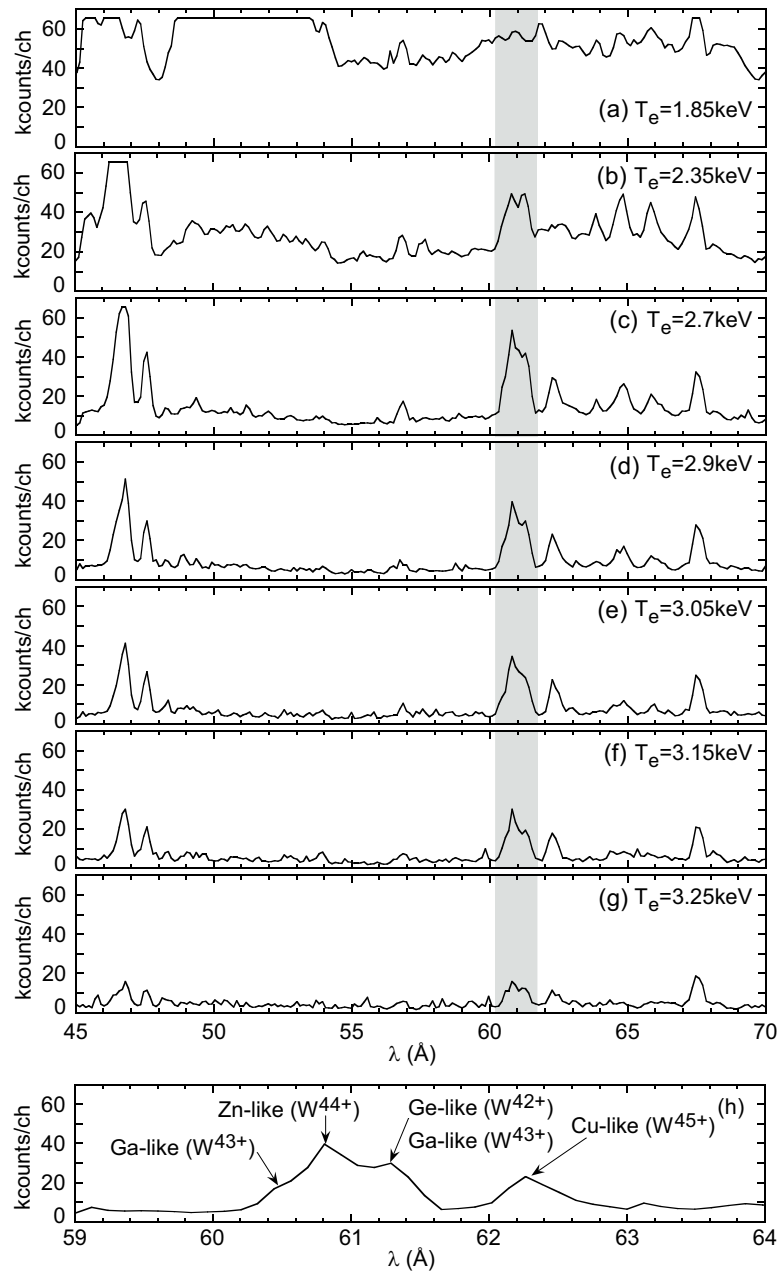


Fig.5 Tungsten EUV spectra from Zn-like ( $W^{44+}$ ) ions at  $60.9\text{\AA}$  in different electron temperature regions of (a)  $1.85\text{keV}$ , (b)  $2.35\text{keV}$ , (c)  $2.7\text{keV}$ , (d)  $2.9\text{keV}$ , (e)  $3.05\text{keV}$ , (f)  $3.15\text{keV}$  and (g)  $3.25\text{keV}$ . Hatched area indicates the vicinity of Zn-like tungsten. Detailed information near Zn-like tungsten [14] is plotted in (h) as an enlarged spectrum of (d).

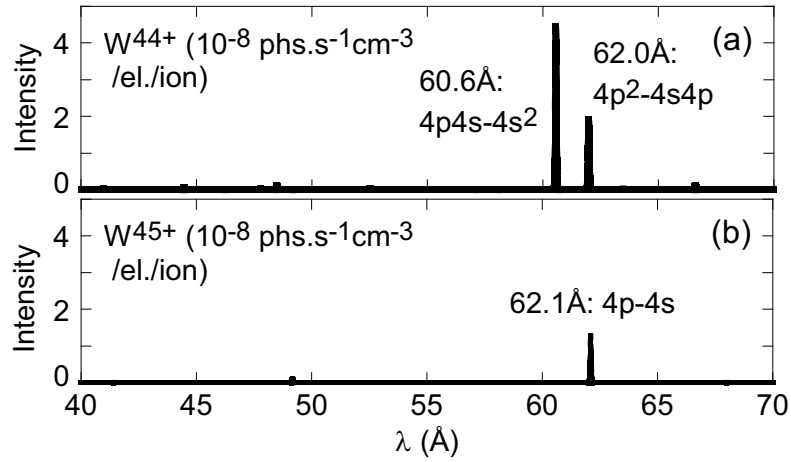


Fig.6 Intensities of (a)  $W^{44+}$  and (b)  $W^{45+}$  transitions at near 61Å calculated from HULLAC code with configuration interaction.

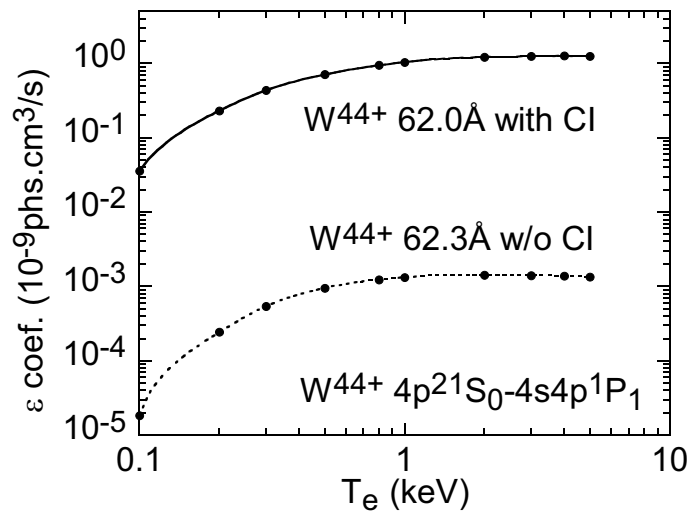


Fig.7 Emission coefficients of Zn-like  $W^{44+}$  forbidden transition ( $4p^2\ ^1S_0-4s4p\ ^1P_1$ ) with (solid line) and without (dotted line) configuration interaction.

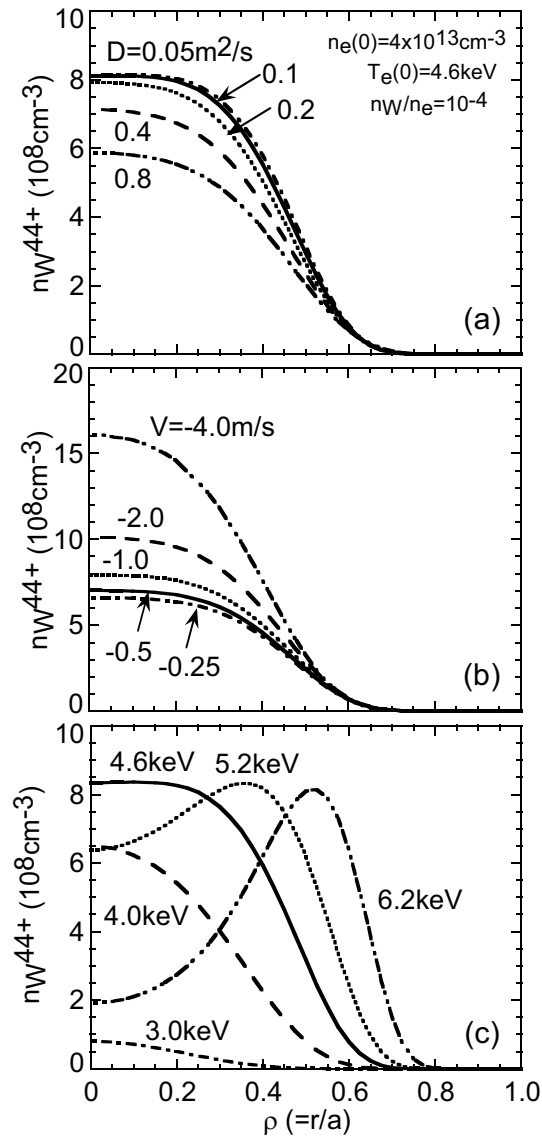


Fig.8 Radial profiles of  $W^{44+}$  density as a parameter of (a) diffusion coefficient, (b) inward convective velocity and (c) central electron temperature. Total tungsten ion density of  $4 \times 10^9 \text{cm}^{-3}$  ( $n_W/n_e = 10^{-4}$ ) is assumed in the calculation with default values of  $D = 0.2 \text{m}^2/\text{s}$  and  $V = -1 \text{m/s}$

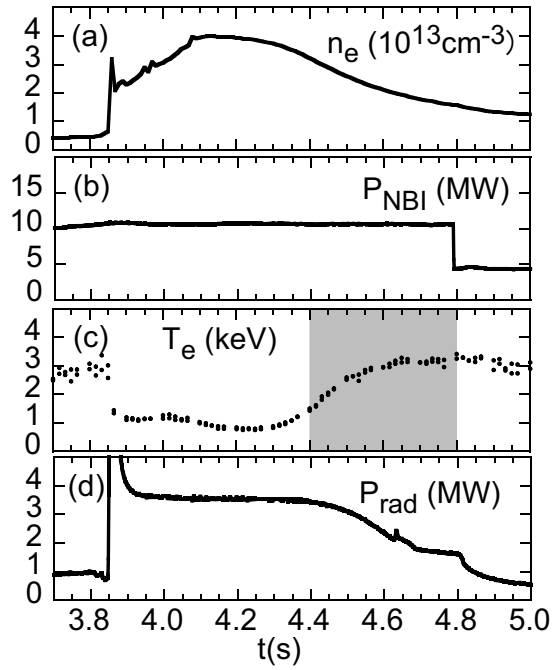


Fig.9 Injection of cylindrical carbon pellet ( $1.2\text{mm}^\phi \times 1.2\text{mm}^L$ ) with tungsten in LHD. The pellet is injected at 3.85s in NBI discharge and Zn-like tungsten is analyzed for 4.4-4.8s indicated with hatched area.

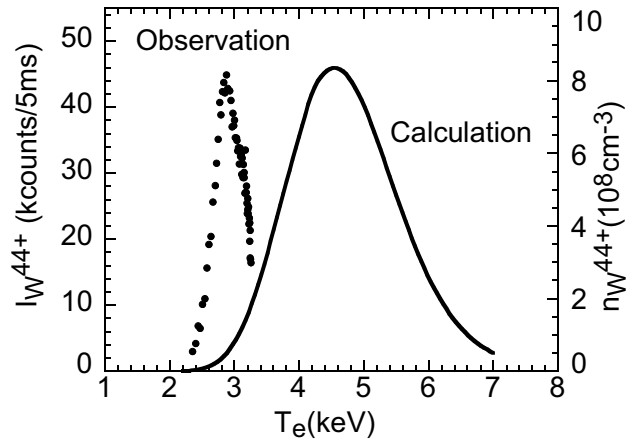


Fig.10 Temperature dependence of Zn-like ( $W^{44+}$ ) 4p-4s transition at  $60.9\text{\AA}$  (observation: solid circles and impurity transport calculation: solid line).

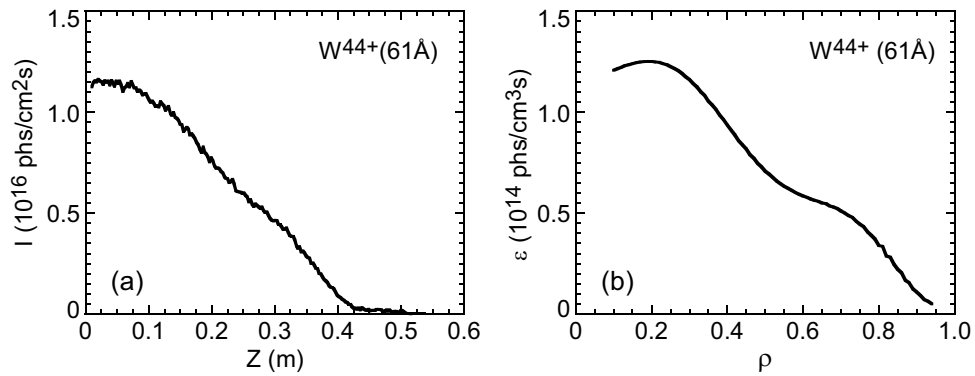


Fig.11 Chord-integrated vertical profile and local emissivity profile of Zn-like ( $W^{44+}$ ) 4p-4s transition at  $60.9\text{\AA}$ .

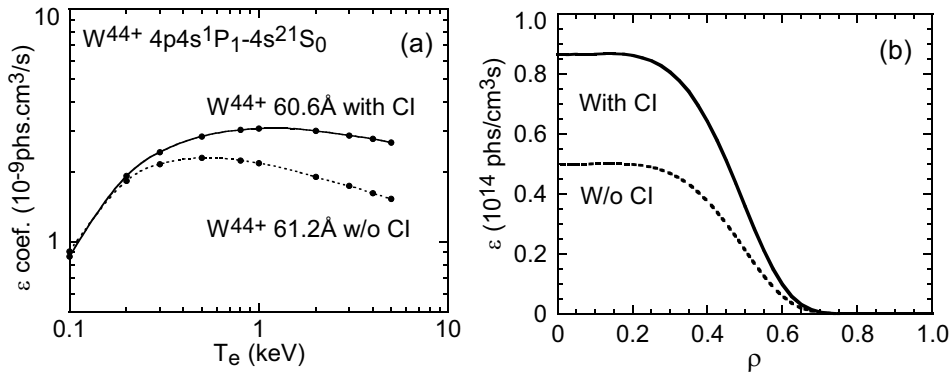


Fig.12 (a) Emission coefficients as a function of electron temperature and (b) local emissivity profiles of Zn-like W ( $W^{44+}$ ) transition at  $60.9\text{\AA}$  with/without configuration interaction calculated by HUULAC code.

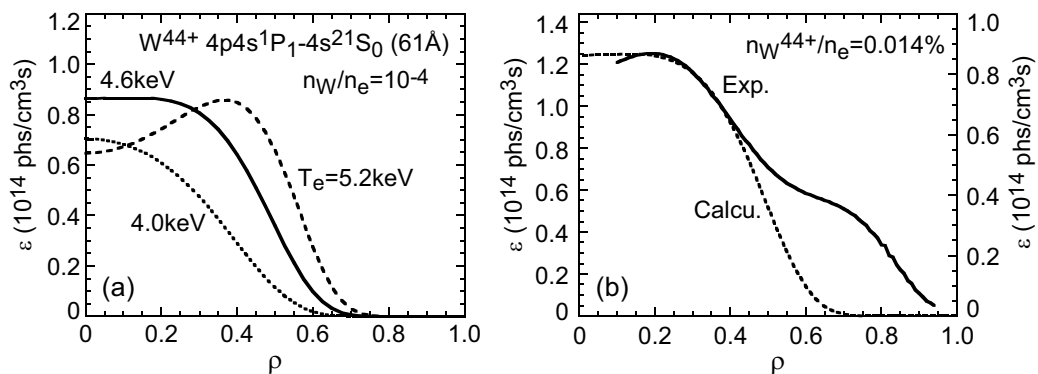


Fig.13 Calculated local emissivity profile of Zn-like ( $W^{44+}$ ) 4p-4s transition at  $60.9\text{\AA}$  as a parameter of (a) central electron temperature and (b) fitting of calculated local emissivity profile at  $T_e=4.6\text{keV}$  to experimentally observed profile.

**Study of EUV spectra from low- and medium-Z impurity ions based  
on a grazing-incidence flat-field EUV spectrometer in HL-2A  
tokamak**

Hangyu Zhou, Zhengying Cui, Shigeru Morita<sup>1</sup>, Ping Sun, Motoshi Goto<sup>1</sup>, Bingzhong Fu, Beibin Feng, Ping Lu, Qingwei Yang, and Xuru Duan

*Southwestern Institute of Physics, P.O.Box 432, Chengdu 610041, China*

*1) National Institute for Fusion Science, Toki 509-5292, Gifu, Japan*

*e-mail: [zhouhy@swip.ac.cn](mailto:zhouhy@swip.ac.cn)*

**Abstract**

EUV spectra have been measured by EUV spectrometer with a holographic varied-line-space (VLS) grating newly installed in HL-2A tokamak to observe the wavelength range of 20-500Å. We observe that carbon, oxygen and iron impurities are dominant in the HL-2A plasmas. Aluminum and neon have been injected based on laser blow-off (LBO) and super-sonic molecular beam injection (SMBI) techniques for studies of spectral identification and impurity transport. Lithium-like AlX and beryllium-like AlIX appear in the wavelength interval of 45-70Å, while lithium-like NeVIII and beryllium-like NeVII is seen in the spectral interval of 70-130Å. Time behaviors of aluminum and neon emissions after LBO are compared with those after SMBI. It indicates that the transport behavior of aluminum after LBO is entirely different from that after SMBI.

**Keywords:** EUV spectra, LBO, SMBI, EUV spectroscopy

## **Introduction**

Impurity study [1,2,3] is significantly important for fusion research, since effective control of impurities can improve plasma performance and reduce divertor heating flux through enhanced radiation loss in the plasma edge. Although the impurity intrinsically exists in the plasma as the origin of vacuum wall, divertor plates and in-vessel components, it is extrinsically introduced by methods of gas-puffing, laser blow-off (LBO) [4,5] and super-sonic molecular beam injection (SMBI) [6]. The impurity ions widely distribute from the edge to the core region of toroidal plasmas depending on the ionization stage. Spectroscopic method [7,8] is indispensable to observe the impurity spectra and to understand the impurity behavior. In HL-2A vacuum ultraviolet (VUV) spectroscopy [9] is firstly developed to observe the line emissions from edge impurities in low ionization stages. Extreme ultraviolet (EUV) spectroscopy is also newly installed [10] on HL-2A to measure the line emissions from core impurity ions in high ionization stages for the study of atomic and molecular processes in addition to the impurity transport study. Furthermore, LBO and SMBI are applied to injected impurities for analyzing spectra and transport.

### **1. Experimental setup**

A schematic view of the EUV spectrometer system is shown in Fig.1. The EUV spectrometer consists of an entrance slit, a holographic varied-line-space (VLS) grating, a back-illuminated charge-coupled device (CCD) and a laser light source for positional calibration of the spectrometer. The specifications of the spectrometer are;

Entrance slit: 30 $\mu$ m or 100 $\mu$ m in width

VLS grating: 1200 grooves/mm at the center

Effective area of grating: 26mm $\times$ 46mm

Curvature radius of grating: 5612mm

and

CCD size: 26.6 $\times$ 6.7mm<sup>2</sup> (1024 $\times$ 256pixels).

The EUV spectrometer can work in the wavelength range of 20-500Å and the spectral resolution is 0.22Å at  $\lambda=200\text{\AA}$ . The EUV spectrometer is maintained at the vacuum pressure of  $10^{-5}$  pa using a pumping system of 300 l/s turbo-molecular and 5 l/s oil-free rotary pumps. The spectrometer sensitivity is absolutely calibrated by comparing the measured bremsstrahlung continuum with calculated one. On the other hand, the VUV spectrometer consists of two interchangeable 1200 grooves/mm gratings with blaze wavelength of 800Å and 1500Å, entrance and spatial-resolved slits and CCD. The wavelength region of 300-3200Å can be observed by changing the grating angle with the spectral resolution of 0.15Å.

The LBO injection system consists of a YAG laser, lens and a target. The YAG laser with the wavelength of 1053nm has the maximum energy of 800mJ and the pulse width of 8ns. The target is fabricated by coating target materials (Al, Ti, Ni and so on) in thickness of several  $\mu\text{m}$  on a quartz glass with size of  $38\times 38\times 1\text{mm}^3$ . The injected number of particles is controlled by adjusting the size of laser spot. The target is set at about 710mm away from the plasma edge. The SMBI system consists of a gas source, an electromagnetic valve, cooling trap and vacuum pump unit. The pressure of injected particles can be varied from 1bar to 30bar, corresponding to injected molecular inventory of  $2\times 10^{17} \sim 6\times 10^{19}$  for one single pulse. Temperature of the injector is changed from the room temperature (300K) to the liquid nitrogen temperature (100K).

## **2. EUV Spectra from HL-2A Plasmas**

EUV spectra have been observed from HL-2A plasmas in normal ohmic discharges with and without LBO and SMBI injection. The dominant impurities in the ohmic discharges are carbon, oxygen and iron. The aluminum and neon are injected into plasmas through LBO and SMBI injection, respectively. The EUV spectrometer can simultaneously measure the line emissions in the wavelength interval of 130Å at shorter wavelength side and 280Å in longer wavelength side, since the spectral dispersion is varied. The temporal resolution is 6ms when the full

vertical binning (FVB) mode is used for the present CCD. The CCD is operated at temperature of 5°C to reduce the thermal noise.

Typical spectra from the ohmic discharges are plotted in Figs. 2(a), (b) and (c) in the wavelength regions of 20-150Å, 150-300Å and 300-500Å, respectively. Hydrogen-like CVI and OVIII and helium-like CV and OVII emissions dominate the spectra in the shorter wavelength region (see Figs. 2(a)), whereas carbon and oxygen emissions in lower ionization stages are dominant in the longer wavelength region (see Figs. 2(c)). The intensity of line emissions in the shorter wavelength region is usually one order of magnitude stronger than that in the longer wavelength region. In addition, the HeII line at 303.38Å is the strongest in the longer wavelength region, which is remained by helium glow discharge cleaning. In Fig. 2(b), the lithium-like OVI and beryllium-like OV emissions are observed with line emissions from metallic impurities such as M-shell ionized iron. The intensity of iron emissions is relatively weak compared to the line emissions from light impurities, in particular oxygen. It indicates that a lot of oxygen still exists in the plasmas. The iron emissions are generally enhanced in ECRH discharges. It is probably due to the increased edge temperature or effect of suprathermal electrons.

The aluminum is injected into HL-2A plasmas at  $t=700\text{ms}$  during ECRH heating with the power of 1.7MW. Typical waveforms of AlX (51.98Å, 330eV) measured with the EUV spectrometer and AlIV (581.91Å, 28eV) measured with the VUV spectrometer are shown in Figs. 3(a) and (b), respectively. The EUV spectra at  $t=712\text{ms}$  after Al injection is studied in the wavelength range of 20-100Å, as displayed in Figs. 3(c). The lithium-like AlX and beryllium-like AlIX emissions dominate the wavelength interval of 45-70Å after the Al injection, while this wavelength interval basically has no line emissions before the Al injection, as shown in Fig. 2(a). Furthermore, it is clear that the decay time of AlX is much shorter than that of AlIV, as given in Figs. 3(a) and (b). It means that the outward transport of impurity in the plasma core is much stronger than that in the plasma edge.

The neon is injected at  $t=600\text{ms}$  in ohmic plasmas. Typical waveforms of lithium-like NeVIII ( $88.09\text{\AA}$ ,  $207\text{eV}$ ) and beryllium-like NeII ( $1399.5\text{\AA}$ ,  $21\text{eV}$ ) are shown in Figs. 4(a) and (b), respectively. The EUV spectra at  $t=618\text{ms}$  after Ne injection is analyzed in the wavelength range of  $20\text{-}150\text{\AA}$ , as plotted in Fig. 4(c). The NeVIII and NeVII emissions dominate the wavelength interval of  $70\text{-}130\text{\AA}$ , while only two weak carbon lines appear in this wavelength interval before the Ne injection (see Fig. 2(a)). The rump-up time of NeVIII is obviously longer than that of NeII (see Figs. 4(a) and (b)), suggesting that the inward transport appears in the plasma core after the SMBI injection. The decay time of NeVIII is longer than that of NeVII, which suggests that the outward transport of impurity in the plasma core is weaker than that in the plasma edge.

### 3. Summary

Typical EUV spectra have been measured with the EUV spectrometer in the wavelength range of  $20\text{-}500\text{\AA}$  of which the temporal resolution is  $6\text{ms}$  and the spectral resolution is  $0.22\text{ \AA}$  at  $\lambda=200\text{\AA}$ . Hydrogen- and helium-like ions in light impurities such as CVI, CV, OVIII and OVII dominate the spectra in the wavelength region of  $20\text{-}150\text{\AA}$ , whereas the spectra is dominated by the line emissions from lower ionized carbon and oxygen emissions in the wavelength region of  $300\text{-}500\text{\AA}$ . The line emissions from metallic impurities such as M-shell ionized iron are also observed in the wavelength region of  $150\text{-}300\text{\AA}$ .

Aluminum and neon have been injected into HL-2A plasmas through LBO and SMBI techniques. Lithium-like AlX and beryllium-like AlIX dominate the wavelength interval of  $45\text{-}70\text{\AA}$ , and lithium-like NeVIII and beryllium-like NeVII occupy the wavelength interval of  $70\text{-}130\text{\AA}$ . Temporal behaviors of AlX and AlIV are studied based on the LBO injection. The result suggests that the outward transport of Al in the plasma core is much stronger than that in the plasma edge. The time behavior of NeVIII and NeII are also studied using SMBI injection technique. It indicates that the outward transport of Ne in the plasma core is weaker than that in the plasma edge.

## **Acknowledgement**

The authors thank all the staffs of HL-2A team for their cooperation. This work has been partially supported by the National Natural Science Foundation of China under Grant No. 11175061 and No. 10975048, and by the JSPS-NRF-NSFC A3 Foresight Program in the field of Plasma Physics (NSFC: No.11261140328).

## **Reference**

- [1] M. Mattioli, C. De Michelis and P. Monier-Garbet, Nucl. Fusion, **35**, 807 (1995).
- [2] K. Asmussen et al, Nucl. Fusion, **38**, 967 (1998).
- [3] Z. Y. Cui et al, Chin. Phys. Lett. **23**, 2143 (2006).
- [4] M. Mattioli et al, Nucl. Fusion, **35**, 1115 (1995).
- [5] E. Scavino et al, Plasma Phys. Control. Fusion, **46**, 857 (2004).
- [6] L. H. Yao et al, Nucl. Fusion, **47**, 1399 (2007).
- [7] M. B. Chowdhuri, S. Morita and M. Goto, Appl. Opt.,**47**,135 (2008).
- [8] C. F. Dong et al, Rev Sci Instrum **81**, 033107 (2010).
- [9] Z. Y. Cui et al, Rev. Sci. Instrum. **81**, 043503 (2010).
- [10] H. Y. Zhou et al, Rev. Sci. Instrum. **83**, 10D507 (2012).

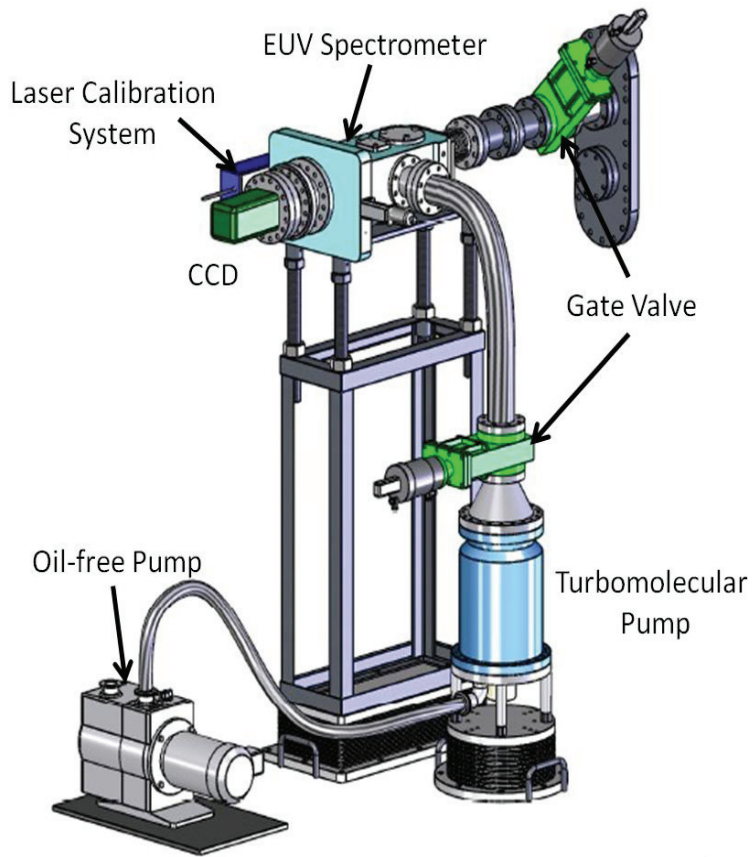


Fig. 1 Schematic view of EUV spectrometer system.

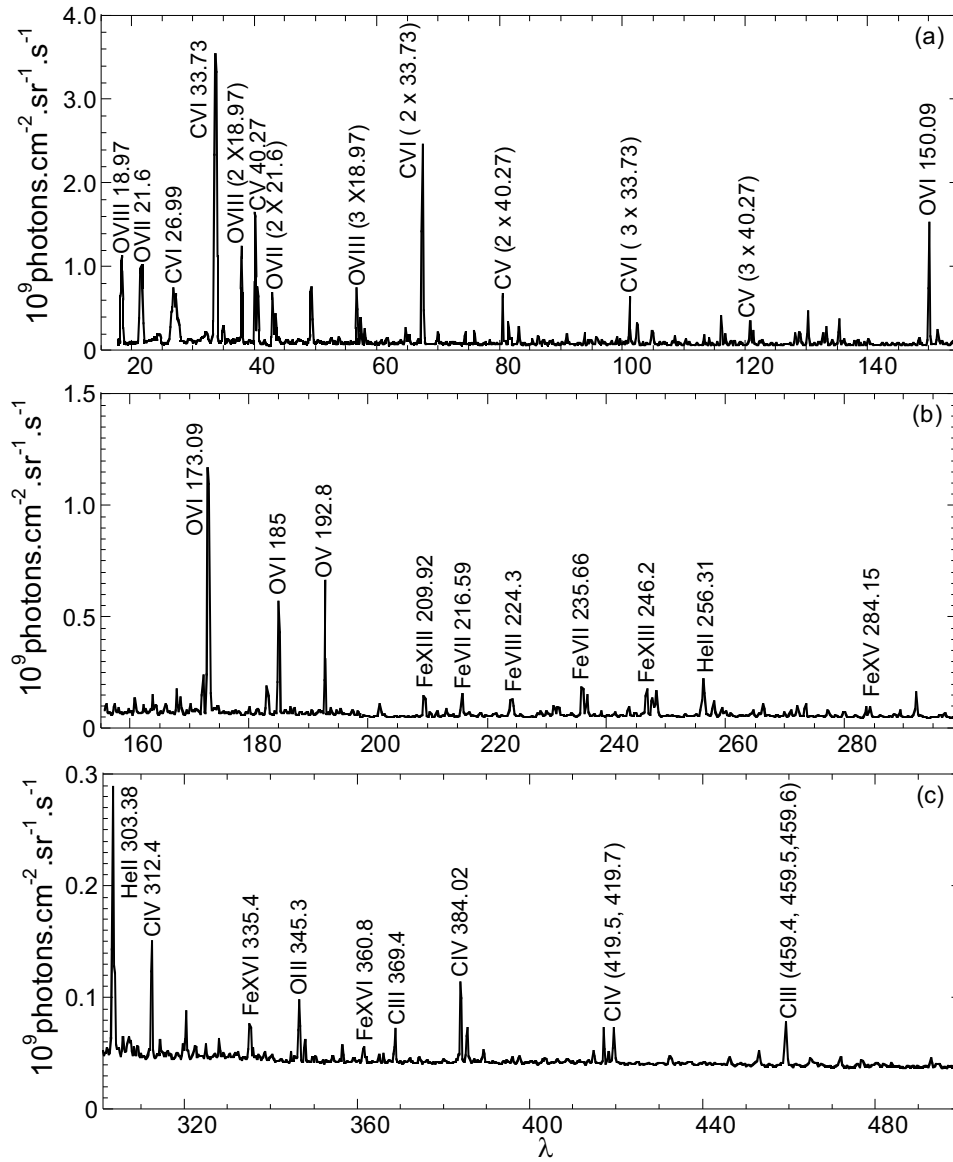


Fig. 2 EUV spectra in (a) wavelength regions of 20-150Å, (b)150-300Å and (c) 300-500Å.

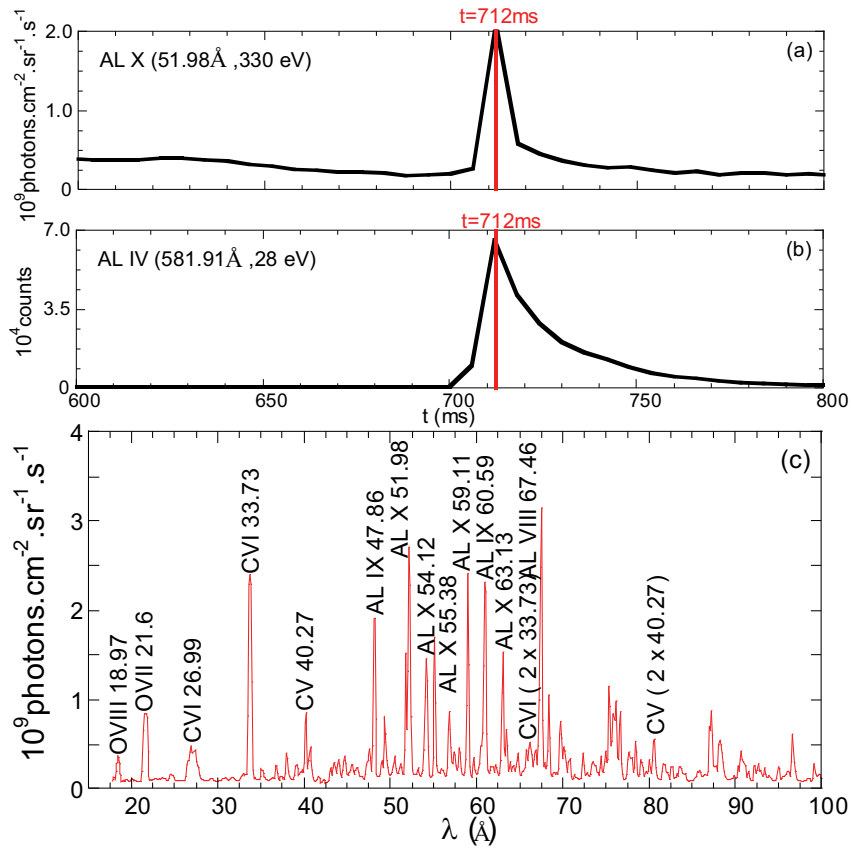


Fig. 3 Waveforms of (a) AlX and (b) AlIV spectra and (c) EUV spectrum after Al injection at  $t=712\text{ms}$ .

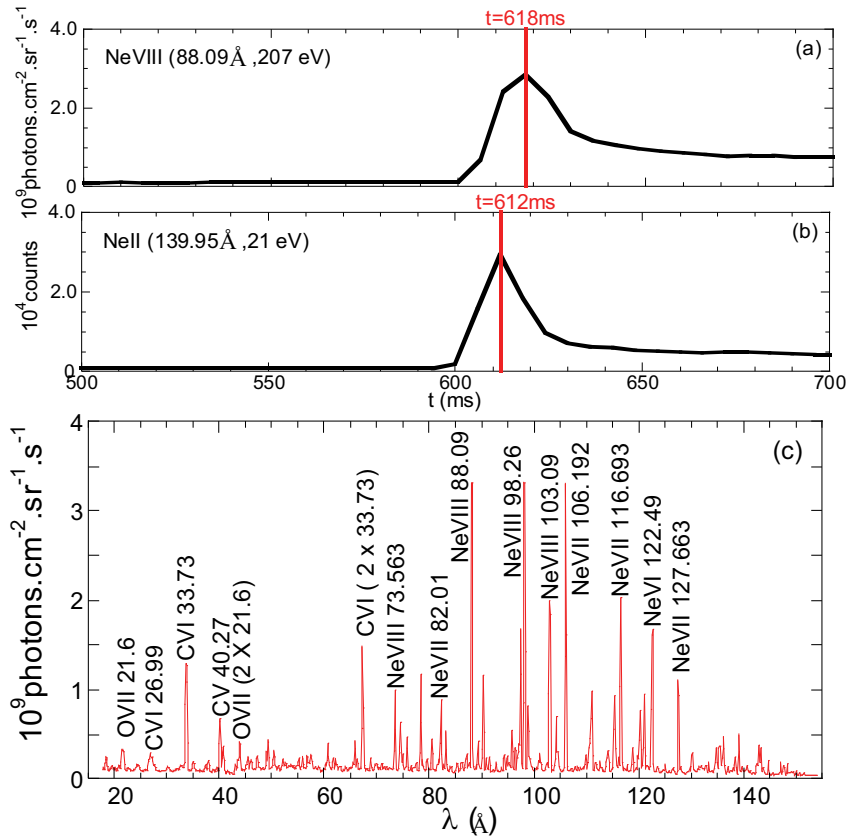


Figure 4: Waveforms of (a) NeVIII and (b) NeII spectra and EUV spectrum after Ne injection at  $t=618\text{ms}$ .

# X-ray and Auger electron study of highly charged ions using resonant coherent excitation

Y. Nakano<sup>a</sup>, A. Hatakeyama<sup>b</sup>, Y. Nakai<sup>c</sup>, K. Komaki<sup>d,e</sup>,  
E. Takada<sup>f</sup>, T. Murakami<sup>f</sup>, T. Azuma<sup>a,g</sup>

<sup>a</sup>*AMO Physcs Laboratory, RIKEN, Japan*

<sup>b</sup>*Department of Applied Physics, Tokyo Univ. of Agriculture and Technology, Japan*

<sup>c</sup>*RIKEN Nishina Center, Japan*

<sup>d</sup>*Graduate School of Arts and Sciences, University of Tokyo, Japan*

<sup>e</sup>*Atomic Physcs Laboratory, RIKEN, Japan*

<sup>f</sup>*National Institute of Radiological Sciences, Japan*

<sup>g</sup>*Department of Physics, Tokyo Metropolitan University, Japan*

*e-mail: nakano-y@riken.jp*

## Abstract

We observed X-ray and Auger electron emissions following the three-dimensional resonant coherent excitation (3D-RCE) of highly charged ions in a Si crystal. Using the polarization control technique, the ions were excited to the specific magnetic substates resulting in anisotropic emissions of de-excitation x-rays. The Auger electron emission was also observed through the selective production of doubly excited states by the double resonance technique in 3D-RCE. These methods are quite useful to study the collision dynamics, decay properties, and structure of highly charged ions relevant to atomic processes in plasma.

**Keywords:** resonant coherent excitation, highly charged ion, x-ray spectroscopy, Auger electron

## 1. Introduction

When energetic ions pass through a crystal, they experience periodical oscillations of electric fields originating from the lattice structure of the crystal. If this oscillating frequency corresponds to a transition energy of the ions, they can be resonantly excited, i.e., the resonant coherent excitation (RCE) takes place. Because the frequency of the oscillating field in the projectile frame increases with their velocity, the use of higher energy ions allows the RCE of higher transition energies in the x-ray domain. The amplitude of the oscillating field is comparable to that of the laser fields focused to  $10^{16}$  W/cm<sup>2</sup>. For these reasons, the RCE process is expected to be a versatile tool for atomic physics in the short wavelength regions not accessible by the laser technologies. Historically, since the

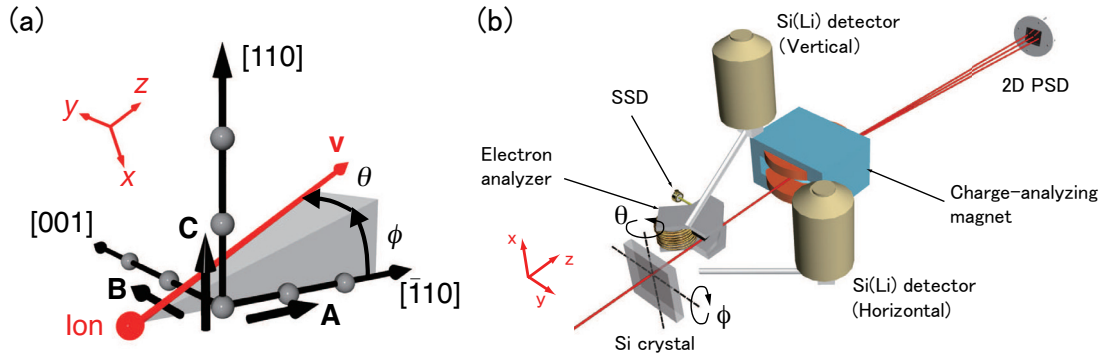


Figure 1: (a) The base vectors for the reciprocal lattice vectors of a Si crystal.  $\theta$  and  $\phi$  are the ion incident angles with respect to the  $[\bar{1}10]$  axis. (b) The schematic layout of the experimental setup.

First prediction by Okorokov [1], the RCE process has been observed exclusively under the "channeling" conditions [2, 3, 4, 5], in which the ion beam was incident parallel to the crystal axes or planes. The channelled ions penetrate the crystal along the open spaces between the atomic strings or planes avoiding the close collisions with target atoms, on the other hand, they undergo the trajectory dependent interactions with the target.

Recently, the use of extremely thin crystal enabled us to observe the RCE of energetic ion out of channeling conditions, which is called three-dimensional RCE (3D-RCE) [6]. The discovery of 3D-RCE provided new opportunities to introduce the polarization control and double resonance technique into the RCE process. Here, we demonstrate the application of the 3D-RCE to the manipulation of electronic states of energetic highly charged ions for the study of the x-ray and Auger electron emission properties of highly charged ions.

## 2. Experiment

In the 3D-RCE process, the projectile ions experience the oscillating fields by traversing the periodic arrays of atomic planes. The frequency at which the ions with a velocity  $\mathbf{v}$  traverse the crystallographic plane specified by a reciprocal lattice vector  $\mathbf{g}$  is given by  $\gamma\mathbf{g}\cdot\mathbf{v}$ , where  $\gamma$  is the Lorentz factor. In the present experiments, we used a Si crystal, which has the diamond structure with a lattice constant  $a = 5.43 \text{ \AA}$ . Taking the base vectors as shown in Fig. 1(a), namely,  $\mathbf{A}^* = (-1, 1, 0)/a$ ,  $\mathbf{B}^* = (0, 0, 1)/a$ , and  $\mathbf{C}^* = (1, 1, 0)/a$ , the reciprocal lattice vector is represented by  $\mathbf{g}_{k,l,m} = k\mathbf{A}^* + l\mathbf{B}^* + m\mathbf{C}^*$ , with the Miller index  $(k, l, m)$ . Thus, the oscillating frequency is given by

$$\gamma\mathbf{g}_{k,l,m} \cdot \mathbf{v} = \frac{h\gamma v}{a} \left\{ \sqrt{2} (k \cos \phi + m \sin \phi) \cos \theta + l \sin \theta \right\}, \quad (1)$$

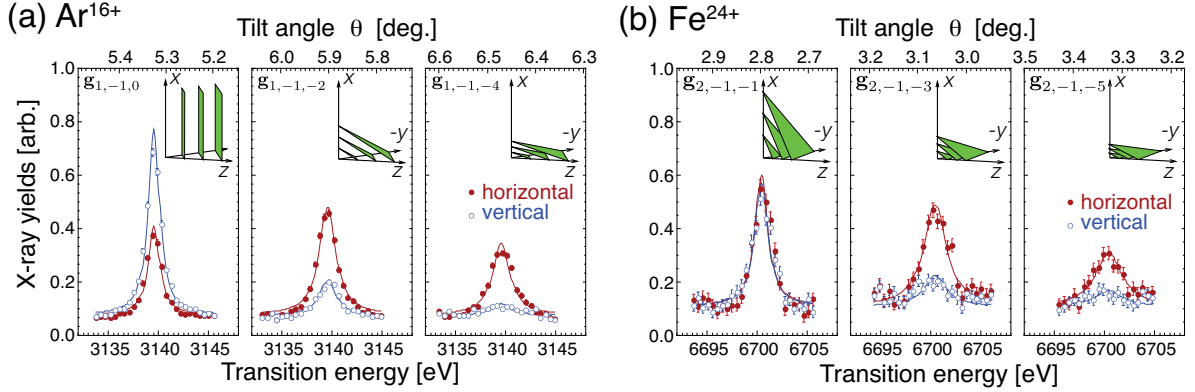


Figure 2: The K  $\alpha$  x-ray yields from (a) 416 MeV/u  $\text{Ar}^{16+}$  and (b) 423 MeV/u  $\text{Fe}^{24+}$  in the horizontal ( $\circ$ ) and vertical ( $\bullet$ ) directions.

where  $\theta$  and  $\phi$  are the incident angles of the beam with respect to the  $[\bar{1}10]$  axis of the crystal. The resonance condition is satisfied when  $h\mathbf{g}_{k,l,m} \cdot \mathbf{v}$  equals to the transition energy of the ions.

A typical experimental setup is shown in Fig. 1(b). The ion beams were accelerated by the Heavy Ion Medical Accelerator in Chiba (HIMAC) at National Institute of Radiological Sciences. The Si crystal was mounted on a high-resolution three-axis goniometer in order to scan the incident angles  $\theta$  and  $\phi$ . We observed the electron and x-ray emissions from the projectile ions as well as the final charge state distribution of the beam.

### 3. Anisotropic x-ray emission

The heliumlike  $\text{Ar}^{16+}$  and  $\text{Fe}^{24+}$  ions were excited from their ground state ( $1s^2$ ) to the  $1s2p$  state at excitation energies of 3139.55 and 6700.41 eV, respectively. We observed the de-excitation x-rays from the ions using the two Si(Li) x-ray detectors installed at  $41^\circ$  from the beam. This allows us to observe the x-rays emitted into  $\sim 90^\circ$  from the beam in the horizontal ( $y$ -) and vertical ( $x$ -) directions in the projectile frame. The RCE spectra were obtained by observing the x-ray yields as a function of the incident angle  $\theta$  around the resonance conditions for different crystallographic planes labelled by  $\mathbf{g}_{k,l,m}$ . The results are shown in Fig. 2(a) and (b) for  $\text{Ar}^{16+}$  and  $\text{Fe}^{24+}$ , respectively. The  $\mathbf{g}_{k,l,m}$  and corresponding directions of atomic planes used in the resonance were denoted in each figure.

Each spectra exhibited characteristic anisotropy reflecting the polarization direction of the oscillating field determined by  $\mathbf{g}_{k,l,m}$ . From the magnetic substate population of the  $1s2p$  state, which is calculated from the polarization direction as  $(2p_x : 2p_y : 2p_z) = (\gamma g_x :$



axis are also shown with the result of Monte Carlo simulation of the electron trajectories in the analyzer. The calculation indicated that more than 10% of the incident ions were excited to the  $2p^2(^1D)$  states by the resonant coherent excitation.

## 5. Summary

The x-ray and Auger electron emissions associated with the 3D-RCE of He-like  $\text{Ar}^{16+}$  and  $\text{Fe}^{24+}$  were observed. The anisotropy of the x-ray emission provided a clear evidence for the alignment of excited states by the linearly polarized oscillating field in the crystal. The double resonance technique enabled us to produce the selective doubly excited states followed by the Auger electron emission. We plan to investigate the angular distribution of the Auger electron emissions with respect to the polarization of the oscillating field, in which the effects of the Breit interaction may show up. In addition to these fundamental experiments at HIMAC, we started to apply this technique to the high-resolution spectroscopy of highly charged uranium ions [11].

This study was supported in part by Grants-in-Aid for Scientific Research (No. 19104010) from Japan Society for the Promotion of Science (JSPS). Y. Nakano acknowledges the support from JSPS (No. 22840050 and 23740311), and from the JSPS-NRF-NSFC A3 Foresight Program in the field of Plasma Physics (NSFC: No.11261140328). A.H. acknowledges support from the “Improvement of Research Environment for Young Researchers” program of MEXT. This experiment was one of the research projects with heavy ions at NIRS-HIMAC.

## References

- [1] V.V. Okorokov, JETP Lett. **2** (1965) 111.
- [2] S. Datz, C.D. Moak, O.H. Crawford, H.F. Krause, P.F. Dittner, J. Gomez del Campo, J.A. Biggerstaff, P.D. Miller, P. Hvelpumd and H. Knudsen, Phys. Rev. Lett. **40** (1978) 843.
- [3] S. Datz, C.D. Moak, O.H. Crawford, H.F. Krause, P.D. Miller, P.F. Dittner, J. Gomez del Campo, J.A. Biggerstaff, H. Knudsen and P. Hvelpumd, Nucl. Instr. and Meth. **170** (1980) 15.
- [4] K. Komaki, T. Azuma, T. Ito, Y. Takabayashi, Y. Yamazaki, M. Sano, M. Torikoshi, A. Kitagawa, E. Takada and T. Murakami, Nucl. Inst. and Meth. B **146** (1998) 19.

- [5] T. Azuma, T. Ito, K. Komaki, Y. Yamazaki, M. Sano, M. Torikoshi, A. Kitagawa, E. Takada and T. Murakami, Phys. Rev. Lett. **83** (1999) 528.
- [6] C. Kondo, S. Masugi, Y. Nakano, A. Hatakeyama, T. Azuma, K. Komaki, Y. Yamazaki, T. Murakami and E. Takada, Phys. Rev. Lett. **97** (2006) 135503.
- [7] Y. Nakano, C. Kondo, A. Hatakeyama, Y. Nakai, T. Azuma, K. Komaki, Y. Yamazaki, E. Takada and T. Murakami, Phys. Rev. Lett. **102** (2009) 085502.
- [8] Y. Ralchenko et al., NIST Atomic Spectra Database Ver. 3.0 (2006).
- [9] N. Andersen, J.W. Gallagher and I.V. Hertel, Phys. Rep. **165** (1988) 1.
- [10] Y. Nakano, S. Suda, A. Hatakeyama, Y. Nakai, K. Komaki, E. Takada, T. Murakami and T. Azuma, Phys. Rev. A **85** (2012) 020701(R).
- [11] Y. Nakano, Y. Takano, T. Shindo, T. Ikeda, Y. Kanai, S. Suda, T. Azuma, H. Bräuning, A. Bräuning-Demian, Th. Stöhlker, D. Dauvergne, Y. Yamazaki, Phys. Scr. **T144** (2011), 014010.

# Theoretical aspects of electron correlations and term dependences in the electronic states of highly charged ions

F. Koike, H. Funaba<sup>1</sup>, M. Goto<sup>1</sup>, D. Kato<sup>1</sup>, T. Kato<sup>1</sup>, S. Morita<sup>1</sup>, I. Murakami<sup>1</sup>, H. A. Sakaue<sup>1</sup>, S. Sudo<sup>1</sup>, C. Suzuki<sup>1</sup>, N. Tanuma<sup>1</sup>, A. Sasaki<sup>2</sup>, X. B. Ding<sup>3</sup>

*Phys. Lab., School of Medicine, Kitasato University 1-15-1 Kitasato 252-0374 Japan*

*1) National Institute for Fusion Science, 322-6 Oroshi-cho, Toki 509-5292, Japan*

*2) Japan Atomic Energy Agency, 8-1-7, Umemidai, Kizugawa, 619-0215, Japan*

*3) Northwest Normal University, Lanzhou 730070, China*

*e-mail: koikef@kitasato-u.ac.jp*

## Abstract

Highly charged atomic ions with large atomic numbers often have open sub-shell electronic structures in outermost shells. They give sometimes highly correlated many electron states, which are of interest in view of the theory of atomic structures as well as of observing characteristic photoemission spectra. EUV light emission spectra of heavy elements are investigated theoretically. By employing a multi-configuration Dirac-Fock method, Gd, and Nd atomic ions are investigated. M1 transitions between the ground state fine structure multiplets are studied for  $W^{26+}$  ions.

**Keywords:** EUV, MCDF, CI, electron correlation, Lanthanide ion, Tungsten ion

## 1 Introduction

The properties of electronic states of highly-charged many-electron atomic ions and their dynamical processes are of interest both from the theoretical point of view and aspects in the development of devices using plasmas containing heavy elements or in other applications. The knowledge of accurate data in heavy elements are indispensable for understanding the atomic processes in such plasmas. As illustrated in Fig.1, in heavy elements the relativistic effects become important for lower lying electronic shells and the effect of electron correlations may become serious in some open-shell ions. Electron correlations must be considered if we investigate the excited electronic states. The use of multi-configuration treatment with relativistic Hamiltonian is one of the most plausible choices for the calculation of such systems; it is crucial to properly take into account the effects of electron correlations on the basis of relativistic scheme of atomic structure descriptions.

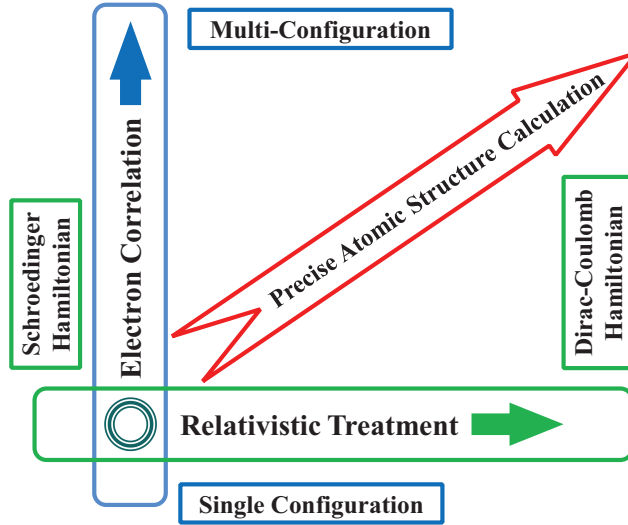


Figure 1: (color on line) Key effects to the accurate electronic states calculation of heavy ions. Relativistic effects become important in ions with large atomic numbers. Electron correlations may cause serious effects in many-electron open-shell ions.

Extreme UltraViolet (EUV) or eXtreme UltraViolet (XUV) light emission is one of the interests for studying the plasmas containing heavy elements. The photoemission spectra due to the transitions between the sub-shell levels in  $N$ -shell open atomic ions are sometimes suffering a strong influence from interactions between the electronic state configurations with different constituent orbitals. Spectral shift and narrowing in the unresolved transition array (UTA) were discussed by O’Sullivan and Faulkner [1], and this narrowing effect gives an advantageous situation to the development of practical EUV light sources. To gain shorter wavelength light emissions, we are suggesting the investigation of heavier elements. Recently, emission spectra at around 6 to 7 nm range from Gd and Nd atomic ions have been measured using Large Helical Device (LHD) at the National Institute for Fusion Science (NIFS), Japan [4]. A Gd or Nd pellet has been injected into the plasma with the highest central electron temperature of 2 to 3 keV, and the emission lines have been observed.

On the other hand, visible light emission is also observable from the ions with large atomic numbers. In open-shell atomic ions, we have multiplets in the ground state due to angular momentum term splittings within the same electronic orbital configuration; optical transitions among the multiplets are forbidden except by magnetic dipole (M1), electric quadrupole (E2), or higher multipole interactions. Term splitting energies come into the visible light region in heavy elements such as tungsten (W). Recently, Komatsu et

al [5] measured the spectra of W ( $Z = 74$ ) ions in EBIT plasmas. The light emissions are due to magnetic dipole (M1) transitions among the ground state multiplets of W highly charged ions. Ding and Koike et al [6] carried out ab-initio calculations for the M1 as well as electric quadrupole (E2) transitions in  $W^{26+}$  ground state multiplets on the basis of a multi-configuration Dirac-Fock (MCDF) method [8–11].

In the present paper, we firstly review the theoretical aspect of the electronic structures and dynamics of highly charged atomic ions with many electrons. We discuss the spectra of photoemissions due to the transitions between  $N$ -sub-shell levels in Gd and Nd highly charged ions. Finally, visible light emissions from W highly charged ions are discussed.

## 2 Structures and dynamics of heavy ions

Generally speaking, a highly-charged many-electron ion often has open sub-shells in its valence shells. Several electronic configurations with similar energies may have the same symmetry especially in the excited states. Interactions between those configurations may play a quite important role for spectral features of optical transition processes. To describe the point clearly, we try to consider the transitions of two interacting states 1 and 2 into the ground state  $g$  following the discussion by Bauche and Bauche et al [7]. Let us take wavefunctions  $\varphi_1$ ,  $\varphi_2$  for the states 1 and 2, respectively, and  $\varphi_g$  for the ground state. Then, we have two excited state hamiltonian matrix elements  $H_{11}$  and  $H_{22}$ , and their mutual interaction  $H_{12}$ , and the ground state hamiltonian matrix element  $H_{gg}$ . The amplitude of electric dipole transitions  $a_1$  and  $a_2$  for the states 1 and 2 may be given by

$$a_i = \langle \varphi_g \| D^{(1)} \| \varphi_i \rangle, \quad i = 1, 2, \quad (1)$$

where  $D^{(1)}$  is the electric dipole transition operator. Due to the configuration interaction  $H_{12}$ , the level energies  $H_{11}$  and  $H_{22}$  will be shifted to  $H'_{11}$  and  $H'_{22}$  as

$$H'_{ii} \cong H_{ii} + \frac{|H_{12}|^2}{H_{ii} - H_{jj}}, \quad i \neq j = 1, 2. \quad (2)$$

And the transition amplitudes  $a_1$  and  $a_2$  will be also modified to  $a'_1$  and  $a'_2$  as

$$a'_i \cong a_i + \frac{H_{12}}{H_{ii} - H_{jj}} a_j, \quad i \neq j = 1, 2. \quad (3)$$

The center of the gravity of transition energies  $\mu$  may be given by

$$\mu = \frac{|a_1|^2 H_{11} + |a_2|^2 H_{22}}{|a_1|^2 + |a_2|^2} + \frac{2a_1 a_2}{|a_1|^2 + |a_2|^2} H_{12}. \quad (4)$$

We can see from Eq.(2) that the energy shift due to the configuration may be quite large if the unperturbed energies  $H_{11}$  and  $H_{22}$  are close each other under the condition that the configuration interaction  $H_{12}$  is significantly large. From Eq.(3) we can derive a similar idea on the modification of transition amplitude.

We introduce the General purpose Relativistic Atomic Structure Program 92 (GRASP92) [8] and 2K (GRASP2K) [11] for the electronic structure of the atomic ions, and the Relativistic Atomic Transition and Ionization Properties (RATIP) code [9,10] for transition wavelengths and strengths. The advantage of these programs is that we can treat the two electron non-local exchange integrals as they are [2]. In this context, we can properly evaluate the electron correlations through configuration interactions including the excited orbitals in configuration state functions (CSF's) in a sophisticated way.

We carried out a series of MCDF calculation for Sr-like atomic ions of  $Z = 48$  to 56. The result of the orbital energy calculation stands for the argumentation made by O'Sullivan and Faulkner [1]. Also, we find that we may expect that the so called the effect of spectral narrowing and shift is quite common to the atomic species with  $Z = 48$  to 56.

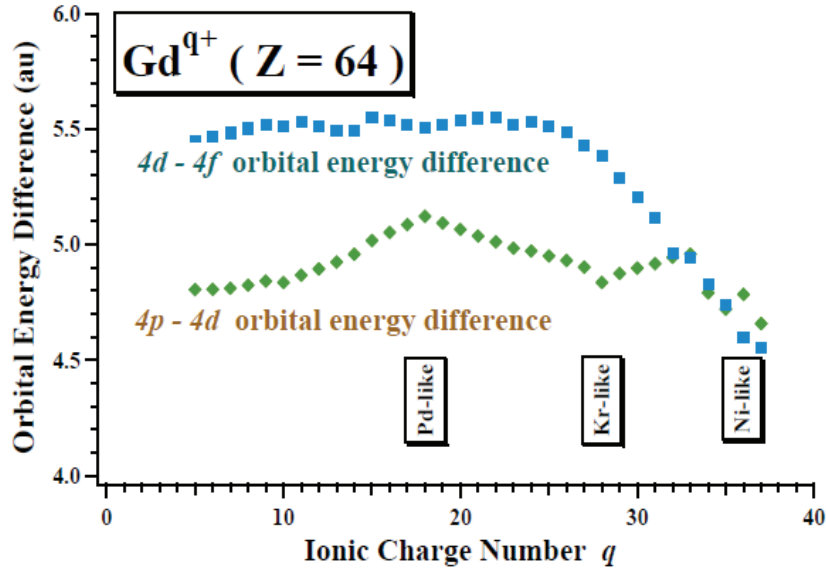


Figure 2: Ionic charge  $q$  dependence of the orbital energy difference in Gd  $N = 4$  atomic orbitals. The calculated range of the charge state is  $q = 5$  to  $q = 37$ .

Further on, there is an interesting feature in the charge state dependence of the orbital energy difference between  $N = 4$  atomic orbitals. Churilov and Kildiarova et al [3] pointed out, that the transition energies between the  $N = 4$  sub-shells decreases when we increase the charge state  $q$  at its highest range. We can verify this effect as of the decrease of the atomic orbital energy differences. In Fig.2, we show the  $q$  dependence of  $4d - 4f$ , and  $4p - 4d$  orbital energy differences in  $\text{Gd}^{q+}$  ions. We can see that the energy differences tend to decrease if  $q$  increases beyond Kr-like charge state. We can expect that the exchange interaction of inter-subshells such as  $4p$  to  $4d$  is smaller than that of intra-subshells such as  $4p$  to  $4p$ ; the sub-shell energy difference may decrease with the decrease of the number of lower lying sub-shell electrons. The atomic orbitals are so optimized as to reflect such exchange interactions.

### 3 Spectral features of Gd and Nd ions

The spectral narrowing of UTA [1] is advantageous for the practical EUV light sources. For shorter wavelength light sources, we should investigate the heavier elements. To gain insight to the role of the intra  $N$ -shell optical transitions, which are relevant for EUV emissions, we calculate the  $4p - 4d$  and  $4d - 4f$  transitions of Gd and Nd ions. The complex spectra from UTA are generated theoretically and compared to the experimental data. By using the GRASP92 package [8], we carry out a set of MCDF calculations for ions with charge states  $q+$  in  $\text{Gd}^{q+}$  with  $q = 15$  to  $37$  and in  $\text{Nd}^{q+}$  with  $q = 15$  to  $32$ , in which the  $N$ -shells are mostly partially filled in their ground states and this causes the complexity of the electronic structures. In MCDF calculations, we optimize the individual single electron atomic orbitals in atomic state functions (ASF's), which consist of the linear combination of configuration state functions (CSF's), numerically by means of the self-consistent field (SCF) iterative procedure. By using the minimal basis sets, we may obtain a physically plausible set of single electron atomic orbitals; we may discuss the physical property of the atomic ions in connection to the character of single electron atomic orbitals. In the present calculations, we included all the CSF's with one electron excitations to the sub-shell orbitals in the  $N$ -shell from the  $N$ -shell orbitals in the ground states. For instance, to calculate  $\text{Gd}^{30+} 1s^2 2s^2 2p^6 3s^2 3p^6 3d^{10} 4s^2 4p^4$ , we considered all the possible one electron excitations from  $4s^2 4p^4$  to  $4p$ ,  $4d$ , and  $4f$  orbitals. We considered the configurations  $4s^2 4p^3 4d$ ,  $4s^2 4p^3 4f$ ,  $4s 4p^5$ ,  $4s 4p^4 4d$ , and  $4s 4p^4 4f$ , and all the possible ASF's are optimized simultaneously, which gives us a set of atomic orbitals that are common throughout the ASF's. By using the RATIP package [9,10], we calculate wavelengths and the strengths of electric dipole (E1) transitions for all the possible combinations of the

ASF's that are obtained by the MCDF procedure. In the case of  $\text{Gd}^{30+}$  ions, for instance, we calculate the transitions to the ground states  $4s^24p^4 - 4s^24p^34d$ ,  $4s^24p^4 - 4s4p^5$ , and  $4s^24p^4 - 4s4p^44f$ , as well as between the excited states  $4s^24p^34d - 4s^24p^34f$ ,  $4s4p^5 - 4s4p^44d$ , and  $4s4p^44d - 4s4p^44f$ . Due to the term splittings both in the ground and the excited states, the spread of the weighted Einstein coefficient  $gA$ -factor distribution would be a couple of ten electron volt if the interference between the  $4p - 4d$  and  $4d - 4f$  transitions is absent.

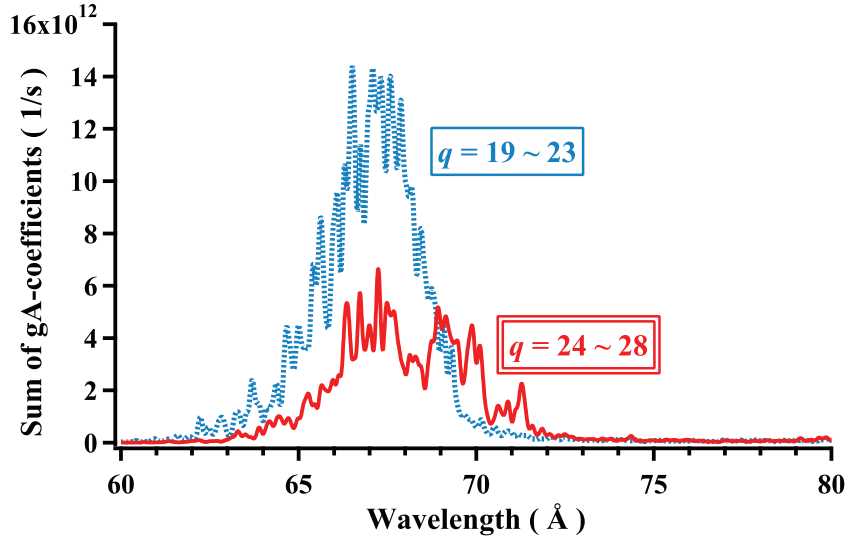


Figure 3: (color on line) Synthesized EUV photoemission spectra of  $\text{Gd}^{q+}$  ions. (Blue) broken line: the sum of  $gA$ -factors of  $\text{Gd}^{q+}$  with  $q = 19$  to  $23$ . (Red) solid line:  $q = 24$  to  $28$ .

In Fig.3, we illustrate the synthesized EUV photoemission spectra of  $\text{Gd}^{q+}$  ions. Theoretical  $gA$ -factors were summed over through selected ranges of the charge state  $q$ . The broken line gives the sum of  $gA$ -factors for transitions between the  $N$ -shell states with  $q = 19$  to  $23$ . The solid line gives the sum of  $gA$ -factors for transitions between the  $N$ -shell states with  $q = 24$  to  $28$ . The corresponding experimental spectra are seen in figure 4 of ref [4].

In Fig.4, we illustrate the synthesized EUV photoemission spectra of  $\text{Nd}^{q+}$  ions. Theoretical  $gA$ -factors were summed over through selected ranges of the charge state  $q$ . The dot dashed line gives the sum of  $gA$ -factors for transitions between the  $N$ -shell states with  $q = 15$  to  $19$ . The dotted line gives the sum of  $gA$ -factors for transitions between the  $N$ -shell states with  $q = 20$  to  $24$ . The solid line gives the sum of  $gA$ -factors for transitions between the  $N$ -shell states with  $q = 24$  to  $33$ . The corresponding experimental spectra

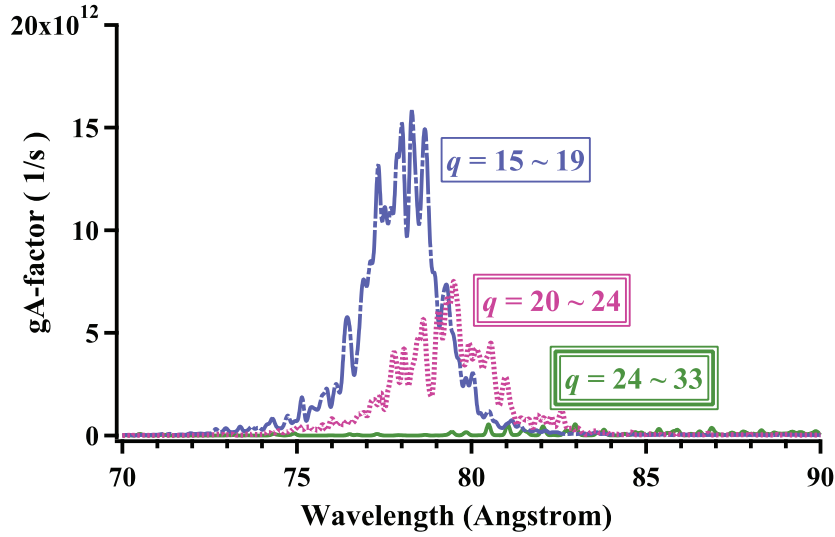


Figure 4: (color on line) Synthesized EUV photoemission spectra of  $\text{Nd}^{q+}$  ions. (Blue) dot dashed line: the sum of  $gA$ -factors of  $\text{Nd}^{q+}$  with  $q = 15$  to  $19$ . (Pink) dotted line:  $q = 20$  to  $24$ . (Green) solid line:  $q = 24$  to  $33$ .

are seen in figure 5 of ref [4].

## 4 M1 and E2 lines in $\text{W}^{26+}$ ground state multiplets

Visible light emission is observable from the ions with large atomic numbers. Recently, Komatsu et al [5] measured the spectra of W ( $Z = 74$ ) ions in EBIT plasmas. The light emissions are due to magnetic dipole (M1) transitions among the ground state multiplets of W highly charged ions. Ding and Koike et al [6] carried out ab-initio calculations for the M1 as well as electric quadrupole (E2) transitions in  $\text{W}^{26+}$  ground state multiplets using GRASP2K [11]. They obtained 388.43 nm for  ${}^3H_4 - {}^4H_5$  M1 transition [6], which is in good agreement with experimental date 389.41 nm [5].

## 5 Conclusion

The accurate theoretical data of the atomic structures and dynamics that include the relativistic effects and the electron correlation effects provide us with a good base for precision analysis of highly charged atomic ions in plasmas. In the present paper, we have

investigated intra  $N$ -shell correlations for open  $N$ -shell Gd and Nd atomic ions. From the view point of atomic multi-configuration Dirac-Fock calculations, which can provide us with plausible shapes for the single electron orbitals by the procedure of non-linear numerical orbital SCF optimization, these effects are due to the coincident agreement of the orbital energy differences in  $N$ -shell. This itself is the outcome of electron correlations, and an MCDF procedure can account for them in the single electron orbitals.

The M1 and E2 transitions between the fine structure multiplets of W ground states have been discussed briefly.

### Acknowledgement

This work was partly supported by the JSPS-NRF-NSFC A3 Foresight Program in the field of Plasma Physics. This work was partly supported by a Grant-in Aid from Japan Society for the Promotion of Science (23246165, 23340185). This work was carried out with the support and under the auspices of the NIFS-collaboration research program (NIFS10KLPF011).

### References

- [1] G. O’Sullivan and R. Faulkner, *Opt. Eng.* **33**, 3978 (1994).
- [2] F. Koike and S. Fritzsche, *J. Phys. Conf. Ser.*, **58** 157 (2007).
- [3] S. S. Churilov, R. R. Kildiarova, et al, *Phys. Scr.*, **80**, 045303 (2009).
- [4] C. Suzuki, F. Koike, et al, *J. Phys. B: At. Mol. Opt. Phys.*, **45**, 135002 (2012).
- [5] A. Komatsu, J. Sakoda, et al, *Phys. Scr.*, **T144**, 014012 (2011).
- [6] X. B. Ding, F. Koike, et al, *J. Phys. B: At. Mol. Opt. Phys.*, **44**, 145004 (2011).
- [7] J. Bauche, C. Bauche, et al, *J. Phys. B: At. Mol. Opt. Phys.* **20** 1443 – 1450 (1987).
- [8] F. A. Parpia, C. F. Fischer, and I. P. Grant, *Compt. Phys. Commun.*, **94**, 249 (1996).
- [9] S. Fritzsche, *J. Elec. Spec. Rel. Phenom.* , **114 –116**, 1155 (2001).
- [10] S. Fritzsche, *Comput. Phys. Commun.* **183**, 1525 (2012).
- [11] P. Joensson, X. He, et al, *Comput. Phys. Commun.* **177**, 597 (2007).

# Absolute $K\alpha$ line spectroscopy for cone-guided fast-ignition targets

NISHIMURA Hiroaki, ZHANG Zhe, NAMIMOTO Takuya, FUJIOKA Shinsuke, KOGA Mayuko, SHIRAGA Hiroyuki, OZAKI Tohru<sup>1</sup>, NISHIKINO Masaharu<sup>2</sup>, KAWACHI Tetsuya<sup>2</sup>, PIROZHKOV Alex. S.<sup>2</sup>, KONDO Kiminori<sup>2</sup>, OKANO Yasuaki<sup>3</sup>, FG-02 Experimental Campaign Team, and AZECHI Hiroshi

*Institute of Laser Engineering, Osaka U., Suita, Osaka, 565-0871 Japan*

*1) Institute for Fusion Science, Toki, Gifu 509-5292 Japan*

*2) Kansai Photon Science Institute, JAEA, Kyoto, 619-0215 Japan*

*3) Institute for Molecular Science, Okazaki, Aichi 444-8585 Japan*

*e-mail: nishimu@ile.osaka-u.ac.jp*

## Abstract

Absolute  $K\alpha$  line spectroscopy is proposed to study laser-plasma interactions taking place in the cone-guided fast ignition targets. A transmission-type spectrometer was developed, and its absolute sensitivity was measured with laser-generated x-rays and radioisotopes, showing good agreement with theoretical predictions. The absolute yield of Au  $K\alpha$  line was measured in the fast ignition experimental campaign performed at ILE Osaka U.. Assuming a single Maxwellian electron spectrum and one-way travel of hot electrons through the cone, energy transfer efficiency of incident LFEX laser to hot electrons was derived.

**Keywords:**  $K\alpha$  line spectroscopy, atomic transition, fast ignition

## 1. Introduction

Fast ignition is recognized as a promising pathway to efficient thermonuclear fusion in laser-driven inertial confinement fusion. A cone-guided CD-shell has been used as a base-line target for the fast ignition experiment. It has long been expected to provide more quantitative information about the hot electron generation and transport in the cone than those derived only with x-ray imaging and neutron detection. Hot electron spectra observed with an electron spectrometer suffer from substantial modification: Although the major fraction of hot electron energy is carried by the component around 1-2 MeV, corresponding spectral information is missing due to the self-generated plasma potential. To solve this problem, Bremsstrahlung x-ray spectra, as a consequence of hot electron propagation in dense plasma, are measured [1]. In addition to this, we propose an absolute  $K\alpha$  line spectroscopy dedicated for quantitative measurement of hot electron generation and transport in the high-Z target. This method has advantage over the Bremsstrahlung measurement since it provides local information about the hot electrons propagating through specific materials composing the cone-guided

target. Combination of the  $K\alpha$  and Bremsstrahlung spectroscopy will improve diagnostic accuracy of hot electron energy distribution function in the cone. In this study, Au was chosen as a tracer since it is one of representative highest-Z materials available for the guide cone, thus better matching with MeV-hot electrons than lower-Z tracers such as Cu.

## 2. High energy $K\alpha$ line spectrometer

A Laue spectrometer was developed to cover high energy range from Mo ( $K\alpha_1$ :17.48 keV,  $K\alpha_2$ :17.37 keV) to Au ( $K\alpha_1$ :68.80 keV,  $K\alpha_2$ :66.99 keV)  $K\alpha$  lines. As shown in Fig.1 the spectrometer consists of a cylindrically curved Quartz (10-11) plate of 0.2 mm in thickness, 14 mm in height and 30 mm in width (direction corresponding to spectral dispersion). The detector can either be an imaging plate (IP) from Fujifilm [2] or a charge coupled device (CCD: Andor Model DH420-FO, 6.7 mm in height and 25 mm in width) with a fiber-optic plate coated with a CsI phosphor of 100  $\mu\text{m}$  in thickness. The Quartz plate is bent with a radius of 170 mm in such that the diffracted x-rays are focused once at the intermediate slit. X-ray components propagating in a straightforward manner are prohibited irradiating the detector directly with a lead pinhole plate located in front of the crystal and a pair of lead shields located at the intermediate x-ray focus. To avoid influence of hard x-rays from plasma on output signal, whole body of the spectrometer and the detector are covered with lead shields. This Cauchois geometry effectively discriminates 0<sup>th</sup>-order component, stray x-rays and fluorescence from spectrometer components such as filters [3, 4]. By varying the distances from the crystal to the source and detector, this spectrometer can cover the energy range of either 10-60 keV (Type-I set) or 30-100 keV (Type-II set) (see Fig. 1 for details).

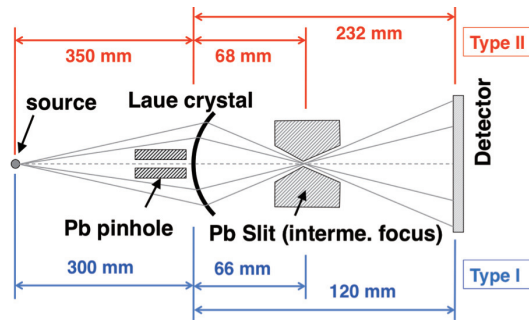


Figure 1 Schematic of the Laue spectrometer system and the distances for Type-I and Type-II setups.

Absolute sensitivity of the Laue spectrometer was defined as follows. First, the overall sensitivity was calibrated using laser-produced-plasma (LPP)  $K\alpha$  lines and radioisotopes (RIs). For RIs, IP was used in place of the CsI/CCD because of the

low-yield-rate of x-rays. Cross-calibration between the IPs and the CsI/CCD was performed at discrete energies. Second, to fully span the energy range, the spectral responses of the individual components of the spectrometer were theoretically calculated and compared to the experimental calibration data [5].

Absolute sensitivity for the Type-I set was measured [6] at J-KAREN laser system at Japan Atomic Energy Agency, Kansai Photon Science Institute [7]. This system delivers a laser pulse of 800 nm in wavelength, 1.8 J in energy and 58 fs in duration. The pulse contrast ratio was typically  $10^{-11}$ . An f/2.67 gold-coated off-axis parabolic mirror was used to focus a *p*-polarized laser beam at an incident angle of 22.5 deg. relative to the target normal. 100- $\mu$ m-thick Mo and Ag planar targets were mounted on a motorized translation stage. The laser focal spot size was varied with translating the target along the laser beam to change laser irradiance. The absolute yield of  $K\alpha$  x-rays was measured with a back-illuminated x-ray CCD operated in a single-photon counting mode. The spectral sensitivity of the CCD was absolutely calibrated in separate by using radioisotopes.

The calibration for the Type-II was taken out with radioisotopes. The line emission at 59 keV from  $^{241}\text{Am}$  (370 kBq), and 77 keV from  $^{226}\text{Ra}$  (3.7 MBq) were used in this calibration. The calibration with  $^{226}\text{Ra}$  was taken out at the OCTAVIAN facility at Osaka University. Due to a long exposure time, IP of Type BAS-TR2025 from Fujifilm was applied [8]. The typical exposure time was 20 to 140 hours. Due to the self-fading effect of IP, the spectral intensities recorded on IP are not in proportion to the exposure time. The absolute sensitivity and fading rate were calibrated in a time range from 5 min to 200 hrs by using the Fuji BAS 1800 IP scanner. The calibration was done at 59 keV by using  $^{241}\text{Am}$ ; for other photon energy, the data in Ref. [9] is considered. In order to compare the data recorded with CsI/CCD in the experiment, a cross calibration between IP and CsI/CCD has also been made.

### 3. Comparison of sensitivity with model predictions

Spectral sensitivity for the Au  $K\alpha$  line was obtained by comparing model prediction with the measurement. Diffraction efficiency for the Quartz crystal was derived with XOP code assuming the Takagi-Taupin model [10], and the spectral sensitivity for the CsI phosphor screen was referred from Ref. [11]. Figure 2 shows the comparison result. The solid line represents the product of calculated diffraction efficiency and spectral sensitivity of CsI. Absolute sensitivities calibrated with laser produced  $K\alpha$  lines and that for a radioisotope are respectively shown with triangles and a circle.

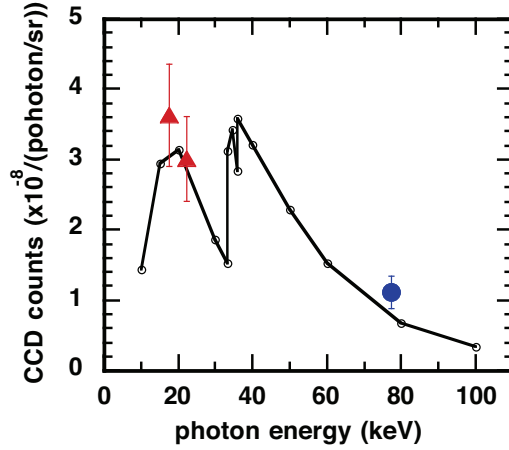


Figure 2 Overall sensitivity of Laue spectrometer system with CsI/CCD detector. The solid line represents a product of spectral sensitivities for the crystal and CsI/CCD. Experimental data points are also plotted for comparison.

#### 4. $K\alpha$ line measurement for Au-cone-guided targets

The absolute yield of Au  $K\alpha$  line was measured in the fast ignition experimental campaign by using Gekko XII and LFEX lasers [12] at ILE, Osaka U.. The target was an Au-cone CD shell. The thickness of the sidewall of the cone was 10  $\mu\text{m}$  and that of the tip was 6  $\mu\text{m}$ . CD shell was typically 500  $\mu\text{m}$  in diameter and 7  $\mu\text{m}$  in thickness. The shell was driven with nine green-laser-pulses from GXII of 1.2 ns in duration and 2 kJ in total energy on target. LFEX laser irradiated the inner wall of the cone tip at the maximum compression of the shell. Energy and duration of the LFEX pulse were respectively 500 $\pm$ 100 J and 1.5 ps, yielding intensity of  $1.2 \times 10^{19}$  W/cm<sup>2</sup> at the cone tip. The density of the core is estimated to be around 10 g/cm<sup>3</sup> and density-radius product is around 0.02 g/cm<sup>2</sup>.

Assuming a single Maxwellian electron velocity distribution and one-way travel of hot electrons through the cone, energy transfer efficiency (TE) of incident LFEX laser to hot electrons was derived according to Salzmann's model [13]. Figure 3 shows the TE given as a function of hot electron temperatures. A typical Au  $K\alpha$  line spectrum observed with the LAUE spectrometer is inset there. Intense continuum line overlapping with the  $K\alpha$  line is due to Bremsstrahlung from the core plasma passing through hot electrons. Two plausible temperatures for the experimental conditions are shown for comparison. One is predicted by Beg's empirical law of  $T_h(\text{keV})=215(I_{18}\lambda_L^2)^{1/3}$  [14], and the other is by Ponderomotive force law of  $T_h(\text{keV})=512((1+0.73I_{18}\lambda_L^2)^{1/2}-1)$  [15]. Here  $I_{18}$  is the normalized laser intensity in units of  $10^{18}$  W/cm<sup>2</sup> and  $\lambda_L$  is the normalized laser wavelength in micron-meter. It is inferred that TE for the present conditions is around 30-50%.

This value can be compared to the case of  $T_h$  measured with an electron spectrometer set along the symmetrical axis of the cone in the forward direction of LFEX laser incidence.  $T_h$  predicted from the slope temperature at 10 MeV electron kinetic energy was 4.1 MeV, resulting in TE over 100 %. Therefore we will attempt to measure the temperature of hot electrons directly at the interaction region by observing Bremsstrahlung continuum.

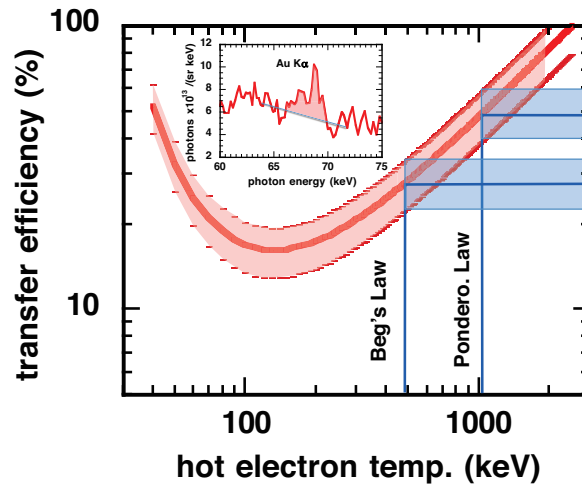


Figure 3 Energy transfer efficiency (TE) from LFEX laser to hot electrons is given as a function of hot electron temperature.

## 5. Summary

$K\alpha$  line spectroscopy, particularly for hard-x-ray region, has been proposed for quantitative measurement of cone-guided fast ignition targets. The Au  $K\alpha$  line from the Au-cone guided target was observed and energy transfer efficiency was provided as a preliminary study. In near future, absolute measurement of hard x-ray continuum will be made together with that of the  $K\alpha$  line to improve accuracy of energy transfer measurements in the cone-guided fast ignition targets. Furthermore, detailed analysis with a hybrid modeling, namely combination of particle-in-cell (PIC) code and hydrodynamic code, will be made for  $K\alpha$  yield to improve understanding of hot electron generation, transport and deposition in the cone-guided target.

## Acknowledgment:

This work was partly supported by the JSPS-NRF-NSFC A3 Foresight Program in the field of Plasma Physics (NSFC: No.11261140328).

## References

- [1] C. D. Chen, P. K. Patel, D. S. Hey, et al., Phys. Plasma **16**, 082705 (2009).

- [2] J. Miyahara, K. Takahashi, et al., Nucl. Instrum. Methods **246**, 572 (1986).
- [3] Y. Cauchois, J. de Physique. **3** 320 (1932).
- [4] J. F. Seely, G. E. Holland, et al., High Energy Density Physics **3**, 263 (2007).
- [5] Z. Zhang, H. Nishimura, et al., Rev. Sci. Instrum. **83**, 053502 (2012).
- [6] Z. Zhang, M. Nishikino, H. Nishimura, et al., Optics Express **19**, 4560 (2011).
- [7] H. Kiriya, M. Mori, Y. Nakai, et al., Opt. Lett. **35**, 1497 (2010).
- [8] J. Miyahara, et al., Nuclear Instrum. Meth. in Phys. Res. Sec. A **246**, 572 (1986).
- [9] A. L. Meadowcroft, C. D. Bentley, et al., Rev. Sci. Instrum., **79**, 113102 (2008).
- [10] XOP code: <http://www.esrf.eu/computing/scientific/xop2.1/>
- [11] A. W. Mengesha, T. D. Taulbee, et al., IEEE Trans. Nuclear Sci. **45**, 456 (1998).
- [12] J. Kawanaka, et al., Journal of Physics: Conference Series **112**, 032006 (2008)
- [13] D. Salzmann, Ch. Reich, I. Uschmann, et al., Phys. Rev. E **65**, 036402 (2002).
- [14] F. N. Beg, A. R. Bell, A. E. Dangor, et al., Physics of Plasmas **4**, 447 (1997).
- [15] S. C. Wilks and W. L. Kruer, IEEE J. Quantum Electronics **33**, 1954 (1997).

# Potential of cold $K\alpha$ radiation generated by an intense ion beam for cold dense plasma diagnostics

KAWAMURA Tohru<sup>†</sup>, HORIOKA Kazuhiko, and KOIKE Fumihiko<sup>a</sup>

*Department of Energy Sciences, Tokyo Institute of Technology, Nagatsuta-cho 4259,  
Midori-ku, Yokohama, Kanagawa, 226-8502 Japan*

*a) Physics Laboratory, School of Medicine, Kitasato University, Kitasato 1-15-1,  
Sagamihara, Kanagawa, 228-8555 Japan*

<sup>†</sup> *e-mail: kawamura@es.titech.ac.jp*

## Abstract

Examined is  $K\alpha$  radiation from low charge chlorine of  $C_2H_3Cl$ -plasma heated by an ion beam for cold dense plasma diagnostics. With relativistic atomic structure calculations, the transition energies of  $K\alpha$  lines are shown to be slightly shifted to a higher-energy side according to the degree of M-shell ionization. Total spectral shift from  $Cl^+$   $K\alpha$  lines up to those with a fully stripped M-shell is found to be about 10 eV. The calculation results with a collisional-radiative-equilibrium condition show clear spectral deformation in the range of the electron temperatures of  $\leq \sim 30$  eV.  $Cl$ - $K\alpha$  lines from atomic states with M-shell electrons can be expected to give us distinct understandings for energy deposition by an ion beam in cold dense plasma.

**Keywords:** heavy ion fusion, energy deposition, cold  $K\alpha$ , spectrum diagnostics

## 1. Introduction

In heavy ion inertial fusion research, energy deposition by incident ion beams is one of critical issues, and many experimental and/or theoretical studies have been intensively done [1, 2]. In the related experiments, Time-Of-Flight (TOF) is one of the most powerful diagnostics in the framework of particle diagnostics [3, 4]. In the category of X-ray diagnostics, which is also one of promising tools for the above purpose, Goel *et al.* [5] demonstrated some numerical calculations of  $K\alpha$  spectra from low- $Z$  target material heated by a proton beam. In their study, because of cold plasma creation and a very small number of M-shell electrons of target material,  $K\alpha$  spectra from atomic states with M-shell electrons do not seem to have enough spectral shift to diagnose plasma temperature, and  $K\alpha$  spectra from those with a partially ionized L-shell are found to be effective. Rzadkiewicz *et al.* [6] experimentally showed direct observation of Si- $K\alpha$  lines from atomic states with L-shell vacancies and chemical bonding with neighbor oxygen. Their study may lead us fruitful understandings for energy deposition by an ion beam, and have a potential to open a new field of cold and/or warm dense matter physics.

In the study of Ref.[7], Cl-K $\alpha$  spectra from polyvinyl-chloride (C<sub>2</sub>H<sub>3</sub>Cl), which is often used in laser-produced-plasma (LPP) experiments and chlorine is doped as a tracer, heated by a He<sup>2+</sup>-beam were examined for dense plasma diagnostic, and a threshold temperature ( $\sim 85$  eV) was found. The created plasma-temperature must be lower than the threshold to trace energy deposition by an incident ion beam. The K $\alpha$  lines from atomic states with a partially ionized L-shell are well-separated spectra with respect to the charge state. However, they are essentially applicable to hot plasma with an electron temperature of near 100 eV for chlorine [8]. With dense plasma creation by an ion beam, K-shell ionization and dielectronic-capture are competed due to a small number density of an incident ion beam. Since the K-shell ionization by an ion beam governs the kinetics of the K $\alpha$  radiation below the threshold, there are some aspects that the K $\alpha$  radiation with a high charge state is not effective for cold plasma diagnostics. In such a case, K $\alpha$  radiation with a lower charge state is preferred. Recently, the demonstration of K $\alpha$  lines from low charge chlorine with M-shell electrons, which are Cl<sup>+</sup>  $\sim$  Cl<sup>7+</sup> and called 'cold-K $\alpha$ ' hereafter, is examined for cold plasma diagnostics [9]. Ionization between lower charge states results in small spectral shift of line radiation. Since K $\alpha$  radiation is due to an atomic transition between L and K-shells, the resultant spectral shift by M-shell ionization is much smaller than that by L-shell ionization. Compared with the study done by Goel *et al.* [5], chlorine has a moderate number of bound electrons in the M-shell to see a small spectral shift, and is expected to be a good candidate for cold dense plasma diagnostics.

In this paper, our past study up to now on K $\alpha$  lines from low charge chlorine with M-shell electrons is surveyed and the latest progress on the study will be also briefly presented.

## 2. Descriptions on Modeling of Atomic Processes

The model of population kinetics considered in this study is presented in Fig.1. The K-shell vacant states are mainly created through inner-shell ionization by ion impacts rather than dielectronic-capture in cold plasma. All the non-radiative processes, namely, KLL-, KLM- and KMM-Auger transitions are included in the model. In solid density plasma heated by an ion beam, the population of K-shell vacant states is very small, and the average charge state of total Cl ions  $Z_{\text{total}} \approx Z_{\text{bulk}} \approx Z_{\text{K-shell vacant}} - 1$ , where  $Z_{\text{bulk}}$  and  $Z_{\text{K-shell vacant}}$  stand for the average charge state of bulk and K-shell vacant states, respectively. Here, it should be noted that Fig.6 in Ref.[7] gives an intensity ratio between cold-K $\alpha$  radiation and high charge one, and the ratio can be an effective index to deduce an electron temperature  $T_e$  in the range of  $50 \text{ eV} \leq T_e \leq 100 \text{ eV}$ , in which the ratios give almost  $0.1 \sim 10$ . For  $T_e \leq 50 \text{ eV}$ , it is suggested that only K $\alpha$  lines from

atomic states with M-shell electrons are applicable.

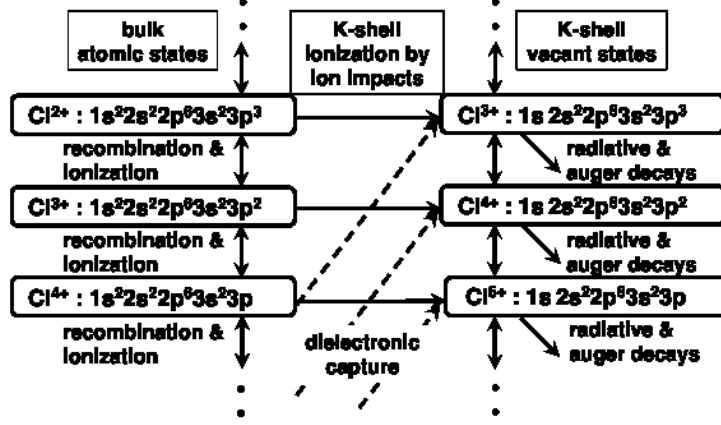


Figure 1: Population kinetics associated with low charge  $K\alpha$  lines.

### 3. Spectral Deformation of $K\alpha$ lines from Atomic States with M-shell Electrons

Emission energies and oscillator strengths of Cl- $K\alpha$  lines are calculated with the use of GRASP92 and RATIP codes, which are based on a multi-configuration Dirac-Fock (MCDF) method [10, 11, 12]. Calculated Cl- $K\alpha$  lines are associated with the charge states of  $Cl^+ \sim Cl^{8+}$ , and they come from ground states with a vacant K-shell, namely  $Cl^+ : 1s2s^22p^63s^23p^5 \rightarrow 1s^22s^22p^53s^23p^5 + h\nu$ ,  $Cl^{2+} : 1s2s^22p^63s^23p^4 \rightarrow 1s^22s^22p^53s^23p^4 + h\nu$ ,  $\dots$ ,  $Cl^{8+} : 1s2s^22p^6 \rightarrow 1s^22s^22p^5 + h\nu$ . The resultant  $K\alpha_1$  and  $K\alpha_2$  are calculated within the accuracy of  $\sim 0.5$  eV compared with one of available data [13].

The typical deformation of a spectral line-shape on the electron temperature is given in Fig.2. Calculated spectra are convolved by Stark broadening with quasi-static electric-microfield, electron impact broadening using a semiclassical expression, natural and Doppler broadenings [14]. In the Doppler broadening calculation, the ion temperature is assumed to be equal to the electron temperature. It is also assumed that the plasma ion density is solid density ( $\approx 8.1 \times 10^{22} \text{ cm}^{-3}$ ), the incident beam is a  $C^{6+}$ -beam, of which current density and mean energy respectively are  $3 \text{ kA/cm}^2$  and  $30 \text{ MeV}$  with the energy spread described by Maxwellian of 10% of the mean energy.

At  $T_e = 5 \text{ eV}$ , the spectrum consists of mainly two  $K\alpha$  components of  $Cl^+$  and  $Cl^{2+}$ . The K-shell vacant states of  $Cl^+ \sim Cl^{3+}$  contribute to the spectrum at  $T_e = 10 \text{ eV}$ . With increase in  $T_e$ , the charge states of the main components are  $Cl^{2+} \sim Cl^{4+}$  in  $T_e = 15 \sim 20 \text{ eV}$ , and the  $K\alpha$  lines from  $Cl^{5+} \sim Cl^{7+}$  have a large contribution in  $T_e \geq 25 \text{ eV}$ . Finally,

the total blue-shift of the  $K\alpha$  lines in  $T_e = 5 \sim 30$  eV is  $\sim 10$  eV and the clear spectral deformation can be observed.

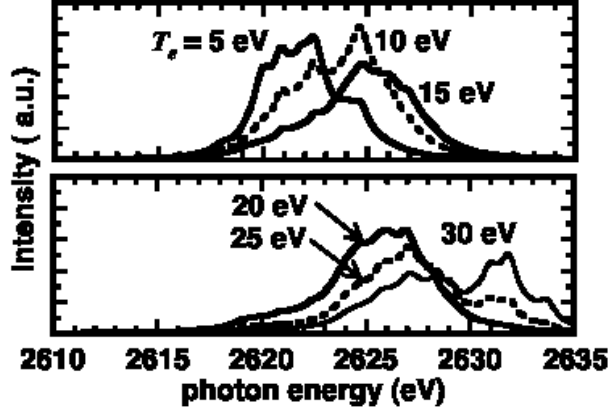


Figure 2: Deformation of a spectral line-shape and blue-shift of cold Cl- $K\alpha$  radiation from a polyvinyl-chloride ( $C_2H_3Cl$ ) plasma. The vertical scale of the spectrum at  $T_e = 5$  eV is scaled down to make a comprehensive comparison with others. The actual vertical scale at  $T_e = 5$  eV must be multiplied by  $\sim 2.86$ . The spectral peak at  $T_e = 5$  eV is the highest.

According to the study done by Kauffman *et al.* [15], the contribution of the multiple ionization  $KL^n$  (here,  $n$  stands for a number of L-shell vacancies.) of neon was discussed. In their study, because of low density plasma free-electron, colliding particles almost come from an incident ion beam. Then, the outer-shell ionization is governed by the multiple ionization  $KL^n$ . On the other hand, in our study, even if the multiple ionization associated with M-shell  $KM^n$  is occurred to chlorine by an incident ion beam, because of high density plasma free-electrons up to  $\sim 10^{23} \text{ cm}^{-3}$ , the degree of M-shell ionization is determined by the surrounding plasma free-electrons. The particle density of an incident ion beam is at most  $10^{13\sim 14} \text{ cm}^{-3}$  and the difference of the colliding particle densities between free-electrons and incident ions is up to 9  $\sim$  10 digits. The contribution of the multiple ionization  $KM^n$  can be neglected. Currently, since there may be some aspects that the multiple ionization plays an important role to determine the degree of ionization, such a atomic process will be studied by numerical simulation in near future.

#### 4. Effects of Satellite Lines and Opacity of Cold- $K\alpha$ Radiation

Concerning satellite lines, atomic states with an excited electron in the outer-shell ( $Cl^{n+} : 1s2s^22p^63s^23p^{(5-n)}nl$ , and  $nl$  stands for a quantum number of the outermost bound-electron.) may have a contribution to the composite spectra. Actually,  $K\alpha$  lines

from the excited states  $1s2s^22p^63s^23p^{(5-n)}3d$  strongly overlap with those from  $\text{Cl}^{n+} : 1s2s^22p^63s^23p^{(6-n)}$  and  $\text{Cl}^{n+1} : 1s2s^22p^63s^23p^{(5-n)}$ . However, due to a large continuum lowering at solid density, an ionization energy of a bound electron is reduced and population of atomic states with a shallow ionization potential is estimated to be small. In Ref.[9], the dependence of continuum lowering on electron temperature is given, resulting in negligible contribution of the atomic states.

To utilize the cold- $K\alpha$  radiation for cold dense plasma diagnostics, opacity effect is also one of critical properties. In one of our past studies [14], highly charged major Cl- $K\alpha$  lines from hot dense plasma are saturated at the plasma thickness of a few microns, and those minor ones at a few tens microns. This is because the final atomic states associated with the  $K\alpha$  lines belong to bulk states. However, the final atomic states of the  $K\alpha$  lines from atomic states with M-shell electrons discussed here are  $\text{Cl}^{n+} : 1s^22s^22p^53l^{(8-n)}$  ( $1 \leq n \leq 6$ ). The binding energies of the L-shell electrons are about 200 ~ 300 eV in accordance with M-shell ionization, and the temperature of bulk-electrons in this study is too low to ionize the electrons. Therefore, those states have a small contribution to determine overall population kinetics, resulting in small opacity. The quantitative study is being done now. In order to estimate the opacity of the cold- $K\alpha$  radiation, an additional Auger transition must be considered. The final states associated with the cold- $K\alpha$  are L-shell vacant states, and K-shell vacant states can be created through the dielectronic-capture from the L-shell vacant states. It means that LMM-Auger transition in succession to other Auger transitions associated with K-shell (double-autoionization) may have a contribution to determine the kinetics of the cold- $K\alpha$  radiation.

## 5. Conclusions

In this paper, our recent studies on the plasma diagnostics with cold- $K\alpha$  radiation is surveyed. To utilize the radiation, clear blue-shift of cold- $K\alpha$  lines must be examined with accurate numerical simulation. In the calculation, the line-shift gives about 10 eV in accordance with M-shell ionization for chlorine, and the clear deformation of spectral shape is also seen in the electron temperatures of  $\leq 30$  eV. The recent progress on this study is also briefly presented, and cold- $K\alpha$  radiation is shown to be one of promising tools for cold dense plasma diagnostics.

## Acknowledgment

This work was partly supported by the JSPS-NRF-NSFC A3 Foresight Program in the

field of Plasma Physics (NSFC: No.11261140328).

## References

- [1] D. H. H. Hoffmann, K. Weyrich, H. Wahl, D. Gardés, R. Bimbot, and C. Fleurier, *Phys. Rev. A* **42**, 2313-2321 (1990).
- [2] T. Peter, and J. Meyer-ter-Vehn, *Phys. Rev. A* **43**, 1998-2014 (1991), *ibid.* **43**, 2015-2030 (1991).
- [3] M. Ogawa, U. Neuner, H. Kobayashi, Y. Nakajima, K. Nishigori, K. Takayama, O. Iwase, M. Yoshida, M. Kojima, J. Hasegawa, Y. Oguri, K. Horioka, M. Nakajima, S. Miyamoto, V. Dubenkov, and T. Murakami, *Laser Part. Beams* **18**, 647-653 (2000).
- [4] J. Hasegawa, N. Yokota, Y. Kobayashi, M. Yoshida, M. Kojima, T. Sasaki, H. Fukuda, M. Ogawa, Y. Oguri, and T. Murakami, *Laser Part. Beams*, **21**, 7-11 (2003).
- [5] B. Goel, N. K. Gupta, W. Höbel, H. Marten, J. J. Macfarlane, and P. Wang, *Nucl. Instr. and Meth. Phys. Res. A* **415**, 576-580 (1998).
- [6] J. Rządziejewicz, A. Gojska, O. Rosmej, M. Polasik, and K. Słabkowska, *Phys. Rev. A* **82**, 012703-1~14 (2010).
- [7] T. Kawamura, K. Horioka, and F. Koike, *Laser Part. Beams* **24**, 261-267 (2006).
- [8] T. Kawamura, H. Nishimura, F. Koike, Y. Ochi, R. Matsui, W. Y. Miao, S. Okihara, S. Sakabe, I. Uschmann, E. Förster, and K. Mima, *Phys. Rev. E* **66**, 016402-1~8 (2002).
- [9] T. Kawamura, K. Horioka, and F. Koike, *Laser Part. Beams* **29**, 135-140 (2011).
- [10] F. A. Parpia, C. Froese Fischer, and I. P. Grant, *Comput. Phys. Commun.* **94**, 249-271 (1996).
- [11] S. Fritzsche, *J. Electr. Spec. Rel. Phenom.* **114-116**, 1155-1164 (2001).
- [12] S. Fritzsche, *Phys. Scr.* **T100**, 37-46 (2002).
- [13] National Astronomical Observatory (2006). Rika Nenpyo (Chronological Scientific Tables 2006), pp.432. Maruzen Co., Ltd., 2005.
- [14] T. Kawamura, T. Schlegel, H. Nishimura, F. Koike, Y. Ochi, R. Matsui, S. Okihara, S. Sakabe, T. Johzaki, H. Nagatomo, K. Mima, I. Uschmann, E. Förster, and D. H. H. Hoffmann, *J. Quant. Spectrosc. Radiat. Transfer* **81**, 237-246 (2003) and references therein.
- [15] R. L. Kauffman, *Phys. Rev. A* **11**, 872-883 (1975).

# Atomic process modeling based on plasma microfield

NISHIKAWA Takeshi

*Graduate School of Natural Science and Technology, Okayama University,*

*3-1-1 Tsushima-naka, Okayama 700-8530, Japan*

*e-mail: nishikawa.takeshi@okayama-u.ac.jp*

## Abstract

An atomic modeling based on the plasma microfield is considered. In the atomic modeling, it is considered that an ion in plasma is immersed in a uniform electric field due to the field values averaged over the other ions in the plasma. Using the modeling, we can compute the average ionization degree of hydrogenic plasmas without any ad hoc parameters to cut off the number of bound states.

**Keywords:** bound state, free state, statistical weight, state density, Saha equation, microfield, average ionization degree

## 1. Introduction

In the state of thermodynamic equilibrium, the ratio of the product of the number density of the  $(Z + 1)$ -charged ion  $N_{Z+1}$ , and that of the electron  $N_e(E)$  of its energy  $E$ , to that of the combined  $Z$ -charged ion  $N_Z$ , is determined by

$$\frac{N_{Z+1}N_e(E)}{N_Z} = \frac{U_{Z+1}}{U_Z} \exp\left(-\frac{E + I_p}{k_B T_e}\right) 2 \frac{4\pi p^2}{h^3} dp. \quad (1)$$

In the expression involving the Boltzmann factor,  $I_p$ ,  $k_B$ , and  $T_e$  denote the ionization potential from the  $Z$ -charged to the  $(Z + 1)$ -charged state, the Boltzmann constant, and the electron temperature, respectively. In the expression involving the number of electron states,  $h$  denotes Planck's constant. With respect to the energy of the free electron and its momentum  $p$ , the expression  $E = p^2/2m_e$  is satisfied, and here,  $m_e$  denotes the mass of the electron. Translating the free electron's momentum to its equivalent energy and integrating Eq. (1) over the energy range of the free electron for  $E > 0$ , we obtain

$$\begin{aligned} \frac{N_{Z+1}N_e}{N_Z} &= \frac{U_{Z+1}}{U_Z} \exp\left(-\frac{I_p}{k_B T_e}\right) \frac{8\pi\sqrt{2m_e^3}}{h^3} \int_0^\infty \sqrt{E} \exp\left(-\frac{E}{k_B T_e}\right) dE \\ &= \frac{U_{Z+1}}{U_Z} \exp\left(-\frac{I_p}{k_B T_e}\right) 2 \left(\frac{2\pi m_e k_B T_e}{h^2}\right)^{3/2}. \end{aligned} \quad (2)$$

This equation is called the Saha equation. Applying the equation to various ionic species including their excited states in plasma, we can compute the population of all ionic species in the plasma along with the average ionization degree obtained by  $Z_{av} = N_e/N_0$  from

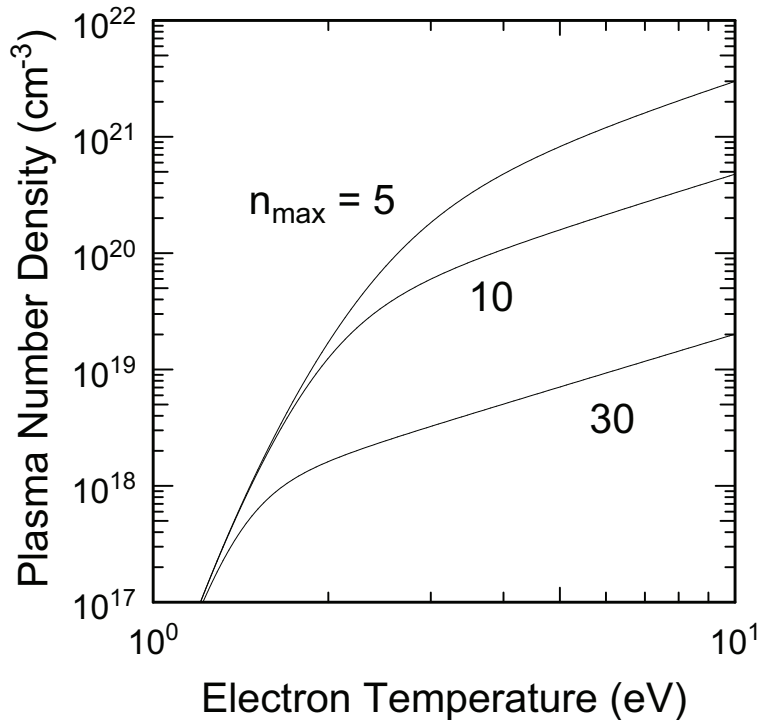


Figure 1: Contours of average ionization degree are 0.5 of hydrogenic plasmas. The maximum principal quantum numbers of the considered bound states are  $n = 5$ , 10, and 30.

this computed population, where  $N_0$  is the total number density of ion and atom defined by  $\sum N_Z$ .

Practically, we need to determine the number of bound states when we apply the Saha equation for realistic plasmas. For the case of hydrogenic plasmas, Fig. 1 shows one of the difficulties arising out of the conventionally used simple model in which the bound states exist up to a fixed maximum principal quantum number. The contours for an average ionization degree of 0.5 are plotted for three cases in which the maximum principal quantum numbers of the considered bound states are  $n = 5$ , 10, and 30. From Fig. 1, it can be observed that the plasma density and its temperature for an average ionization degree of 0.5 varies depending on the maximum principal quantum number of the bound state in the atomic process model. For a given temperature and density of a plasma in thermal equilibrium, however, a unique value of an average ionization degree must be computed. In order to address this ambiguity, I have developed a simple atomic model based on the plasma microfield for hydrogenic plasmas[1,2].

## 2. Bound State

In the atomic model based on the plasma microfield, hydrogenic ions are assumed to be immersed in a statistically distributed uniform electric field, i.e., the microfield in the plasma. As a result, the potential profile around the ion in plasma is given by the superposition of the ion's Coulomb potential  $Z_a e / 4\pi\epsilon_0 r$  and the potential due to the uniform external field  $F$ ; here,  $Z_a$ ,  $e$ , and  $\epsilon_0$  denote the nuclear charge of the ion, the elementary charge, and the permittivity of free space, respectively. The hydrogenic ion has a bound state whose energy is given by  $-m_e e^4 Z_a^2 / 8\epsilon_0^2 h^2 n^2$ , and this energy is assumed to be unchanging even in the external electric field. In this case, the potential distribution around the ion shows a saddle point. The height of the saddle point varies as the function of the strength of the uniform external electric field. I determine that the electronic state is that of a free electron for energies above this saddle point and that the energy values below the saddle point indicate bound states. From the above assumption, the threshold electric field till which the bound state  $n$  exists is given as

$$F_n^c = \frac{\pi m_e^2 e^5 Z_a^3}{64 \epsilon_0^3 h^4 n^4}. \quad (3)$$

The probability that the bound state  $n$  exists is given by the expression

$$w_n = \int_0^{F_n^c} dF P(F), \quad (4)$$

where  $P(F)$  represents the distribution function of the microfield. Using the Holtsmark field, given as

$$H(\beta) = F_0 W(F) = \frac{2}{\pi} \beta \int_0^\infty x \exp[-x^{3/2}] \sin(\beta x) dx, \quad (5)$$

as the statistically distributed uniform microfield  $F$ , we can compute Eq. (4), where  $\beta = F/F_0$ , as

$$F_0 = 2\pi \left( \frac{4N_p}{15} \right)^{2/3} \frac{Z_p e}{4\pi\epsilon_0}, \quad (6)$$

where  $N_p$  and  $Z_p$  denote the number density and the charge state of the perturbing ion, respectively. The term  $F_0$  is called the Holtsmark normal field strength[3].

### 3. Free State

In the conventional atomic process modeling, the translation of the electron's momentum to its equivalent energy in the free-state density calculations is carried out using the equations  $E = p^2/2m_e$  and  $2 \cdot 4\pi p^2 dp/h^3$ . In the present modeling, an ion is assumed to be in a potential that is composed of the Coulomb potential of its nucleus and the potential due to the uniform external field. To accommodate this effect, we rewrite the relation

between the electron's energy and momentum at  $(r, \theta)$  in the spherical coordinates inside the ion sphere radius  $R_0$  as

$$\frac{p^2}{2m_e} = E + \frac{1}{4\pi\epsilon_0} \frac{Z_a e^2}{r} + eFr \cos \theta. \quad (7)$$

The ion sphere has a radius  $R_0$  such that

$$\frac{4\pi}{3} R_0^3 N_0 = 1 \quad (8)$$

Here,  $N_0$  denotes the total number density of the atom and ion. The second term on the right hand side of Eq. (7) indicates the contribution of the Coulomb potential of the nucleus and the third term indicates that of the plasma microfield.

However, the free-state density obtained by the simple atomic model based on the microfield is not practically acceptable since the free-state density has been computed as larger than that of a bound electron of the same energy. Detailed investigations show that the difficulty is induced on the potential far beyond the saddle point inside the ion sphere of radius  $R_0$ . Such a large electric field by which the saddle point is sufficiently inside the ion sphere occurs even in the low density plasmas, although the probability is relatively small. The assumption that the large electric field mostly due to the nearest ion is uniform within the ion sphere radius is inconsistent with the potential measured in real plasmas. In order to overcome this difficulty, we have attempted to compute the free-state density by estimating the contribution of the field values beyond the saddle point assuming the mirror symmetry of the potential with respect to the saddle point.

Figure 2 shows the energy dependence of the state densities of the free and bound states of hydrogenic plasma by using the above-mentioned potential modeling. The energy dependence curves are plotted for six cases from  $N_i = 10^{16} \text{ cm}^{-3}$  to  $10^{21} \text{ cm}^{-3}$ . Here,  $N_i$  denotes the number density of ion. From Fig. 2, the quantum states up to the principal quantum number of  $n = 8$  are almost completely existing for  $N_i = 10^{16} \text{ cm}^{-3}$ . From the state value of  $n = 9$ , the bound state densities gradually decrease, while the free-state density appears and gradually increases as the principal quantum number becomes larger. Experimentally[4], the bound-bound spectrum from for state values  $n = 2$  to 8 in hydrogenic plasma with  $N_i = 1.8 \times 10^{16} \text{ cm}^{-3}$  can be clearly observed, while those for  $n \geq 9$  are merged with the free-bound spectrum although the bound-bound spectrum is broadened due to the Stark effect. For  $N_i = 9.3 \times 10^{16} \text{ cm}^{-3}$ , the bound-bound spectra from for state values of  $n = 2$  to 6 can be clearly observed while our model posits bound state existence up to  $n = 6$  for  $N_i = 10^{17} \text{ cm}^{-3}$ .

#### 4. Average Ionization Degree

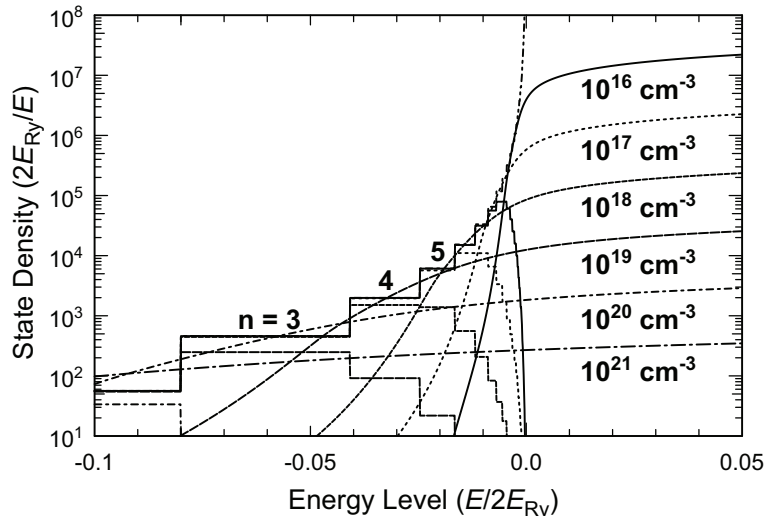


Figure 2: State density with modification in potential assuming the mirror symmetry with respect to saddle point for various ion number densities ranging from  $N_i = 10^{16} \text{ cm}^{-3}$  to  $10^{21} \text{ cm}^{-3}$  for hydrogenic plasmas.

Using the model, we can also compute the average ionization degree of various plasmas. In the case of the present model, the free state density is changed to be that described in Sec. 4 denoted by  $f(E)$ , and the resulting relation between two different charge states becomes

$$\frac{N_{Z+1}N_e}{N_Z} = \frac{U_{Z+1}}{U_Z} \exp\left(-\frac{I_p}{k_B T_e}\right) \int_{E_{\min}}^{\infty} f(E) \exp\left(-\frac{E}{k_B T_e}\right) dE. \quad (9)$$

It is noted that the lower range of the integration on  $E$ ,  $E_{\min}$  has been changed to be from 0 to the larger value of just potential at the point,  $-e^2 Z/4\pi\epsilon_0 r - eFr \cos \theta$  or potential at the saddle point,  $-2e\sqrt{\frac{eZ_0 F}{4\pi\epsilon_0}}$  since the state density of which energy is below the value of its saddle point is assumed to be bound in this model. Figure 3 shows the average ionization degree of hydrogenic plasma. The dotted curves in Fig. 3 are the results obtained using Eq. (2), while the solid curves are those obtained by Eq. (9). From Fig. 3, it is observed that the contours including the potential effect in the free-state density deviate slightly to the lower temperature region since the free-state density exists continuously from the bound state. The deviation is not very large; however, the deviation grows larger as the plasma density increases.

## 5. Conclusions

I draw attention to one of the features of the present model in comparison with other models in which the concept of the ion sphere is used[5]. Most atomic models

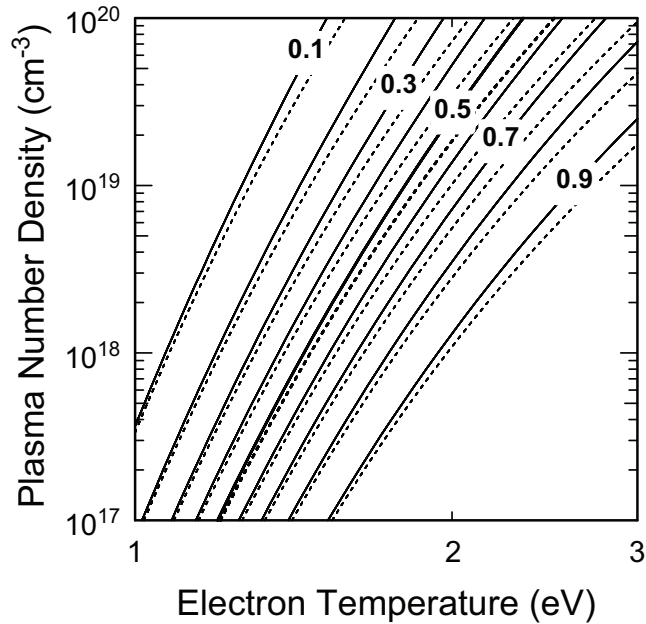


Figure 3: Average ionization degree of hydrogenic plasma. The potential is assumed to be mirror symmetry with respect to the saddle point.

that apply the concept of an ion sphere only consider the plasma effects on the resulting potential in a spherical fashion. Therefore, we sometimes encounter the difficulty of the sudden disappearance of a bound state at a given threshold density when we compute the average ionization degrees over a wide range of plasma density and temperature. Using the present model, we can avoid such difficulties since the bound states gradually decrease as the density increases.

### Acknowledgement

This work was partly supported by the JSPS-NRF-NSFC A3 Foresight Program in the field of Plasma Physics (NSFC: No.11261140328).

### References

- [1] T. Nishikawa, *Astrophysical J.* **532**, 670 (2000).
- [2] T. Nishikawa, *Plasma and Fusion Science* **7**, 1401142 (2012).
- [3] H. R. Griem, *Spectral line broadening by plasmas* (Academic Press, New York, 1974) p. 17.
- [4] W. L. Wiese, D. E. Kelleher, and D. R. Paquette, *Phys. Rev. A* **6**, 1132 (1972).
- [5] For example, I. Shimamura and T. Fujimoto, *Phys. Rev. A* **42**, 2346 (1990).

# Multiple Ionization Dynamics of Ar<sub>2</sub> by Slow Highly Charged Ions

ICHIMURA Atsushi<sup>1</sup> and OHYAMA-YAMAGUCHI Tomoko<sup>2</sup>

<sup>1</sup>*Institute of Space and Astronautical Science (JAXA), Sagami-hara 252-5210, Japan  
e-mail: ichimura@isas.jaxa.jp*

<sup>2</sup>*Tokyo Metropolitan College of Industrial Technology, Shinagawa 140-0011, Japan  
e-mail: yamaguti@s.metro-cit.ac.jp*

## Abstract

Multiple ionization dynamics of rare gas dimers by slow highly charged ions is investigated with the three-center Coulombic over-barrier model. Quasi-molecule formation of an electron at the distant atomic site from the projectile is shown sensitive to partial screening of ion-core charge at the near atomic site due to electrons already forming quasi-molecules. It is found that the screening effect suppresses simultaneous chained electron removal from both sites and hence enhances charge-asymmetric ion pair formation. The ion pair distribution measured in Ar<sup>9+</sup> + Ar<sub>2</sub> collisions (Matsumoto J *et al.* 2010 *Phys. Rev. Lett.* **105** 263202) is well reproduced by taking a screening factor of  $s = 0.4$  in the model.

**Keywords:** highly charged ion, rare gas dimer, three-center over-barrier model, screening effect, dissociating ion pair distribution

## 1. Introduction

Much attention has been called to Coulomb explosion of molecules in collisions with slow (velocities of  $v \ll 1$  au) highly charged ions. Recent progress of the experimental technique of recoil-ion momentum spectroscopy [1] permits us to measure the dissociating ion pair distribution in the collisions [2,3]. Such observations are of great interest from a viewpoint of multi-center multi-electron dynamics. In contrast with a covalent diatomic molecule, however, little effort has been devoted to a rare gas dimer. In the rare gas dimer, because of its large internuclear distance, a range of selectron motion is well localized in either atomic site in a time scale of the collision. It is expected that such a characteristic structure gives intriguing multiple ionization dynamics.

About ten years ago, we proposed a three-center Coulombic over-barrier model to describe multiple ionization of rare gas dimers with slow highly charged ions [4]. In a preceding work [5], stimulated by an experiment done at GANIL [3], we modified the model so as to incorporate a screening effect during a collision. The screening effect

was found crucial to explaining the population of charge-asymmetric ion pairs such as  $(Q, Q') = (2, 0)$ .

In the present work, we carry out systematic calculations based on the modified model to reveal how the screening affects the ion pair distribution and show how it explains the result of measurement in  $\text{Ar}^{9+} + \text{Ar}_2$  collisions [3].

## 2. Three-center over-barrier model

We treat a process of multiple ionization (actually electron transfer) of a rare gas dimer BC with a slow highly charged ion  $A^{q+}$ . The outermost electrons at respective atomic sites, B and C, in the target dimer are supposed to sequentially form quasi-molecules with projectile  $A^{q+}$ . During this course, the target state is labelled by a pair of charge states  $(Q_B, Q_C)$  and evolves in respective steps either as  $(Q_B, Q_C) \rightarrow (Q_B + 1, Q_C)$  or as  $(Q_B, Q_C) \rightarrow (Q_B, Q_C + 1)$ . Accordingly the active electron in the former process is taken as  $t_B = Q_B + 1$  in site B, while that in the latter process is taken as  $t_C = Q_C + 1$  in site C, where  $t_{B,C}$  denotes the rank of an electron in each atom. It is assumed for simplicity that the electron never returns to the target once trapped in a quasi-molecule; we only consider the *way in* process to derive partial cross sections of ion pair  $(Q, Q')$  formation when  $q \gg Q, Q'$ .

Relevant one-electron dynamics is described by a three-center Coulomb potential,

$$U(\mathbf{r}) = -\frac{q_A}{|\mathbf{r} - \mathbf{R}_A|} - \frac{q_B}{|\mathbf{r} - \mathbf{R}_B|} - \frac{q_C}{|\mathbf{r} - \mathbf{R}_C|}, \quad (1)$$

with three ion core charges  $q_A, q_B$  and  $q_C$ . Virtually in any case, this potential has two saddle points, lower one ( $U_{\text{low}}$ ) and higher one ( $U_{\text{high}}$ ). Stark-shifted energies of active electrons localized at atomic sites B and C are given by

$$E_B = -I(t_B) - \frac{q_C}{2d} - \frac{q_A}{|\mathbf{R} - \mathbf{d}|}, \quad (2)$$

$$E_C = -I(t_C) - \frac{q_B}{2d} - \frac{q_A}{|\mathbf{R} + \mathbf{d}|}, \quad (3)$$

where  $I(t)$  denotes the atomic  $t$ -th multiple ionization potential; nuclear configuration is represented by a relative vector  $\mathbf{R} = \mathbf{R}_A - (\mathbf{R}_B + \mathbf{R}_C)/2$ , with intra-dimer vector  $\mathbf{d} = (\mathbf{R}_B - \mathbf{R}_C)/2$  being fixed during a collision. Hence we can formulate the *over-barrier criterion* of quasi-molecule formation in such a way as either saddle height  $U_{\text{low}}$  or  $U_{\text{high}}$  gets lower than either electron energy  $E_B$  or  $E_C$ . A set of the criterions was generally given according to the potential topography with three centers and two saddle points [4,5]. The  $(Q_B, Q_C)$  evolution along a given collision trajectory is determined by applying the “rule

of first arrival” to the alternative of active site B or C. It should be noted that the over-barrier criterion may give two-electron *chained* processes (simultaneous electron removal from both sites) as  $(Q_B, Q_C) \rightarrow (Q_B + 1, Q_C + 1)$  [4,5]. This mechanism is illustrated in figure 1.

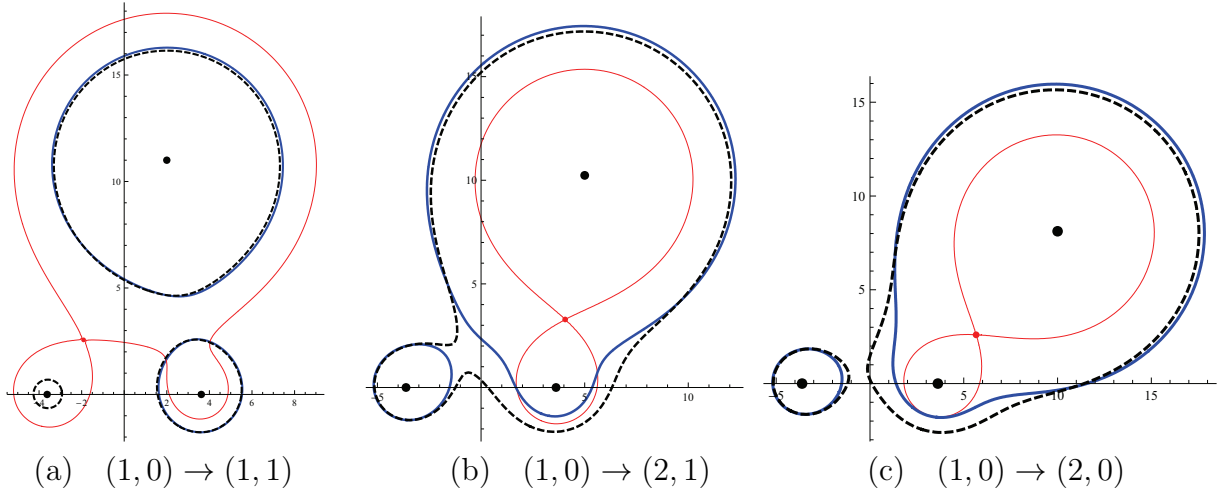


Figure 1: Competing equipotential surfaces  $U_B(\mathbf{r}) = E_B$  and  $U_C(\mathbf{r}) = E_C$  at critical nuclear configurations for the second electron removal following  $(0, 0) \rightarrow (1, 0)$  in the  $(Q_B, Q_C)$  evolution. The surfaces are calculated for  $A^{9+} + Ar_2$  with a screening parameter of  $s = 0.4$  and plotted in the  $x - y$  plane ( $x \equiv \mathbf{r} \cdot \hat{\mathbf{d}}$ ) with the origin taken at the midpoint of sites B and C. Thin solid lines represent the surfaces of just forming relevant quasi-molecules for  $t_C = 1$  electron in panel (a) and for  $t_B = 2$  in (b) and (c). Thick solid lines indicate the surfaces for alternative electrons,  $t_B = 2$  in (a) and  $t_C = 1$  in (b) and (c), just *before* the quasi-molecule formation, with dashed lines just *after* that. It is found in panel (b) that, resultantly, the  $t_C = 1$  electron also forms a quasi-molecule at identical nuclear configuration; a simultaneous two-electron chained process  $(1, 0) \rightarrow (2, 1)$  occurs at a configuration taken in panel (b), while it does not occur in (a) and (c).

The ion core charges in equations (1—3) are effectively taken as

$$q_A = q, \quad q_B = Q_B + 1, \quad q_C = (1 - s) \times Q_C,$$

for active site B, and

$$q_A = q, \quad q_B = (1 - s) \times Q_B, \quad q_C = Q_C + 1,$$

for active site C [5]. Here is introduced a *screening* factor  $s$  ( $0 \leq s \leq 1$ ) as a parameter. The screening effect during a collision comes from a situation peculiar to a rare gas dimer

that the electron cloud at site B and that at C are well separated from each other; the electrons already forming quasi-molecules from the non-active site (supposing B) still partially screen their original ion core when seen from the active site (C) and also from the active saddle point. Note that electron removal from B and that from C are *not* correlated at all when  $s = 1$  (*i.e.*, the independent event model).

### 3. Results and Discussion

The model is applied to  $A^{9+} + Ar_2$  collisions with active electrons  $1 \leq t_B, t_C \leq 4$ .

Critical nuclear configurations for ion-pair  $(Q, Q')$  formation are plotted in figure 2 for a screening factor of  $s = 0.4$  as an example. As seen from the figure, the critical configurations for quasi-molecule formation from site B (near site to the projectile) compose concentric circles around site B, while those from site C (far site) compose fragmented segments around site C. A pair of the former and latter curves merge into a curve composed of critical configurations of two-electron chained processes. This pattern of the critical curves varies sensitively with the parameter  $s$ , especially in a region of  $0.3 \lesssim s \lesssim 0.5$ . As the screening factor  $s$  increases, the simultaneous two-electron chained processes such as  $(1, 0) \rightarrow (2, 1)$  and  $(2, 1) \rightarrow (3, 2)$  are suppressed; hence the populations of charge-asymmetric ion pairs such as  $(2, 0)$  and  $(3, 1)$  are enhanced.

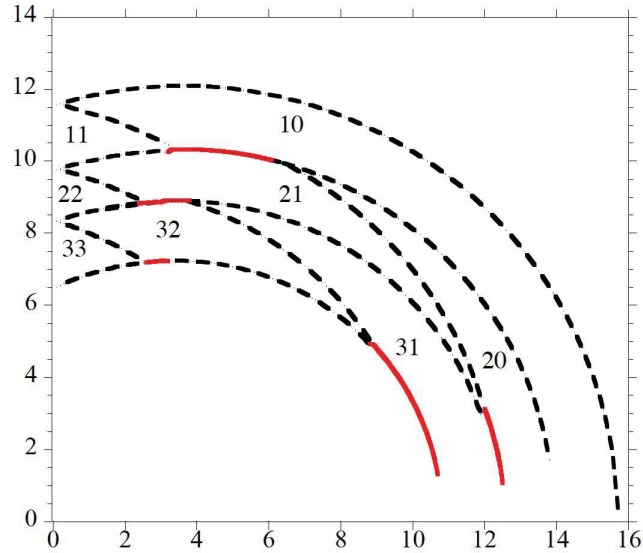


Figure 2: Critical curves for ion-pair  $(Q_B, Q_C)$  formation in the first quadrant of nuclear configuration  $X - Y$  plane, calculated for  $A^{9+} + Ar_2$  collisions with screening parameters of 0.4. The critical curves shown include the two-electron chained processes (solid lines) and unchained processes (dashed lines).

Ion pair  $(Q, Q')$  formation cross sections are calculated for randomly oriented target dimers using the critical configurations obtained above. The result with different values of the screening factor  $0 \leq s \leq 1$  are shown in figure 3, where comparison with experiment [3] is also made. As clearly seen from the figure, the  $(Q, Q')$  distribution is sensitive to the parameter  $s$  in the calculation. A partial screening model with  $s = 0.4$  considerably well reproduces the overall distribution observed in the experiment. The value of  $s = 0.4$  has been confirmed the best choice throughout the domain of  $0 \leq s \leq 1$ . In contrast, the model without screening ( $s = 0$ ) and that with full screening ( $s = 1$ ) indicate tremendous deviations from the experiment in particular in charge-asymmetric channels  $(2,0)$  and  $(3,1)$ , although giving a reasonable agreement in symmetric channels  $(1,1)$  and  $(2,2)$ . It is noted that these two models show opposite directions of deviation from the experiment in  $(2,0)$  and  $(2,1)$  channels. It is also found from the figure that the calculated distribution varies with the screening parameter drastically around  $s \sim 0.4$ .

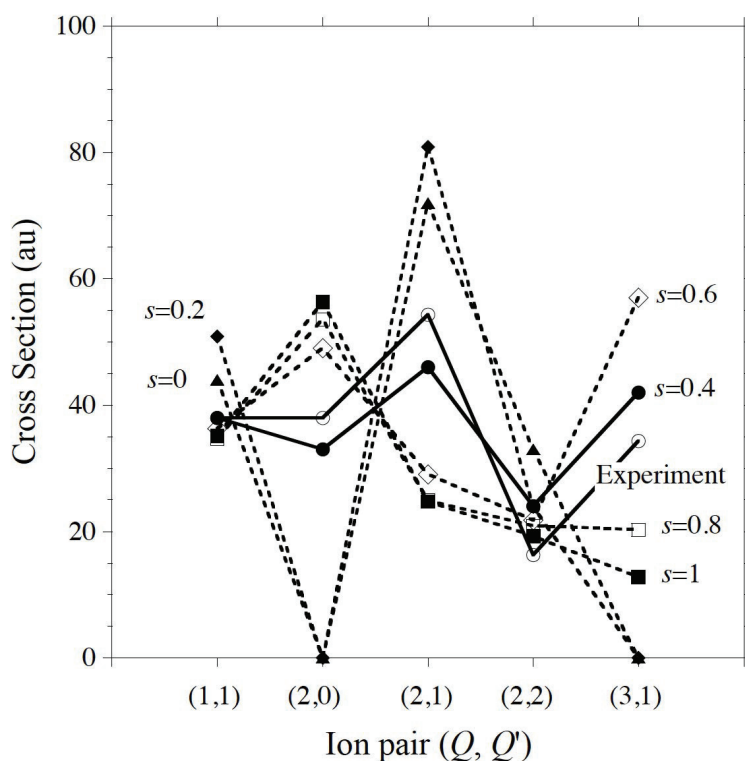


Figure 3: Screening parameter dependence of the ion-pair  $(Q, Q')$  formation cross sections in  $A^{9+} + Ar_2$  collisions:  $s = 0.0$  (full triangles),  $s = 0.2$  (full diamonds),  $s = 0.4$  (full circles),  $s = 0.6$  (open diamonds),  $s = 0.8$  (open squares), and  $s = 1.0$  (full squares). The experimental result [3] (open circles) is also shown and normalized to the model result with  $s = 0.4$  at  $(Q, Q') = (1, 1)$ .

In the present paper, we have described the multiple ionization dynamics of rare gas dimers by slow highly charged ions with the three-center Coulombic over-barrier model. The screening effect during a collision is analyzed in detail and found to alter the ion pair distributions crucially. The distribution observed in a recent experiment for  $\text{Ar}^{9+} + \text{Ar}_2$  collisions is best reproduced by taking a screening factor of  $s = 0.4$ .

### Acknowledgement

Stimulating discussions with H. Shiromaru, J. Matsumoto, A. Cassimi, and X. Flécharde are gratefully acknowledged. This work was supported by the TMU University-College Joint Project and the JSPS-NRF-NSFC A3 Foresight Program in the field of Plasma Physics (NSFC: No.11261140328).

### References

- [1] Ullrich J *et al.* 2003 *Rep. Prog. Phys.* **66** 1463.
- [2] Kaneyasu T, Azuma T, and Okuno K 2005 *J. Phys. B: At. Mol. Opt. Phys.* **38** 1341.
- [3] Matsumoto J *et al.* 2010 *Phys. Rev. Lett.* **105** 263202; *ibid.* 2011 *Physica Scripta T* **144** 014016.
- [4] Ohyama-Yamaguchi T and Ichimura A 2003 *Nucl. Instrum. Methods* **205** 620.
- [5] Ohyama-Yamaguchi T and Ichimura A 2011 *Physica Scripta T***144** 014028.

# Theoretical Investigation of Total and State-Dependent Charge Exchange in $O^{6+}$ Collisions with Atomic Hydrogen

Y. Wu,<sup>1,2,\*</sup> P. C. Stancil,<sup>1</sup> D. R. Schultz,<sup>3,4</sup> Y. Hui,<sup>4</sup> H. P. Liebermann,<sup>5</sup> and R. J. Buenker<sup>5</sup>

<sup>1</sup>*Department of Physics and Astronomy and the Center for Simulation Physics,  
University of Georgia, Athens, Georgia 30602-2451, USA*

<sup>2</sup>*Institute of Applied Physics and Computational Mathematics, P.O. Box 8009, Beijing 100088, China*

<sup>3</sup>*Department of Physics, University of North Texas, Denton, Texas 76203-5017, USA*

<sup>4</sup>*Physics Division, Oak Ridge National Laboratory, Oak Ridge, Tennessee 37831-6372, USA*

<sup>5</sup>*Fachbereich C-Mathematik und Naturwissenschaften,  
Bergische Universität Wuppertal, D-42097 Wuppertal, Germany*

The charge exchange process has been found to play a dominant role in the production of X-rays and/or extreme ultraviolet photons emitted from cometary and planetary atmospheres and from the heliosphere. Charge exchange cross sections, especially state-selective cross sections, are necessary parameters in simulations of this X-ray emission. In the present work, charge exchange, particularly single electron capture, due to collisions of ground state  $O^{6+}(1s^2\ ^1S)$  with atomic hydrogen has been investigated theoretically using the quantum-mechanical molecular-orbital close-coupling method (QMOCC). The multi-reference single- and double-excitation configuration interaction approach has been applied to compute the adiabatic potentials and nonadiabatic couplings, and the atomic basis sets used have been optimized with a method proposed previously to obtain accurate descriptions of the high-lying Rydberg states of highly charged ions. Total and state-selective cross sections are calculated for energies between 0.1 eV/u and 10 keV/u. The QMOCC results are compared to available experimental and theoretical data as well as to new atomic-orbital close-coupling (AOCC) and classical trajectory Monte Carlo (CTMC) calculations. A recommended set of cross sections, based on the QMOCC, AOCC, and CTMC calculations, are deduced which should aid in X-ray modeling studies.

PACS numbers: 34.10.+x, 34.20.Mq, 34.70.+e

## I. INTRODUCTION

Over the past decade and a half, there have been important advances in soft X-ray and extreme ultraviolet investigations of solar system objects [1–11] through observations by the *XMM-Newton*, *Chandra*, and *Suzaku* observatories. For example, solar wind charge exchange (SWCX) has been identified as a primary source of the soft X-ray background, contributing at the same order or more as the diffuse cosmic X-ray emission which includes the extragalactic, galactic halo, and so-called Local Bubble components, [12]. In some X-ray sub-bands, SWCX even plays the dominant role [8, 10]. In the SWCX mechanism, X-ray photons are generated following charge exchange between highly charged, heavy solar wind ions and the neutral species in cometary atmospheres [1], the heliosphere [2, 3], the geocorona [5, 6] and planetary atmospheres [7]. Further, these X-rays can be used to diagnose the SW composition, evolution, velocity, and flux, as well as the distribution of the neutral gas density. To predict these emissions and compare with observations, knowledge of total and state-selective charge exchange data is required.

Charge exchange between oxygen ions and neutral species H,  $H_2$ , and He in the heliosphere, atmospheres

and the geocorona are of particular interest because oxygen is a primary minor solar wind ion species. In addition, X-ray emission from the auroral regions of Jupiter is believed to be due to radiative decay from highly-excited, high-charge-state O and S ions produced following charge transfer with neutral atmospheric species  $H_2$ , H, and He [13–15].

Though there have been advances in the investigation of charge exchange, accurate, systematic, and conveniently available data are sparse, particularly at the final-quantal-state-resolved level. For  $O^{6+} + H$  collisions, the available calculations include a quantum mechanical molecular-orbital close-coupling (QMOCC) investigation by Shipsey *et al.* [16] and classical trajectory Monte Carlo (CTMC) computations [16, 17] of single electron capture (SEC). Total SEC cross section measurements were obtained between 0.1 and 100 keV/u by Meyer *et al.* [18], Crandall *et al.* [19], Phaneuf *et al.* [20], and Djikamp *et al.* [21]. Also, Phaneuf *et al.* [22] and Janev *et al.* [23] gave recommended total SEC cross sections, and we note that these follow the measurements of Phaneuf *et al.* [20] which disagree with the QMOCC calculations of Shipsey *et al.* [16].

To help resolve such disagreements among the available data sets, to extend their range, and to provide the detailed results needed in applications, in the present paper, charge exchange between  $O^{6+}$  and H for SEC was investigated systematically using the QMOCC [24, 25], atomic-orbital close-coupling (AOCC) [27] and CTMC

---

\*Electronic address: yongwu@physast.uga.edu

[28, 29] methods. Accurate total and state-selective cross sections are provided for a large collision energy range.

In the QMOCC calculations, the adopted adiabatic potentials and nonadiabatic couplings have been obtained with the multi-reference single- and double-excitation configuration interaction (MRDCI) approach [30, 31], and the atomic basis sets used have been optimized with the method proposed previously [26] to obtain accurate descriptions of the high-lying Rydberg states of highly charged ions. The QMOCC results are compared to available experimental and theoretical data and extended to higher collision energies by the AOCC and CTMC calculations reported here. It should be noted that the collision energy is given in units of eV/u, the center-of-mass energy per reduced mass, which is identical to the incident ion energy per ion mass. Otherwise, atomic units (a.u.) are used throughout unless noted.

## II. THEORETICAL METHODS

As there are no theoretical methods readily applicable over the entire energy range considered (0.1 eV/u - 1000 keV/u), three different approaches have been utilized to study of  $O^{6+} + H$  collisions in different energy regimes, but generally with narrow regions of overlap. For the collision energy range 0.1 eV/u - 10 keV/u, the QMOCC method was utilized to obtain total and state-selective cross sections; for 150 eV/u - 200 keV/u, the AOCC method was used; and for 100 eV/u - 1000 keV/u, the CTMC method was used.

### A. QMOCC method

#### 1. Electronic Structure Calculation

In a collision of  $O^{6+}$  with atomic hydrogen resulting in SEC, an electron is transferred from the hydrogen atom to the oxygen ion in a valence state with principal quantum number  $n$  most likely equal, in decreasing order of likelihood, to 4, 5, or 3. Because the electrons originally attached to  $O^{6+}$  remain in the tightly-bound 1s shell, the captured electron's state is essentially hydrogen-like in character. Wu *et al.* [26] have developed a hybrid basis set consisting of two components: i) the standard Dunning neutral atom basis [32] and ii) a one-electron basis of hydrogen-like orbitals. The latter component was optimized to reproduce nearly exactly the hydrogen-like Rydberg ion energies. We adopt this approach here.

Considering  $O^{5+}$  as a hydrogen-like ion with effective nuclear charge  $Z^*=6$ , a large Gaussian basis set (17s, 11p, 9d, 6f, 3g) has been optimized and used for oxygen. A (6s, 3p, 2d, 1f) basis contracted to [4s, 3p, 2d, 1f] was employed for hydrogen [32]. In the present work, an *ab initio* MRDCI calculation [30, 31] has been carried out to compute the adiabatic potentials and nonadiabatic coupling matrix elements of the  $[OH]^{6+}$  system. Fif-

teen  ${}^2\Sigma^+$  electronic states in  $A_1$  symmetry and ten  ${}^2\Pi$  electronic states in  $B_1$  symmetry have been computed. A full configuration interaction calculation was applied for internuclear distances between 1.0 and 40 a.u. Relative asymptotic energies of the  $[OH]^{6+}$  system have been obtained and compared with the corresponding experimental atomic spectroscopic data [33] in Table I. The largest error in the relative asymptotic energies of the  $[OH]^{6+}$  system is about 0.03 eV for the important channels with  $n$  of 3, 4, and 5. Given the optimized basis, the nonadiabatic radial and rotational coupling elements were calculated by applying a finite-difference method [30].

### 2. Scattering Calculations

The QMOCC method has been described thoroughly in previous work [24, 25] and outlined in reference [26]. With the electronic potentials and couplings, a coupled set of second-order differential equations is solved and matched to the plane-wave boundary conditions at large internuclear separation ( $R=200$ ) to obtain the  $K$ -matrix, and from it the  $S$ -matrix [24]. The total charge exchange cross section with initial state  $\alpha$  to final state  $\beta$  is then given by

$$\sigma_{\alpha\rightarrow\beta} = \frac{\pi}{k^2} \sum_J (2J+1) |(S_J)_{\alpha\beta}|^2, \quad (1)$$

where the unitary  $S$ -matrix for each partial wave  $J$  is defined as

$$S_J = [I + iK_J]^{-1} [I - iK_J]. \quad (2)$$

$I$  is the identity matrix and  $k$  denotes the wave number for center-of-mass motion of the initial ion-atom channel. The procedure described above is carried out until the cross section converges with increasing number of partial waves.

### B. AOCC method

For intermediate collision energies, the AOCC approach [27] has been utilized. In this method, the time-dependent electronic wavefunction is expanded in terms of atomic orbitals of the isolated target and projectile. Here we employ the method of Kuang and Lin [36, 37], using a straightline trajectory for the projectile's motion, and including functions that span not only the bound states but also partially (discretely) the continuum. Since the approach considers the collision system as possessing one active electron, we have adopted a model potential [38] to represent the interaction of this electron with the  $O^{6+}$  core. Eigensolution using the Kuang and Lin functions, in this potential for the oxygen ion and the Coulomb potential for an electron interacting with

TABLE I: Comparison between the experimental data [33] and the MRDCI calculation for the relative asymptotic energies (in eV) of the  $[\text{OH}]^{6+}$  system. The energies  $E_1$  have been obtained with the optimized Gaussian basis set functions.  $\Delta E_1$  is the corresponding energy difference between the calculations and measurements  $E_0$ . Note that different energy zero points are adopted for  $\Delta E_1^{(1)}$  and  $\Delta E_1^{(2)}$ .

Asymptotic atomic state	Mol. State	$E_1^a$	$E_0$	$\Delta E_1^{(1)}$	$\Delta E_1^{(2)}$
$\text{O}^{5+}(1s^2 2s^2 S) + \text{H}^+$	$1^2\Sigma^+$	0.0	0.0	0.0	-0.10554
$\text{O}^{5+}(1s^2 2p^2 P^o) + \text{H}^+$	$2^2\Sigma^+$	11.94053	11.949	0.00847	-0.09707
	$1^2\Pi$	11.94025	11.949	0.00875	-0.09679
$\text{O}^{5+}(1s^2 3s^2 S) + \text{H}^+$	$3^2\Sigma^+$	79.28353	79.35482	0.07129	-0.03425
$\text{O}^{5+}(1s^2 3p^2 P^o) + \text{H}^+$	$4^2\Sigma^+$	82.50969	82.58751	0.07782	-0.02772
	$2^2\Pi$	82.50958	82.58751	0.07793	-0.02761
$\text{O}^{5+}(1s^2 3d^2 D) + \text{H}^+$	$5^2\Sigma^+$	83.57185	83.64292	0.07107	-0.03447
	$3^2\Pi$	83.57137	83.64292	0.07155	-0.03399
$\text{O}^{5+}(1s^2 4s^2 S) + \text{H}^+$	$6^2\Sigma^+$	105.63847	105.7208	0.08233	-0.02321
$\text{O}^{5+}(1s^2 4p^2 P^o) + \text{H}^+$	$7^2\Sigma^+$	106.94461	107.0397	0.09509	-0.01045
	$4^2\Pi$	106.94439	107.0397	0.09531	-0.01023
$\text{O}^{5+}(1s^2 4d^2 D) + \text{H}^+$	$8^2\Sigma^+$	107.3888	107.4794	0.0906	-0.01494
	$5^2\Pi$	107.38842	107.4794	0.09098	-0.01456
$\text{O}^{5+}(1s^2 4f^2 F^o) + \text{H}^+$	$9^2\Sigma^+$	107.40948	107.5039	0.09442	-0.01112
	$6^2\Pi$	107.4091	107.5039	0.0948	-0.01074
$\text{O}^{5+}(1s^2 5s^2 S) + \text{H}^+$	$10^2\Sigma^+$	117.53785	117.6226	0.08475	-0.02079
$\text{O}^{5+}(1s^2 5p^2 P^o) + \text{H}^+$	$11^2\Sigma^+$	118.19015	118.2908	0.10065	-0.00489
	$7^2\Pi$	118.18982	118.2908	0.10098	-0.00456
$\text{O}^{5+}(1s^2 5d^2 D) + \text{H}^+$	$12^2\Sigma^+$	118.41965	118.5104	0.09075	-0.01479
	$8^2\Pi^+$	118.4191	118.5104	0.0913	-0.01424
$\text{O}^{5+}(1s^2 5f^2 F^o) + \text{H}^+$	$13^2\Sigma^+$	118.42436	118.5264	0.10204	-0.0035
	$9^2\Pi$	118.42412	118.5264	0.10228	-0.00326
$\text{O}^{5+}(1s^2 5g^2 G) + \text{H}^+$	$14^2\Sigma^+$	118.42992	118.5276	0.09768	-0.00786
	$10^2\Pi$	118.42966	118.5276	0.09794	-0.0076
$\text{O}^{6+}(1s^2 ^1S) + \text{H}(1s^2 S)$	$15^2\Sigma^+$	124.12817 <sup>a</sup>	124.23371	0.10554	0

<sup>a</sup>The Coulomb repulsion  $5/R$  has been subtracted at  $R = 100$  a.u between  $\text{O}^{5+}$  and  $\text{H}^+$

the proton in atomic hydrogen, was used to produce the basis set.

For each collision energy considered, solution of the coupled equations determined by inserting the expansion into the Schrödinger equation was then performed, and probabilities for transitions to these states were computed as a function of impact parameter, yielding the cross sections for charge exchange to individual states within the basis set. For the higher collision energies considered here, up to 199 basis states were used (up to 90 on the atomic hydrogen atom from the 1s level to 11f, and up to 109 on the  $\text{O}^{5+}$  product ion from 2s to 10g, with many of the highest states in the pseudocontinuum). For the lowest collision energies, the basis had to be reduced for numerical stability, containing as few as 89 states (10 on the hydrogen atom, 1s - 3d, and 79 on the oxygen ion, 2s - 8g).

### C. CTMC method

Applicable for collision energies beginning somewhat higher than for AOCC, the CTMC approach was applied, which has the advantage of providing charge exchange cross sections to high principal quantum number. This method simulates a collision by sampling trajectories stemming from initial electronic orbits within a large ensemble of configurations [28, 29]. The motion of the particles is determined by an iterative solution of Hamilton's equations of motion using either Coulomb (for the electron - proton interaction in H) or model (for the electron -  $\text{O}^{6+}$  and proton -  $\text{O}^{5+}$  interactions) potentials. At an asymptotic distance, the classical binding energies are then calculated to determine if an inelastic or reactive event occurred. Applying classical-quantum correspondence relations [39, 40], the final  $n, l$  quantum state after charge exchange can then be determined based on the

binding energy and angular momentum of the electron if it is bound to the projectile ion.

### III. RESULTS AND DISCUSSION

For the collision energy range of the QMOCC calculation (0.1 to  $10^4$  eV/u), the exoergic channels are the most important for charge exchange and, therefore, 22 states were considered, which included  $3\ ^2\Sigma^+ - 15\ ^2\Sigma^+$ , and  $2\ ^2\Pi - 10\ ^2\Pi$ . As can be seen in Table I, the energy gaps between the  $2\ ^2\Sigma^+$  and  $3\ ^2\Sigma^+$  states, and between  $1\ ^2\Pi$  and  $2\ ^2\Pi$ , are about 70 eV in the asymptotic region. Consequently, charge exchange to  $1\ ^2\Sigma^+$ ,  $2\ ^2\Sigma^+$  and  $1\ ^2\Pi$  is not expected to be significant for the range of collision energies considered using the QMOCC method. For higher collision energies, the AOCC and CTMC methods have been used to obtain the total and state-selective ( $nl$ -dependent) cross sections including endoergic channels.

#### A. Potentials and Couplings

In the present QMOCC calculation, radial and rotational couplings were considered. As a sequence of the initial channel symmetry of  $^2\Sigma^+$ , channels in both  $^2\Sigma^+$  and  $^2\Pi$  symmetries are needed. In Figure 1(a), the adiabatic potentials are presented for the important  $n = 3, 4,$  and  $5$  channels for both  $^2\Sigma^+$  and  $^2\Pi$  symmetries. In Figure 1(b) and Figure 1(c), the region of the avoided crossings for  $n = 4$  and  $5$  are displayed in detail owing to their importance in the charge exchange calculation. As there are a large number of channels in the current QMOCC calculation, only the radial and rotational couplings for the dominant  $n = 4$  channels are presented, as shown in Figures 2 and 3, respectively. We note that the rotational coupling elements, in Figure 3 for example, are divided by  $R^2$  in the coupled-channel equations, so that their contribution approach zero as  $R$  goes to infinity.

#### B. Cross sections

Using the adiabatic potentials and the nonadiabatic coupling matrix elements obtained with the MRDCI method, QMOCC calculations were performed to obtain the total and state-selective cross sections for  $O^{6+}$  collision with atomic hydrogen for the collision energies 0.1 eV/u - 10 keV/u. In Figure 4, the total cross sections are presented and compared with the available experimental and theoretical data as well as the current AOCC and CTMC calculations. There is good agreement between the present QMOCC calculation and the only other available low-energy calculation, that by Shipsey *et al.* [16], except for energies larger than 2 keV/u. Good agreement between the present QMOCC and AOCC calculations is also achieved in the overlapping energy range of 150

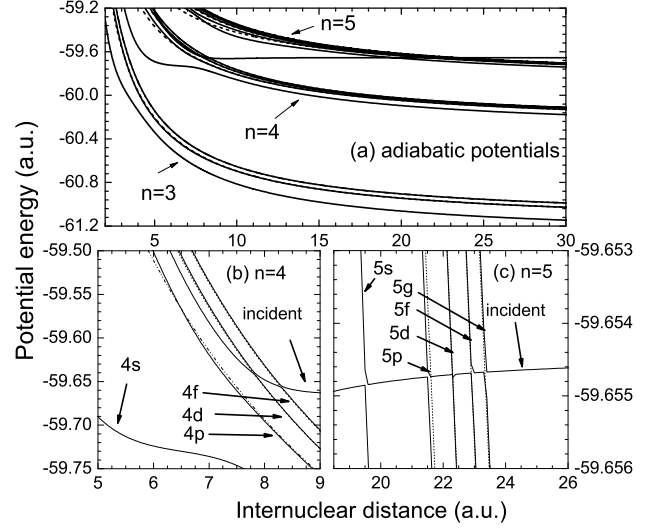


FIG. 1: Adiabatic potentials for  $[OH]^{6+}$  states as a function of internuclear distance. (a): adiabatic potentials for  $n=3, 4,$  and  $5$  channels; (b): adiabatic potentials near the vicinity of the avoided crossings for  $n = 4$  channels; (c) adiabatic potentials near the vicinity of the avoided crossings for  $n = 5$  channels.

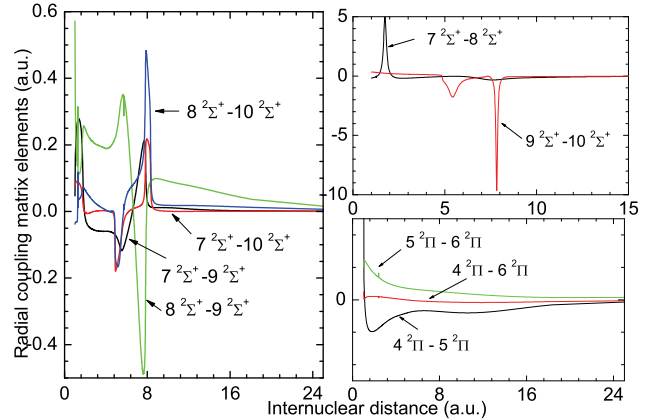


FIG. 2: (Color online) Nonadiabatic radial couplings for the dominant  $n = 4$  channels for both  $^2\Sigma^+$  and  $^2\Pi$  states.

eV/u - 2 keV/u. Compared with the available low energy measurements of Crandall *et al.* [19], Phaneuf *et al.* [20], and Dijkkamp *et al.* [21], there is fair agreement with the QMOCC total cross section. However, the QMOCC total cross section falls mostly within the experimental error bars except for  $E > 2$  keV/u and  $E < 150$  eV/u. Compared with the QMOCC calculation of Shipsey *et al.* and the current AOCC results, the current QMOCC calculations agree better with these measurements for  $E <$

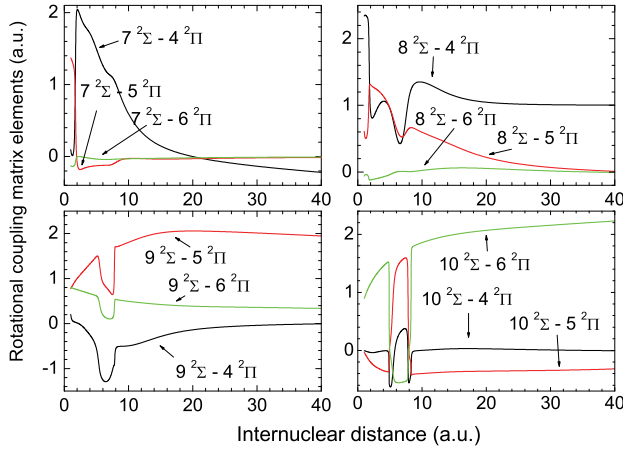


FIG. 3: (Color online) Nonadiabatic rotational couplings for the dominant  $n = 4$  channels.

2 keV/u.

For  $2 < E < 10$  keV/u, the results of the current AOCC calculations agree with all measurements. The AOCC results also agree quite well with CTMC data above about 50 keV/u. Below this energy, the CTMC total cross section displays the expected plateau stemming from the lack of underbarrier, specifically quantum mechanical, charge exchange. The present CTMC results are also consistent with much earlier calculations (not shown in Figure 4 for clarity of the figure) by Olson and Salop [17] and Shipsey *et al.* [16] using CTMC but with an effective charge model of the interaction potentials, but differ slightly in the shape of the curve below about 100 keV/u. We also note that there is good agreement between the AOCC and CTMC results and the only available measurement [18] at high collision energies.

Based on the QMOCC, AOCC, and CTMC calculations, along with the available experimental data, a set of cross sections has been deduced, with the total shown in figure 5, which should aid in X-ray modeling studies. Note that significant rotational coupling effects in the very low collision energy range have been found in the current QMOCC investigation. The underlying dynamical mechanism will be discussed in detail in a separate paper [41].

In Figure 6, the state-resolved cross sections are presented for  $n = 3, 4,$  and  $5$ . At the  $n$ -resolved level,  $n = 4$  dominates almost the entire energy range shown in the figure, while the  $n = 5$  cross sections increase steeply with incident energy, exceeding that of  $n = 4$  at about 5 keV/u. This behavior is a consequence of the avoided crossings at very short internuclear distance, which becomes important at intermediate collision energy. Over the energy range of 0.1 eV/u to 10 keV/u, the contribution from the  $n = 3$  channel is negligible as predicted by the QMOCC calculations. At the  $l$ -resolved level, the  $4d$

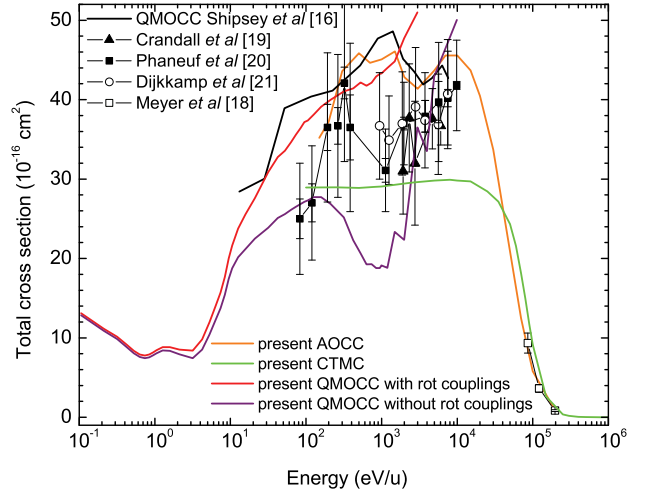


FIG. 4: (Color online) Total SEC cross sections for  $O^{6+}(1s^2) + H(1s) \rightarrow O^{5+}(1s^2 nl) + H^+$ : Comparisons of the total cross section from the present QMOCC, AOCC, and CTMC calculations with the available measurements.

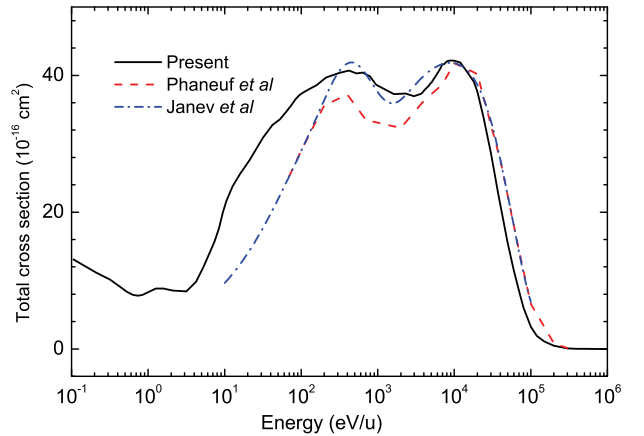


FIG. 5: (Color online) The recommended total cross section for  $O^{6+}(1s^2) - H(1s)$  collisions.

channel dominates for energies between 1 and 4 eV/u, while for lower and higher energies, the  $4f$  and  $4p$  are the primary capture channels, respectively.

The  $n$ -resolved cross sections obtained with the QMOCC, AOCC, and CTMC methods are compared in Figure 7. Note that CTMC  $n = 8$  and AOCC  $n = 7$  cross sections have not been presented to make it easier to distinguish the individual curves. There is excellent agreement between all methods for the dominant,  $n=4$  cross section. For the second most important channel,  $n=5$ , there is also excellent agreement between the

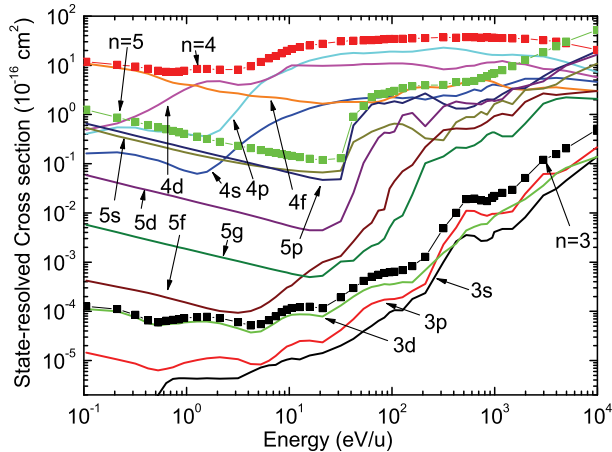


FIG. 6: (Color online) QMOCC SEC calculations of  $l$ -, and  $n$ - resolved cross section for  $O^{6+} + H$  collisions.

QMOCC and AOCC results for 150 to 800 eV/u, but the CTMC results reverse the ordering of  $n=3$  and  $n=5$  for  $E < 20$  keV/u. The steep rise in the  $n = 5$  QMOCC cross section for  $E > 1$  keV/u is likely due to basis set truncation so that the AOCC results for these channels are likely more reliable in this energy range. For  $n > 5$ , the AOCC and CTMC methods give similar  $n$ -resolved cross sections.

Figure 8 compares the QMOCC and AOCC  $l$ -resolved cross sections for  $n = 4$ . There is reasonable agreement in most cases with each of the  $l$ -specific cross sections overlapping, but crossing at different energies. The one exception is the  $4f$  cross section for which there is a factor of about two difference throughout the overlapping range of energies for this state which is very high in the basis set for both QMOCC and AOCC. We have determined a recommended curve for all the  $n, l$ -resolved states individually by utilizing the QMOCC cross sections typically for  $E < 500$  eV/u, the AOCC results above 5 keV/u, and the CTMC and AOCC results above about 100 keV/u (or CTMC alone for high  $n$ -levels), and made a smooth transition between these regimes. The recommended total cross section is obtained by summing the  $n, l$ -resolved recommended curves so that it is consistent with them.

In Figure 9, the recommended total SEC cross section for  $O^{6+} + H$  collision is compared with our previous results for  $N^{6+}$ , previous calculations for  $C^{6+} + H$  (recommended curve [42], AOCC [43]), and measurements ( $C^{6+} + H$  [20, 44],  $N^{6+} + H$  [26], and  $O^{6+} + H$  [20, 21]). The effect of core electrons on the charge exchange process can be examined by comparing different ions with the same charge. There is fair coincidence for the  $N^{6+} + H$  and  $O^{6+} + H$  systems, which have one and two electrons in the tightly-bound  $1s$  shell, respectively. For energies less than 10 keV/u, slight differences exist related to the

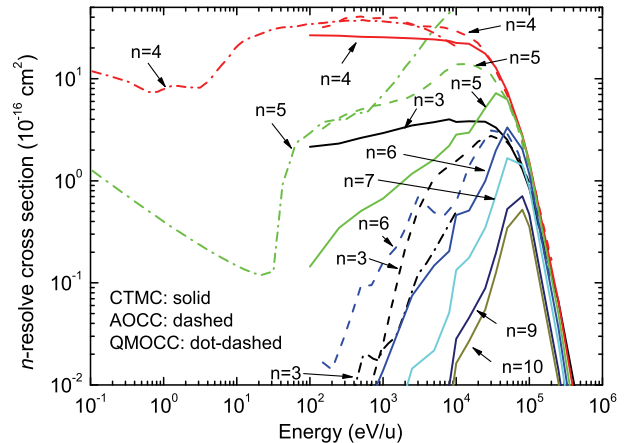


FIG. 7: (Color online)  $n$ -resolved cross section comparison between the QMOCC, AOCC, and CTMC calculations. Dot-dashed lines: present QMOCC calculation; Dashed lines: present AOCC calculation; Solid lines: present CTMC calculation.

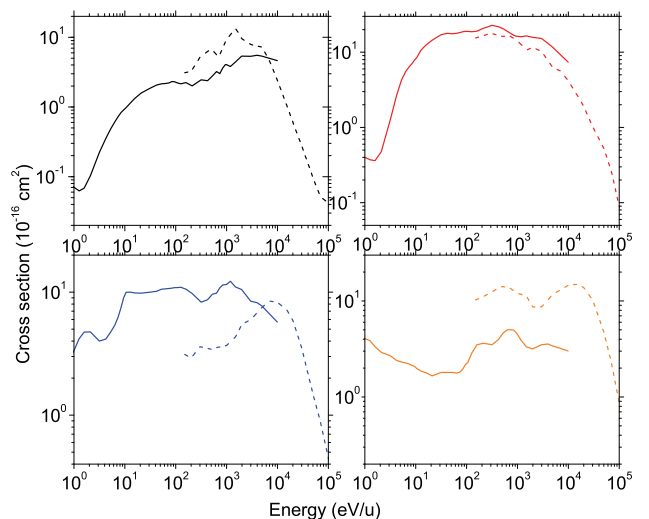


FIG. 8: (Color online)  $l$ -resolved cross section comparison between the QMOCC (solid curves) and AOCC (dashed curves) calculations for  $n = 4$ .

number of capture channels and their symmetry, while for energies larger than 10 keV/u, the total cross sections converge as the core effect becomes negligible. However, large differences are evident for  $C^{6+} + H$ , in which case the initial ion is bare. As the collision energy increases to about 1 keV/u, the core effect becomes less important with the  $C^{6+}$  cross section approaching that of the  $O^{6+}$  and  $N^{6+}$  cross sections. These trends are evi-

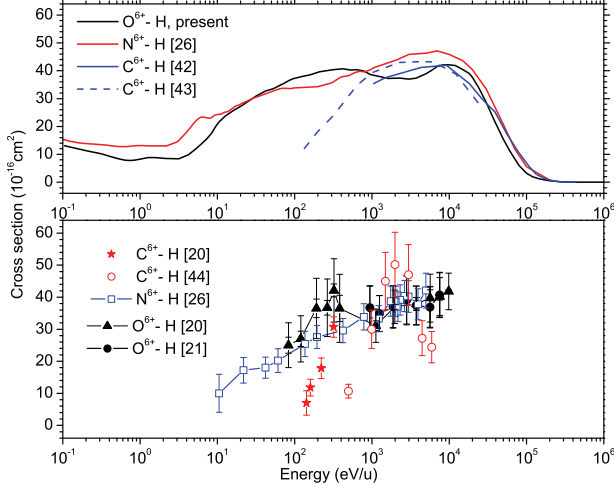


FIG. 9: (Color online) Total SEC cross section comparison between  $C^{6+}$ ,  $N^{6+}$ , and  $O^{6+}$  with H.

dent in both the experimental and theoretical total SEC cross sections suggesting for collision energies less than  $\sim 500$  eV/u, that the atomic structure of the incident and product ions cannot be ignored.

For convenience in astrophysical modeling, the total and state-selective rate coefficients for charge exchange in collision of  $O^{6+}$  with H were calculated. These are compared with the total rate coefficient for  $N^{6+} + H$  in Figure 10. A small difference between the total rate coefficient is evident for temperatures  $T < 10^7$  K, which is consistent with the small difference in the total cross sections presented in Figure 9. For the  $l$ -resolved rate coefficients for  $O^{6+} + H$ , as shown in Figure 11 along with those for  $N^{6+} + H$ , the  $n = 4, l$  channels dominate, while the  $n = 5, l$  channels' contributions increase with increasing temperature becoming significant for  $T > 10^7$  K. Note that the total rate coefficients were obtained with the recommended cross section, while the state-selective values were computed using the QMOCC results. Compared with the total rate coefficients, there are much larger differences in the state-selective rate coefficient not only for  $T < 10^7$  K, but also for higher temperatures, where the total rate coefficients are nearly the same for these two systems.

#### IV. CONCLUSIONS

Charge exchange for collisions of  $O^{6+}(1s^2 \ ^1S)$  and atomic hydrogen have been investigated systematically utilizing three different methods (QMOCC, AOCC, and CTMC). Total and state-selective cross sections have been computed for the large collision energy range of 0.1 eV/u - 1000 keV/u. For the QMOCC method, a hybrid

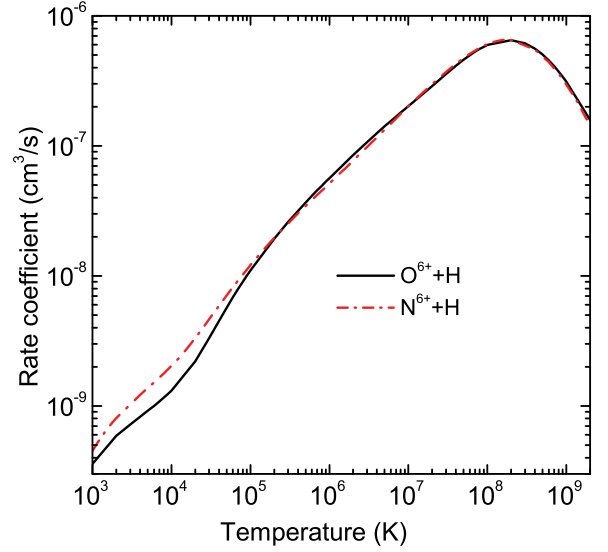


FIG. 10: (Color online) Total theoretical SEC rate coefficients for collision of  $O^{6+} + H$  and  $N^{6+} + H$ .

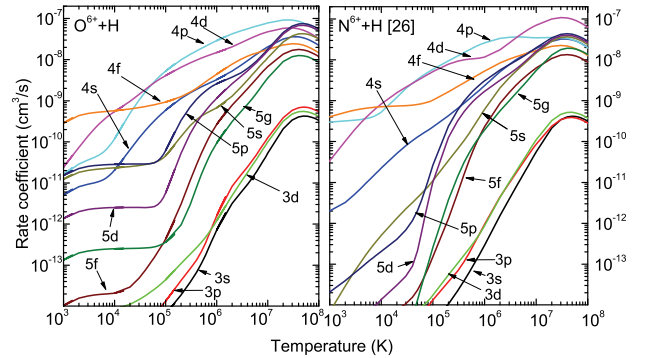


FIG. 11: (Color online)  $n, l$ -resolved SEC rate coefficients for  $O^{6+} + H$  and  $N^{6+} + H$ .

brid basis set was applied within a MRDCI calculation to obtain accurate adiabatic potentials and nonadiabatic coupling matrices. Generally, there is good agreement between the present QMOCC, AOCC, and CTMC results and with the available experimental and theoretical data. SEC cross sections were obtained at the total,  $n$ -, and  $l$ -specific levels. Based on the present QMOCC, AOCC, and CTMC calculations, a recommended set of cross sections has been deduced that will aid in X-ray spectral modeling investigations.

## Acknowledgments

This work was partially supported by NASA grants NNX09AC46G and NNG09WF24I from the Astronomy

and Physics Research and Analysis Program. Y.W. also acknowledges the National Natural Science Foundation of China (Grant Nos. 11025417, 10974021, and 10979007).

- 
- [1] Lisse C M, Dennerl K, Enghauser J, Harden M, Marshall F E, Mumma M J, Petre R, Pye J P, Ricketts M J, Schmitt J, Trmper J, and West R G 1996 *Science*, **274**, 5285, 205
- [2] Cox D P 1998, *Lect. Notes Phys.*, **506**, 121
- [3] Cravens T E, Robertson I P, and Snowden S L 2001 *J. Geophys. Res.*, **106**, 24883
- [4] Robertson I P, Cravens T E, Snowden S, and Linde T 2001 *Space Sci. Rev.*, **97**, 401
- [5] Robertson I P, and Cravens T E 2003 *Geophys. Res. Lett.*, **30**, 8, 22
- [6] Robertson I P, and Cravens T E 2003 *J. Geophys. Res.*, **108**, A10, LIS 6
- [7] Wargelin B J, Markevitch M, Juda M 2004 *Astro. J.*, **607**, 1, 596
- [8] Koutroumpa D, Acero F, Lallement R, Ballet J, and Kharchenko V 2007 *Astronomy & Astrophysics* **475**, 901
- [9] Koutroumpa D, Lallement R, Kharchenko V, Dalgarno A, Pepino R, Izmodenov V, and Quémerais E 2006 *Astronomy & Astrophysics*, **460**, 289
- [10] Koutroumpa D, Smith R K, Edgar R J, Kuntz K D, and Plucinsky P P 2011 *Astro. J.*, **726** 91
- [11] Simcic J, Schultz D R, Mawhorter R J, Greenwood J B, Winstead C, McKoy B V, Smith S J, 2010 *Astro. J.* **722** 435
- [12] Kuntz K D, and Snowden S L 2000 *Astro. J.*, **543**, 1, 195
- [13] Horanyi M, Cravens T E, and Waite J H Jr. 1988 *J. Geophys. Res.*, **93**, 7251
- [14] Kharchenko V A, Bhardwaj A, Dalgarno A, Schultz D R, and Stancil, P C 2008 *J. Geophys. Res. A*, **113**, 8229
- [15] Hui Y, Schultz D R, Kharchenko V A, Bhardwaj A, Branduardi-Raymont, G, Stancil P C, Cravens T E, Lisse C M, & Dalgarno A 2010, *J. Geophys. Res. A*, **115**, 07102
- [16] Shipsey E J, Browne J C and Olson R E 1981 *J. Phys. B*, **24** 869.
- [17] Olson R E and Salop A, *Phys. Rev. A* 1977 **16** 531.
- [18] Meyer F W, Phaneuf R A, Kim H J, Hvelplund P, and Stelson P H, *Phys. Rev. A* 1979 **19** 515.
- [19] Crandall D H, Phaneuf R A, and Meyer F W, *Phys. Rev. A* 1979 **19** 504.
- [20] Phaneuf R A, Alvarez I, Meyer F W, and Crandall D H, *Phys. Rev. A* 1982 **26** 1892.
- [21] Dijkkamp D, Ciric D, de Boer A, de Heer F J, and Vlieg E, *J. Phys. B* 1985 **18** 4763.
- [22] Phaneuf R A, Janev R K, and Pindzola M S, in *Atomic Data for Fusion* 1987 Vol. 5, ORNL-6090.
- [23] Janev R K, Winter H P, and Fritsch W 1995 in *Atomic and Molecular Processes in Fusion Edge Plasma*, Janev R. K. (ed.). Plenum Press, New York, p. 341.
- [24] Zygelman B, Cooper D L, Ford M J, Dalgarno A, Gerratt J, Raimondi M, 1992 *Phys. Rev. A* **46**, 3846.
- [25] Wang J G, Stancil P C, Turner A R, and Cooper D L, 2003 *Phys. Rev. A* **67**, 012710; Wang J G, Stancil P C, Turner A R, and Cooper D L, 2004 *Phys. Rev. A* **69**, 062702.
- [26] Wu Y, Stancil P C, Liebermann H P, Funke P, Rai S N, Buenker R J, Schultz D R, Hui Y 2011 *Phys. Rev. A* **84**, 022711.
- [27] Fritsch W and Lin C D 1991 *Phys. Rep.* **202**, 1.
- [28] Abrines R and Percival I C, 1966 *Proc. Phys. Soc.* **88** 861.
- [29] Olson R E and Salop A 1977 *Phys. Rev. A* **16** 531.
- [30] Buenker R J, and Peyerimhoff S D 1974 *Theoret. Chim. Acta* **35**, 33; 1975 *Theoret. Chim. Acta* **39**, 217; Buenker R J, *Int. 1986 J. Quantum Chem.* **29**,435; Buenker R J, 1980 in *Proceedings of the Workshop on Quantum Chemistry and Molecular Physics*, ed. P. G. Burton (University of Wollongong Press, Wollongong, Australia, 1980), p. 1. 5. 1.; Buenker R J, 1981 *Studies in Physical and Theoretical Chemistry* (ed. R. Carbo), *Current Aspects of Quantum Chemistry* Vol. 21, p.17 (Elsevier, Amsterdam, 1982); Buenker R J, *Studies in Physical and Theoretical Chemistry* (ed. R. Carbo), *Current Aspects of Quantum Chemistry* 1981 Vol. 21, p.81 (Elsevier, Amsterdam, 1982).
- [31] Buenker R J and Phillips R A 1985 *J. Mol. Structure (THEOCHEM)* **123**, 291; Krebs S, and Buenker R J 1995 *J. Chem. Phys.* **103**, 5613; Buenker R J and Krebs S 1999 in *Recent Advances in Multireference Methods* (ed. K. Hirao), p. 1. (World Scientific, Singapore).
- [32] Dunning T H Jr. 1989 *J. Chem. Phys.* **90**, 1007.
- [33] Kelly R L, 1987 *J. Phys. Chem. Ref. Data* **16**, Suppl. 1, 1.
- [34] Bransden B H and McDowell M R C, 1992 *Charge Exchange and the Theory of Ion-Atom Collisions* (Clarendon Press, Oxford, 1992).
- [35] Turner A R, Cooper D L, Wang J G, and Stancil P C 2003 *Phys. Rev. A* **68**, 012704.
- [36] Kuang J and Lin C D 1996 *J. Phys. B* **29**, 1207.
- [37] Kuang J and Lin C D 1996 *J. Phys. B* **29**, 5443.
- [38] Edgu-Fry E, Wech A, Stuhlman J, Lee T-G, Lin C D, and Cocke C L 2004 *Phys. Rev. A* **69**, 052714.
- [39] Becker R L and MacKellar A D 1984 *J. Phys. B: At. Mol. Phys.* **17** 3923.
- [40] Schultz D R, Stancil P C, and Raković M J 2001 *J. Phys. B* **34**, 2739.
- [41] Wu Y, Stancil P C, Buenker R J, and Schultz D R (unpublished).
- [42] Janev R K, Phaneuf R A and Hunter H T 1988 *Atomic Data and Nuclear Data Tables* **40**, 249.
- [43] Fritsch W and Lin C D 1984 *Phys. Rev. A* **29** 3039.
- [44] Panov M N, Basalaev A A and Lozhkin K O 1983 *Phys. Scr.* **T3**, 124.

# Observations of EUV spectra from tungsten and lanthanide ions in LHD

SUZUKI Chihiro, KOIKE Fumihiko<sup>1</sup>, MURAKAMI Izumi, KATO Takako,  
GOTO Motoshi, NAKANO Tomohide<sup>2</sup>, TAMURA Naoki, SUDO Shigeru,  
HARTE Colm S<sup>3</sup>, and O'SULLIVAN Gerard<sup>3</sup>

*National Institute for Fusion Science, 322-6 Oroshi-cho, Toki 509-5292, Japan*

*1) School of Medicine, Kitasato University, 1-15-1 Kitasato, Minami-ku, Sagamihara  
252-0374, Japan*

*2) Japan Atomic Energy Agency, 801-1 Mukoyama, Naka 311-0193, Japan*

*3) University College Dublin, Belfield, Dublin 4, Ireland*

*e-mail: csuzuki@nifs.ac.jp*

## Abstract

We have measured EUV spectra from tungsten, gadolinium and neodymium ions in optically thin plasmas produced in the Large Helical Device (LHD) at the National Institute for Fusion Science. Following the injections of solid pellets into hydrogen plasmas, EUV spectra were recorded by a grazing incidence spectrometer under the conditions with various electron temperatures. It has clearly been observed that the spectral feature changes from discrete to quasicontinuum as the electron temperature decreases. Several spectral lines from charge states in the neighborhood of Cu-like ions were identified in the discrete features. The atomic structure calculations suggest that the quasicontinuum emissions largely arise from  $\Delta n=0$  transitions of open 4f subshell ions.

**Keywords:** EUV spectra, tungsten, gadolinium, neodymium, UTA, LHD

## 1. Introduction

Extreme ultraviolet (EUV) emission spectra from highly charged high  $Z$  ions have recently drawn considerable attention in terms of some applications as well as basic atomic physics. In fusion research, tungsten will be used as a plasma-facing component in the forthcoming International Thermonuclear Experimental Reactor (ITER) [1]. For future development of semiconductor lithography, highly charged lanthanide ions are being considered as potential light sources around 6.7 nm after the commercial use of sources using tin plasmas at 13.5 nm [2,3].

This article reviews the recent measurements of EUV spectra from tungsten, gadolinium and neodymium ions in optically thin plasmas produced in the Large Helical Device (LHD) at the National Institute for Fusion Science [4–6]. Magnetically confined torus plasma can be considered as an ideal light source from highly charged ions of high- $Z$  impurities

without complicated opacity effects often observed in laser-produced plasmas. Therefore the present study would provide experimental databases useful for the benchmarking with theoretical calculations of the temperature/ $Z$  dependence of spectral feature.

## 2. Experiment

The LHD is one of the largest devices for magnetically confined fusion research and is equipped with several superconducting helical and poloidal coils [7]. Small amounts of solid tungsten, gadolinium and neodymium hydride are introduced by a tracer encapsulated solid pellet (TESPEL) [8] into a low density background hydrogen plasma of which density is of the order of  $10^{19} \text{ m}^{-3}$ . Total number of the injected tracer material is of the order of  $10^{17}$  atoms. The LHD is equipped with five sets of neutral beam injection (NBI) systems as a main heating device. Spatial profiles of electron density and temperature are measured by a laser Thomson scattering diagnostic system [9] with spatial and temporal resolution of about 20 mm and 33 ms, respectively.

Following the pellet injections, EUV spectra are recorded by a 2 m Schwob Fraenkel grazing incidence spectrometer [10], groove density of which is  $600 \text{ mm}^{-1}$ , under the conditions with various electron temperatures. The spectrometer contains two microchannel plates with phosphor screens coupled via fiber optic conduit to a 2048 channel silicon photodiode array thus permitting the simultaneous recording of two different spectral regions. Note that the measured spectra are line-integrated ones along the region with different electron temperature represented by the Thomson scattering diagnostic data. The frame rate of the detector was typically 0.2 s in this study and the overall spectral resolution is about 0.01 nm. The wavelength of the spectrometer is carefully calibrated by observing known lines from impurities in other discharges.

## 3. Results and discussion

Tungsten spectra were observed around 5 nm and 18 nm regions [4,5]. Discrete spectral feature is observed only in the 5 nm region when the electron temperature is higher than 3 keV. A quasicontinuum spectral feature referred to as unresolved transition array (UTA) is usually observed in the 5 nm region in lower temperature plasmas. A broad quasicontinuum feature in the 18 nm region appears only in very low temperature plasmas below 1 keV, and its peak position moves to shorter wavelength side as the temperature increases.

Figure 1 shows three different EUV spectra in the 5 nm region with a tungsten pellet injection when the peak electron temperature were (a) 3.5 keV, (b) 0.5 keV and (c) 1.1 keV. The discrete lines around 4.7 nm and 6.1 nm in Fig. 1 (a) are identified as emissions from

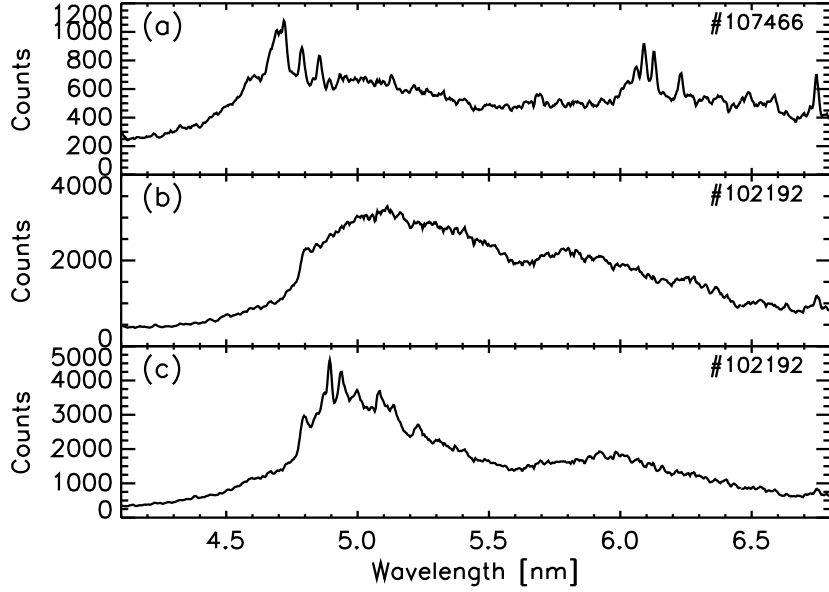


Figure 1: Three different types of EUV spectra around 5 nm with a tungsten pellet injection under the peak electron temperature of (a) 3.5 keV , (b) 0.5 keV and (c) 1.1 keV.

highly charge states in the neighborhood of Cu-like tungsten ions ( $W^{39+}$ – $W^{45+}$ ) found for the first time in LHD. Note that a weak quasicontinuum background is still observed due probably to the emission from the low temperature edge region. On the other hand, only a quasicontinuum emission was observed in Fig. 1 (b). Under the intermediate temperature shown in Fig. 1 (c), the spectral feature is basically quasicontinuum except for some discrete structure around 4.9 nm due to charge states close to Ag-like tungsten ions ( $W^{27+}$ – $W^{29+}$ ).

Figure 2 shows three different types of EUV spectra in the 6.0–9.3 nm region measured in the same discharge with a gadolinium pellet injection [6]. The spectra in Fig. 2 (a), (b) and (c) correspond to the timings when peak electron temperatures were 2.2, 0.24 and 1.0 keV, respectively. A characteristic hollow plasma was formed in the period of Fig. 2 (b) as the plasma temperature locally became almost zero near the core region. A sparse spectrum with many discrete lines was observed in Fig. 2 (a). Several discrete spectral lines were identified as Ni- and Cu-like ions. On the other hand, clear spectral narrowing of the UTA took place around 6.8 nm in Fig. 2 (b), together with the appearance of some discrete lines of Ag- and Pd-like ions. In Fig. 2 (c), the bandwidth of the UTA structure from open 4p/4d subshell ions became broader and the center wavelength moved slightly to longer wavelength around 6.9 nm. We have observed the same trend of the EUV

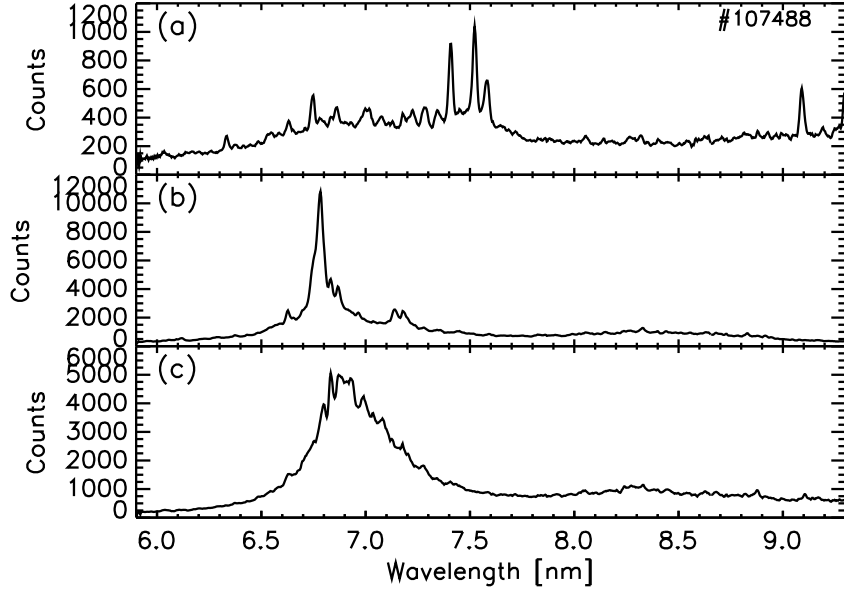


Figure 2: Three different types of EUV spectra in the 6.0–9.3 nm region measured in the same discharge with a gadolinium pellet injection when the peak electron temperatures are (a) 2.2, (b) 0.24 and (c) 1.0 keV.

spectral feature also in another discharge with a neodymium pellet injection although the center wavelength of the UTA from neodymium ions is around 8.0 nm. These observations imply drastic change in charge state distribution in the plasma caused by the change in electron temperature.

The atomic structure calculations have been performed for open  $N$  shell tungsten ions using FAC and Cowan’s codes. Wavelengths and line strengths for  $n=4-4$ ,  $4-5$  and  $5-5$  transitions of  $W^{7+}-W^{27+}$  have been calculated using the Cowan’s code to establish the region of the emission and to give an insight into the observed spectra [4,5]. Because of the large number of levels arising from the open 4f subshell, it was necessary to make some adjustments to the code to permit the handling of large matrices. The results indicate that the quasicontinuum emissions in the 5 nm and 18 nm regions largely arise from  $n=4-4$  and  $5-5$  transitions, respectively, and that the contributions of open 4f subshell ions should be important.

For more detailed analysis, we have tried to simulate the observed tungsten spectra in Fig. 1 (a) and (b) using FAC code. Though the code calculations were performed for  $W^{14+}-W^{71+}$  including the effect of configuration interaction, only  $n=4-4$  transitions were considered in the calculation for  $W^{14+}-W^{24+}$  due to the limited computational time. A

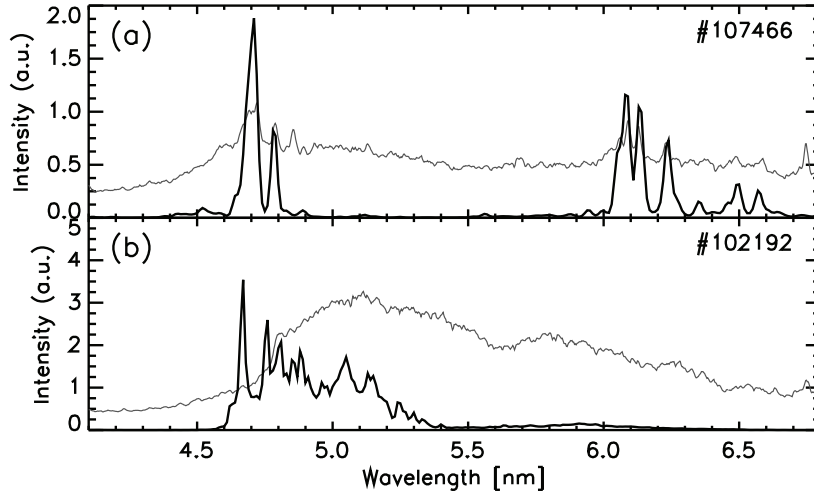


Figure 3: Measured (grey) and synthesized (solid) spectra at an electron temperature of (a) 3 keV and (b) 0.5 keV.

spectrum for each ion stage was calculated using collisional-radiative model, assuming the measured plasma parameters. Then synthesized spectra were obtained by assuming appropriate ion abundances. The results are shown in Fig. 3 where the measured and the synthesized spectra are drawn by grey and solid lines, respectively. As shown in Fig. 3 (a), the intensities and positions of several sharp peaks from  $W^{39+}-W^{45+}$  at 3 keV are in good agreement with the observation. In contrast, it was difficult to reproduce the measured spectrum obtained at 0.5 keV as shown in Fig. 3 (b). In particular, the disagreement of intensity is significant at the measured broad structure around 5.7 nm. It may be necessary to include  $n=4-5$  transitions though it would require huge computational time.

The trend of the UTA feature of gadolinium ions shown in Fig. 2 (b) and (c) agrees qualitatively with FAC and Cowan's code calculations published in previous papers [2,11] which concluded that the center wavelength of the band moves toward shorter wavelength as the ion stage increases up to Ag-like ions around 6.8 nm, while it moves back to longer wavelength as the ion stage further goes up beyond Ag-like ions. The more detailed theoretical analysis of the measured spectra for gadolinium ions have been performed using a group of computer codes GRASP92, which will be reported in the near future.

#### 4. Conclusion

We have measured different types of EUV spectra from tungsten ( $Z=74$ ), gadolinium ( $Z=64$ ) and neodymium ( $Z=60$ ) ions in optically thin LHD plasmas with a pellet injection

by a grazing incidence spectrometer. The measured spectral features of tungsten ions have been compared with calculations of FAC and Cowan's codes. The quasicontinuum UTA features in the 5 nm and 18 nm regions are primarily due to  $n = 4-4$  and  $5-5$  transitions, respectively. A large contribution of charge states lower than  $W^{27+}$  is suggested in both wavelength regions. Drastic change in the spectral feature of gadolinium and neodymium has been clearly observed following the change in electron temperature. Several discrete lines in the highest and the lowest temperatures have been identified as  $n = 4-4$  or  $4-5$  transitions of Ni-, Cu-, Ag- and Pd-like ions.

### Acknowledgement

This work was partly supported by the JSPS-NRF-NSFC A3 Foresight Program in the field of Plasma Physics (NSFC: No.11261140328). This work was carried out with the support and under the auspices of the NIFS collaboration research program (NIFS10KLPF011, NIFS10KLPF010). This work was also supported by a grant-in-aid for Young Scientists (B) from Japan Society for the Promotion of Science. The authors acknowledge the LHD experiment group for their assistance.

### References

- [1] R. A. Pitts et al, Phys. Scr., **T138**, 014001 (2009).
- [2] S. S. Churilov et al, Phys. Scr., **80**, 045303 (2009).
- [3] D. Kilbane and G. O'Sullivan, J. Appl. Phys., **108**, 104905 (2010).
- [4] C. S. Harte et al., J. Phys. B: At. Mol. Opt. Phys., **43**, 205004 (2010).
- [5] C. Suzuki et al., J. Phys. B: At. Mol. Opt. Phys., **44**, 175004 (2011).
- [6] C. Suzuki et al., J. Phys. B: At. Mol. Opt. Phys., **45**, 135002 (2012).
- [7] A. Komori et al, Nucl. Fusion, **49**, 104015 (2009).
- [8] S. Sudo and N. Tamura, Rev. Sci. Instrum., **83** 023503 (2012).
- [9] K. Narihara et al, Rev. Sci. Instrum., **72**, 1122 (2001).
- [10] J. L. Schwob et al, Rev. Sci. Instrum., **58**, 1601 (1987).
- [11] T. Otsuka et al., Appl. Phys. Lett., **97**, 111503 (2010).

# Lasing Potential of Extreme Ultraviolet Light Using Recombining Nitrogen Plasma

YAMAMURA Shuhei<sup>†</sup>, OZAWA Takuya, HORIOKA Kazuhiko,  
and KAWAMURA Tohru

*Department of Energy Sciences, Tokyo Institute of Technology  
Nagatsuta 4259, Midori, Yokohama, Kanagawa, 226-8502, Japan*

<sup>†</sup> *e-mail* : [yamamura.s.aa@m.titech.ac.jp](mailto:yamamura.s.aa@m.titech.ac.jp)

## Abstract

Hydrogen-like nitrogen plasma is expected as one of light sources to generate extreme ultraviolet (EUV) light. A hydrogen-like nitrogen ion emits a photon at 13.4 nm with an optically allowed transition from  $n = 3$  to  $n = 2$ , where  $n$  stands for a principal quantum number. We focus on the properties of the population inversion between  $n = 3$  and  $n = 2$ , and estimate the lasing potential by numerical simulation. In our previous study, higher gain-length products  $GL$  are obtained and desired plasma conditions are found. In this paper, our study up to now is surveyed and the effect of photo processes due to amplified EUV light during the propagation in plasma is considered. The present status of this study will be also briefly reported.

**Keywords:** Hydrogen-like nitrogen plasma, Population inversion, Photo processes

## 1. Introduction

A development of a short-wavelength light source has been promising for industrial applications in variety of fields, for example, micro-fabrication technology, elucidation of atomic and/or molecular structure of material, and biological science [1]. The typical wavelength of extreme ultraviolet (EUV) light is 5 - 40 nm, and the experiments for EUV light generation have been done by high current discharge and/or intense laser irradiation. At the moment, the related experiments to generate EUV light source at 13.5 nm by discharge produced plasma has been performed for the next generation semiconductor lithography [2]. Hydrogen-like nitrogen plasma is also one of promising light sources for the purpose. A hydrogen-like nitrogen ion emits a photon at 13.4 nm with an optically allowed transition from  $n = 3$  to  $n = 2$ . Here,  $n$  stands for a principal quantum number. The wavelength is near that for the next generation semiconductor lithography. An experiment for the lasing of the EUV light by high current discharge was performed, however there was no lasing [3].

In this study, we focus on the properties of the population inversion between  $n = 3$  and  $n = 2$ , and estimate the lasing potential by numerical simulation. Estimated are plasma

conditions for the lasing with high gain-length products  $GL$ . In general,  $GL > 5$  is needed [4]. In our previous study, plasma conditions giving  $GL > 10$  were estimated [5]. Since the propagation of the EUV light were not considered in the calculation, photo processes by the EUV light are being examined now. In this paper, we will survey our previous study, and briefly report the progress on the contribution of photo processes.

## 2. Calculation Conditions

In this calculation, to demonstrate a recombining phase, stepwise cooling shown in Fig.1 is adopted. Ion density is kept constant to exclude the effect of plasma hydrodynamic motion, and lasing potential can be estimated in the viewpoint of atomic population kinetics. In Fig.1,  $T_H$  and  $T_L$  are an initial and a final electron temperatures before and after cooling, respectively. The detail descriptions on the atomic population kinetics can be referred to Ref.[5].

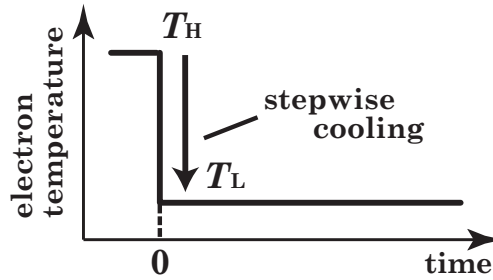


Figure 1: Time evolution of an electron temperature profile.

## 3. Calculation Results and Discussion

Fig.2 shows a typical time evolution of the population densities per statistical weights of hydrogen-like nitrogen ions.  $T_H$  and  $T_L$  are assumed to be 300 eV and 10 eV, respectively. The ion density  $n_i$  is  $10^{18} \text{cc}^{-1}$ . It is found that the population inversion is created between  $n = 3$  and  $n = 2$ . The duration of the population inversion becomes shorter with increase in an ion density  $n_i$  [5,6]. Fig.3 shows the corresponding gain coefficient with the plasma condition. Since the resultant gain  $G$  shows a time-dependent feature, a time-averaged gain is estimated to get insight into the lasing potential. Furthermore, the maximum plasma length  $L$  can be approximately estimated by the product of  $c\tau_e$ , where  $c$  is a speed of light and  $\tau_e$  is the duration of the population inversion (see Fig.3). At  $n_i = 10^{18} \text{cc}^{-1}$ , a high lasing property is obtained.

In our previous study, the processes associated with doubly excited states are consid-

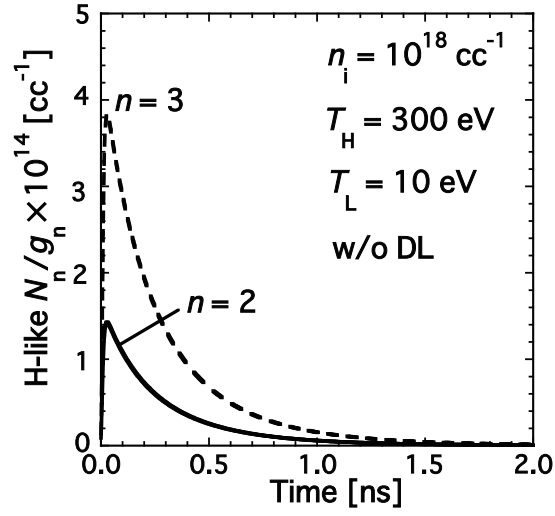


Figure 2: Time evolution of population densities per statistical weights of hydrogen-like nitrogen ions at  $T_H = 300$  eV,  $T_L = 10$  eV, and  $n_i = 10^{18} \text{cc}^{-1}$ . In the figure, “DL” means “dielectronic-capture ladderlike processes”.

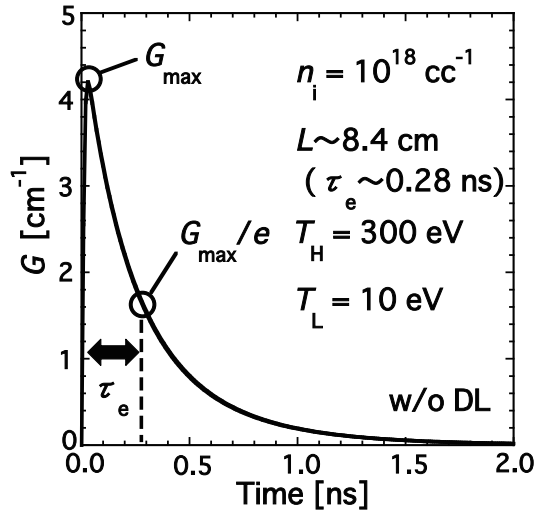


Figure 3: Time evolution of gain coefficient at  $T_H = 300$  eV,  $T_L = 10$  eV, and  $n_i = 10^{18} \text{cc}^{-1}$ . In the figure, “DL” means “dielectronic-capture ladderlike processes”.

ered. The processes are called dielectronic-capture ladderlike (DL) processes, which is proposed by Fujimoto *et al* [7]. The DL processes implicitly include doubly excited states of which outermost electron is in a higher orbital. In Figs.2 and 3, such processes are not included. With the plasma condition shown in Figs.2 and 3, the DL deexcitation is dominant. The DL deexcitations from  $n = 3$  and  $4$  to  $n = 2$  reduce the gain [5,6].

Fig.4 shows the time-averaged gain-length products  $G_{ave}L$  at  $T_L = 10$  eV. At  $n_i = 10^{18} \text{cc}^{-1}$ ,  $G_{ave}L > 10$  is found. In the calculation, however, only collisional processes are included to estimate  $G_{ave}L$ , so photo processes associated with the EUV radiation of 13.4 nm are considered to clarify the property of the EUV light amplification during the propagation in nitrogen plasma.

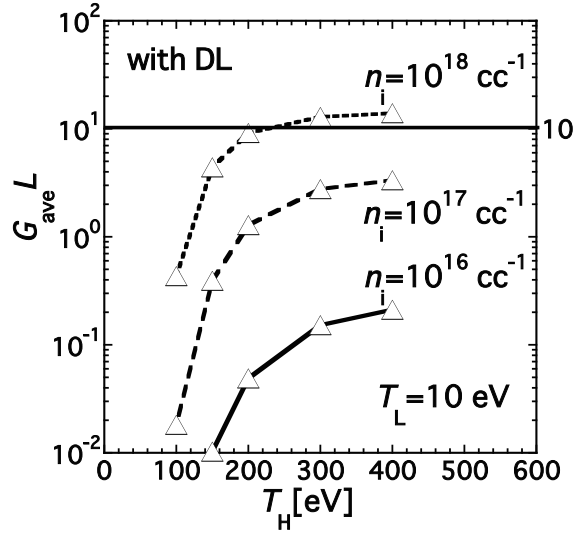


Figure 4: Time-averaged gain-length products  $G_{ave}L$  at  $T_L = 10$  eV.

Fig.5 shows a comparison of rate coefficients between collisional deexcitation and photo excitation at  $T_L = 10$  eV and  $n_i = 10^{18} \text{cc}^{-1}$ . An average ionization degree of nitrogen is assumed to be 6. At the amplified EUV light intensity  $> 0.2 - 0.4 \text{ mW/cm}^2/\text{Hz}$ , it is found that the photo excitations by the EUV light can affect the population densities of  $n = 3$  and  $n = 2$ . In this study, the population inversion is broken due to the collisional deexcitation with DL processes between  $n = 3$  and  $n = 2$ . However, it seems that the photo excitations compensate for breaking of the population inversion. We are developing a rate equation solver with such photo processes as seen in Fig.5 coupled with radiative transfer.

#### 4. Summary and Future Plan

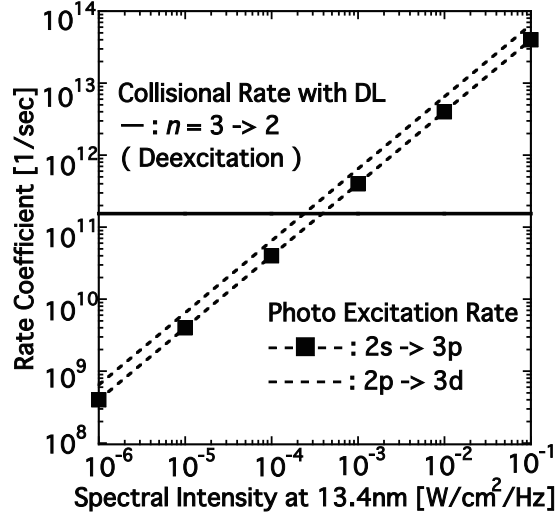


Figure 5: Comparison of rate coefficients between collisional deexcitation and photo excitation at  $T_L = 10$  eV and  $n_i = 10^{18} \text{cc}^{-1}$ . The photo excitation of 2p - 3s transition can be negligible due to its small oscillator strength.

In this paper, we surveyed our previous study, and the recent progress is briefly presented. At  $T_L = 10$  eV and  $n_i = 10^{18} \text{cc}^{-1}$ , high gain-length products can be obtained. It is found that the DL processes have a large contribution to make the population inversion.

Photo excitations between  $n = 3$  and  $n = 2$  must be considered at the amplified EUV light intensity  $> 0.2 - 0.4 \text{ mW/cm}^2/\text{Hz}$  to estimate the radiative property of the EUV light. We will report the results elsewhere.

### Acknowledgement

This work was partly supported by the JSPS-NRF-NSFC A3 Foresight Program in the field of Plasma Physics (NSFC: No.11261140328).

### References

- [1] D. T. Attwood, *Soft X-rays and extreme ultraviolet radiation*, Cambridge University Press (1999).
- [2] Y. Kuroda, K. Hayashi, H. Kuwabara, M. Nakajima, T. Kawamura, and K. Horioka, *NIFS-PROC-90*, 73 (2012).
- [3] Y. Sakai, S. Takahashi, T. Hosokai, M. Watanabe, G-H. Kim, and E. Hotta, *J. Appl.*

- Phys.*, **107**, 083303 (2010).
- [4] R. C. Elton, *X-ray lasers*, Academic Press, INC. (1990).
- [5] T. Ozawa, S. Yamamura, N. Tatsumura, K. Horioka, and T. Kawamura, *Phys. Plasmas*, **19**, 063302 (2012).
- [6] S. Yamamura, T. Ozawa, K. Horioka, and T. Kawamura, to appear in *NIFS-PROC*.
- [7] T. Fujimoto, and T. Kato, *Phys. Rev. A*, **32**, 1663 (1985).

## The Second Announcement

# The 4<sup>th</sup> China-Japan Joint Seminar on Atomic and Molecular Processes in Plasma (AMPP2012)

Jul. 30 – Aug. 4, 2012, Lanzhou, China

### ➤ Scientific Sessions and Publication of the Proceedings

1. All the participants who give a contribution are kindly requested to give an oral presentation for about 30 minutes; 20 minutes will be for talk, and 5-10 minutes for discussion.
2. We will supply the high-definition projector connected with laptop. A Windows-based laptop with Acrobat Reader and Microsoft PowerPoint 2007 is available. The participant is requested to supply their presentation material by CD-ROM or flash disk. If you would like to use the conventional Overhead Projector (OHP), please let us know as early as possible.
3. The contributions to this seminar will be published as one of the issues in the NIFS Research Report series. The details of the instruction for the submission will be announced at the seminar.
4. Selected papers of the contributions will be organized to submit to the relevant international journal. The details will be announced at the seminar.

### ➤ Registration and Fee

Only on-site registration is available, the registration fee will be charged in Chinese Yuan (CNY).

The fee for full registration attendee is CNY 3,000. It includes: full access to all the Scientific Program, book of abstracts, tea/coffee breaks. The fee for student attendee is CNY 1,500. The fee for accompanying person is CNY 1,000. The payment can ONLY be made by CASH. It is also convenient to take cash from the Automatic Teller Machine (ATM) by Visa/Master Card or CITI Bank card.

### ➤ Social program

After the academic talks in the seminar room, we will continue open discussion on the way to Labrang Monastery, Sanke Grasslands in Xiahe county and HIRFL-CSR in Institute of Modern Physics, CAS, Lanzhou.

The Labrang Monastery is located at the foot of the Phoenix Mountain northwest of Xiahe County in Gannan Tibetan Nationality Autonomous Prefecture, Gansu Province. It is one of the six great monasteries of the Geluk (Yellow Hat) school of Tibetan Buddhism. The monastery was built in 1710 by Jiamuyang, the first Living Buddha, and now it is the largest cultural center of the Tibetan Buddhism in Gansu, Qinghai and Sichuan provinces after being built and rebuilt by the Living Buddhas of the ages.

Sanke Grasslands, covering an area of around 70 square kilometers, is a lonely, beautiful place that is a nice change for those from bustling Lanzhou. There are only 4,000 Tibetan nomads on the grasslands. They are living in Tibetan style canvas tents.

### ➤ Arrival and Accommodation

The local organizers will be looking forward to your arrival in the Expert Building of Northwest Normal University on Jul. 30, 2012. In order to help the participants to arrive at the hotel, the local organizers will send some colleagues to the Lanzhou Zhongchuan airport to meet the participants at there.

For convenience of the arrangement, all the participants are encouraged to inform their arrival and departure dates, times, and the flight numbers to [dingxb@nwnu.edu.cn](mailto:dingxb@nwnu.edu.cn) in advance. The local organizers also need your passport number (or ID number for Chinese participants) and your date of birth to book the insurance if you would like to take part in the excursion to Xiahe.

Hotel rooms will be arranged for all the participants by the local organizers.

### ➤ Weather and Temperature

The weather is likely to be hot (the highest temperature approaches 35°C) and dry in Lanzhou but cold (the lowest temperature approaches 7°C) and humid in Xiahe. Especially, the temperature difference between the day and night is quite big (about 35,28°C in the day and 17,7°C in the night in Lanzhou and Xiahe, respectively). The local organizers suggest you to bring a coat or water-proof hard shell with fleece for you. We also suggest the participants to wear comfortable shoes to have a nice excursion.

It is also noticeable that the altitude of Lanzhou is 1,500 meters, while the altitude of Xiahe is mostly higher than 3,000 meters. It is recommended to take some usual medicine travel with you.

### Contact

Prof. Dr. Dong Chenzhong  
Email: [dongcz@nwnu.edu.cn](mailto:dongcz@nwnu.edu.cn)  
Phone: +86-(0)931-7970186  
Fax: +86-(0)931-7971503  
Mail: Northwest Normal University,  
Anning East Road 967, Anning, Lanzhou  
730070 China

Dr. Fumihiko Koike  
Email: [koikef@kitasato-u.ac.jp](mailto:koikef@kitasato-u.ac.jp)  
Phone: +81-(0) 42-778-9225, 8029  
Fax: +81-(0) 42-778-8441  
Mail: Kitasato University, Kitasato  
1-15-1 Sagamihara  
228-8555 Japan

### Seminar Secretary

Dr. Ding Xiaobin  
Email: [dingxb@nwnu.edu.cn](mailto:dingxb@nwnu.edu.cn)  
Alternative Email: [ding.xiaobin2004@gmail.com](mailto:ding.xiaobin2004@gmail.com)  
Phone: +86-(0)931-7970186

**For more information, please visit:** <http://ampp.nwnu.edu.cn/>

## AMPP2012 Program

Tuesday, 31st July, 2012

Time		Title
08:30-09:30	<b>C. Z. Dong</b> Opening, Welcome address, Group Photo	
09:30-10:30	<b>Chair: S. Morita</b>	
09:00-10:00	Y. Sakai	Light emission from sputtered or backscattered atoms on tungsten surfaces under ion irradiation
10:00-10:30	D. Hoffmann	High Energy Density Physics with Intense Ion and laser Beams
10:30-10:50	<b>Coffee Break</b>	
10:50-12:20	<b>Chair: J. Yan</b>	
10:50-11:20	Y. T. Zhao	Interaction of low energy highly charged ions with solids and plasma
11:20-11:50	H. Tanuma	Laboratory Experiments for Revealing Soft X- ray Emissions from Solar Wind Charge Exchange
11:50-12:20	L. F. Zhu	Accurate dynamic parameters of noble atoms studied by high-resolution inelastic X-ray scattering
12:20-14:30	<b>Lunch</b>	
14:30-16:00	<b>Chair:H. Nishimura</b>	
14:30-15:00	H. Sakaue	Spectroscopy of highly charged tungsten ions with EBITs
15:00-15:30	M. G. Su	Laser Induced Plasma spectroscopy and Its Applications on Element Analysis
15:30-16:00	N. Nakamura	Dielectronic recombination of highly charged heavy ions studied with the Tokyo electron beam ion trap
16:00-16:20	<b>Coffee Break</b>	
16:20-17:50	<b>Chair:L. F. Zhu</b>	
16:20-16:50	G. Y. Liang	A simulation package --- SASAL for soft X-ray and EUV spectroscopy of astrophysical and laboratory
16:50-17:20	K. Takahashi	Doubly Excited States and Their Dissociation Processes of Simple Molecules

17:20–17:50 S. X. Tian Imaging Dynamics of the Dissociative Electron Attachment to Molecules

17:50–18:20 Y. B. Fu Relativistic Study on Dielectronic Recombination

**Wednesday, 1st August, 2012**

**08:30–10:30 Chair:H. Tanuma**

08:30–09:00 S. Morita Recent progress on the study of atomic spectroscopy in LHD and collaboration with China on high-Z impurity spectroscopy

09:00–09:30 H. Y. Zhou Study of EUV spectra from low-Z and medium-Z impurity ions based on a grazing-incidence flat-field EUV spectrometer in HL-2A plasmas

09:30–10:00 Y. Nakano X-ray and Auger electron study of highly charged ions using resonant coherent excitation

10:00–10:30 Y. M. Li Study of excitation for Alkali-like ions with complete-coupling iteration method

**10:30–10:50 Coffee Break**

**10:50–12:20 Chair:G. Y. Liang**

10:50–11:20 F. Koike Theoretical aspects of electron correlations and term dependences in the electronic states of highly charged atomic ions

11:20–11:50 J. L. Zeng Radiative opacity of high-Z plasmas by hybrid DLA and DCA models

11:50–12:20 H. Nishimura Quantitative hard x-ray spectroscopy for energy transport in high intensity laser produced plasma

**12:20–14:30 Lunch**

**14:30–16:00 Chair:S. X. Tian**

14:30–15:00 X. Gao An effective eigenchannel R-matrix method for calculating electron-ion scattering processes with spectroscopic precision

15:00–15:30 T. Kawamura Potential of cold K-alpha radiation generated by an intense ion beam for cold dense plasma diagnostics

15:30–16:00 B. W. Li Recent progress in source development for EUV lithography and other applications

**16:00–16:20 Coffee Break**

**16:20–17:50 Chair:H. Sakaue**

- |             |              |   |
|-------------|--------------|---|
| 16:20–16:50 | T. Nishikawa | Atomic process modeling based on plasma microfield  |
| 16:50–17:20 | C. C. Sang   | Energies, Auger and radiative probabilities of doubly-excited states $1s23l3l'$ for Be-like neon  |
| 17:20–17:50 | L. Y. Xie    | Relativistic distorted-wave study on electron impact excitation and polarization of line radiation of many electron atoms and highly charged ions |
| 17:50–18:20 | Q. H. Yuan   | Non-thermal atmospheric pressure plasma jets driven with dual-frequency power sources   |

**Thursday, 2nd August, 2012**

**08:30–10:30 Chair:J. L. Zeng**

- |             |             |  |
|-------------|-------------|--|
| 8:30–9:00   | A. Ichimura | Multiple ionization of Ar <sub>2</sub> by slow highly charged ions                           |
| 09:00–09:30 | Y. Wu       | Theoretical investigation of charge exchange between highly-charged solar wind ions and H&He |
| 09:30–10:00 | C. Suzuki   | Observations of EUV spectra from tungsten and lanthanide ions in LHD                         |

**10:00–10:20 Coffee Break**

**10:20–11:20 Chair:F. Koike**

- |             |             |  |
|-------------|-------------|--|
| 10:20–10:50 | S. Yamamura | Lasing Potetial of Extreme Ultraviolet Light Using Recombining Nitrogen Plasma |
| 10:50–11:20 | L. Zhang    | Initial Measurement of Deuterium Molecular Spectrum in the EAST Edge           |

**11:20–13:00 Lunch**

**13:00–18:00 Excursion & HIRFL Tour**

# AMPP2012 Registered Participants

Date: July 5, 2012

No	FirstName	LastName	affiliation	email	abstract	sub	Nationality
1	Xiang	Gao	Beijing Computational Science Research Center	<a href="mailto:xgao@csrc.ac.cn">xgao@csrc.ac.cn</a>	An effective eigenchannel R-matrix method for calculating electron-ion scattering processes with spectroscopic precision	ok	China
2	Yasuhiro	Sakai	Dept. of Physics, Toho Univ.	<a href="mailto:sakai@ph.sci.toho-u.ac.jp">sakai@ph.sci.toho-u.ac.jp</a>	Light emission from sputtered or backscattered atoms on tungsten surfaces under ion irradiation	ok	Japan
3	Shuhei	Yamamura	Department of Energy Sciences, Tokyo Institute of Technology	<a href="mailto:yamamura.s.aa@m.titech.ac.jp">yamamura.s.aa@m.titech.ac.jp</a>	Lasing Potential of Extreme Ultraviolet Light Using Recombining Nitrogen Plasma	ok	Japan
4	Toru	Kawamura	Department of Energy Sciences, Tokyo Institute of Technology	<a href="mailto:kawamura@es.titech.ac.jp">kawamura@es.titech.ac.jp</a>	Potential of cold K-alpha radiation generated by an intense ion beam for cold dense plasma diagnostics	ok	Japan
5	Hiroyuki	Sakaue	National Institute for Fusion Science (NIFS)	<a href="mailto:sakaue@nifs.ac.jp">sakaue@nifs.ac.jp</a>	Spectroscopy of highly charged tungsten ions with EBITs	ok	Japan
6	Karin	Takahashi	Department of Physics, Rikkyo University	<a href="mailto:karin@rikkyo.ac.jp">karin@rikkyo.ac.jp</a>	Doubly Excited States and Their Dissociation Processes of Simple Molecules	ok	Japan
7	Chihiro	Suzuki	National Institute for Fusion Science	<a href="mailto:csuzuki@nifs.ac.jp">csuzuki@nifs.ac.jp</a>	Observations of EUV spectra from tungsten and Lanthanide ions in LHD	ok	Japan
8	GUIYUN	LIANG	National Astronomical Observatories, CAS	<a href="mailto:gyliang@bao.ac.cn">gyliang@bao.ac.cn</a>	A simulation package --- SASAL for soft X-ray and EUV spectroscopy of astrophysical and laboratory	ok	China
9	Hajime	Tanuma	Department of Physics, Tokyo Metropolitan University	<a href="mailto:tanuma-hajime@tmu.ac.jp">tanuma-hajime@tmu.ac.jp</a>	Laboratory Experiments for Revealing Soft X-ray Emissions from Solar Wind Charge Exchange	ok	Japan

10	Cuicui	Sang	Department of Physics, Beijing Institute of Technology, Beijing 100081, P. R. China.	<a href="mailto:sangcc@126.com">sangcc@126.com</a>	Energies, Auger and radiative probabilities of doubly-excited states $1s23l3l'$ for Be-like neon	China
11	Takeshi	NISHIKAWA	Graduate School of Natural Science and Technology, Okayama University, 3-1-1 Tsushima-naka, Okayama 700-8530, Japan	<a href="mailto:nisikawa@elec.okayama-u.ac.jp">nisikawa@elec.okayama-u.ac.jp</a>	Atomic process modeling based on plasma microfield	Japan
12	Yunfeng	Xu	University of Science and Technology of China	<a href="mailto:bona@mail.ustc.edu.cn">bona@mail.ustc.edu.cn</a>	Positive and Negative Photoion Spectroscopy Study of Several Polyatomic molecules Using Synchrotron Radiation	China
13	xianjin	Zeng	Hefei National Laboratory for Physical Sciences at the Microscale and Department of Chemical Physics, University of Science and Technology of China, Hefei, Anhui	<a href="mailto:xjzeng@mail.ustc.edu.cn">xjzeng@mail.ustc.edu.cn</a>	Velocity slice imaging study of dissociative electron attachment resonances in CF <sub>4</sub>	China

14	hongkai	Li	Hefei National Laboratory for Physical Sciences at the Microscale and Department of Chemical Physics, University of Science and Technology of China, Hefei, Anhui	<a href="mailto:lhk226@mail.ustc.edu.cn">lhk226@mail.ustc.edu.cn</a>	Velocity slice imaging study of dissociative electron attachment resonances in CF <sub>4</sub>	China
15	Lei	Xia	Hefei National Laboratory for Physical Sciences at the Microscale and Department of Chemical Physics, University of Science and Technology of China, Hefei, Anhui	<a href="mailto:xialstar@mail.ustc.edu.cn">xialstar@mail.ustc.edu.cn</a>	Velocity slice imaging study of dissociative electron attachment resonances in CF <sub>4</sub>	China
16	Yuji	Nakano	RIKEN	<a href="mailto:nakano-y@riken.jp">nakano-y@riken.jp</a>	X-ray and Auger electron study of highly charged ions using resonant coherent excitation	Japan
17	Hiroaki	Nishimura	Institute of Laser Engineering, Osaka University	<a href="mailto:nishimu@ile.osaka-u.ac.jp">nishimu@ile.osaka-u.ac.jp</a>	Quantitative hard x-ray spectroscopy for energy transport in high intensity laser produced plasma	Japan
18	ShanXi	Tian	Department of Chemical Physics University of Science and Technology of China	<a href="mailto:sxtian@ustc.edu.cn">sxtian@ustc.edu.cn</a>	Imaging Dynamics of the Dissociative Electron Attachment to Molecules	China
19	Hangyu	Zhou	Southwestern Institute of Physics	<a href="mailto:zhouhy@swip.ac.cn">zhouhy@swip.ac.cn</a>	Study of EUV spectra from low-Z and medium-Z impurity ions based on a grazing-incidence flat-field EUV spectrometer in HL-2A plasmas	China
20	Yueyin	Qi	Jiaxing College	<a href="mailto:qi_yying@yahoo.com.cn">qi_yying@yahoo.com.cn</a>	Undecided	China

21	Shigeru	MORITA	National Institute for Fusion Science (NIFS)	<a href="mailto:morita@nifs.ac.jp">morita@nifs.ac.jp</a>	Recent progress on the study of atomic spectroscopy in LHD and collaboration with China on high-Z impurity spectroscopy	ok	Japan
22	Jiaolong	Zeng	National university of defense technology	<a href="mailto:jiaolongzeng@hotmail.com">jiaolongzeng@hotmail.com</a>	Radiative opacity of high-Z plasmas by hybrid DLA and DCA models	ok	China
23	Bowen	Li	University College Dublin	<a href="mailto:libw2007@gmail.com">libw2007@gmail.com</a>	Recent progress in source development for EUV lithography and other applications	ok	Ireland
24	Yong	Wu	Institute of Applied Physics and Computational Mathematics, Beijing, China	<a href="mailto:wu_yong@iapcm.ac.cn">wu_yong@iapcm.ac.cn</a>	Theoretical investigation of charge exchange between highly-charged solar wind ions and H&He	ok	China
25	Wenjun	Xiang	Department of Physics, College of Science, National University of Defense Technology	<a href="mailto:xiangwenjun89@163.com">xiangwenjun89@163.com</a>	Double Auger decay rates of single- and double-core-hole states for neon isonuclear sequence	ok	China
26	ATSUSHI	ICHIMURA	Institute of Space and Astronautical Science, JAXA	<a href="mailto:ichimura@isas.jaxa.jp">ichimura@isas.jaxa.jp</a>	Multiple ionization of Ar <sup>2+</sup> by slow highly charged ions	ok	Japan
27	Yongtao	Zhao	Institute of Modern Physics, Chinese Academy of Sciences	<a href="mailto:zhaoyt@impcas.ac.cn">zhaoyt@impcas.ac.cn</a>	Interaction of low energy highly charged ions with solids and plasma	ok	China
28	Dieter	Hoffmann	Technische Universität Darmstadt, Institut für Kernphysik	<a href="mailto:hoffmann@physik.tu-darmstadt.de">hoffmann@physik.tu-darmstadt.de</a>	Undecided		German

29	KeLin	Gao	Wuhan Institute of Physics and Mathematics, CAS, China	<a href="mailto:Klgao@wipm.ac.cn">Klgao@wipm.ac.cn</a>	undecided		China
30	Jun	Yan	Institute of Applied Physics and Computational Mathematics,	<a href="mailto:yan_jun@iapcm.ac.cn">yan_jun@iapcm.ac.cn</a>	undecided		China
31	Yueming	Li	Institute of Applied Physics and Computational Mathematics,	<a href="mailto:li_yueming@iapcm.ac.cn">li_yueming@iapcm.ac.cn</a>	Study of excitation for Alkali-like ions with complete-coupling iteration method	ok	China
32	Zhihu	Yang	Institute of Modern Physics, CAS	<a href="mailto:z.yang@impcas.ac.cn">z.yang@impcas.ac.cn</a>	Visible light emission produced by interaction of highly ionized Krq+ ions with Al surface	OK	China
33	Fumihiro	Koike	Physics Laboratory, School of Medicine, Kitasato University	<a href="mailto:koikef@kitasato-u.ac.jp">koikef@kitasato-u.ac.jp</a>	Theoretical aspects of electron correlations and term dependences in the electronic states of highly charged atomic ions	ok	Japan
34	Linfan	Zhu	University of Science and Technology of China	<a href="mailto:lfzhu@ustc.edu.cn">lfzhu@ustc.edu.cn</a>	Accurate dynamic parameters of noble atoms studied by high-resolution inelastic X-ray scattering	Ok	China